Reconfigurable Microwave Semiconductor Plasma Antenna

S. M. SALMAN

A Thesis Submitted to the University of Sheffield for the Degree of

Doctor of Philosophy in Electronic and Electrical Engineering

February 2017

Abstract

Reconfigurable antennas have been a subject of rapidly increased interest during the past decades. This has been prompted by the increased demand on new wireless communications technology in both civilian and military directions. Moreover, different types of reconfigurations have been identified and investigated to keep up with the demand for new technologies.

In this research, the possibility of designing reconfigurable Dielectric Resonator Antennas (DRAs) have been explored with different types of reconfigurability directions, especially with the increased interest in the area of DRAs during the past three decades. These results have been satisfactory in general. The main aim of this research is to experiment with different reconfigurability designs, each purpose is to achieve one type of reconfigurability or more. This includes, polarisation reconfigurability in Chapter Three, frequency agility in Chapters Four and Five, beam steering and gain agility in Chapter Five. Furthermore, this research main aim has been to investigate new ways to exploit the advantages of the semiconductor plasma in reconfigurable antennas. However, research's limited resources led to reduce the efforts in this area to only one experiment, which is presented in Chapter Six, based on a similar design presented in Chapter Four. Although the results have been conflicted for the last experiment, the results shown that the used reconfigurability medium (AlGaN/GaN HFETs) can be benefitted better from it in other application.

Two models have been introduced for polarisation reconfigurability, a hemispherical DRA couple with reconfigurable annular slot excitation, and a notched rectangular DRA with reconfigurable parasitic strip(s). Both designs shown the possibility of achieving LP/CP radiations.

In addition, rectangular DRAs that are excited with single, as well as multiple, slot have been studied. Prototypes have been built and measured with reasonable agreement between practical and simulated results.

Furthermore, the work has been extended to study a reconfigurable DRA linear array where several designs have been investigated including single and dual-slot for two and four-element linear arrays. The single-slot model reconfiguration resulted in the expected beam steering alongside the array direction. On the other hand, both frequency tuning and beam steering have been achieved with the dual-slots models.

Finally, the semiconductor plasma reconfigurable antennas have been considered with the investigation of AlGaN/GaN HFETs as a replacement for the well investigated and presented silicon SPIN diodes. The prototype has been measure and discrepancies between measurements and simulations have been discussed.

In summary, this research shown the possibility to explore more area in dielectric resonator antennas reconfigurability. This includes, polarisation changing, frequency/mode tuning, beam steering, and gain control. In addition, it has been shown that DRA reconfigurability can benefit in the from semiconductor technology and antenna miniaturisation techniques to operate at higher frequencies with excellent performance.

ACKNOWLEDGMENT

After the praise to the Almighty Allah for all his bestowing on me, I want to thank my parents for their unlimited love and support, alongside the support from my brothers, sister, and the rest of my relatives.

I would like to give my full gratitude to my supervisors, Dr. Salam Khamas and Dr. Greg Cook, for their continuous support, guidance and patience.

I want to thank all my friends who supported my efforts to accomplish this work. In addition, I would like to thank everyone gave me any advice or offered their technical support required in this research.

In addition, special thanks for the Iraqi Cultural Attaché for their support during my studies. Finally, I want my employee, the University of Al-Nahrain in Iraq, for providing me with this opportunity to achieve my goals.

PUBLICATIONS

S. M. Salman, S. K. Khamas and G. G. Cook, "Slot fed SPIN diode reconfigurable dielectric resonator antenna," *Antennas and Propagation Conference (LAPC), 2014 Loughborough*, Loughborough, 2014, pp. 336-339.

Contents

LIST OF FIGURES

LIST OF TABLES

LIST OF ACRONYMS

2DEG	Two-Dimensional Electron Gas
AR	Axial ratio
CP	Circular Polarisation
DRA	Dielectric Resonator Antenna
FET	Field Effect transistor
HFET	Heterostructure Field Effect Transistor
LP	Linear Polarisation
MEMS	Microelectromechanical systems
RDRA	Rectangular DRA
RF	Radio Frequency
SPIN Diode	Surface PIN Diode
TE	Transverse Electric
TEM	Transverse Electromagnetic
TM	Transverse Magnetic

LIST OF SYMBOLS

c Speed of Light in the Vacuum

k_0 Wave Number

ϵ_r Dielectric Constant

λ_0 Free-Space Wavelength

σ Electric Conductivity S/m

Chapter One

Reconfigurable Antennas

1.1 Introduction

Over the last couple of decades, a wide variety of wireless data transfer and communications techniques have been invented and developed for both public civilian as well as private military applications. Each technique may, or may not, share the same frequency band with other techniques, hence a significant proportion of the required hardware infrastructure could be built in the same device such as mobile phones that operate various techniques including Wi-Fi, Bluetooth, 3G, 4G, etc. [1, 2]. This has promoted the need of antennas that can be used as transceiver for more than single frequency band. This could be achieved either by designing a multiple band antenna, which might become extremely complex for more than two bands or by designing a reconfigurable antenna. Nowadays, reconfigurable antennas draw considerable attention owing to the wide range of design techniques and reduced complexity.

1.2 Definition and Classification

Antenna reconfigurability could be defined as the ability to change the radiation properties, such as operating frequency, impedance, bandwidth, polarisation, and/or radiation patterns, by altering the antenna's electrical or mechanical characteristics. Researchers prefer to design antennas by changing a single characteristic at a time while keeping the others unchanged [3].

Antenna reconfiguration could be categorised according to its aim or means, or in other words according to the reconfigured characteristics or mechanism.

1.2.1 Reconfiguration Approaches and Mechanisms

Reconfigurable antennas could be classified according to the employed method to achieve the reconfigurability feature [4]. The used techniques can be categorised as follows:

I. Mechanical Changes Approach:

This is the oldest method, which has been around since the 1930s and it can lead to a wide range of reconfigurability in frequency, azimuth, beam width, etc. [4].

This type of reconfiguration could be implemented by changing one, or more, parameter of the antenna's structure, such as the shape or size. Changing the length of radio aerial might be the simplest example of this type of reconfiguration since varying the length of a quarter wavelength dipole results in a different operating frequency without altering the radiation pattern or bandwidth. This demonstrates the possibility of changing one radiation parameter without any significant change to the other parameters. However, in most cases, it is expected that the change will be in more than one parameter. In addition, parameters simultaneous is not the only challenge that faces engineers, since actuation technique and its impact on the performance and interference with electromagnetism is the other issue to deal with [1, 5-7].

II. Reconfigurable Arrays

It has been shown through numerous studies that several types of array reconfigurations can be achieved by the ON/OFF switching of selected

elements, or by physically altering the position of the array elements. It should be noted that this represents a popular method in radio telescope applications [4, 8, 9].

III. RF Switches

This represents the most common approach to design reconfigurable antennas as the reconfigurability is basically an ON-OFF process that can be achieved using simple switches to establish a connection between two metal plates. These switches could be classified into two categories, semiconductor switches that consist of field effect transistors (FETs), or PIN diodes, and micro-electromagnetic switches (MEMS) [10]. As their name implies, MEMSs are rather small mechanical switches that could be activated using electromagnetic force induced by introducing DC bias. MEMSs have three main types: ohmic, capacitive and cantilever, which can be employed depending on the contact type.

MEMSs offer low insertion losses, high linearity, limited distortion, and they are easier to integrate compared to semiconductor switches. This is in conjunction with a higher frequency range to work with. However, MEMSs have two issues that still need to be considered during the design; first is the discharge sensitivity and heat, which are caused by excessive biasing and temperature. The second issue is due to the mechanical parts and self-actuation, MEMSs can handle a small amount of RF power compared with other semiconductor switches counterparts [11]. However, the significance of these limitations has been minimised recently due to the fabrication advances. Further, MEMS are gaining new acceptance due to the miniaturisation ability that helps to build on-chip MEMS systems [11, 12].

IV. Varactor Diodes

These diodes act as voltage controlled variable capacitors. Their usefulness has been proven in tuning the antennas operating frequency as has been demonstrated in earlier research studies. For example, the lower band of a slotted dual-band monopole antenna has been tuned in a frequency range of 1.6 to 2.23 GHz by sweeping the varactor's capacitance from 0.1 to 0.7 pF [13]. Varactor diodes have been employed in numerous research studies, where viable reconfiguration results have been demonstrated such as improving the performance of microstrip rectangular patches [14], improving the gain and efficiency with frequency tuning for a high gain Partially Reflective Surface (PRS) antenna [15], and enhancing the S_{12} isolation for lower band two 4G designed PIFAs [16]. However, it has been shown that antenna tunability is limited by the capacitance tuning range of the varactor diode. In addition, the equivalent series resistance of the varactor diode can decrease the antenna's efficiency [4].

V. Material Properties Changes

The ability to change material properties such as conductivity, permittivity, permeability, as well as the physical shape, have received considerable attention in designing reconfigurable antennas [1, 4]. As an example, using surface PIN diodes to change the conductivity was the subject of several research studies during the last decade [1-4], and it is one of the main elements of this research and will be discussed in more details later in this chapter.

Further, ferroelectric materials have received attention due to the relation between the dielectric constant and the applied electric field bias, which can be

summarised as [17]

$$n = \frac{\varepsilon(0)}{\varepsilon(E_0)} \quad (1)$$

$$n_r = \frac{\varepsilon(0)-\varepsilon(E_0)}{\varepsilon(0)} = 1 - \frac{1}{n} \quad (2)$$

where, n is the material tunability, $\varepsilon(0)$ is the dielectric constant at zero electric field, E_0 is the applied electric field, $\varepsilon(E_0)$ is dielectric constant at the electric field presence, and n_r is the relative tunability. On the other hand, it should be noted that the tangent loss, $tan(\delta)$, of these materials are not ignorable. In addition, the dielectric constant is sensitive to temperature variation, and with higher dielectric constant, material tunability, tangent loss and temperature sensitivity are higher too. This led to the consideration of an important factor that helps to choose an optimum design, which known as the Commutation Quality Factor (K) and it is quantified as

$$K = \frac{(n-1)^2}{n.tan\delta(U_{min}).tan\delta(U_{max})} \quad (3)$$

where U_{min} and U_{max} are the minimum and maximum applied voltages [17].

Ferroelectric materials have been widely used in scanning applications. One of the examples is a microstrip antenna with a substrate that is made of a modified $Ba_{0.65}Sr_{0.35}TiO_3$ ceramic polymer composite. This highly tunable composite has been used with an applied voltage of up to 200 V resulting in a scanning margin over 30° [18]. A steerable dielectric resonator phased array antenna was designed in conjunction with a tunable loaded line phase shifter with barium strontium titanate (BST) to fabricate a metal-insulator-metal (MIM) varactor. A control voltage of up to 50 V has been applied, which resulted in a beam steering range of ±30° [19].

Using similar method to ferroelectric materials, the permeability of a ferrite material will be affected by applied magnetic field. A rectangular microstrip antenna with a ferrite substrate has been tuned over nearly three octaves using an axial DC magnetic field along the excitation [20]. Another example is a tuned helical antenna that is based on a ten layer ferrite LTCC package with the antenna DC biased to be used as magnetic field excitation source beside its role as an antenna. This method helped in reducing the antenna size as well as cutting the demagnetisation effect. The antenna has the advantage of a 10% tuning range with an unbiased state operating frequency around 13 GHz [21]. A dielectric resonator quasi TE_{011} mode was tuned using a DC based ferrite rod placed in the centre of the resonator, and a 3.4% frequency tuning has been reported with a desirable quality factor aver tuning range [22].

Piezoelectric materials are usually used for reconfiguration actuation. One of these examples is the bonding of a piezoceramic material (PZT) with a thick metallised substrate to bend it inside and outside in order to steer the beam of a cylindrical shaped reflector [23]. Another work suggested using a PZT material for switching activation in tuning an inverted-F antenna from ~1.23 GHz at no actuation status down to 1.15 GHz at full activation [24]. A microstrip antenna circular mode has been reconfigured into RHCP and LHCP using two piezoelectric transducers that are connected to the antenna. The reconfiguration has been activated by connecting one of the transducers to the aperture and disconnect the other resulting in an axial ratio of less than 1 dB [25].

Electromagnetic-bandgap (EBG) structures provide bandgap properties of damping surface-waves propagation due to its metal-dielectric periodic structure [26]. It has been demonstrated in an earlier study that a compact size EBG based reconfigurable antenna is feasible [27]. In that study, a quasi-Yagi based microstrip antenna with MEMS

adjustable EBG cells has been designed to be used for pattern reconfiguration, which resulted in a 360° azimuth coverage reconfiguration in the upper half of the antenna. In another study, PIN diodes have been used to build active cylindrical EBG structure based antenna by providing active Partial Reflecting Surface (PRS) with discontinuous metallic strips [28], where the beam-width has been reconfigured by controlling the PINs status.

The introduction of metamaterials that allow electromagnetic field smart control has opened the door for a new line of reconfigurable antennas research in particular with the distinctive properties of negative refractive index, phase velocity, permittivity and permeability. The attention has been given to the resonance frequency tuning as well as achieving reconfigurability in impedance bandwidth, beam steering, beam width agility, and pattern reconfiguration [29]. For example, metamaterial based reconfigurable PRS that are controlled using a varactors grid has been reported, where it has demonstrated that by changing the varactors, the capacitance of the metamaterial, and subsequently reflection and transmission coefficients, change, which shifts the centre frequency [30].

Antenna reconfigurability using electric properties of the liquid crystals gained a lot of attention since the turn of the current millennia. Permittivity in liquid crystals is tunable by applying DC voltage to the material. It has been reported that the permittivity of the material can be tune up to 30% [31, 32]. A tunable liquid crystal microstrip patch antenna achieved 4% frequency tuning around 5 GHz operating frequency with radiation efficiencies ranges from 20% with 0 V DC bias up to 40% when 10 V DC bias was applied [33]. On the other hand, a folded reflecarray antenna based on liquid crystal substrate achieved beam steering range of ±6º at operating frequency at 78 GHz, with gain reaching up to 29.7 dBi. In addition, it has been shown that this antenna can be suitable for two-dimensional beam agility under the proper DC biasing application [34].

1.2.2 Characteristics Reconfiguration and Mechanism Selection

Although there is no specific method to design a reconfigurable antenna or to choose the most suitable technique, it is possible to assign the reconfigured antenna characteristics with the proper techniques. For example, while all the mentioned techniques are good for reconfiguring the frequency response, switches and material changes are the most useful to reconfigure the polarisation [1, 35].

Therefore the following three steps need to be followed [35]:

1. Choosing the required characteristic that needs to be reconfigured as there are four main antenna reconfigurations characteristics, operating frequency, polarisation, radiation pattern, hybrid or compound reconfiguration.
2. According to the antenna to be used and its type, it is possible to enclose the suitable techniques within the antenna
3. From the valid techniques and the required reconfiguration, it should be possible to decide on the technique with the best advantages and minimum effects on the antenna characteristics that are not supposed to change as well as a marginal effect on the antenna impedance.

A summary of the characteristics reconfiguration available in the literature can be itemised as [1, 35]:

Frequency reconfigurable antennas: This type deals with frequency tuning and it involves two categories; continuous and switchable tuning. The first is achieved by a smooth change in the operating frequency, or frequency band, using tunable materials or components that change their status in an indiscrete

way. This includes varactors diodes, mechanical changes and material changes. On the other hand, switchable tuning is used for hopping from one operating frequency, or band, to another. This is mostly achieved using RF switches, although mechanical changes have demonstrated high reliability for switchable reconfigurable frequency antennas. Several examples have been discussed in the previous subsection such as those reported in [14] and [25], while examples of using RF switches will be discussed in a later section.

Polarisation reconfigurable antennas: Polarisation is attributed to the current flow direction, which needs to be controlled in order to change the polarisation. In addition, current behaviour is related to the feed type and position, antenna's structure and material [1]. Therefore, reconfiguring the polarisation could be achieved for circular and/or linear polarisation by altering the feed or antenna structure using RF switches, or material changes for cases such as microstrip antennas with tunable substrate [36].

Radiation pattern reconfigurable antennas: Radiation patterns depend on the current distribution. This could be shown from antennas' basic radiation equation [37]

$$\vec{I}L = Q\vec{v} \qquad (4)$$

where $\vec{I}$ is the time-changing current (A/s), L is the length of the current element (m), Q is the charge (C), and $\vec{v}$ is time change of velocity of the charge (m/s^2) [37].

This makes it difficult to change the radiation pattern without affecting the operating frequency since manipulating the current distribution needs structural changes [1]. Literature shows that this type of reconfiguration could be achieved using mechanical changes, array tuning and materials changes, such

as those listed in [28].

Compound reconfigurable antennas: This is followed to alter more than one characteristic of the antenna simultaneously or separately. Usually uses electronic control for a large number of switches such as an aperture consisting of electrically small patches connected by RF switches. The necessary structure arrangement of the ON/OFF switches should be determined, for the needed characteristics, with the aid of an optimisation algorithm [38].

1.3 Advantages and Disadvantages

Reconfigurable antennas offer numerous advantages over their conventional counterparts by designing a single antenna that performs the functionality of multiple antennas. Although this usually provides economic benefits, these benefits cannot be achieved all the time, since reconfigurable antennas for some applications need extra costly parts and control system to achieve better performance, which leads to a performance versus cost optimisation dilemma [1].

Furthermore, it is possible to accomplish a smaller compact design that is suitable for many applications such as those used in portable devices. However, this depends on the type of the antenna and reconfigurability as well as the used device to control it. Recent studies have been reported for integrated reconfigurable antenna technology where multiple possibilities to create a number of configurations have been demonstrated for multiple cases [1, 39, 40].

Technology advances in both software and hardware also facilitate the design of software controlled reconfigurable antennas that are capable of

accommodating new wireless communications requirements for devices that have been introduced prior to the development of these technologies. This can be achieved by a straightforward update to the device software [39]. The advantages of reconfigurable antennas can be summarised as [41]: Multiple operations in a single system, which minimise the cost and volume, allows integration, and control mutual coupling effects. In addition, these antennas eliminate the need for filtering and enhance out-of-band rejection. Furthermore, software control provides extra capabilities to interact with different situations. On top of that, reconfigurable antennas are suitable for multi-task operations.

On the other hand, reconfigurability needs a control element, which results in a complex design since a power source is generally needed to derive the control mechanism. This results in an additional operation cost, which in some cases could be considerably expensive. However, in a smaller design, this may not exceeds few AAA batteries. Each additional circuit and connection will affect the radiation, polarisation and operating frequency, and extra isolation and/or proper arrangement must be considered. In many cases, changing the operating frequency requires one matching circuit or more to keep the gain as high as possible. In the cases of more complex designs, this will result in a considerably higher cost [1].

Although it has been shown that reconfigurable antennas design may represent a real challenge, the benefits exceed the drawbacks if the proper mechanism is adopted and a proper design methodology is followed.

1.4 Reconfigurable Semiconductor Antennas

Reconfigurable semiconductor antennas could be classified into two types: RF/Microwave semiconductor switches and semiconductor plasma. Semiconductor switches, as mentioned before, have two devices that are widely used to connect/disconnect metallic plates and parts; PIN diodes and FETs. Semiconductor plasma could be achieved by injecting high amount of charge carriers inside a semiconductor solid-state medium, and could be classified into two types depending on the carriers' injection technique: DC bias injected plasma or laser illumination injected plasma [1, 4].

1.4.1 RF/Microwave Semiconductor Switches

These types are widely known as solid-state switches. PIN diodes and FETs have some differences, which could be summarised as follows [4]:

- ON/OFF control: PIN diode is controlled by a DC signal, and activated by turning ON the current source, while FETs are controlled by the gate voltage and must be turned ON by turning OFF the source of the control while keeping the drain-source voltage ON. This may lead to the need of some complexity in the driver circuits for PIN diodes *due to the need for current control and protection circuit*.
- At higher RF radiation power, PIN diodes need lower DC activation power compared to FETs.
- PINs are more immune to electrostatic discharge damage.
- PINs OFF capacitance could be reduced by applying a higher reverse voltage, while the FETs' OFF capacitances are much less affected by

reverse voltage.

- PIN diodes have a higher switch Figure-Of-Merit (FOM) compared to FETs as explained in the following paragraph. On the other hand, there is no lower limit for the FETs, while PINs diodes have a lower operating frequency limit, which is generally around ten Mega Hertz.

The FOM defines the switching cutoff frequency f_c, which is nearly ten times the highest operating frequency limit of the switch. FOM is defined as following [4]

$$f_c = \frac{1}{2\pi C_{off} R_{on}} \qquad (5)$$

where, C_{off} is the reverse bias or OFF capacitance and R_{on} is the forward bias or ON resistance of the switch.

A PIN diode consists of an intrinsic semiconductor wide layer (I), with two end regions that are heavily doped in order to create the P-type and N-type layers that can be used for ohmic contacts of the DC bias as shown in Figure 1.1.

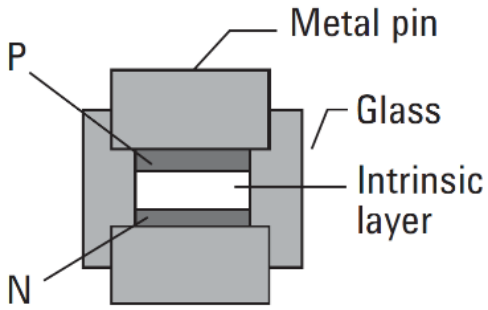

Figure 1.1 PIN Diode Layout [5].

When a forward bias is applied, the equivalent circuit of the diode is illustrated in Figure 1.2(a), which consists of a series parasitic inductance (L) and a very low resistance (R_S).

The value of L depends on the geometry of the diode, while the resistance value is inversely proportional to the applied current, and it can be in the order of few ohms or even a fraction of an ohm.

The reverse bias will result in the equivalent circuit shown in Figure 1.2(b). The total capacitance C_T consists of the parasitic capacitance C_P and diode junction capacitance C_J. The value of the capacitance could be reduced by applying a higher reverse voltage. The high value reverse resistance R_P results from the depletion of the I-region of charge.

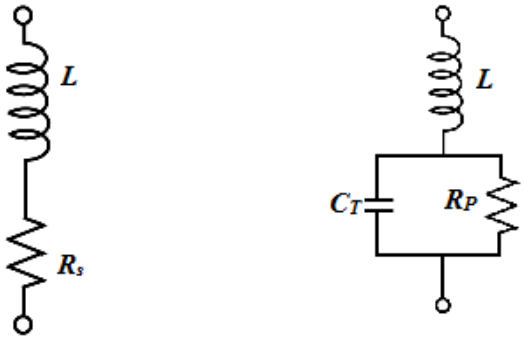

(a) (b)

Figure 1.2 PIN diode Equivalent Circuits, (a) Forward Bias, (b) Reverse Bias

A field effect transistor (FET) diagram is illustrated in Figure 1.3. The FET operates by applying a voltage between the drain D and the source S to drive a current through the channel while controlling the amount of passing carriers by applying a voltage controlled electromagnetic field that creates a depletion region inside the channel. If the controlled voltage that is applied between the gate G and the source S exceeds a certain point (V_P), the depletion region will be large enough to cut the channel and stop the current's flow.

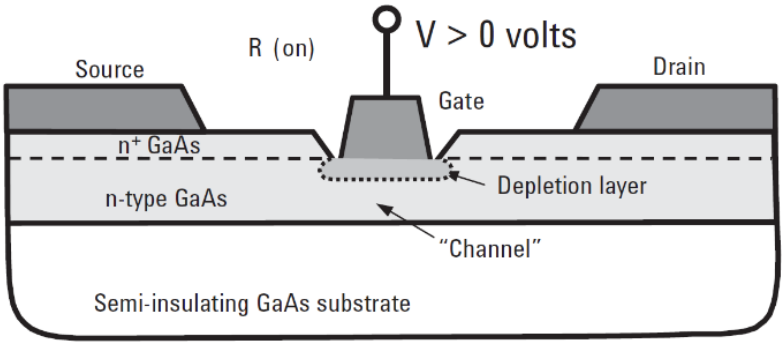

(a)

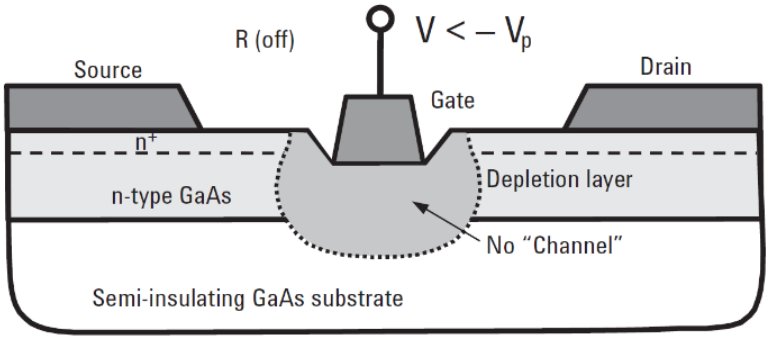

(b)

Figure 1.3 FET Configuration [10], (a) FET ON, (b) FET OFF

1.4.2 Reconfigurable Plasma Antennas

Recent interest in developing plasma antennas has emerged from the fact that plasma has good electrical conductivity (σ) range of from around 10^4 S/m to around couple of hundred thousand S/m or even more under the condition of existing high density of charge carriers. The ability of disappearance provides a higher speed of reconfiguration over other types especially the mechanically reconfigured antennas. Furthermore, tuning ability, size and the possibility of replacing metallic parts have attracted considerable attention in both civilian and military applications [42, 43].

Plasma antennas could be classified into two types; gas plasma and

semiconductor plasma. The second type could be categorised according to its activation technique, i.e. optical or a DC bias activation. Each type will be discussed in this Chapter, but the main focus will be on the DC bias activated semiconductor plasma because it is the basis of the design in the last Chapter.

I. Gas Plasma Antenna

The generation of plasma in a gas medium regained a noticeable research interest during the first decade of this century. As an alternative to metallic antennas with controlled conductivity, as well as the ability of instantaneous disappearance, gas plasma antennas have been considered for a number of military applications [44, 45].

Transmitting and receiving RF/microwave frequencies, stealth, reconfigurability, acting as reflectors against certain frequencies, security against electronic warfare, capability of using mechanical reconfigurability means, and noise reduction were the main proved advantages of this antenna type [46]. The major problem is that gas must be contained inside plastic, or glass, tubes, which is vulnerable to fraction. However, this can be solved using appropriate materials to protect the tube from excessive heating.

Three parameters are essential in the design of plasma antennas; plasma frequency (ω_p), reflective index (n) and plasma conductivity (σ). These parameters can be calculated using the following equations [47]:

$$\omega_p = \sqrt{\frac{n_0 e^2}{m_e \varepsilon_0}} \tag{6}$$

$$n^2 = \varepsilon_r = 1 + \frac{{\omega_p}^2}{\omega(j\nu - \omega)} = 1 - \left[\frac{{\omega_p}^2}{\nu^2 + {\omega_p}^2}\left(1 + j\frac{\nu}{\omega}\right)\right] \tag{7}$$

$$\sigma = \frac{\varepsilon_0 \omega_p^2}{v} \quad (8)$$

where, n_0 is the electron density in m^{-3}, e is the charge density of the electron in C, m_e is the electron mass in kg, ε_0 is vacuum permittivity, ε_r is the complex relative permittivity of the plasma, ω is the frequency in rad/sec, and v is the electron natural collision frequency in Hz.

From equations (7) and (8) it can be noticed that the only variable is the plasma frequency, which is dependent on the electron density as illustrated in equation (6). As a result, equation (8) can be re-written as

$$\sigma = \frac{\varepsilon_o}{v} \frac{n_o e^2}{m_e \varepsilon_o} = \frac{n_o e^2}{v m_e} \quad (9)$$

This means that gas medium plasma antenna behaviour and characteristics can be reconfigured by controlling the electron density inside the medium. This can be achieved by changing either the applied electrical charging power or the applied pressure on the gas. Furthermore, it is possible to find the relation between carrier mobility and plasma conductivity using the following equation [47]

$$\mu_e = \frac{\sigma}{e n_e}, \text{ or } \sigma = \mu_e e n_e \quad (10)$$

Several research articles have been published on the design of gas plasma antennas such as monopole, dipole, loop, reflector antennas and frequency selected surfaces (FSSs). One of the earliest designs is a plasma folded monopole antenna using laser guided electric discharge in the atmosphere. The resulting radiated/received signal power had ±1 dB variation compared to its Copper counterpart, with the thermal noise being the only noticeable major

problem [41]. Another research has investigated the design of a dipole antenna using two gas filled glass tubes to represent plasma columns [48]. The result of that research demonstrated the effects of applied power on the antenna effective length and the relation of the resonance frequency with plasma frequency and plasma effective length. In addition, the use of a circle of other controlled columns around the plasma dipole as either reconfigurable plasma cylindrical antenna, cylindrical antenna with a director, or parabolic cylindrical antenna has been investigated and validated in [48]. These studies also included a reconfigurable reflector around a monopole antenna with a pattern controlled using gas plasma inside fluorescent tubes that are distributed circularly around the monopole, and by ON/OFF switching of specific fluorescent tubes, the beam has been steered to 0°, 90°, and 180° directions with a gain of 6.7 dBi and an 87% efficiency [49]. The same idea has been followed by distributing 40 tubes around a monopole in a square shaped distribution, and 8 beam shapes of the radiation pattern have been created by choosing the reflecting tubes alongside the original omnidirectional radiation pattern of the monopole when all the tubes are OFF [50]. Furthermore, gas plasma has proved its usefulness in replacing metallic parts of a frequency selective surface (FSS) applications, with the plasma offer filtering and tuning capacity by changing the plasma density. This is beside the stealth ability that can be achieved by simply switching the system ON and OFF. Reflectivity scaling factor was needed to obtain current modes similar to that of a perfectly conducting FSS array to achieve the desired results. This work has been experimented on two designs; switchable band stop filter and switchable reflector [51].

II. Optically Induced Semiconductor Plasma

Solid-state plasma has generated a noticeable interest in the reconfigurable antenna research, especially with the advances in semiconductor technologies, which paved the way to the emergence of new flexible antenna technology. One of the most popular techniques to create a semiconductor plasma is to apply light with the proper wavelength on the semiconductor substrate. If the illumination power is greater than the semiconductor's band gap, electron-hole pairs will be induced inside the medium leading to the creation of a plasma medium with sufficient carrier density [51].

The calculation of the relative complex permittivity demonstrates a difference compared to that used with the gas medium plasma. This can be attributed to two main reasons: Firstly, is the contributions of both electrons and holes effect that is included in the resulting equations (11 and 12), and secondly is the fact that a semiconductor crystal lattice causes high dielectric constant values due to its polarizability. The free carriers interact with polarizability of the crystal lattice of the semiconductor which leads to reducing the dielectric constant. This effect is a function of frequency as shown in the following equations [52]

$$\varepsilon_p = \varepsilon_r - \sum_{i=e,h} \frac{\omega_{pi}^2}{\omega^2 + v_i^2}\left(1 + j\frac{v_i}{\omega}\right) \tag{11}$$

$$\omega_{pi}^2 = \frac{n_i e^2}{m_i^* \varepsilon_0}, (i = e, h) \tag{12}$$

where i=e, h refers to the electrons and holes, m* is the effective mass of electrons and holes, and ε_r is the relative permittivity of the semiconductor without plasma.

Earlier studies demonstrate that achievable carrier density of 10^{17} to 10^{18}

carrier/cm^3 is sufficient to get a semi-metallic response from the substrate [53, 54]. Several designs were evaluated at microwave and Terahertz frequencies. Silicon and other semiconductor compounds have been investigated both theoretically and practically to create reconfigurable antennas. For example, a slot-coupled microstrip patch antenna has been designed to be reconfigured by optically induced plasma in the semiconductor substrate at the end tip of the feeding stub. This is to change the amplitude of the radiation pattern, which has been dropped by ~20 dB by increasing the concentration of the carriers from 0 to 4.5×10^{18} carriers/m^3. The technique was used to control an array of patch antennas [51]. Beam steering in the range of ±15° has been achieved for a millimetre-wave antenna using photo-induced plasma gratings (PIPG) in a Silicon plate. The aperture, which is fed using tunnel-coupled dielectric waveguide, has been induced with plasma using a light pumping through various photo masks to create both linear and elliptic polarisations [55]. An investigation of using Indium Antimonide in building THz range dimer antennas proved that with the plasmonic resonance there is an improvement in the field enhancement factor by 100-1000 times. This depends on choosing the proper dimensions of the rods and the gap. Furthermore, the carriers' concentration photo-tuning ability allows choosing an enhancement factor for an optimised application [54].

A conductivity of 16000 S/m, is possible to be achieved for a Silicon wafer with carriers density of 10^{18} carrier/cm^3, μ_e= 800 cm^2/V.s (maximum), μ_h=200 cm^2/V.s, and e=1e.V= 1.60217657 C [56, 57]. Although this conductivity is incomparable with Copper's conductivity (5.96×10^7 S/m), it is sufficient for most of the RF and Microwave applications.

III. Semiconductor Plasma Antennas Using Surface PIN Diodes

The ability of inducing carriers in a semiconductor using DC biasing means it is possible to eliminate the need of a light source, which results in a simpler design. The main element in this type is the Surface P-I-N diode, or basically an S-PIN diode. These lateral devices were designed to allow a sufficient carrier density, which provides semi-metallic components that can be activated using a DC control [58]. Numerous designs have been reported during the last decade that demonstrated the viability of using S-PIN diodes as plasma channels providing a good control on the desired radiation pattern and frequency.

The S-PIN diode is a basic element that acts as a Plasma Island when a sufficient DC power is applied. It specifies the shape of the antenna's radiating and non-radiating regions. Silicon is the preferred semiconductor material in fabricating these diodes due to a number of parameters such as a low forward biasing resistance. In addition, the high resistive Silicon wafer allows higher carriers lifetime. Furthermore, multilayer structures are used that provides lower RF loses. This is in conjunction with a large size fabrication available at a minimised cost, widely available fabrication technology as well as excellent mechanical and thermal properties in comparison with other semiconductor materials. At the same time, implementing SPIN diodes using other popular semiconductor materials such as GaAs is usually associated with difficulties and restrictions such as a difficult and expensive interconnection in conjunction with a lower electron mobility that causes limitations in some designs [59].

The SPIN diode that is illustrated in Figure 1.4 is similar to a regular PIN diode with an intrinsic channel between N and P regions that have a 2×10^{16} electrons

and holes density per cm^3 at the metal contacts' ends [60].

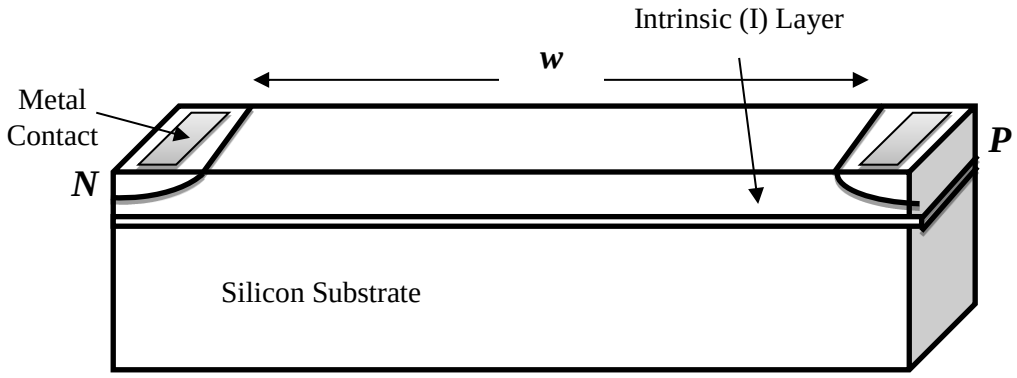

Figure 1.4 SPIN Diode Device Diagram

The diode length (*w*) is determined by the carrier diffusion length, which is equal the square of the multiplication of carrier lifetime (~5μs for Si) and a diffusion constant (estimated about $35cm^2/s$ for Si). This means that a diode of 100-200 μm length is capable of providing a carrier density of 10^{18} carrier/cm^3 in the case of 2-3 skin depth layer thickness, which depends on the frequency range. Extending the length to several hundreds of micrometres will allow carrier concentration in the range of 10^{16}-10^{17} carrier/cm^3, which is useful in many applications. Choosing the width of the diode is also important because of the losses in carrier density due to the side walls reflection and absorbing [58]. In order to minimise this effect, the width of the diode must be not less than 100μm. The intrinsic layer is based on a highly resistive silicon substrate and separated from it by a thin oxide layer. The metal contacts dimensions should be minimised as much as possible, i.e. shorter than 0.1*w*, so that the device can totally disappears at the 'OFF' state. It is also useful to cover the top of the diode with a moisture protection material such as phosphorus-doped silica glass (PSG) [61]. Lateral trenches are used to separate the adjacent diodes for electrical isolation.

Unlike the bulky RF switches, the SPIN diodes are dynamically defined switches that are implemented on the surface of a dielectric substrate using an uncomplicated available technology, which allows high resolution definition of antennas. Further, SPIN diodes are designed to achieve specific conductivity characteristics, which leads to its main drawback of dimensional and, hence, operating range limitation, while RF switches, such as conventional PIN diodes, depend on several parameters such as isolation, switching time, and the breakdown voltage. This also suggests that RF switches may have different shapes rather than rectangular, e.g. cylindrical, while the SPIN diodes are mainly lateral devices. Nonetheless, the advantages of the SPIN diodes allow them to replace RF switches in many applications, especially where circuit integration required.

IV. Previous Designs for Reconfigurable Antennas Using SPIN Diodes

The first published papers on employing SPIN diodes for the reconfigurable antennas designs have reported monopole, dipole, and *x-y* grid that has been used for several designs and eventually was used as binary holographic antenna as described later in this section [58, 62-64].

Other designs that will be discussed in this section include a reconfigurable leaky wave microstrip antenna design [65], and waveguides with reconfigurable slots [2, 59, 61, 66, 67].

A reconfigurable monopole with four sections, which is illustrated in Figure 1.5, has been reported in [64]. The first section is a metal wire with a length of 10.8 mm, while the other three sections have equal lengths of 5.5 mm and consist of SPIN diodes that are connected in series with each other. Each diode

is 0.5 mm long. The experiment has been carried out by turning 'OFF' all active elements, then by turning 'ON' the first one, first two, and all the three SPIN diodes, respectively. This results in shifting down the operating frequency as a result of increasing the overall monopole length. The operating frequencies for each case are 3.25 GHz, 2GHz, 1.6 GHz, and 1.5 GHz respectively. It has been noted that the physical length of the antenna in each case is less than quarter the wavelength by a range of ~ 1:2. This is owing to the effects of the dielectric substrate, which reduces the effective wavelength as expected.

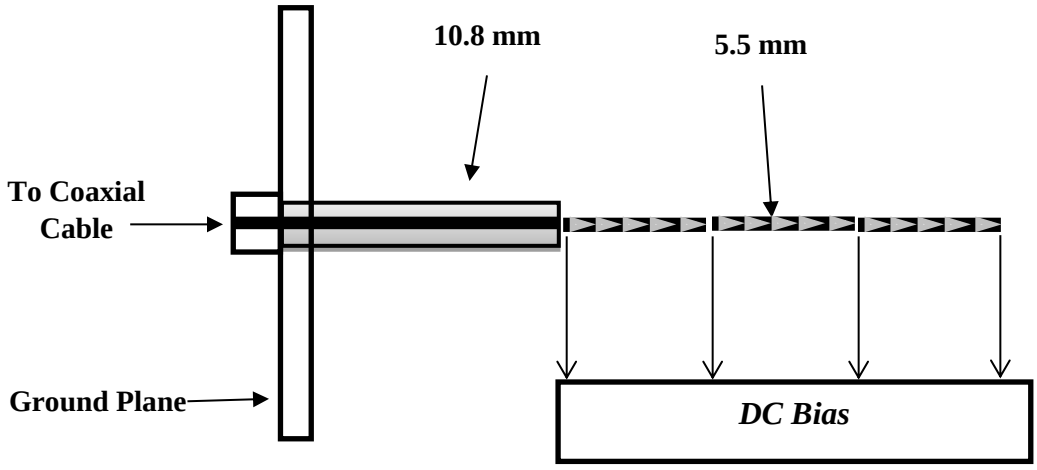

Figure 1.5 Reconfigurable Monopole [58]

The same article proposed a cross dipole design with five sections in each leg as illustrated in Figure 1.6. This allows the antenna to operate in a frequency range of 2-20 GHz. This experimental has been conducted using two different lengths for the SPIN diodes; 200 µm and 140 µm. The antenna response has been improved by 4 dB using the smaller dimensions, which proves the calculations of the best SPIN diodes length.

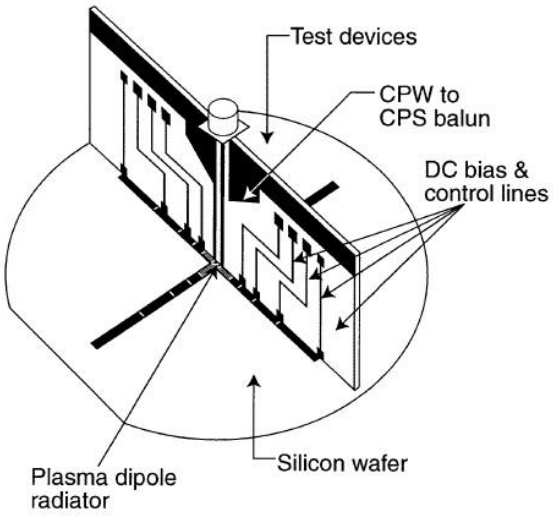

Figure 1.6 Reconfigurable Cross Dipole [58]

Figure 1.7 illustrates a general view of an *x-y* grid reconfigurable antenna [60], which includes from bottom to the top: DC bias and control circuit board, feeding pins for the diodes passing through dielectric holder, and SPIN diodes silicon wafer that is covered by a dielectric composite to allow proper propagation with feeding dipole on the top.

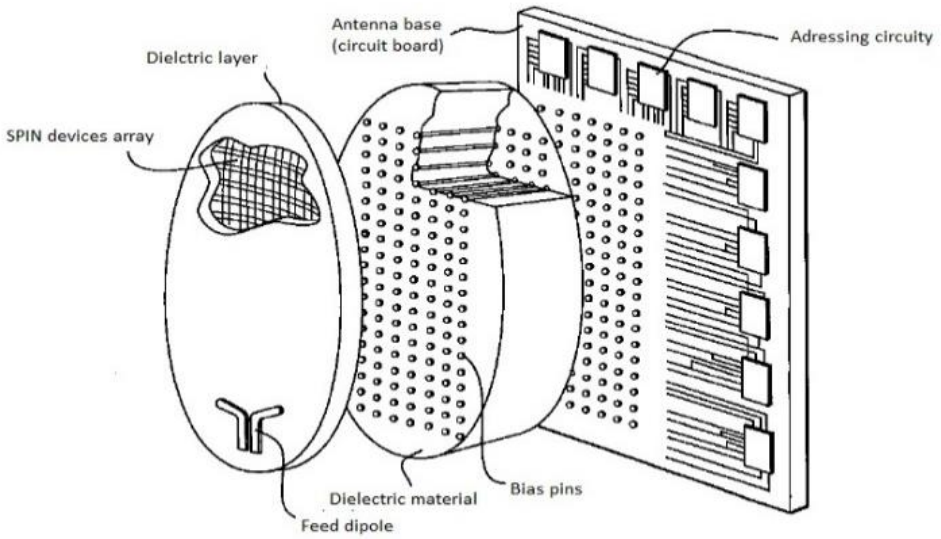

Figure 1.7 x-y Grid Block Diagram [60]

Figures 1.8(a) and (b) show simplified distributions of the (250×250) μm^2 diodes with the purpose of demonstrating the creation of reconfigurable dipole and loop antennas.

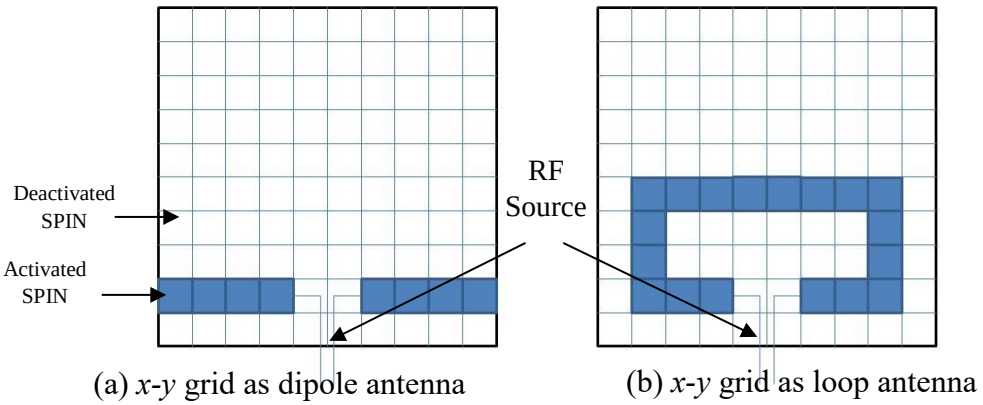

Figure 1.8 x-y Grid Diagram and Configuration

Figure 1.9 demonstrates how to use the grid to represent a binary holographic antenna, where the white and black regions represent 'ON' and 'OFF' SPIN diodes respectively [60].

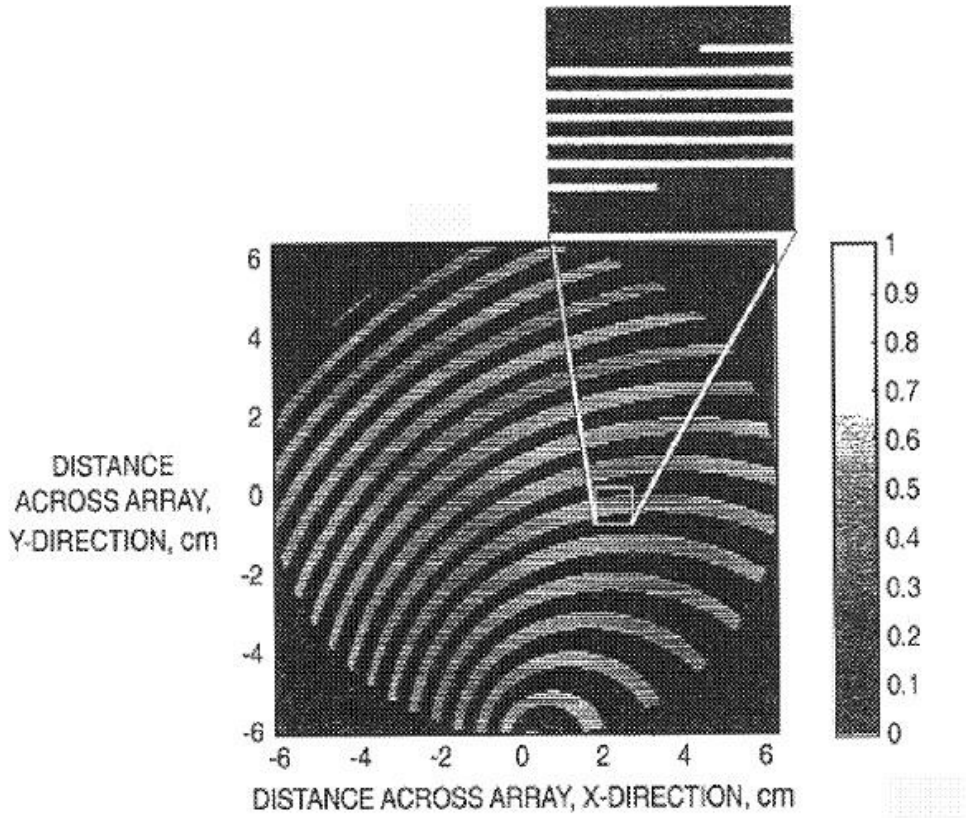

Figure 1.9 Reconfigurable Holographic Antenna [60]

A reconfigurable leaky-wave microstrip antenna has been reposed in [65]. As

illustrated in Figure 1.10, a metallic sheet with a width of '*W*' and a length of '*L*' that is fed through a strip line on a 350 μm thick highly resistive silicon substrate. The substrate is positioned on a reflective metallic reflector. Choosing L=2.5λ, has demonstrated that by activating the series of SPIN diodes, the width of the microstrip antenna can be expanded, which leads to a beam angle steering. Also, this can result in changing the cut-off frequency.

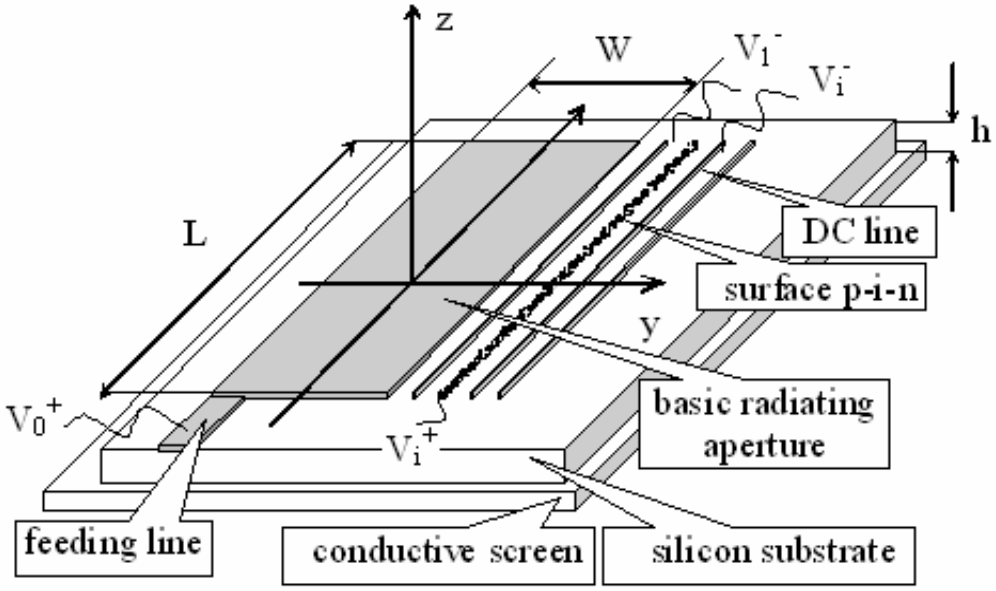

Figure 1.10 Reconfigurable Microstrip Antenna [65]

A couple of designs have been reported for a rectangular waveguide with a reconfigurable aperture [67]. In the first, a series of inclined slots have been placed on the narrow wall of the waveguide as illustrated in Figure 1.11. Each slot contains two SPIN diodes that are connected to a metallic connector, which covers almost half the reconfigurable slot aperture area. Three combinations have been suggested to introduce a variable distance between the leaky slots by switching the SPINs 'ON' and 'OFF' periodically, the one to switch OFF initially is the first diode of each five 'OPEN SLOT' and turn the other four ON 'CLOSED SLOTS'. This will create a 1 OFF-4 ON-1 OFF combination (or simply

1-4ON-1). Using the same idea, 1-6ON-1 and 1-8ON-1 combinations have been created. This design is useful in reconfiguring the radiation pattern for a fixed frequency or changing the operating frequency for a fixed radiation direction, although this demonstrates reconfigurability in discrete steps.

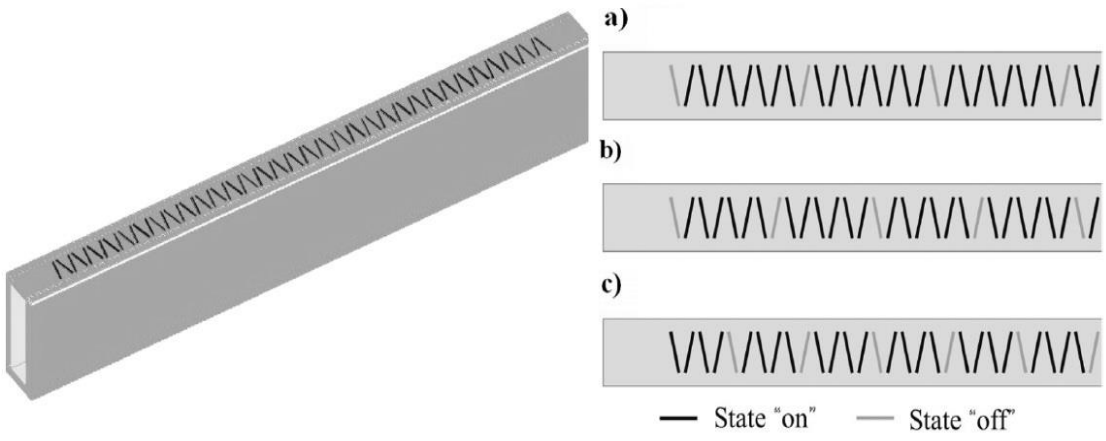

Figure 1.11 Reconfigurable Aperture Waveguide [67]

The second model used two approaches as shown in Figure 1.12. The first employs four single slots, while the second employs four pairs with shift between the paired slots. Similar to the first model, the slots were placed on the narrow side of the waveguide. In both cases with opening on a slot/pair (SPIN OFF) and activating other slots closed (SPINs ON). This results in changing the frequency bandwidth for an operating frequency of 36.5 GHz. The results also demonstrate high losses in the activated slots which, theoretically should not radiate. The best radiation has been achieved when the slot closest to the source is 'OPEN'.

The use of SPIN diodes also demonstrates compatibility for sub-THz frequencies as well as mm-wave frequencies. By using the second model with four single slots array, this design has been investigated at frequency of ~ 360 GHz. The results stated that at this range of frequencies, the plasma conductivity must be at least in the order of hundreds Siemens per meter, which is much higher than that required for frequency range of tens

of Giga Hertz, to be considered as metallic like regions [59].

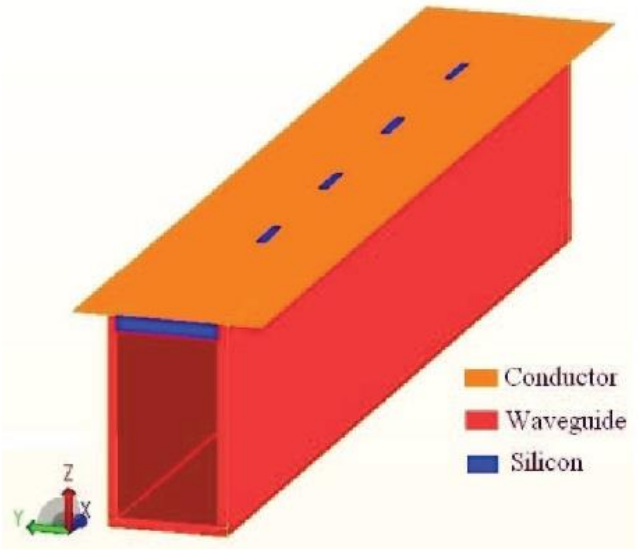

(a) Waveguide General View

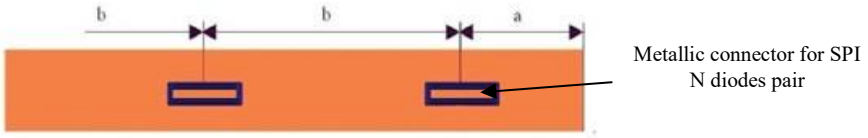

(b) Single Slot Array Top View

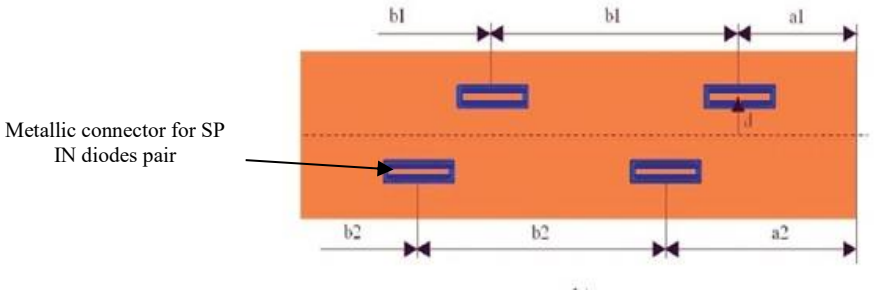

(c) Shifted Paired Slots Array Top View

Figure 1.12 Reconfigurable Aperture Waveguide [66]

1.5 Fabrication Challenges

The choice of the best available material for the SPIN diodes fabrication represents a clear challenge. As explained earlier, the most suitable material for plasma antenna is Silicon owing to the high carrier life time, large size, low cost, good mechanical and thermal properties and the availability of high quality technology. On the other hand, it has been reported that other materials such as GaAs crystalline has been studied theoretically [59, 66], where a considerable manufacturing difficulty has been demonstrated due to the connection requirements as well as the high MMIC cost for in the used range of frequencies. This is in conjunction with a relatively high cost due to low carrier life time, which limits the size of the device.

It should be noted that the dimensions' limitation represents a key challenge for using a semiconductor plasma to create high frequency antennas. The thickness of the silicon SPIN diode required to create enough carriers for plasma is around 2-3 times the skin depth, which ranges between 35µm and 50µm. Furthermore, the length of the I-region is 100-200 µm to obtain the required 10^{18} carrier/cm^3. However, if the length is in the order of several hundreds of microns, then carrier density in the order of 10^{17} carrier/cm^3 can be obtained, which is sufficient for many applications. The same requirements apply for other semiconductor compounds such as GaAs that require even shorter dimensions, hence it is suitable for limited size applications [66].

The manufacturing process involves creating the SPIN on a high resistive silicon substrate and separate it by a thin layer of isolator such as SiO_2 to ensure that carriers are isolated from the substrate bulk and confined to the active layer.

Using Silicon overcomes most of the fabrications difficulties, while using other materials requires more complex processes and fabrications, which increases the fabrication cost.

In this research, AlGaN/GaN Heterostructure Field Effect Transistor (HFET) has been proposed and used to convey plasma islands instead of SPIN diodes. This is mainly because of budget limits and the availability of the materials and manufacturing facilities inside the university.

The structure of HFET is as shown in Figure 1.13, where it can be noticed that the HFET has three terminals, source, drain and gate, with the same control mechanism, i.e. it is similar to the traditional FET. This type consists of a thin $Al_xGa_{x-1}N$ layer, which has a wide band gap, thicker GaN and a substrate that is usually made of a sapphire [68]. A two dimensional electron gas (2DEG) sheet will be created around AlGaN/GaN connection. Studies have shown that in the thin volume of the confined sheet, carriers' density could be in the order of a single digit multiplied by 10^{12} per cm^2. While the volume density is variable, in some areas it exceeds 10^{20} per cm^3 [69, 70]. These numbers are promising for a device that confines a strong plasma islands. On the other hand, it will be very tricky to describe it as the ideal choice for solid state plasma applications, due to a rather small size, which limits the skin depth due to the thin plasma region.

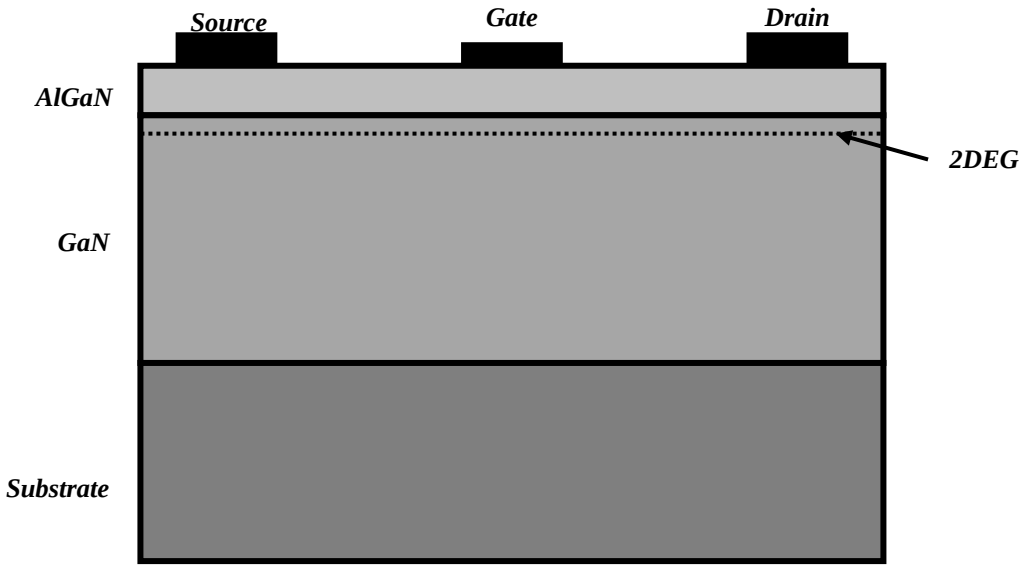

Figure 1.13 HFET Layout

1.6 Integration of Reconfigurable Antennas

Advancements in technology have allowed integration in all areas of communications, and reconfigurable antennas are not an exception. The MEMS are promising in this area due to the ease of integration with low power requirements, low loss and distortion factors [13]. This have been demonstrated in numerous papers over the last decade, such as an 8×8 pixel patch antenna, which, can alter the operation of the antenna in multiple ways [71], and an active phase shifter (APS) based on two 1-bit MEMS to control vector sum method through two low noise amplifiers. These two MEMS cooperate with Wilkinson power divider to provide a (0°/180°) shift each, which allows a 360° shift. These components have been implemented using the SiGe process [72].

Furthermore, it has been demonstrated that SPIN diodes offer considerable benefits as discussed in the previous section. Simple silicon integration techniques provided excellent results [1, 2, 58].

The recent advances in the integration of reconfigurable antennas and new requirements of new applications such as multiple input multiple output (MIMO) channels and cognitive radios have introduced the software controlled reconfigurable antennas, using techniques such as FPGA and microcontrollers [72].

1.7 Harmonics Generation Due to Active Devices

Active semiconductor devices used to control antennas reconfigurability and in active integrated antennas (AIA), such as PIN and varactor diodes, are non-linear devices, which causes to generate harmonics for the fundamental operating frequencies[73]. The non-linearity of these devices cannot be ignored for various reasons since this can generate high harmonics distortion, notable radiation at harmonics frequencies, and notable gain reduction. Furthermore, multi-input multi-output (MIMO) systems can have a serious

case of harmonics intermodulation, especially when different ports operate at different frequencies [74, 75].

A couple of articles has been published discussing the issue of modes harmonics generations in active antennas and how to deal with it in mode generation and its harmonics in active integrated antennas (AIA) such as patch microstrip antennas and dielectric resonator antennas. It has been suggested that a shorting pin alongside a slot loaded antenna to reduce the return losses of the second and third harmonics by 6.7 dB and 17.7 dB respectively in a patch antenna [76]. A miniaturised microstrip-fed slot antenna has been achieved with great suppression rate for the second and third harmonics [77]. The second harmonic in a slot-coupled rectangular DRA by inserting extra two slots parallel to the feeding aperture. It has been shown, with careful calculations, it is achievable to tune the second harmonic for this configuration without having a major effect on the impedance characteristics of the resonance mode fundamental frequency [78].

Harmonics generated due to active elements non-linearity have been theoretically and practically with the aim to reduce its effects. A frequency-tunable microstrip line-fed printed antenna has been designed with varactor diodes as active frequency tuning elements. The second and third harmonics have been reduced by mismatching the antenna impedance at the harmonics frequencies [75]. A reconfigurable fractal dipole antenna has been design with open circuit stub to eliminate higher order harmonics generated due to the use of three pairs PIN diodes. In addition, DC blockers and DC lines also contributed to the elimination of suppression of the harmonics where the second order harmonic has been totally eliminated [79]. Other methods to eliminate harmonics, such as turning OFF PIN diodes with reverse DC bias instead of just turning the bias OFF, since the RF power can cause the generation of the harmonics within the diode. In addition, reducing mutual

coupling and inserting harmonics traps can be useful in harmonics suppression, especially in the case of intermodulation in MIMO systems [80].

1.8 Thesis Outline

In this research, the main focus has been to investigate the possibilities of reconfiguring dielectric resonator antennas using semiconductor switches. Hence, the research goal is to deliver new contributions in this field. This has been achieved by modifying conventional dielectric resonator antennas and to study the possibility of establishing a reliable reconfigurable dielectric resonator antenna theoretically and practically. Thus, this work can be divided into the following:

1. Chapter One: This chapter has established the theory of the reconfigurable antennas in addition to adequate amount of literature review.
2. Chapter Two: The theory of dielectric resonator antennas and its analysis will be introduced, along with some mathematical analysis. In addition, several shapes and excitation techniques will be discussed. Furthermore, an introduction to reconfigurable DRA designs will be reviewed. Finally, the theory of antenna arrays and DRA arrays will be discussed.
3. Chapter Three: Two designs are introduced in this chapter for antenna polarisation reconfigurability. Both designs have shown reasonable and encouraging results.
4. Chapter Four: Frequency agility and mode reconfiguration have been studied in this chapter. All designs based on microstripline-fed reconfigurable-slots coupled dielectric resonator antenna. The reconfigurable slots turning ON/OFF contribute to the changes in the DRA field excitement process, which in turn change the operating TE mode.
5. Chapter Five: Reconfigurable DRA arrays based on the designs introduced in

Chapter Four have been studied and analysed. Although the results were below overall satisfaction, the concept has been proven, and with a better-chosen design, these results can be improved.

6. Chapter Six: A reconfigurable semiconductor plasma dielectric resonator antenna has been studied based on chapter four first design. The semiconductor plasma medium has been switched from silicon SPIN diode to AlGaN/GaN HFET, which resulted in conflicted results, since the device proven to work properly, however, it proven unsuitable the chosen application due to its complexity and its frequency operating range.
7. Chapter Seven: Thesis summary will be introduced in the final chapter with brief discussion. In addition, few suggestions for future work will discussed.

1.9 Summary

Although the use of reconfigurable antennas dates back to the first half of the last century, the subject had evolved dramatically over the last two decades due to the unprecedented advances in modern digital communications.

The techniques used in antenna reconfiguration were defined and classified into two systems. The first was according to the used technique, which ranged from mechanical changes and array rearrangement to electrically controlled RF switches and varactor diodes, in addition to material changes approach. The second classification was according to the antennas' reconfigured property, which includes frequency, polarisation, radiation pattern, and hybrid reconfiguration.

Since this work is focused on semiconductor plasma reconfigurable antennas, this topic received more attention compared other types, taking into consideration, and compare,

the performance with respect to its counterparts in both semiconductor RF switches and gas plasma antennas.

The employed techniques in semiconductor plasma have been reviewed, and the use of AlGaN/GaN HFET as an alternate to silicon-over-isolator (SOI) SPIN diodes has been discussed briefly, as it will be discussed in more details in a later Chapter.

The introduction of integration techniques in reconfigurable antenna systems had shown its advantages, and how more promising designs could be achieved that utilise the capability of a dedicated software control. This approach allows the creation of a new generation of highly adaptable, large scale controlled reconfigurable antenna elements. This facilitates employing the existing reconfigurable antennas in new communications techniques using only software updates that are uploaded to system controllers such as FPGAs and microcontrollers.

References

[1] J. T. Bernhard, "Reconfigurable Antennas," Synthesis Lectures on Antennas, vol. 2, no. 1, pp. 1-66, 2007/01/01 2007.

[2] Y. Yashchyshyn, K. Derzakowski, and J. Modelski, "Extending Functionalities of Waveguide Slot Antennas by Means of Reconfigurable Aperture," in Microwave Conference, 2008. EuMC 2008. 38th European, 2008, pp. 258-261.

[3] J. T. Bernhard, "Reconfigurable Multifunction Antennas: Next Steps fot the Future," in Microwave, Antenna, Propagation and EMC Technologies for Wireless Communications, 2007 International Symposium on, 2007, pp. K2- 1-K2- 4.

[4] R. L. Haupt and M. Lanagan, "Reconfigurable Antennas," IEEE Antennas and Propagation Magazine, vol. 55, no. 1, pp. 49-61, 2013.

[5] J. T. Bernhard, E. Kiely, and G. Washington, "A smart mechanically actuated two-layer electromagnetically coupled microstrip antenna with variable frequency, bandwidth, and antenna gain," IEEE Transactions on Antennas and Propagation, vol. 49, no. 4, pp. 597-601, 2001.

[6] J. C. Langer, J. Zou, C. Liu, and J. T. Bernhard, "Micromachined reconfigurable out-of-plane microstrip patch antenna using plastic deformation magnetic actuation," IEEE Microwave and Wireless Components Letters, vol. 13, no. 3, pp. 120-122, 2003.

[7] B. Tomasic, J. Turtle, L. Shiang, R. Schmier, S. Bharj, and P. Oleski, "The geodesic dome phased array antenna for satellite control and communication - subarray design, development and demonstration," in Phased Array Systems and Technology, 2003. IEEE International Symposium on, 2003, pp. 411-416.

[8] E. Kiely, G. Washington, and J. Bernhard, "Design and development of smart

microstrip patch antennas," Smart materials and structures, vol. 7, no. 6, p. 792, 1998.

[9] H. Steyskal, J. K. Schindler, P. Franchi, and R. J. Mailloux, "Pattern synthesis for TechSat21 - a distributed space-based radar system," IEEE Antennas and Propagation Magazine, vol. 45, no. 4, pp. 19-25, 2003.

[10] Agilent_Technologies, "Understanding RF/Microwave Solid State Switches and their Applications," Literature no. 5989-7618EN, 2010.

[11] P. D. Grant, M. W. Denhoff, and R. R. Mansour, "A Comparison between RF MEMS Switches and Semiconductor Switches," in MEMS, NANO and Smart Systems, 2004. ICMENS 2004. Proceedings. 2004 International Conference on, 2004, pp. 515-521.

[12] N. Haridas et al., "Reconfigurable MEMS Antennas," in Adaptive Hardware and Systems, 2008. AHS '08. NASA/ESA Conference on, 2008, pp. 147-154.

[13] H. Mirzaei and G. V. Eleftheriades, "A Compact Frequency-Reconfigurable Metamaterial-Inspired Antenna," IEEE Antennas and Wireless Propagation Letters, vol. 10, pp. 1154-1157, 2011.

[14] R. B. Waterhouse and N. V. Shuley, "Frequency agile microstrip rectangular patches using varactor diodes," in Antennas and Propagation Society International Symposium, 1992. AP-S. 1992 Digest. Held in Conjuction with: URSI Radio Science Meeting and Nuclear EMP Meeting., IEEE, 1992, pp. 2188-2191 vol.4.

[15] A. R. Weily, T. S. Bird, and Y. J. Guo, "A Reconfigurable High-Gain Partially Reflecting Surface Antenna," IEEE Transactions on Antennas and Propagation, vol. 56, no. 11, pp. 3382-3390, 2008.

[16] C. Yoon, S. G. Hwang, G. C. Lee, H. C. Lee, and H. D. Park, "A reconfigurable antenna using varactor diode for LTE MIMO applications," Microwave and

Optical Technology Letters, vol. 55, no. 5, pp. 1141-1145, 2013.

[17] A. Tagantsev, V. Sherman, K. Astafiev, J. Venkatesh, and N. Setter, "Ferroelectric materials for microwave tunable applications," Journal of electroceramics, vol. 11, no. 1-2, pp. 5-66, 2003.

[18] Y. Yashchyshyn and J. W. Modelski, "Rigorous analysis and investigations of the scan antennas on a ferroelectric substrate," IEEE Transactions on Microwave Theory and Techniques, vol. 53, no. 2, pp. 427-438, 2005.

[19] M. Nikfalazar et al., "Steerable Dielectric Resonator Phased-Array Antenna Based on Inkjet-Printed Tunable Phase Shifter With BST Metal-Insulator-Metal Varactors," IEEE Antennas and Wireless Propagation Letters, vol. 15, pp. 877-880, 2016.

[20] R. K. Mishra, S. S. Pattnaik, and N. Das, "Tuning of microstrip antenna on ferrite substrate," IEEE Transactions on Antennas and Propagation, vol. 41, no. 2, pp. 230-233, 1993.

[21] F. A. Ghaffar and A. Shamim, "A Ferrite LTCC Based Dual Purpose Helical Antenna Providing Bias for Tunability," IEEE Antennas and Wireless Propagation Letters, vol. 14, pp. 831-834, 2015.

[22] J. Krupka, A. Abramowicz, and K. Derzakowski, "Tunable dielectric resonator bandpass filter," in Microwaves, Radar and Wireless Communications. 2000. MIKON-2000. 13th International Conference on, 2000, vol. 2, pp. 517-520 vol.2.

[23] Y. Hwan-Sik and W. Gregory, "Piezoceramic actuated aperture antennae," Smart Materials and Structures, vol. 7, no. 4, p. 537, 1998.

[24] K. Aljonubi, R. J. Langley, I. Reaney, and A. O. AlAmoudi, "Piezoelectric reconfigurable antenna," in Antennas and Propagation Conference (LAPC), 2013 Loughborough, 2013, pp. 47-50.

[25] S. H. Hsu and K. Chang, "A Novel Reconfigurable Microstrip Antenna With Switchable Circular Polarization," IEEE Antennas and Wireless Propagation Letters, vol. 6, pp. 160-162, 2007.

[26] Y. Li, F. Mingyan, C. Fanglu, S. Jingzhao, and F. Zhenghe, "A novel compact electromagnetic-bandgap (EBG) structure and its applications for microwave circuits," IEEE Transactions on Microwave Theory and Techniques, vol. 53, no. 1, pp. 183-190, 2005.

[27] Y. Xue-Song, W. Bing-Zhong, and W. Weixia, "Pattern reconfigurable patch antenna with two orthogonal quasi-Yagi arrays," in 2005 IEEE Antennas and Propagation Society International Symposium, 2005, vol. 2B, pp. 617-620 vol. 2B.

[28] A. Edalati and T. A. Denidni, "Reconfigurable Beamwidth Antenna Based on Active Partially Reflective Surfaces," IEEE Antennas and Wireless Propagation Letters, vol. 8, pp. 1087-1090, 2009.

[29] G. Oliveri, D. H. Werner, and A. Massa, "Reconfigurable Electromagnetics Through Metamaterials—A Review," Proceedings of the IEEE, vol. 103, no. 7, pp. 1034-1056, 2015.

[30] A. Ourir, S. N. Burokur, and A. D. Lustrac, "Electronically reconfigurable metamaterial for compact directive cavity antennas," Electronics Letters, vol. 43, no. 13, pp. 698-700, 2007.

[31] F. Yang and J. R. Sambles, "Determination of the permittivity of nematic liquid crystals in the microwave region," Liquid Crystals, vol. 30, no. 5, pp. 599-602, 2003/05/01 2003.

[32] S. Mueller et al., "Broad-band microwave characterization of liquid crystals using a temperature-controlled coaxial transmission line," IEEE Transactions on

Microwave Theory and Techniques, vol. 53, no. 6, pp. 1937-1945, 2005.

[33] L. Liu and R. J. Langley, "Liquid crystal tunable microstrip patch antenna," Electronics Letters, vol. 44, no. 20, pp. 1179-1180, 2008.

[34] S. Bildik, S. Dieter, C. Fritzsch, W. Menzel, and R. Jakoby, "Reconfigurable Folded Reflectarray Antenna Based Upon Liquid Crystal Technology," IEEE Transactions on Antennas and Propagation, vol. 63, no. 1, pp. 122-132, 2015.

[35] J. Costantine, Y. Tawk, and C. Christodoulou, Design of Reconfigurable Antennas Using Graph Models (Design of Reconfigurable Antennas Using Graph Models). Morgan & Claypool, 2013, p. 148.

[36] P. J. Rainville and F. J. Harackiewicz, "Magnetic tuning of a microstrip patch antenna fabricated on a ferrite film," IEEE Microwave and Guided Wave Letters, vol. 2, no. 12, pp. 483-485, 1992.

[37] K. Fleisch and J. Kraus, "Electromagnetics with applications," New York: McGraw-Hill, 1999.

[38] L. N. Pringle et al., "A reconfigurable aperture antenna based on switched links between electrically small metallic patches," IEEE Transactions on Antennas and Propagation, vol. 52, no. 6, pp. 1434-1445, 2004.

[39] J. Costantine, Y. Tawk, S. E. Barbin, and C. G. Christodoulou, "Reconfigurable Antennas: Design and Applications," Proceedings of the IEEE, vol. 103, no. 3, pp. 424-437, 2015.

[40] C. G. Christodoulou, Y. Tawk, S. A. Lane, and S. R. Erwin, "Reconfigurable Antennas for Wireless and Space Applications," Proceedings of the IEEE, vol. 100, no. 7, pp. 2250-2261, 2012.

[41] Z. Dai, S. Liu, Y. Chen, and N. G. Nanjing, "Development and investigation of reconfigurable plasma antennas," in Microwave and Millimeter Wave Technology

(ICMMT), 2010 International Conference on, 2010, pp. 1135-1137.

[42] R. Kumar and D. Bora, "A reconfigurable plasma antenna," Journal of applied physics, vol. 107, no. 5, p. 053303, 2010.

[43] R. Kumar and D. Bora, "Wireless communication capability of a reconfigurable plasma antenna," Journal of Applied Physics, vol. 109, no. 6, p. 063303, 2011.

[44] I. Alexeff, T. Anderson, S. Parameswaran, E. P. Pradeep, J. Hulloli, and P. Hulloli, "Experimental and theoretical results with plasma antennas," IEEE Transactions on Plasma Science, vol. 34, no. 2, pp. 166-172, 2006.

[45] M. Pourbagher, J. Nourinia, and N. Pourmahmud, "Reconfigurable plasma antennas," Indian Journal of Science and Technology, vol. 5, no. 6, pp. 2928-2932, 2012.

[46] A. Fridman and L. A. Kennedy, Plasma physics and engineering. CRC press, 2004.

[47] T. Dwyer, J. Greig, D. Murphy, J. Perin, R. Pechacek, and M. Raleigh, "On the feasibility of using an atmospheric discharge plasma as an RF antenna," IEEE Transactions on Antennas and Propagation, vol. 32, no. 2, pp. 141-146, 1984.

[48] H. Ja et al., "A Reconfigurable Monopole Antenna With Fluorescent Tubes Using Plasma Windowing Concepts for 4.9-GHz Application," IEEE Transactions on Plasma Science, vol. 43, no. 3, pp. 815-820, 2015.

[49] T. Yamamoto and T. Kobayashi, "A reconfigurable antenna using fluorescent lamps," in Antennas and Propagation (ISAP), 2014 International Symposium on, 2014, pp. 89-90.

[50] T. Anderson, I. Alexeff, and J. Raynolds, "Plasma frequency selective surfaces," in Plasma Science, 2003. ICOPS 2003. IEEE Conference Record - Abstracts. The 30th International Conference on, 2003, p. 237.

[51] T. Fukusako, H. Shiraishi, S. Itakura, Y. Kasano, and N. Mita, "Microstrip adaptive array antenna using semiconductor plasma and genetic algorithm," in Microwave Conference, 1999 Asia Pacific, 1999, vol. 1, pp. 76-79 vol.1.

[52] A. Jonscher, "Solid state plasma phenomena," British Journal of Applied Physics, vol. 15, no. 4, p. 365, 1964.

[53] M. R. Chaharmir, J. Shaker, M. Cuhaci, and A. R. Sebak, "Novel photonically-controlled reflectarray antenna," IEEE Transactions on Antennas and Propagation, vol. 54, no. 4, pp. 1134-1141, 2006.

[54] V. Giannini, A. Berrier, S. A. Maier, J. A. Sánchez-Gil, and J. G. Rivas, "Scattering efficiency and near field enhancement of active semiconductor plasmonic antennas at terahertz frequencies," Optics express, vol. 18, no. 3, pp. 2797-2807, 2010.

[55] V. A. Manasson, L. S. Sadovnik, V. A. Yepishin, and D. Marker, "An optically controlled MMW beam-steering antenna based on a novel architecture," IEEE Transactions on Microwave Theory and Techniques, vol. 45, no. 8, pp. 1497-1500, 1997.

[56] "http://www.ioffe.ru/SVA/NSM/Semicond/Si/electric.html#Basic (11-02-2014)."

[57] "http://www.ele.uri.edu/Courses/ele533/mobility.html (11-02-2014)."

[58] A. E. Fathy et al., "Silicon-based reconfigurable antennas-concepts, analysis, implementation, and feasibility," IEEE Transactions on Microwave Theory and Techniques, vol. 51, no. 6, pp. 1650-1661, 2003.

[59] Y. Yashchyshyn, K. Derzakowski, and P. Bajurko, "Reconfigurable semiconductor antenna for sub-THz frequencies," in Antennas and Propagation (EuCAP), 2013 7th European Conference on, 2013, pp. 537-540.

[60] G. C. Taylor, A. Rosen, A. E. Fathy, P. K. Swain, and S. M. Perlow, "Surface PIN

device," ed: Google Patents, 2003.

[61] Y. Yashchyshyn, J. Marczewski, and D. Tomaszewski, "Investigation of the S-PIN Diodes for Silicon Monolithic Antennas With Reconfigurable Aperture," IEEE Transactions on Microwave Theory and Techniques, vol. 58, no. 5, pp. 1100-1106, 2010.

[62] G. C. Taylor, S. M. Perlow, A. Rosen, A. E. Fathy, S. Kanamaluru, and M. Esherbiny, "Reconfigurable antenna," ed: Google Patents, 2003.

[63] A. Fathy et al., "Silicon based reconfigurable antennas," in Microwave Symposium Digest, 2001 IEEE MTT-S International, 2001, vol. 1, pp. 377-380 vol.1.

[64] A. Fathy, A. Rosen, F. McGinty, G. Taylor, S. Perlow, and M. ElSherbiny, "Silicon based reconfigurable antennas," in Antennas and Propagation Society International Symposium, 2000. IEEE, 2000, vol. 1, p. 325 vol.1.

[65] Y. Yashchyshyn and J. Modelski, "A reconfigurable leaky-wave microstrip antenna," in 2005 European Microwave Conference, 2005, vol. 1, p. 4 pp.

[66] Y. Yashchyshyn and K. Derzakowski, "Reconfigurable antenna for mm-wave spatial multiplexing," in Microwave Radar and Wireless Communications (MIKON), 2012 19th International Conference on, 2012, vol. 1, pp. 243-246.

[67] Y. Yashchyshyn, J. Marczewski, K. Derzakowski, J. W. Modelski, and P. B. Grabiec, "Development and Investigation of an Antenna System With Reconfigurable Aperture," IEEE Transactions on Antennas and Propagation, vol. 57, no. 1, pp. 2-8, 2009.

[68] M. A. Khan, A. Bhattarai, J. Kuznia, and D. Olson, "High electron mobility transistor based on a GaN-AlxGa1− xN heterojunction," Applied Physics Letters, vol. 63, no. 9, pp. 1214-1215, 1993.

[69] J. Tirado, J. Sanchez-Rojas, and J. Izpura, "2D simulation of static surface states in AlGaN/GaN HEMT and GaN MESFET devices," Semiconductor science and technology, vol. 20, no. 8, p. 864, 2005.

[70] Y. Chang, K. Tong, and C. Surya, "Numerical simulation of current–voltage characteristics of AlGaN/GaN HEMTs at high temperatures," Semiconductor science and technology, vol. 20, no. 2, p. 188, 2005.

[71] B. A. Cetiner, H. Jafarkhani, Q. Jiang-Yuan, Y. Hui Jae, A. Grau, and F. D. Flaviis, "Multifunctional reconfigurable MEMS integrated antennas for adaptive MIMO systems," IEEE Communications Magazine, vol. 42, no. 12, pp. 62-70, 2004.

[72] E. Ozturk, M. H. Nemati, M. Kaynak, B. Tillack, and I. Tekin, "SiGe process integrated full-360° microelectromechanical systems-based active phase shifter for W-band automotive radar," IET Microwaves, Antennas & Propagation, vol. 8, no. 11, pp. 835-841, 2014.

[73] M. J. Cryan, G. R. Buesnel, and P. S. Hall, "Analysis and control of harmonic radiation from active integrated oscillator antennas," IEEE Transactions on Microwave Theory and Techniques, vol. 50, no. 11, pp. 2639-2646, 2002.

[74] J. B. Yan, S. Yong, and J. T. Bernhard, "Intermodulation and Harmonic Distortion in Frequency Reconfigurable Slot Antenna Pairs," IEEE Transactions on Antennas and Propagation, vol. 62, no. 3, pp. 1138-1146, 2014.

[75] I. Elfergani et al., "Reconfigurable antenna design for mobile handsets including harmonic radiation measurements," IET microwaves, antennas & propagation, vol. 6, no. 9, pp. 990-999, 2012.

[76] S. Kwon, B. M. Lee, Y. J. Yoon, W. Y. Song, and J.-G. Yook, "A harmonic suppression antenna for an active integrated antenna," IEEE Microwave and Wireless Components Letters, vol. 13, no. 2, pp. 54-56, 2003.

[77] H. Kim and Y. J. Yoon, "Microstrip-fed slot antennas with suppressed harmonics," IEEE transactions on antennas and propagation, vol. 53, no. 9, pp. 2809-2817, 2005.

[78] A. Guraliuc, G. Manara, P. Nepa, G. Pelosi, and S. Selleri, "Harmonic tuning for Ku-band dielectric resonator antennas," IEEE Antennas and Wireless Propagation Letters, vol. 6, pp. 568-571, 2007.

[79] S. A. Hamzah, M. Esa, N. N. N. A. Malik, and M. K. H. Ismail, "Reconfigurable harmonic suppressed fractal dipole antenna," in Microwave Conference Proceedings (APMC), 2012 Asia-Pacific, 2012, pp. 800-805: IEEE.

[80] J.-B. Yan, S. Yong, and J. T. Bernhard, "Intermodulation and harmonic distortion in frequency reconfigurable slot antenna pairs," IEEE Transactions on Antennas and Propagation, vol. 62, no. 3, pp. 1138-1146, 2014.

Chapter Two

Dielectric Resonator Antennas

2.1 Introduction

In 1939, the first paper was published to prove that various shape dielectrics could be used as high frequency resonators, with the mathematical calculations for the values of the resonance frequencies and dielectric losses [1]. Since then, dielectric resonators have been employed in communications systems over the first half of the twentieth century. However, they have been used mainly as energy storage units in microwave circuits with the dielectrics used have high dielectric constants and high unloaded Q-factor [2]. This energy storage appears due to electromagnetic waves induced inside a dielectric will be reflected from the walls back and forth. The interaction between these reflected waves results in the stored energy in the form of a standing wave [3].

In the early 1980s, the interest in these dielectric components has been shifted towards using them as radiating antenna elements in their own right. One of the main reasons behind this growing interest is the rapid increase in the used frequency range. This forces the antenna engineers to face the dilemma of low efficiency metallic antennas at high frequencies such as the millimetre wave range. In contrast, the main source of power losses in dielectric resonators is due to imperfect dielectric properties [4]. The increased interest has been demonstrated by the huge influx of published papers and patents in this area. It has been reported that more than 800 papers and numerous patents have been published by the end of the first decade of the 21st century in conjunction with two books that are already heavily cited in this literature [5]. Further, by the end of 2015, searching

the exact phrase "Dielectric Resonator Antenna" at IEEE XPLORE (http://ieeexplore.ieee.org/) alone returned 1140 publications.

2.2 DRA Characteristics

Dielectric resonator antennas offer major properties that provide a considerable design flexibility [4]. Firstly, the dielectric size is related to the free-space wavelength, λ_0, by a factor of $\lambda_0/\sqrt{\varepsilon_r}$, where ε_r is the material's dielectric constant. As a result, smaller dielectric dimensions are needed due to the decrease in wavelength. Further, the size can be reduced further using a material with a higher permittivity. In addition, the Q-factor is a function of the dielectric aspect ratio, which gives the designers more options. On top of that, there many materials types with low loss characteristics that allow the design of efficient antennas. Additionally, wide range of operating frequencies is possible owing to availability of a comprehensive range of dielectric constants.

Finally, several modes could be excited in the same antennas which provide several radiations patterns at different frequencies. These modes are mainly labelled as the transverse electric (TE) and transverse magnetic (TM) and associated with an axis that refers to the direction in which the electric or magnetic component vanish respectively [2]. The mode with the lowest resonance frequency usually called the dominant mode [4].

These characteristics provide a wide range of options to choose from in the design of efficient antennas. However, this can also add some complexity to the design, and fabrication might be somewhat expensive depending on the material type and the excitation requirements. This is mostly related to complex DRA geometries as will be discussed later in this Chapter as well as the high precision in the dimensions that are required in some applications.

2.3 Shapes and Modes

There are several dielectric resonator geometries that have been studied in the literature as illustrated in Figure 1. The most commonly used dielectric resonator antennas shapes are: hemispherical, cylindrical and rectangular. Some other special shaped dielectric resonators have also been studied for antenna characteristics improvements. Some of these shapes are illustrated in Figure 2.1 d to r [2, 4].

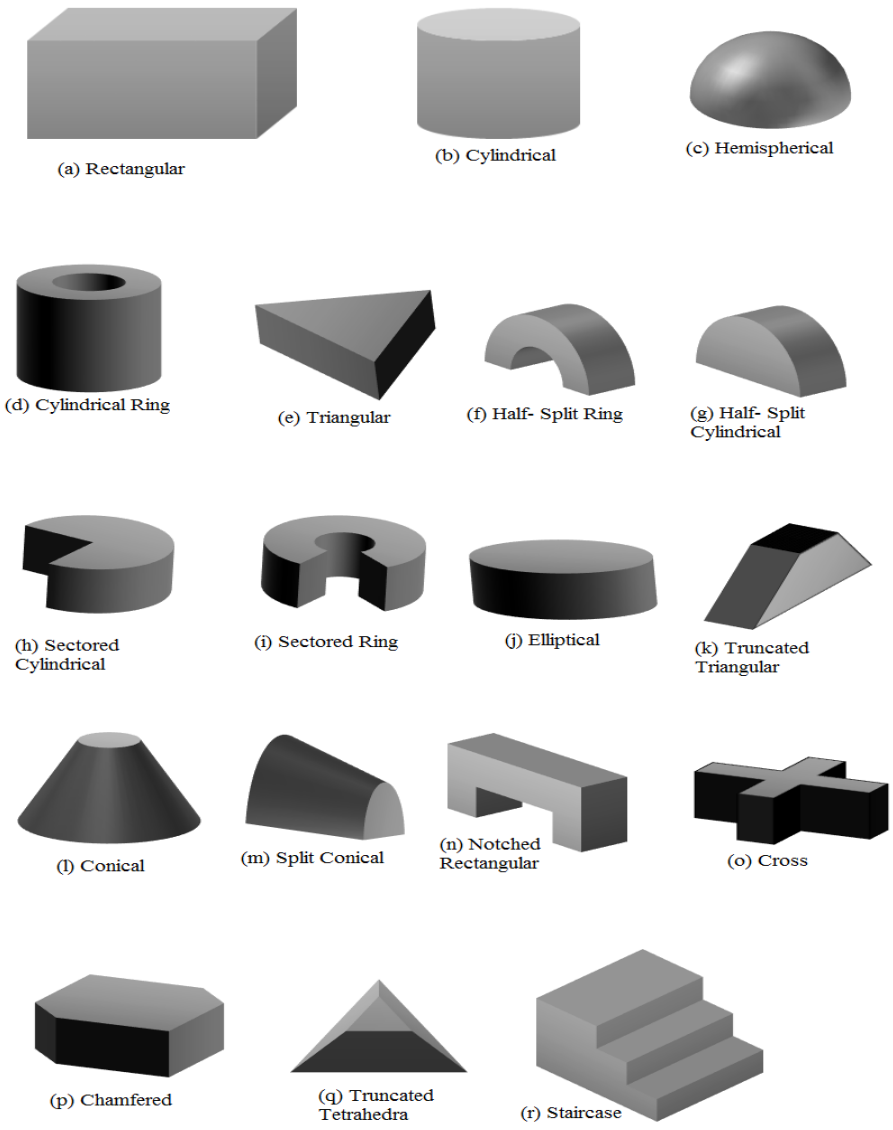

Figure 2.1 Various Dielectric Resonators Shapes [2, 4]

2.3.1 Standard Dielectric Resonators Shapes and Their Modes

i. Hemispherical DRA:

In 1967, a study has been published on the electromagnetic resonance of a spherical dielectric [6]. Investigations of the changes in the resonance frequency and Q-factor with dielectric constants in the range of 1-100 has been presented alongside calculations for both the stored and radiated energies as well as classifications for the TE and TM modes. Following that paper, more articles have been published that are focused on the design of hemispherical dielectric resonator antennas [4].

The hemispherical dielectric resonator shown in Figure 2.2 offers two degrees of freedom in the design; radius (a) and dielectric constant ε_r. There are two types of modes for this shape, transverse electric (TE) and transverse magnetic (TM) filed modes. The fundamental mode for the TE mode is TE_{111}, which is equivalent to a short horizontal magnetic dipole, while TM_{101} is the fundamental TM mode which is equivalent to a short electric monopole, with radiation patterns shown in Figure 2 (b) [2, 4]. From this figure, it can be noticed that the radiation patterns of the TE_{111} mode is similar to the of the assumed short horizontal magnetic dipole, taking in consideration the effect of the ground plane on the radiation shape. The same can be stated about the relation of the radiation pattern of TM_{101} mode and to that of a short electric monopole.

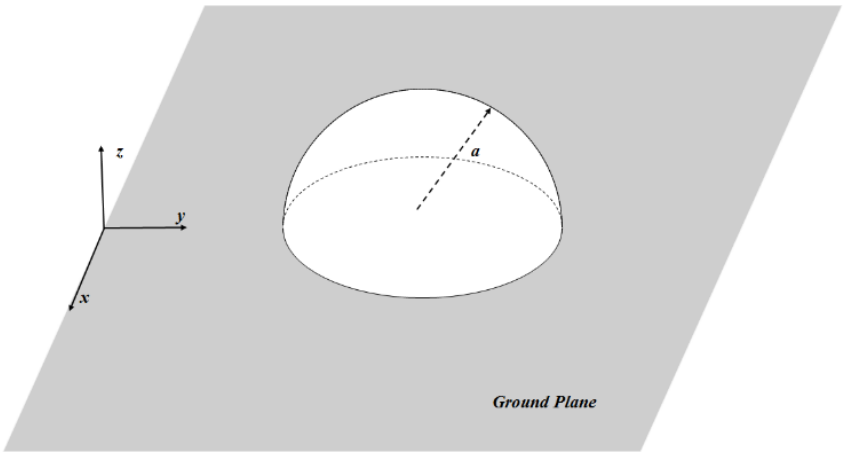

(a)

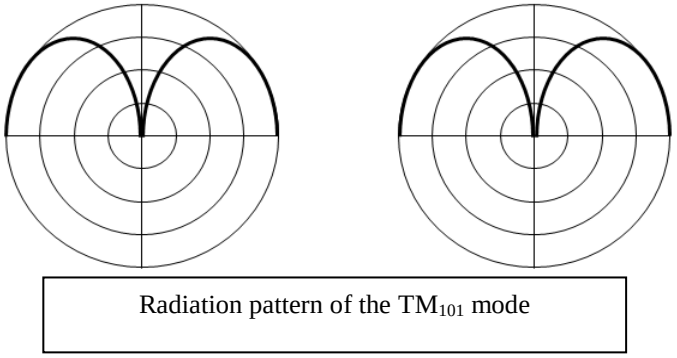

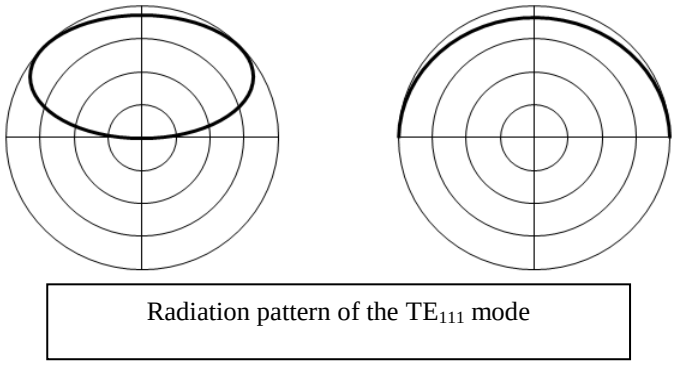

(b)

Figure 2.2 Hemispherical DRA (a) Diagram and (b) Basic modes with the H-field at φ=0° (*x*-*z* plane) on the Left and the E-field at φ=90° (*y*-*z* plane) on the Right.

The resonance frequency for TE_{111} mode could be calculated from the characteristics equation [4]

$$\frac{J_{1/2}(\sqrt{\varepsilon_r}k_0a)}{J_{2/3}(\sqrt{\varepsilon_r}k_0a)} = \frac{H_{1/2}^{(2)}(k_0a)}{\sqrt{\varepsilon_r}H_{1/2}^{(2)}(k_0a)} \quad (2.1)$$

in which $J_u(x)$ is the first-order Bessel function, $H_v^{(2)}(x)$ is the second-order Hankel function, and (a) is the radius of the dielectric. The wave number, k_0, is a complex value, and by solving the transcendental equation (2.1) for k_0, the resonance frequency f can be determined as [4]

$$f = \frac{4.3317\, Re(k_0a)}{a_{cm}} \quad (2.2)$$

The Q-factor of this mode is given by [4]

$$Q = \frac{Re(k_0a)}{2Im(k_0a)} \quad (2.3)$$

A simplified method for designing a hemispherical dielectric resonator antenna has been derived using the following equations [4]

$$Re(k_oa) = 2.8316\varepsilon_r^{-0.47829} \quad (2.4)$$

$$Q = 0.08 + 0.796\varepsilon_r + 0.0122\varepsilon_r^2 - 3\times10^{-5}\varepsilon_r^3 \quad (2.5)$$

An alternative design approach is to use the graph shown in Figure 2.3 to obtain both $Re(k_0a)$ and Q-factor. It is also possible to calculate the bandwidth if the maximum acceptable voltage standing wave ratio s is available as following [4]

$$BW = \frac{\Delta f}{f_0} = \frac{s-1}{\sqrt{s}Q} \quad (2.6)$$

Following identical approach equations (2.2) and (2.3) can be used to obtain the resonance frequency and Q-factor for the TM_{101} mode by solving the following transcendental equation for k_o [4]

$$\frac{1}{\sqrt{\varepsilon_r}k_0a} - \frac{J_{1/2}(\sqrt{\varepsilon_r}k_0a)}{J_{2/3}(\sqrt{\varepsilon_r}k_0a)} = \frac{\sqrt{\varepsilon_r}}{k_0a} - \sqrt{\varepsilon_r}\frac{H_{1/2}^{(2)}(k_0a)}{H_{1/2}^{(2)}(k_0a)} \quad (2.7)$$

Again, simplifications were provided using simplified equations as [4]

$$Re(k_o a) = 4.47226\varepsilon_r^{-0.505} \tag{2.8}$$

for $\varepsilon_r \leq 20$

$$Q = 0.723 + 0.932\varepsilon_r - 0.0956\varepsilon_r^2 - 0.00403\varepsilon_r^3 - 5\times10^{-5}\varepsilon_r^4 \tag{2.9}$$

for $\varepsilon_r > 20$

$$Q = 2.621 - 0.574\varepsilon_r + 0.08212\varepsilon_r^2 + 2.59\times10^{-4}\varepsilon_r^3 \tag{2.10}$$

As a result, the graph can be obtained for design simplification as shown in Figure 2.4.

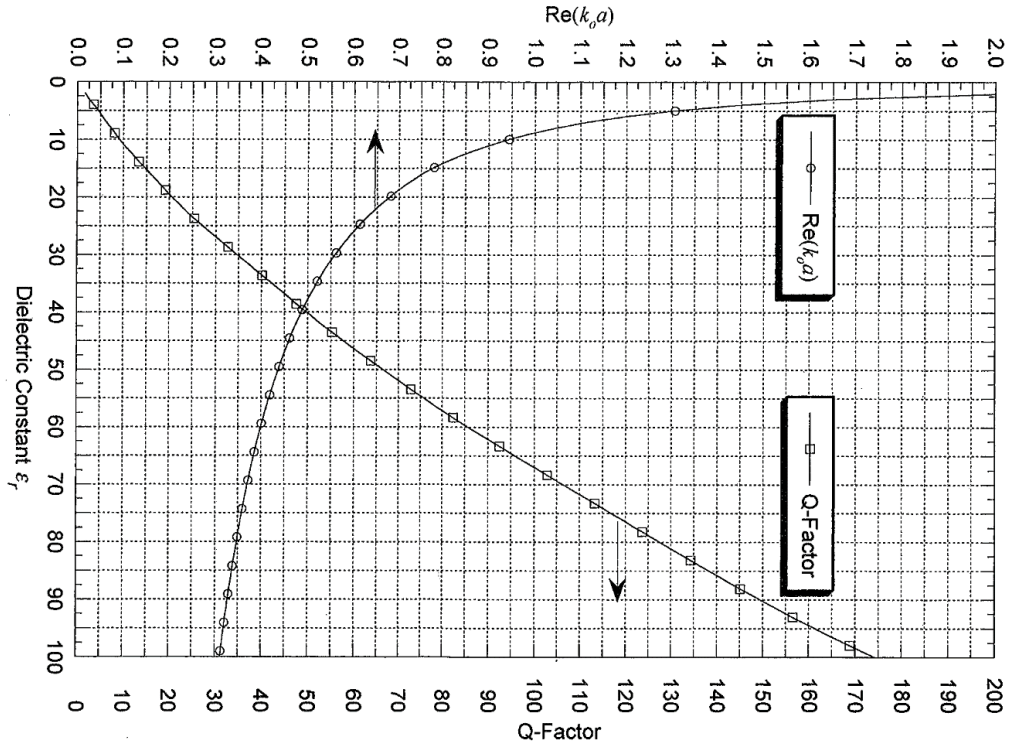

Figure 2.3 TE_{111} Design Graph [4]

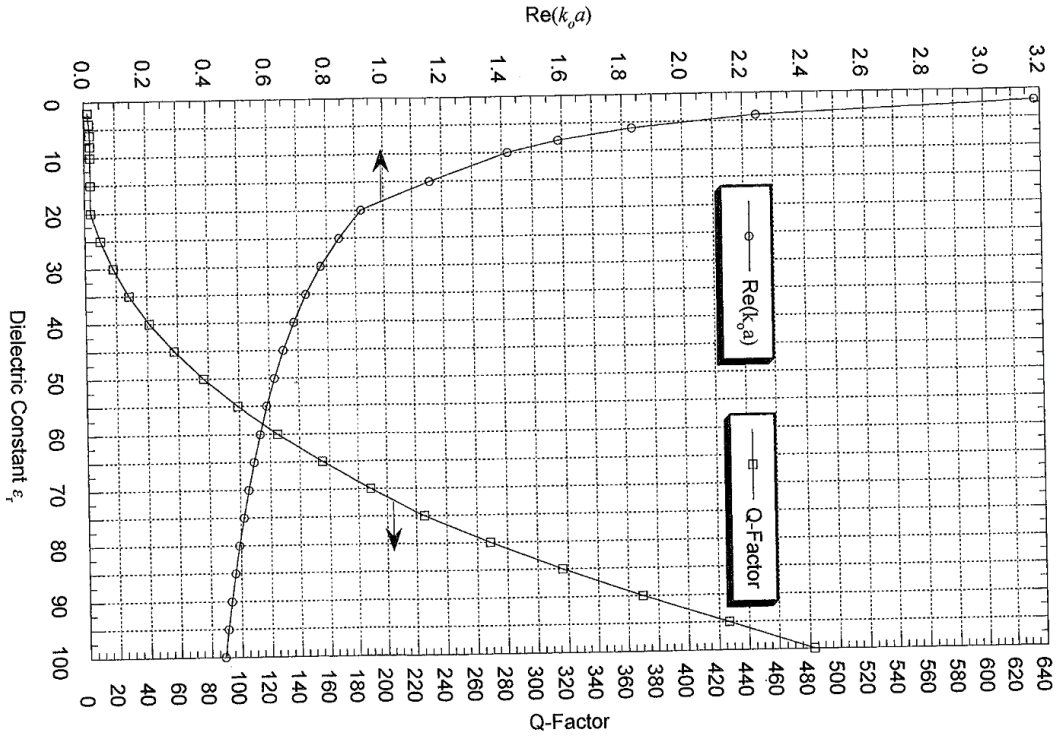

Figure 2.4 TM_{101} Design Graph [4]

ii. Cylindrical DRA:

Until the 1980s, cylindrical dielectrics were used mainly in microwave circuit applications. However, an article has been published in 1983 that is focused on the investigation of the modes and radiation properties of the cylindrical dielectric resonator antenna [6].

The cylindrical DRA shown in Figure 2.5 has three design parameters; height (*h*), radius (*a*), and a dielectric constant ε_r. With two dimensions to consider, the aspect ratio, a/h, offers an extra advantage for this type over the hemispherical counterpart. This is evident by allowing flexibility to manipulate the dimensions in order to obtain the same resonance frequency with different size, and Q-factor, which provides a more suitable choice for different requirements [4]. There are three basic modes to be considered for a cylindrical

DRA; transverse electric TE, transverse magnetic TM and hybrid HE. The three lowest order modes are $TE_{01\delta}$, $TM_{01\delta}$ and $HE_{11\delta}$ [**Error! Reference source not found.**4].

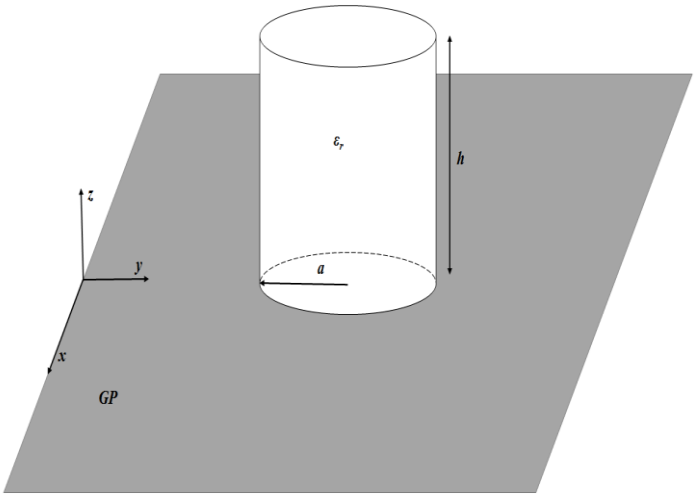

Figure 2.5 Cylindrical DRA Diagram

Unlike the hemispherical DRA, exact resonance frequency for a cylindrical DRA cannot be calculated. This related to the complex mathematical modelling and analysis due to the shape's edges of the geometry [7]. Therefore, an approximation model has been introduced in which an open-circuit boundary condition has been assumed, where both of the circular faces are assumed as magnetic walls, i.e. $H_z=0$. Additionally, the tangential electric and magnetic fields inside the geometry that are perpendicular to those two faces have been assumed to be continuous. By considering resonator boundaries as isotropic, and assuming that all the radiated fields vanish at an infinite distance [8, 9]. These assumptions have provided a highly accurate approximation for both low and high dielectric constants [4].

Due to the geometry's two dimensions, equation (2.2) should be rewritten as [4]

$$f = \frac{4.3317\ Re(k_0 a)}{h(a/h)} \tag{2.11}$$

where h is the height of the cylinder. For the $TE_{01\delta}$ mode

$$k_0 a = \frac{2.237}{\sqrt{\varepsilon_r + 1}} \left\{ 1 + 0.2123 \frac{a}{h} - 0.00898 \left(\frac{a}{h} \right)^2 \right\} \quad (2.12)$$

$$Q = 0.078192 \varepsilon_r^{1.27} \left\{ 1 + 17.31 \left(\frac{h}{a} \right) - 21.57 \left(\frac{h}{a} \right)^2 + 1.86 \left(\frac{h}{a} \right)^3 - 1.98 \left(\frac{h}{a} \right)^4 \right\} \quad (2.13)$$

and for the $TM_{01\delta}$ mode

$$k_0 = \frac{\sqrt{3.83^2 + \left(\frac{\pi a}{2h} \right)^2}}{\sqrt{\varepsilon_r + 2}} \quad (2.14)$$

$$Q = 0.008721 \varepsilon_r^{0.888413} e^{0.0397475 \varepsilon_r} \left\{ 1 - \left(0.3 - 0.2 \frac{a}{h} \right) \left(\frac{38 - \varepsilon_r}{28} \right) \right\}$$

$$\times \left\{ 9.498186 \frac{a}{h} + 2058 \left(\frac{a}{h} \right)^{4.322261} e^{-3.50099 \left(\frac{a}{h} \right)} \right\} \quad (2.15)$$

For the $HE_{11\delta}$ mode [4]

$$k_0 a = \frac{6.324}{\sqrt{\varepsilon_r + 2}} \left\{ 0.27 + 0.36 \frac{a}{2h} + 0.02 \left(\frac{a}{2h} \right)^2 \right\} \quad (2.16)$$

$$Q = 0.01007 \varepsilon_r^{1.3} \frac{a}{h} \left\{ 1 + 100 e^{-2.05 \left(\frac{a}{2h} - \frac{1}{80} \left(\frac{a}{h} \right)^2 \right)} \right\} \quad (2.17)$$

The six equations (2.12-2.17) returns high accuracy results, but for $a/h >> 1$ and $a/h << 1$, the results accuracy drop considerably [4].

It is also possible to use graphs to achieve solutions in a similar way to that used in designing hemispherical resonators. These graphs are shown in Figures 2.6-2.8 for $TE_{01\delta}$, $TM_{01\delta}$ and HE11δ modes respectively [4].

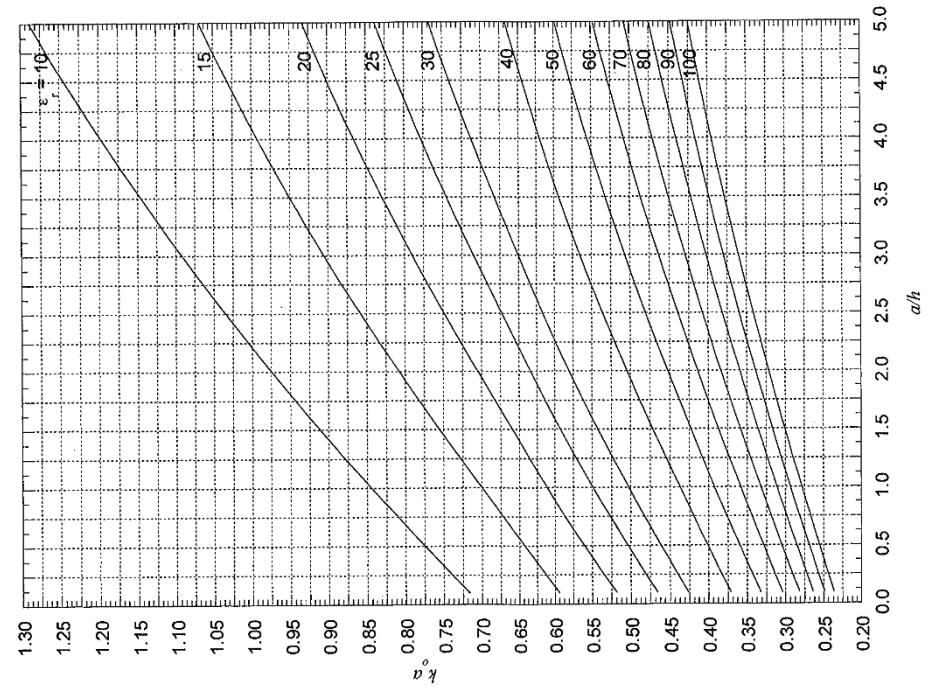

(a) k_0a

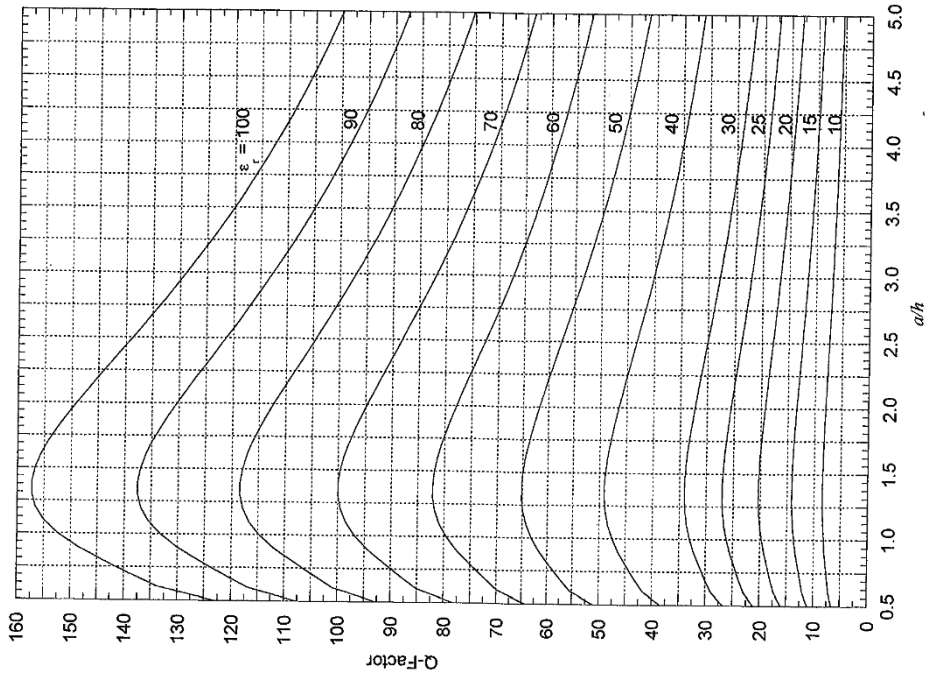

(b) Q-factor

Figure 2.6 $TE_{01\delta}$ Design Graph [4]

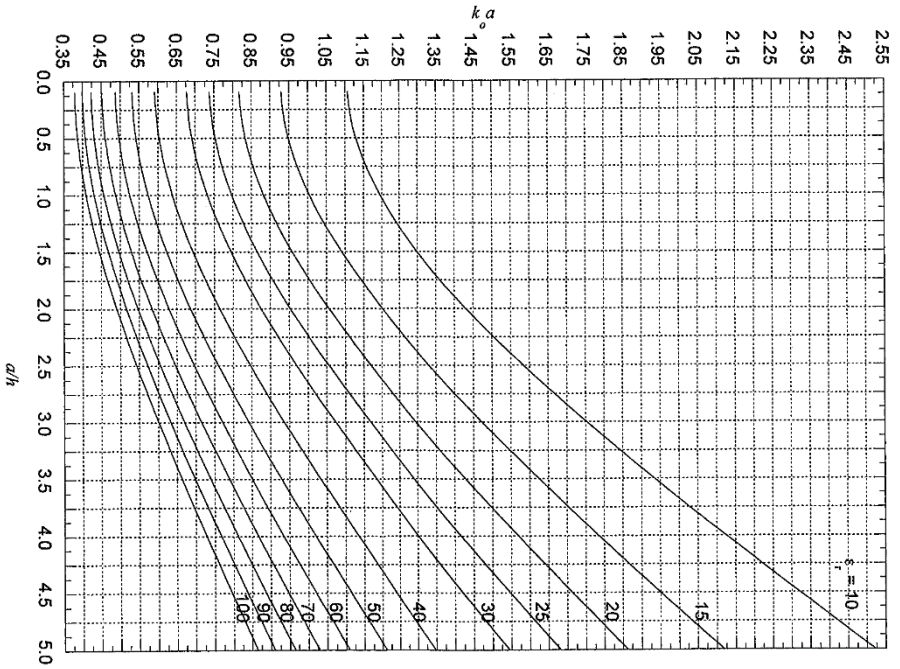

(a) k_0a

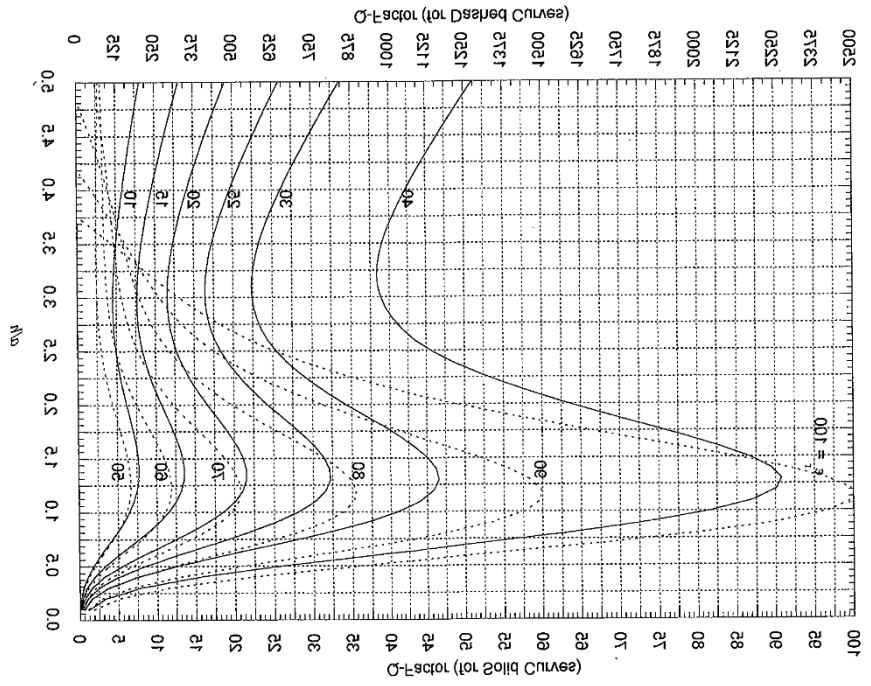

(b) Q-factor

Figure 2.7 $TM_{01\delta}$ Design Graph [4]

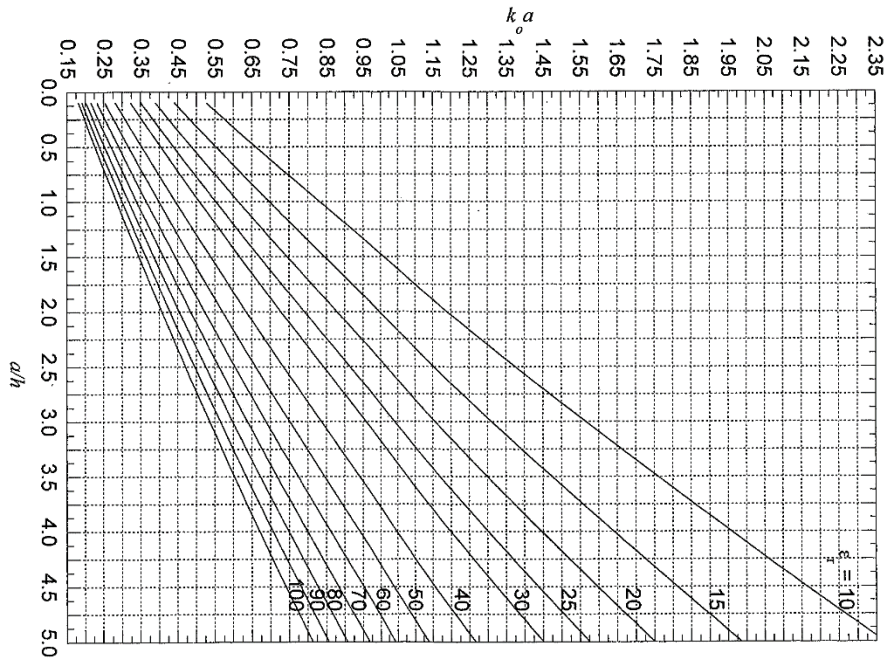

(a) k_0a

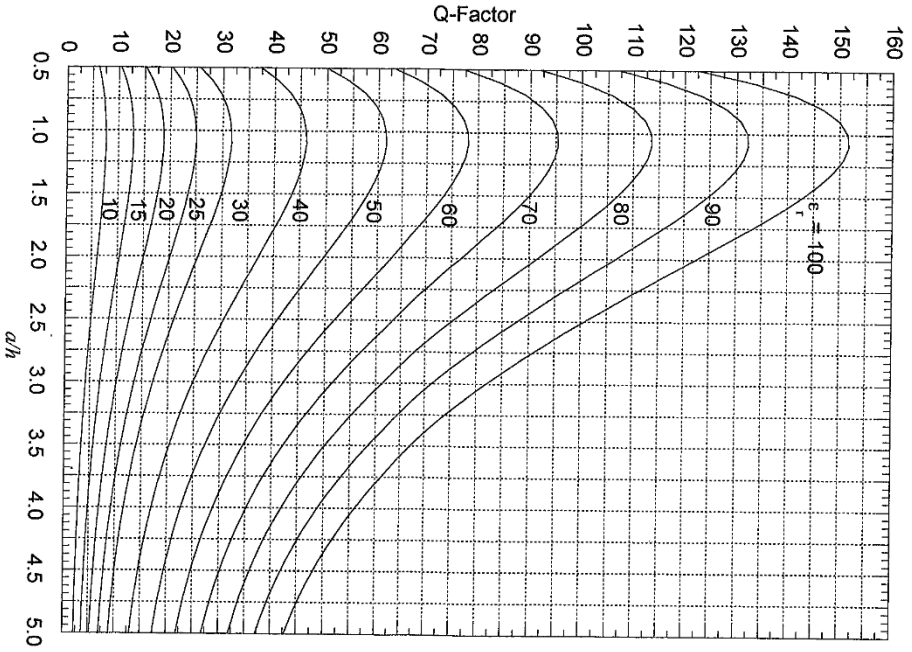

(b) Q-factor

Figure 2.8 $HE_{11\delta}$ Design Graph [4]

iii. Rectangular DRA:

In the first half of the 1960s, couple of studies have been published that are focused on the analysis of rectangular dielectric resonators, especially with high dielectric constants [9, 10].

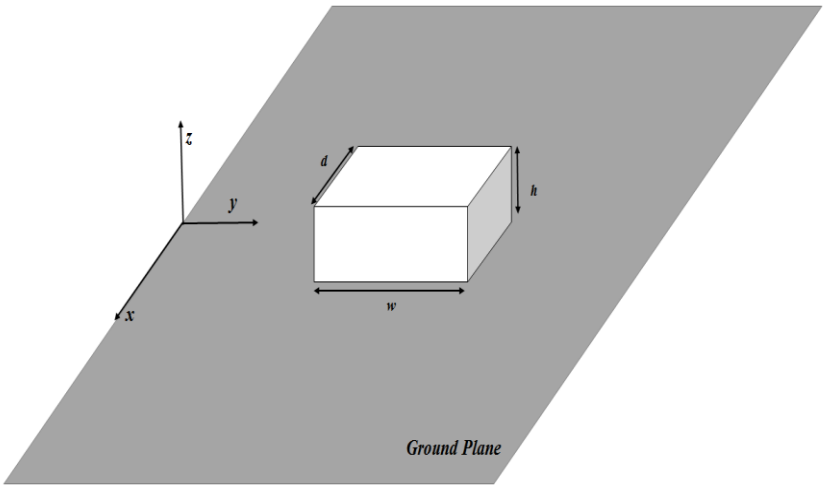

Figure 2.9 Rectangular DRA Diagram

Figure 2.9 illustrates the layout of the rectangular resonator. In addition to the dielectric constant ε_r, this configuration has three variables; width *w*, height *h*, and depth *d*. This allows extra step of design flexibility compared the cylindrical counterpart that offers the two ratios, *w/h* and *w/d* [4]. On the other hand, mathematical modelling and analysis of the RDRA are more complicated due to the increased number of edges in the geometry. A popular method to analyse a rectangular DRA is known as the dielectric waveguide model [2]. In this method, the top and side faces are considered as magnetic walls, while the lower face can be considered as a perfect electric wall since the resonator is usually placed on a conductive ground plane. In addition, it is possible to analyse a dielectric block with a height of $b=2h$ to replace the ground plane effects, and with all six perfect magnetic walls, the same analogy used with the cylindrical dielectric could be applied to

calculate the generated TE and TM modes, but since TM modes were never practically excited, its existence is questionable, and only TE modes are usually excited [11].

The resonator can radiate TE modes in a similar way to a short magnetic dipole located along one of the three axes, generating TE^x, TE^y, or TE^z modes, with resonance frequencies that are dependent on the three dimensions and dielectric constant. For the case when $w > d > b$, the lowest resonance mode will be $TE^x_{\delta 11}$. The resonance frequency f_0 could be obtained by solving the transcendental equation [4]

$$k_x tan(k_x d/2) = \sqrt{(\varepsilon_r - 1)k_0^2 - k_x^2} \tag{2.18}$$

where

$$k_0 = \frac{2\pi}{\lambda_0} = \frac{2\pi f_0}{c}, k_x = \frac{\pi}{d}, k_y = \frac{\pi}{w}, k_z = \frac{\pi}{b} \tag{2.19}$$

and

$$k_x^2 + k_x^2 + k_x^2 = \varepsilon_r \, k_0^2 \tag{2.20}$$

It can be proved that the resonance frequency for any mode may be derived from equation (2.20) as [3, 4]

$$f_{lnm} = \frac{c}{2\pi\sqrt{\varepsilon\mu}} \sqrt{\left(\frac{m\pi}{w}\right)^2 + \left(\frac{n\pi}{wb}\right)^2 + \left(\frac{l\pi}{d}\right)^2} \tag{2.21}$$

in which l, m, n are positive integers.

For a $TE^x_{\delta mn}$ mode, the l term was discarded, and the fraction of a half-cycle of the field variation along the z direction (δ) can be calculated as

$$\delta = \frac{k_x}{\pi/d} \tag{2.22}$$

When $w > d$ and $w > b$, the fields inside the resonator can be obtained using the dielectric waveguide model as [4]

$$H_x = \frac{(k_y^2+k_z^2)}{j\omega\mu_0}\cos(k_x x)\cos(k_y y)\cos(k_z z) \quad (2.23)$$

$$H_y = \frac{(k_y k_x)}{j\omega\mu_0}\sin(k_x x)\sin(k_y y)\cos(k_z z) \quad (2.24)$$

$$H_z = \frac{(k_z k_x)}{j\omega\mu_0}\sin(k_x x)\cos(k_y y)\sin(k_z z) \quad (2.25)$$

$$E_x = 0 \quad (2.26)$$

$$E_y = k_z \cos(k_x x)\cos(k_y y)\sin(k_z z) \quad (2.27)$$

$$E_y = -k_y \cos(k_x x)\sin(k_y y)\cos(k_z z) \quad (2.28)$$

By assuming magnetic walls that are parallel to the *z*-axis, it can be shown that

$$k_y = \frac{m\pi}{w}, \; k_y = \frac{m\pi}{w} \quad (2.29)$$

The E-field distribution for a number of $TE^x_{\delta mn}$ modes inside the dielectric are illustrated in Figure 2.10. Furthermore, the effect of the ground plane evident through the absence of even values of *m*.

It should be noted that the above analysis can be employed for the TE^y and TE^z modes. In fact, many articles use the TE^z mode as a basis for the analysis [1-3].

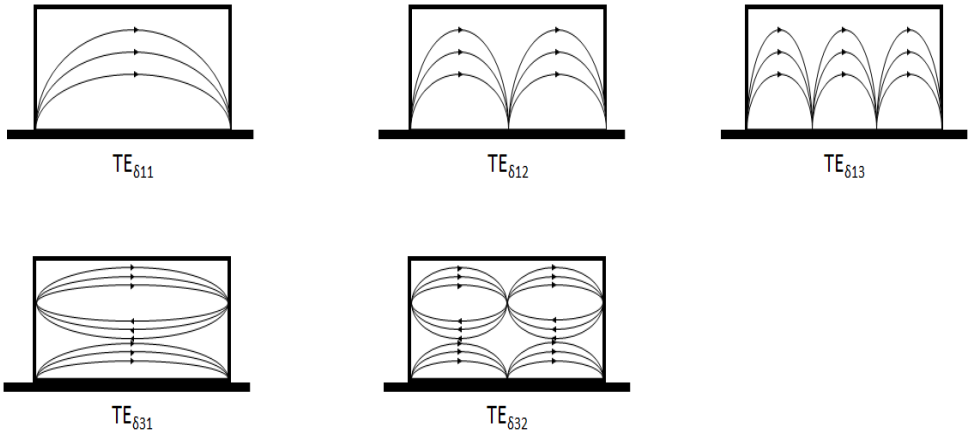

Figure 2.10 Electric Field Distribution of few Rectangular DRA Modes

From the analysis presented above, design calculation equations have been derived that can be utilized to generate design graphs as illustrated in Figure 11 **Error! Reference source not found.**[4]. By defining a normalised frequency *F* as

$$F = \frac{2\pi w f_0 \sqrt{\varepsilon_r}}{c} \tag{2.30}$$

where *c* is the speed of light in vacuum (3×10^8 m/s). Rearranging equation (2.30), and assuming the reference scale units for *w* and f_0 are in cm and GHz respectively, then the following expression can be achieved

$$f_{0\,GHz} = \frac{15F}{w_{cm}\pi\sqrt{\varepsilon_r}} \tag{2.31}$$

The solution for *F* can be obtained by solving the dielectric resonator transcendental equation using curve fitting approximation that results in the following equations, or by using the derived graph in Figure 2.11-a [4].

$$F = a_0 + a_1(w/b) + a_2(w/b)^2 \tag{2.32-a}$$

$$a_0 = 2.57 - 0.8(d/b) + 0.42(d/b)^2 - 0.05(d/b)^3 \tag{2.32-b}$$

$$a_1 = 2.71(d/b)^{-0.282} \tag{2.32-c}$$

$$a_2 = 0.16 \quad (2.32\text{-d})$$

The Q-factor can be calculated as

$$Q = \frac{2\omega W_e}{P_{rad}} \quad (2.33)$$

where ω is the angular frequency ($2\pi f_0$), W_e are the stored energy, and P_{rad} is the radiated power, where

$$W_e = \frac{\varepsilon_0 \varepsilon_r wbdA^2}{32}\left(1 + \frac{sin(k_x d)}{k_x d}\right)\left(k_y^2 + k_z^2\right) \quad (2.34)$$

in which A is a constant related to the field amplitudes, and

$$P_{rad} = 10k_0^4 |p_m|^2 \quad (2.35)$$

where the magnetic diploe moment p_m is

$$p_m = \frac{-j\omega 8\varepsilon_0(\varepsilon_r - 1)A}{k_x k_y k_z} \sin(k_x d/2)\hat{\mathrm{x}} \quad (2.36)$$

The solution for the Q-factor can be simplified using the graphs derived from equations (2.33-2.36) as presented in Figures 2.11 (b-i) for the normalised Q-factor (Q_e), which can be calculated from [4]

$$Q_e = \frac{Q}{\varepsilon_r^{3/2}} \quad (2.37)$$

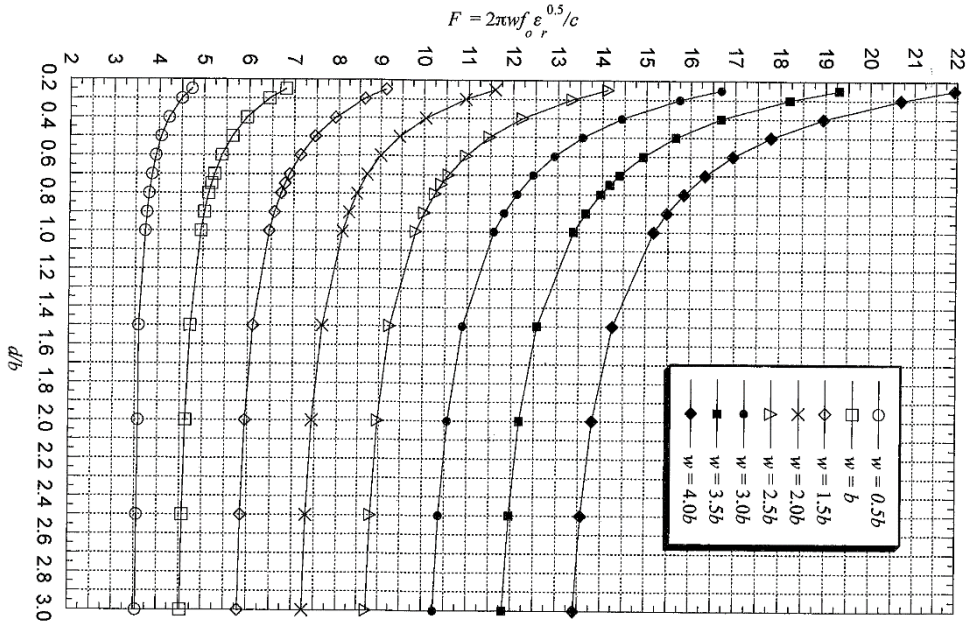

(a) Normalised Frequency

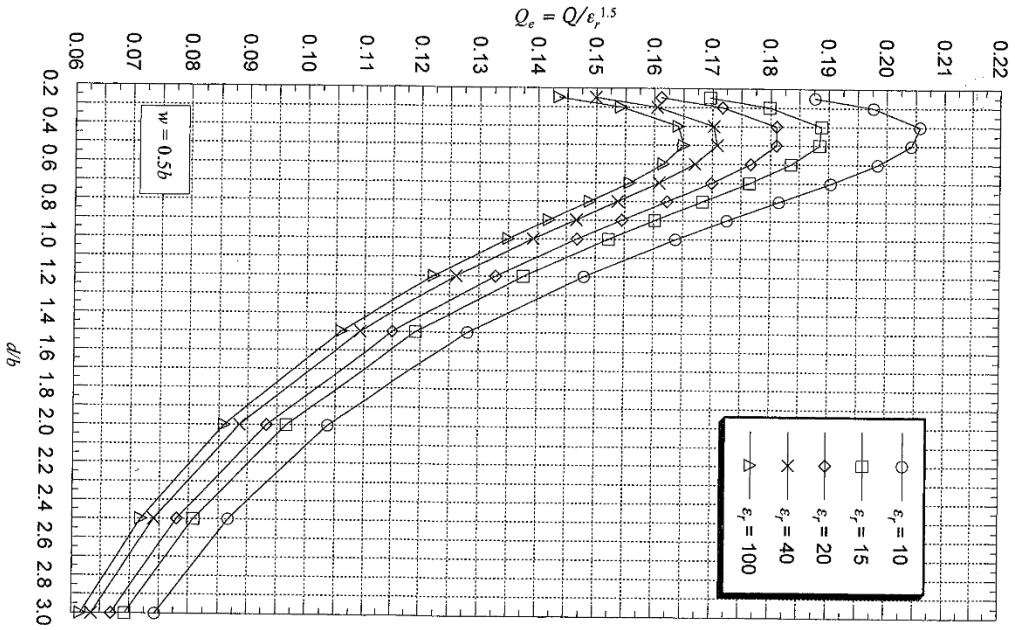

(b) Q-Factor for *w=0.5b*

Figure 2.11 Rectangular DRA Design Graph [4]

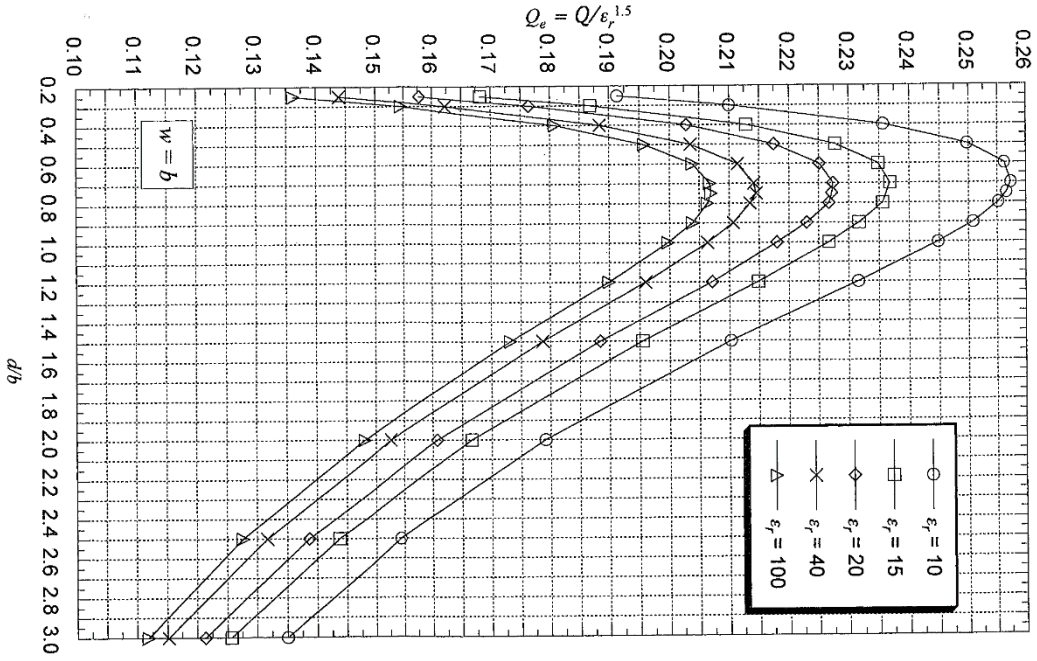

(c) Q-Factor for $w=b$

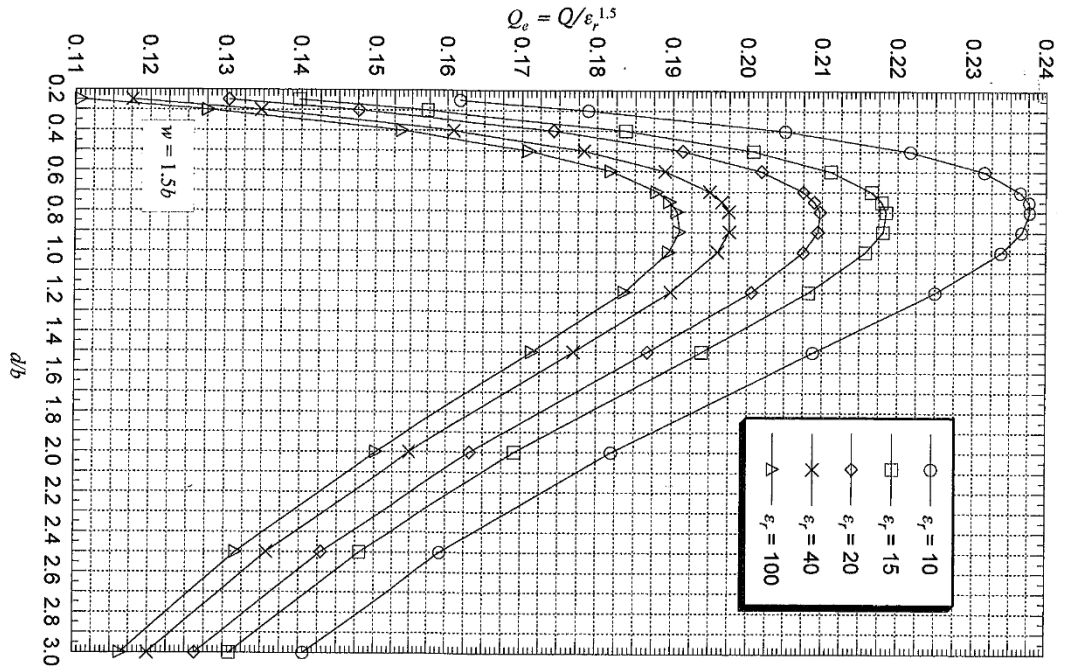

(d) Q-Factor for $w=1.5b$

Figure 2.11 Continued

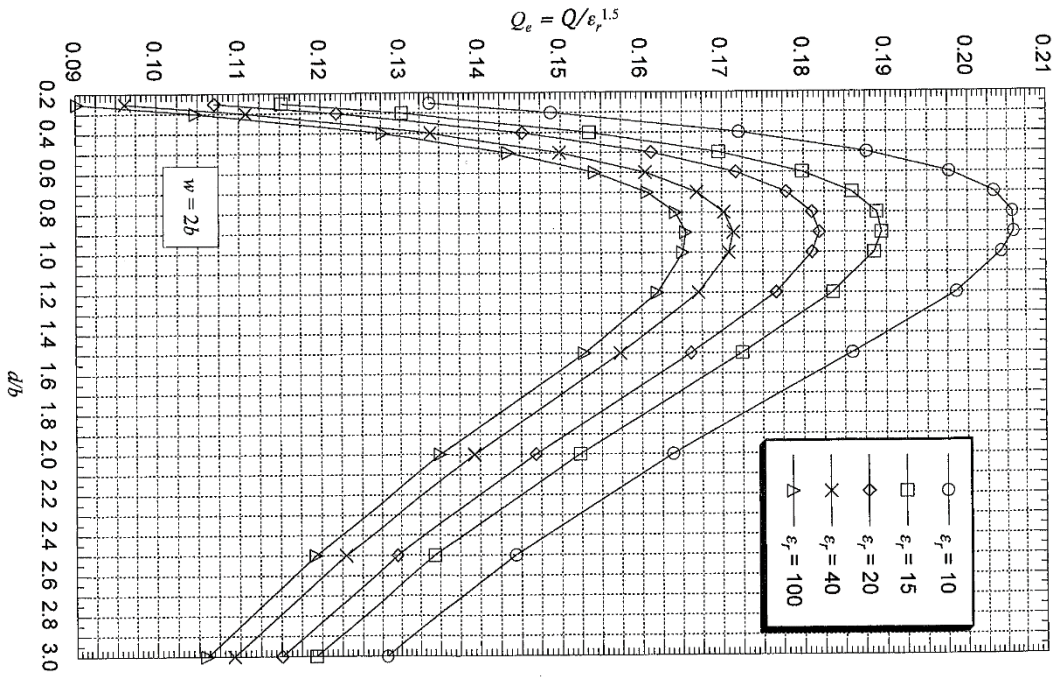

(e) Q-Factor for *w=2b*

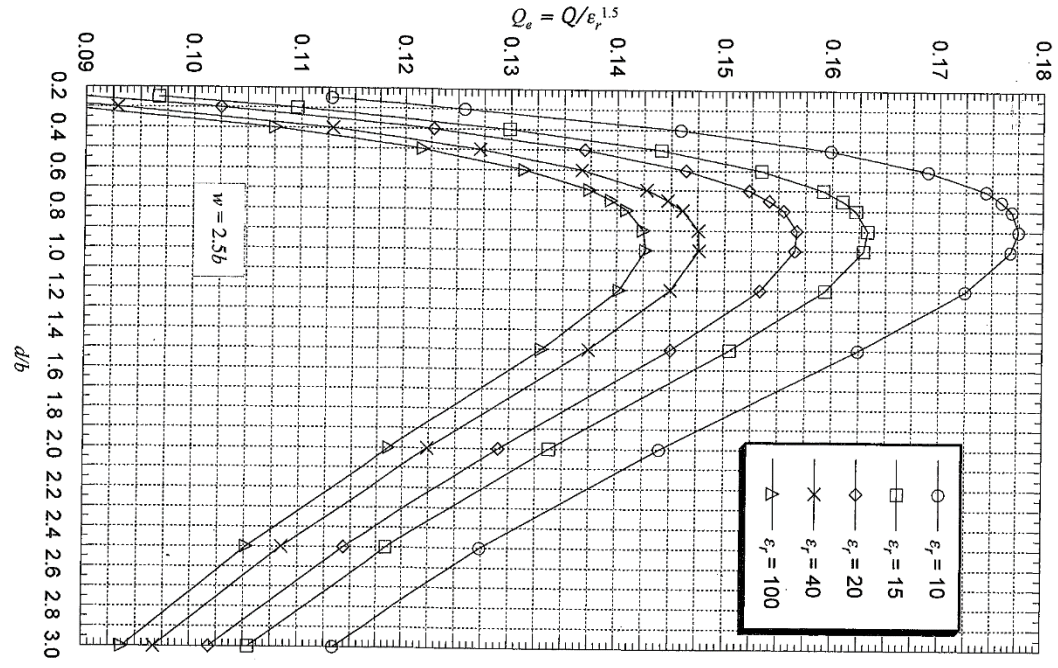

(f) Q-Factor for *w=2.5b*

Figure 2.11 Continued

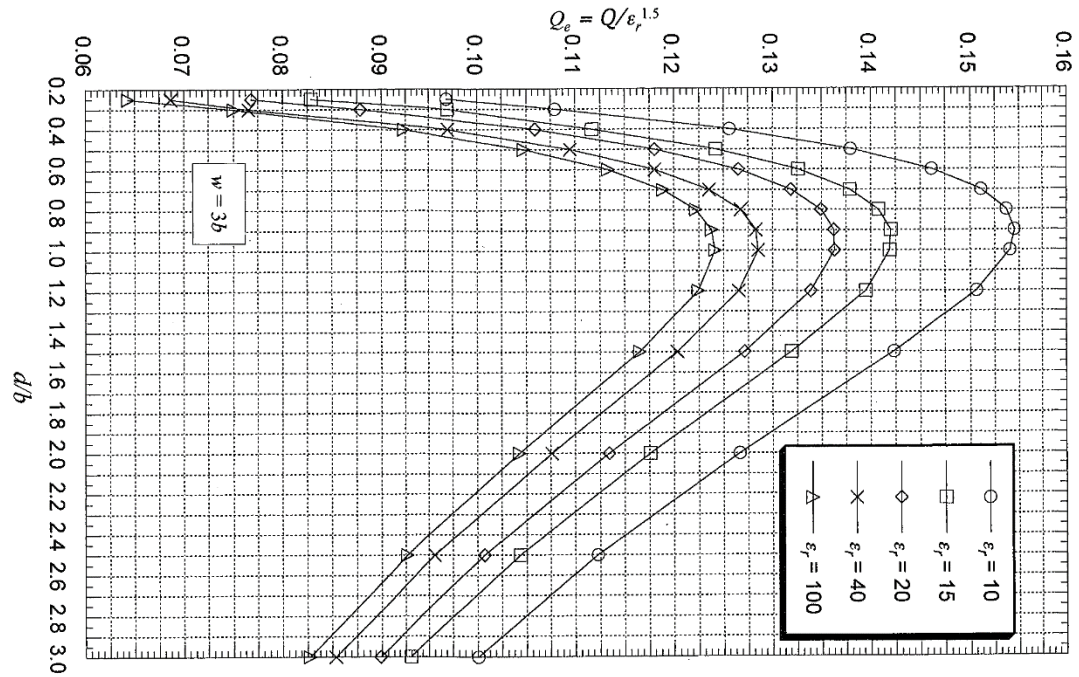

(g) Q-Factor for *w=3b*

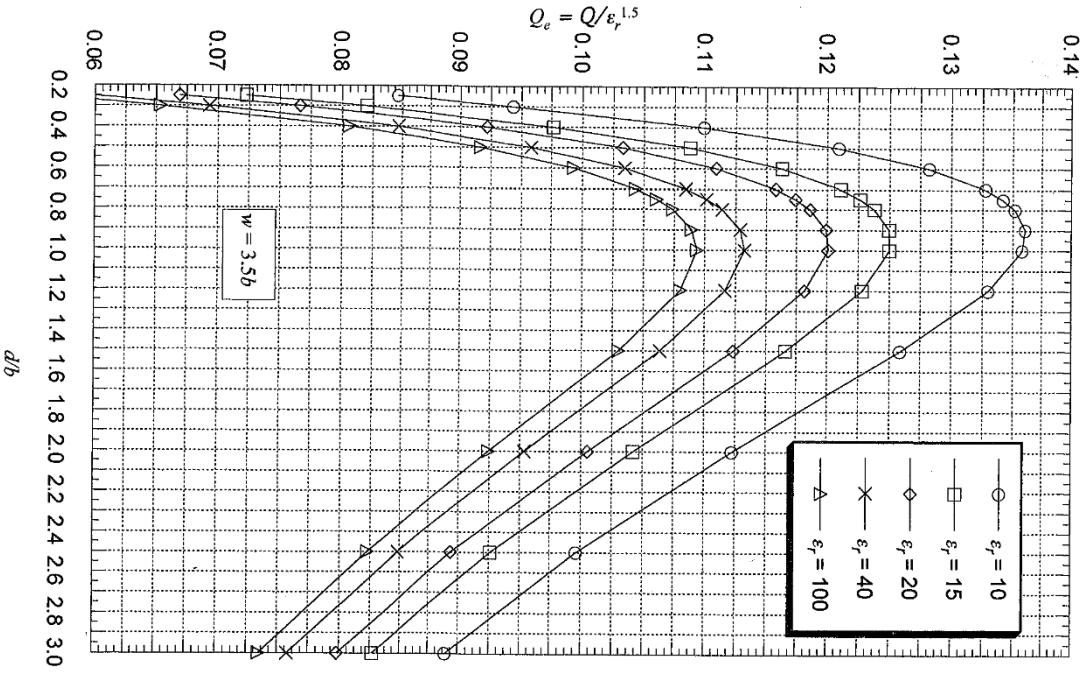

(h) Q-Factor for *w=3.5b*

Figure 2.11 Continued

2.3.2 More Complex DRA Geometries

Most of the non-standard shaped DRAs are derived either from their standard counterparts or represent hybrid geometries. Therefore, these configurations can be categorized into five types; modified hemispherical, modified cylindrical, modified rectangular, hybrid, and other shaped dielectric resonators [4].

i. Hemispherical Based DRA Geometries:

A multilayer hemispherical dielectric resonator has been suggested to overcome the design parameters limitations and to improve impedance bandwidth as well as radiation characteristics [2, 4]. This can be achieved by creating a central hemispherical air gap inside the resonator and above the ground plane to double the impedance bandwidth as reported in [12]. The hemispherical air gap can be replaced by a dielectric counterpart to achieve alternative results. It has been reported that a multilayer, or coated, dielectric resonator impedance offers a wider bandwidth. These results have been attributed to the fact there is a discontinuity between the two adjacent materials that leads to a reduction in the reflected power at the resonator–air interface [2]. This also provides an increase in the impedance bandwidth [2].

A half-hemispherical dielectric resonator has been investigated in [13]. In that study, a bisected dielectric with a narrow gap separation has been probe-fed to generate a monopole-like radiation. This resulted in a 35% impedance bandwidth with a 5 dBi gain and a radiation efficiency of ~99% [13].

ii. Cylindrical Based DRA Geometries:

The half-split cylindrical DRA shown in Figure 2.3-g has been proposed originally to generate the $TE_{01\delta}$ mode with a relatively low Q-factor in order to increase the impedance

bandwidth. A minimum bandwidth of 6% been achieved, and a 10% bandwidth has been reported [14, 15]. An alternative study suggested the use of a multilayer half-split cylindrical that is rested on one of the sides and probe fed to achieve a measured impedance bandwidth of 84% [16].

A cylindrical ring dielectric resonator as illustrated in Figure 2.3-d has been introduced to generate the $TM_{01\delta}$ mode. This geometry, which radiates similar to an electric monopole, has been proved to be useful for compact antenna applications with a dielectric height of 0.1λ, and a reduced Q-factor [17].

Other DR configurations have been derived from the cylindrical and cylindrical ring resonators [4]. These include sectored cylindrical and cylindrical ring DRAs [2, 4], as well as an elliptical DRA [18]. These DRA geometries are shown in Figure 2.3 h-j, respectively.

iii. Rectangular Based DRA Geometries:

Figure 2.3-n illustrates a notched rectangular DRA that offers the same advantages as those of the hollow hemispherical DRA [4]. It has been reported that introducing the airgap can provide an impedance bandwidth enhancement by a factor of ~3 times that of a solid RDRA [19]. This configuration will be discussed in more details in the next Chapter.

Furthermore, a circular polarisation radiation has been generated by chopping two opposite corners of a rectangular DRA creating what is known as the chamfered DRA [20]. Another method to generate the circular polarisation is to employ a cross DRA that generates two TE_{111} mode fields with quadrant phase difference [21].

iv. Alternative DRA Geometries:

Other geometries have been studied and analysed in literature, such as triangular, tetrahedral DRAs [22], as well as several shapes of stepped DRA such as staircase, stepped rectangular, and stepped cylindrical DRAs [5].

v. Hybrid Configurations:

These geometries can be created by merging different dielectric DRA shapes and other antenna types. The purpose behind these designs is to enhance the impedance bandwidth or combining the operations of two antennas in a single system. Examples for these antennas include DRA-loaded monopole [23], and microstrip patch-cylindrical DRA [24].

2.3 DRA Coupling

Determining the proper coupling mechanism between the input signal and the dielectric resonator is as important as the DRA dielectric constant and dimensions. The overall radiation characteristics depend on the proper feed choice to achieve an optimum coupling efficiency and hence generating the required mode and radiation pattern. There are several common techniques for feeding the dielectric resonator antennas. These are; aperture coupling, probe, microstripline, coplanar, and dielectric image guide coupling [2, 4, 5]. A brief description of each type is given in the following sections, with more focus on the aperture and probe coupling because of their inclusion in this research. In addition, a brief discussion about the conformal strips will be included in the probe coupling section.

2.3.1 Aperture Coupling

This excitation approach is based on using a microstrip-fed slot antenna that is loaded with a DRA. The DRA permittivity should be higher than that of the substrate. There are numerous slot shapes that can be employed to excite the DRA such as rectangular, annular, cross-shaped, and C-shaped slots [21]. Resonance frequency and impedance bandwidth are functions of the permittivity and the DRA aspect ratio [21]. Few techniques have been proposed to excite a DRA through slots, the most commonly used two are microstrip lines [25] and a coaxial cable [26].

Rectangular slots are commonly used in conjunction with the stripline and they can be either narrow or wide according to their width to length ratio. The main difference between those two types is the bandwidth. Further, it is important to choose the correct substrate with the right parameters such as the loss tangent (tan δ) and relative permittivity (ε_r). Loss tangent defined as "metric of the quantity of electric energy that is converted to heat by a dielectric" [27], and it is mathematically defined as

$$\tan(\delta) = \frac{\varepsilon_r''}{\varepsilon_r'} = \frac{\sigma}{\omega\varepsilon} \qquad (2.38)$$

where ε_r'' and ε_r' are the imaginary and real dielectric constants respectively, σ is the conductivity, ω is the angular frequency and ε is the dielectric constant [28].

As for the microstripline-fed rectangular-slot DRA shown in Figure 2.12, it is the most common technique for aperture coupling. The antenna is usually fed by a microstrip line with an open circuit termination due to fabrication easiness and design freedom [4]. By mounting the dielectric upon the slot, the latter behaves as a magnetic dipole activating the transverse electromagnetic mode that is suitable inside the dielectric resonator [29]. In this case, the microstripline guide signal to the DRA through the aperture which

behaves as the magnetic dipole which radiate through the dielectric resonator. This magnetic dipole, which is parallel to the dipole's longest direction as shown in Figure 2.12 (b), cause, for example, the excitement of the $TE_{\delta 11}$ for the rectangular DRA if placed under the centre of the DRA by permitting a strong coupling of the magnetic field for the DRA [4]. The microstripline has the benefit of impedance matching freedom which is not available in other slot feeding techniques such as probe feeding. The technique requires only to extend the length of the microstripline by $\lambda_g/4$ beyond the slot and terminate it as an open-circuit stub [4].

The coupling in this type is typically lower than desired, and it can be improved by employing the techniques that are used for slot antenna. These include the use of matching network, shifting the feed from the off the slot centre, increase the stub more than $\lambda/4$ which increase the reactivity in the input impedance, and inclining the strip line angle with respect to the slot, or shift the DRA so that it is located off the slot centre [4, 29]. The steps for designing microstrip line fed slot coupled RDRA are explained in Chapter 4.

The annular slots proved to be useful in improving the DRA impedance bandwidth in comparison to rectangular slots [30]. This type of aperture can support the generation of both linear and circular polarisation. The linear polarisation can be achieved by simply using a single feed with a regular annular slot [30], while the circular polarisation can be excited either by adding another feed in quadrant with the first one [30], or by shorting the slot at a specific point [26, 31], or using perturbed annular slots [32].

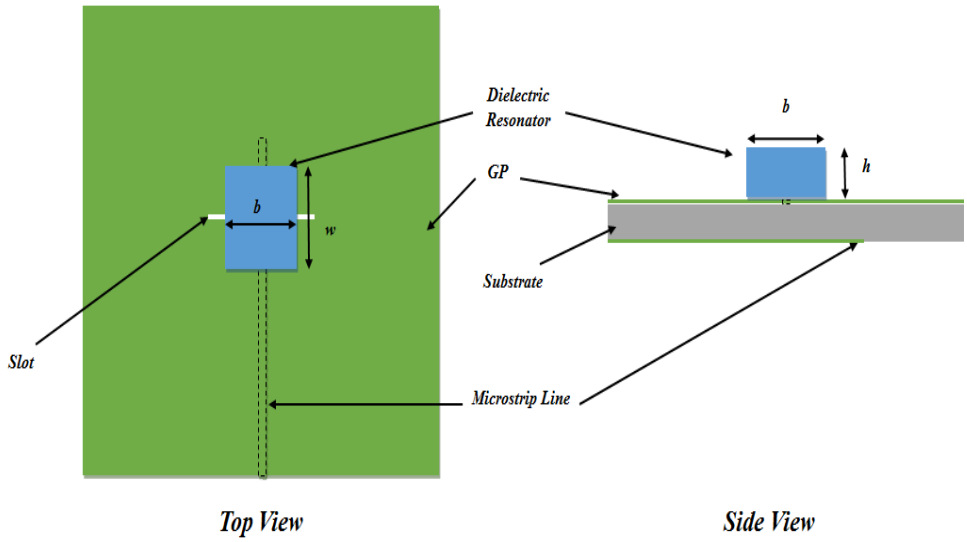

(a)

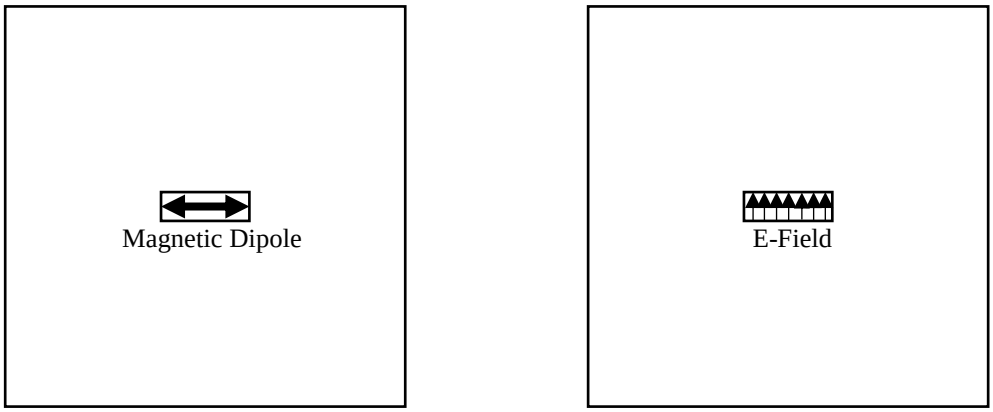

(b)

Figure 2.12 Microstripline-Fed Rectangular Slot DRA (a) Antenna Diagram, and (b) Field Distribution inside the Slot

2.3.2 Probe Coupling

The probes can be considered an equivalent to vertical electric current that generates magnetic field around it [4]. A coaxial probe can be placed inside a pre-drilled gap in the DRA that is connected at the lower end to an SMA connector [7, 33]. Alternatively,

excitation can be achieved by placing the probe in an adjoined position to the dielectric surface [34]. Another approach is to use an adhesive backed flat metallic strip that can be mounted on planar and curved DRA surfaces [35]. A microstrip line can also be used to feed the flat strip [36]. The use of the flat strip line excitation has the advantage of enhanced flexibility of controlling bandwidth enhancement compared to a coaxial probe excitation [4]. Also, embedded probes require drilling a solid dielectric, which is usually associated with air gaps that alter the DRA characteristics [37].

A maximum coupling efficiency can be achieved by placing the probe, or strip, in a location with a strong electric field of the desired mode that is parallel to the probe, or strip axis [4].

Conformal strip coupling was first suggested to solve the poor coupling between the strip feed and the hemispherical DRA due to the surface curvature. This technique improved the matching as well as the radiation pattern [38]. Since then several applications have been reported based on conformal strips such as achieving a circular polarisation radiation from a hemispherical DRA using dual strips [39], and a square using a conformal spiral excite a singly-fed circularly polarised hemispherical DRA [40].

2.3.3 Microstrip Line Coupling

In this type of excitation, the ground plane is situated below the substrate. The microstrip line can be used for DRA excitation either by direct coupling where the line is terminated under the resonator in a location that is chosen to achieve optimum impedance matching [41]. Alternatively, side coupling can be chosen in which the strip line cross the substrate that is separated from the resonator by a specific distance, which is calculated to achieve an optimum coupling efficiency [4]. The second type is popular with DRA arrays, due to simplicity and low coupling requirements, especially for high dielectric constant

resonators [4].

2.3.4 Coplanar Coupling

There are three types of coplanar coupling, the first and simplest is the open-circuit coplanar waveguide, which behaves like the direct open-circuit microstrip line. This approach is used for direct coupling. The second type is the stub-loaded lines, and the third type is the coplanar loops. The latter two techniques are used to improve impedance matching [4].

2.3.5 Dielectric Image Guide Coupling

This technique is similar to the side microstrip line coupling with both the dielectric guide and the dielectric resonator placed on a metallic ground plane. This technique eliminates the conductor losses of the metallic strip line and proved to be useful for exciting series fed DRA array, even with dielectric constants lower than that coupled with the microstrip line technique [4].

2.4 Reconfigurable Dielectric Resonator Antennas

In line with other antenna types, the configurability of DRAs has been demonstrated in numerous research studies where different approaches have been considered to reconfigure the characteristics of various DRA types. These approaches are focused on controlling the characteristics by either changing the feed/coupling characteristics, dielectric properties, or the relative position for coupling with respect to the dielectric resonator. A surge in the reconfigurable antenna research topic has been expanded to include DRAs. For example, Ferrite resonator antennas (FRA) have been used for frequency tuning and linear/circular polarisation reconfiguration [42, 43]. The FRA is a

dielectric resonator antenna that uses a dielectric ferrite material. The frequency of an FRA can be tuned by introducing a DC controlled magnetic field to change the permeability of the dielectric. For a rectangular FRA, equation (2.31) needs to be altered to accommodate the changes in μ to [4]

$$k_x tan(k_x d/2) = \sqrt{\mu_{eff}(\varepsilon_r - 1)k_0^2 - k_x^2} \tag{2.39}$$

in which,

$$k_x = \sqrt{\mu_{eff}\varepsilon_r k_0^2 - k_y^2 - k_z^2} \tag{2.40}$$

and the effective permeability

$$\mu_{eff} = \mu \pm \kappa \tag{2.41}$$

where κ is the coupling coefficient, which depends on the magnetisation of the ferrite with respect to the feed axis, i.e. parallel or perpendicular, and it is inversely proportional to the frequency. The ± sign indicates the possibility to increase or decrease the frequency, and it depends on the direction of magnetisation [4, 42].

It is also possible to use FRA magnetisation to reconfigure the polarisation from linear to circular. For example, a cylindrical resonator made out of ferrite material has been excited by a rectangular slot to generate the $HE_{11\delta}$ mode along the slot's longest axis, which excites a linear polarisation at the absence of the magnetic bias, in which the FRA acts as a regular DRA. However, by applying the magnetic bias in a perpendicular direction to the slot's equivalent magnetic dipole, the field of the original linear polarisation is reduced while the perpendicular field is boosted, which generates a circular polarisation

[43].

Furthermore, it has been reported that it is possible to use two switchable probes to feed a cylindrical DRA with a 90° phase separation in order to generate a linear polarisation by switching ON one of the probes, or a circular polarisation by switching ON both, of them. In addition, the antenna radiation can be turned OFF if both probes are switched OFF [44].

Another technique has been introduced for the frequency tuning of a disk loaded cylindrical and ring DRAs by changing the size of the metal disk. The study demonstrated that the operating frequency increases with the reduction of the disk size and vice versa [45].

In addition, beam steering has been achieved using multiple probes around a cylindrical DRA. The main beam has been steered to different directions by activating one, or more, probe(s) with equal, or different, powers [46]. Several configurations have been derived from this technique in later studies to achieve the same goal [47-49]. A similar approach has been employed for a hollow cylindrical DRA with four switchable probes that are located inside the airgap [50].

An alternative steering technique that is based on mechanical means has been introduced using a cylindrical DRA that is surrounded by a DRA ring that consists of two pars. The smaller part has a dielectric constant equal to that of the cylindrical DRA, while the large part has a considerably higher dielectric constant. By rotating the ring, and hence changing the angle of the lower permittivity component, the main beam can be steered to a different direction [51].

Rectangular DRA frequency tuning has been proposed by loading one of the DRA sides

with a metallic wall that is connected to the ground plane by three active elements; PIN diodes for discrete values, or varactor diodes for continuous tuning. Initially, an experimental work has been conducted using metallic tabs to represent the PIN diodes, which demonstrated the practicality of the idea [52]. An additional work has been presented by metallically loading two opposite DRA sides, which showed that the only drawback was gain losses due to the active elements resistive characteristics. However, these can be reduced by increasing the bias current. Additionally, using PIN diodes as well as varactor diodes allows more flexibility in the tuning process [53].

The use of liquids in DRAs is not unusual, as it has been reported that the DRA frequency can be tuned by changing water level inside a cylindrical container with a feeding probe inside [46, 51]. By changing water level, basically, the height of the DRA changes and hence the resonant frequency. A varactor diode can be connected to the probe for electronic impedance matching [54].

Using slugs controlled airgaps under the DRA, and below the substrate, has proved to affect the mode's capacitive coupling, which leads to change the operating frequency. By pushing these metallic slugs inside or outside, the operating frequency will be reduced or increased, respectively [55]. A cylindrical DRA that is excited by an annular slot has been proposed to excite the $HEM_{21(1+\delta)}$ mode with a reconfigurable steerable pattern using eight switches to control the main beam direction by turning ON one PIN diode only [56].

An example that has been mentioned in the first chapter was that of a dielectric resonator phased array with a pattern reconfigurability that has been achieved by tuning the phase shifters using MIM varactors. By tuning the feed, the phase shift results in steering the main beam by a range of ±30° [57].

2.5 Dielectric Resonator Antenna Arrays

Few reconfigurable dielectric resonator antenna arrays have been studied and presented some encouraging results. Hence this research will study a couple of models in this area.

2.5.1 Antenna Arrays Theory

Antennas arrays overcome the limitations that are imposed by a single element such as gain enhancement and beam steering [58]. A proper arrangement of the array elements can increase the antenna efficiency and improve the radiation characteristics in comparison to a single antenna [59]. In addition, for antennas that are affected by the aperture size, such as reflector dishes and radio telescopes, antenna arrays have the same advantages of a single large antenna of high sensitivity and gain. As a result, it is possible to replace one large antenna with an array of small elements. In addition, by calculating the right weight ratio and phase separating each consecutive elements, the interference can be minimised and the main beam direction can be controlled [59]. The radiated power of an array is a complex summation of those from the individual elements., This summation can be either additive or subversive depending on the distribution of the elements and the angle of the radiated field [58, 60]. Therefore, the equation for the total radiated field must consider the individual elements distribution in the given configuration, the relative excitation weight for each element, the phase difference and the relative distance between each two consecutive elements with respect to the wavelength, as well as the elements' radiation patterns [58-60]. The literature offers an extensive mathematical analysis for the arrays far field radiation pattern. However, in this research, only the final analysis resultant equations are presented. Considering the array of *N* identical elements as illustrated in Figure 2.13, the total radiated field is the product of a single element radiation pattern by the Array Factor (*AF*), or in other words [4, 58, 60]

$$AP = 20\log(EP.AF) \tag{2.39}$$

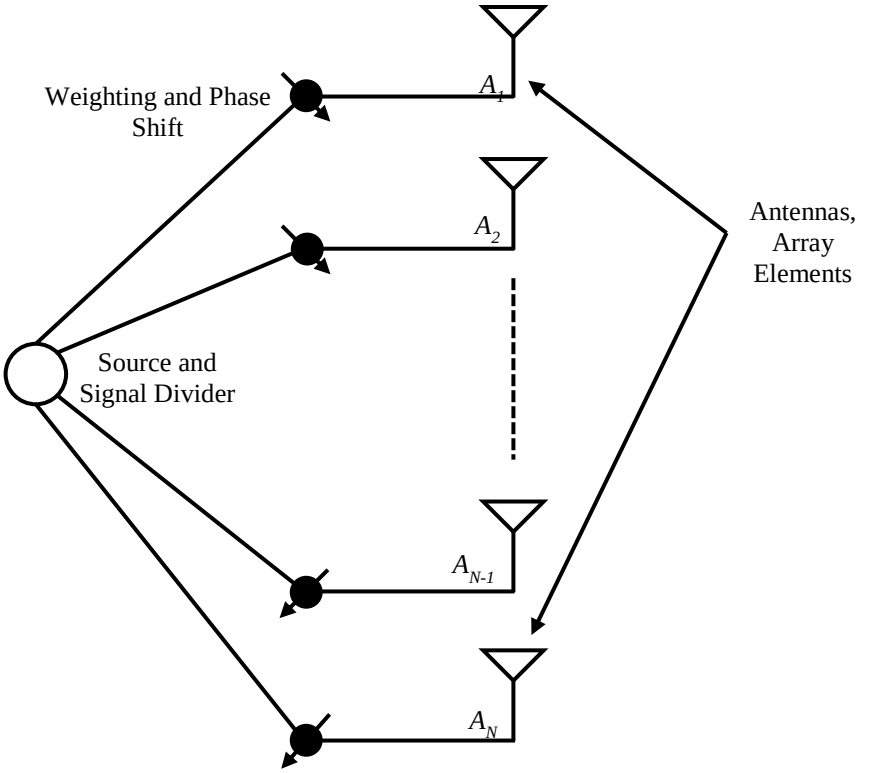

Figure 2.13 Antenna Arrays Configurations

where *AP* is the total radiated field pattern, *EP* is the single element's radiation field and *AF* can be calculated as [4, 58, 60]

$$AF = \sum_{n=1}^{N} \boldsymbol{A_n} e^{j\Psi_n} \tag{2.40}$$

$$\Psi_n = k_0 x_n \sin\theta\cos\varphi + k_0 y_n \sin\theta\sin\varphi \tag{2.41}$$

In the above equation, k_0 is the free-space wave number, x_n and y_n are the Cartesian co-ordinates of the n*th* element, and $\boldsymbol{A_n}$ is the complex voltage excitation defined as

$$\boldsymbol{A_n} = A_n e^{j\beta_n} \tag{2.42}$$

in which A_n and β_n are the excitation's amplitude and phase, respectively. As mentioned earlier, numerous array configurations have been studied and reported in the literature that can be classified as linear, planar and conformal as well as three dimensional [4, 58]. On the other hand, planar configurations can be rectangular, triangular, and circular [4, 58]. In this chapter, the main focus will be on reconfigurable linear arrays that are popular owing to their simplicity [58], with, usually, identical elements that can be distributed with either a uniformly or nonuniformly [61]. The uniform arrays involve equally spaced elements either uniform or nonuniform amplitude excitation[61]. In the case of uniformly excited arrays, the main beam direction is either normal or parallel to the array axis for broadside or endfire radiations, respectively [58, 61].

For a linear array, the array factor can be simplified assuming $A_n = A_0$, $\beta_n = \beta$, and the elements' separation distance is d. Therefore, the normalised array factor can be expressed as [4, 58]

$$AF = 1 + e^{j(kd\cos\theta+\beta)} + e^{j2(kd\cos\theta+\beta)} + \cdots + e^{j(N-1)(kd\cos\theta+\beta)} \quad (2.43)$$

$$AF = \sum_{n=1}^{N} e^{j(n-1)\psi} \quad (2.44)$$

where,

$$\psi = k_0 d\sin\theta_0 + \beta \quad (2.45)$$

$$\theta_0 = \sin^{-1}\left(\frac{-\beta}{k_0 d}\right) \quad (2.46)$$

Multiplying equation (2.43) by $e^{j\psi}$ gives

$$(AF)e^{j\psi} = e^{j\psi} + e^{j2\psi} + e^{j3\psi} + \cdots + e^{jN\psi} \quad (2.47)$$

Subtracting (2.44) from (2.47) provides

$$AF = \frac{(e^{jN\psi}-1)}{(e^{j\psi}-1)} = e^{j(N-1)\psi/2}\left[\frac{e^{j(\frac{N}{2})\psi}-e^{-j(\frac{N}{2})\psi}}{e^{j(\frac{1}{2})\psi}-e^{-j(\frac{1}{2})\psi}}\right] \quad (2.48)$$

Hence,

$$AF = e^{j(N-1)\psi/2}\left[\frac{\sin(N\psi/2)}{\sin(\psi/2)}\right] \quad (2.49)$$

Considering that the reference point is in the centre of the array,

$$AF = \left[\frac{\sin(N\psi/2)}{\sin(\psi/2)}\right] \quad (2.50)$$

From the above equations, it is possible to determine the mainlobe direction, beam-width, nulls, and the side-lobes' direction [61].

Nonuniform amplitude excitation can be used to change specific characteristics such as the main-lobe direction, beamwidth, and side-lobes. However, equations (2.45-46, 2.50) are not valid for this case, and the polynomial equations (2.40-42) must be considered [61].

Amplitude uniformity can be obtained by splitting the power equally at the feeding network junctions. Power division is determined by the branched transmission lines characteristics impedances ratio [4]. Assuming the input line characteristics impedance is Z_{o1}, and Z_{o2}, Z_{o3} for the branches of a two-element feed network as shown in Figure 2.14. For a lossless junction, the input powers P_1, P_2, and P_3, are given by [4]

$$P_2/P_3 = Z_{o3}/Z_{o2} \quad (2.51)$$

$$P_1 = P_2 + P_3 \quad (2.52)$$

Impedance matching must be considered to achieve a maximum power transfer, which can be achieved when [4]

$$Z_{o1} = Z_{02} \parallel Z_{03} \tag{2.53}$$

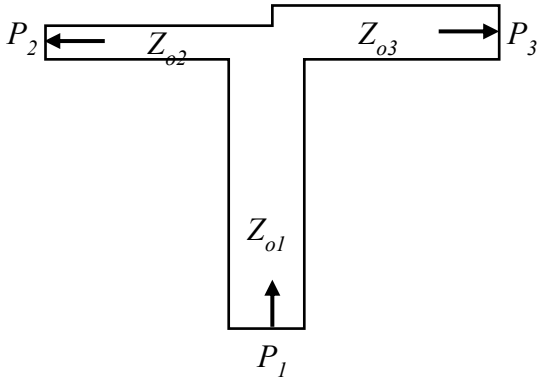

Figure 2.14 Power-Splitter Junction [4]

Non-uniform arrays can have either variable separation distances or different phases that is also known as progressive phasing [61]. The first study related to the non-uniformly spaced elements has been published back in 1960, where it has been shown that they outperform the uniform counterpart due to the degree of freedom over the uniformly spaced array, which allows some design manipulation to improve the radiation characteristics [62]. Then, numerous studies have been published suggesting specific syntheses to achieve the required radiation patterns [61]. As mentioned earlier, the shift in the excitation phase determines the main-lobe direction, hence using non-uniform phase shifting offers an extra degree of freedom in the array design albeit at the expense of an increased complexity [61]. Figure 2.15 presents the passive phase delay technique that can be employed to achieve the excitation phase shift for both series and parallel feeding networks [4]. For example, two elements array radiation pattern is controlled by the elements spacing *d* as well as each elements' excitation phase, Φ_1 and Φ_2, i.e. for a series excitation [4]

$$\frac{d+2p}{\lambda_g} = \frac{\Phi_2 - \Phi_1}{2\pi} \tag{2.54}$$

and for a parallel excitation

$$\frac{d-2p}{\lambda_g} = \frac{\Phi_2 - \Phi_1}{2\pi} \tag{2.55}$$

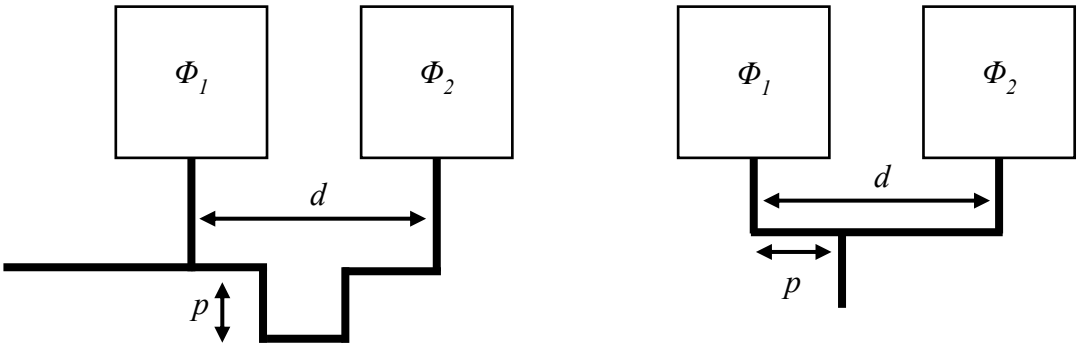

Figure 2.15 Series (Left) and Parallel (Right) Passive Delay Networks [4]

There are two techniques to feed an array; series and parallel feeds. In the first, the network is usually smaller due to the reduced number of required junctions as well as the shorter transmission line length. On the other hand, in a parallel feed, all elements are usually fed using identical line sections, which leads to an identical phase shift that can provide a wider impedance bandwidth due to the reduced chances of impedance mismatch [4]. In linear arrays, the usual radiation pattern is narrow in the array direction and wide in the perpendicular direction, which is called the fan-shaped radiation pattern [5]. This fact is essential for choosing of the coupled plane, i.e. E-field or H-field coupling, the proper excitation technique, as well as the spacing between successive elements.

Due to the small DRA element's size, the spacing between successive elements is usually small in terms of the wavelength. This may increase the mutual coupling, which can

complicate the design process as each element radiates to the adjacent elements and hence distort the originally expected radiation characteristics [2, 4]. Mutual coupling depends on a number of factors such as the chosen elements' characteristics, relative spacing and the feeding network structure [2, 4]. It is important to take mutual coupling effects into consideration since its presence leads to undesirable effects on the radiation pattern sidelobes levels as well as the beam-width [4].

2.5.2 DRA Arrays

DRA arrays can be arranged linearly to change the required radiation pattern properties or to generate a CP wave using linearly polarised elements [2]. In this section, the focus is on linear arrays since this Chapter is dedicated to the design of reconfigurable linear DRA arrays.

2.5.2.1 Linear DRA Arrays

These arrays share similar theoretical concepts of other array types with respect to serial and parallel feeding as well as amplitude and phase excitation [2, 4]. Therefore, numerous designs for linear DRA arrays have been investigated and implemented [2, 4, 5]. As mentioned earlier, the first DRA array research has been published back in 1981 [63]. A series of DR elements have been suggested as suitable array candidates by exciting them using either a dielectric waveguide or an image guide. This investigation proved that the design and implementation of a high gain DRA arrays are possible and low cost arrays are achievable for large scale manufacturing [63]. Since then, other designs have been proposed that are based on using parallel microstrip line feeding slot-coupled DRAs as a feasible linear array [5]. Several examples can be traced in the literature such as a 4-element parallel fed rectangular DRA array designed for low-side lobes applications [64]. In addition, a 2-element parallel fed cylindrical DRA array has been reported in which a couple of configurations have been investigated; the H-field array and E-field array where

the array direction is parallel to the named plane direction of the field of interest [65]. Other types of parallel excited arrays include a probe fed DRA array have been proposed, such as 2-element and 4-element disk parallel probe fed DRA arrays with a microstrip line network to feed the probes [34, 66]. Furthermore, several configurations have been accomplished for serially fed DRA arrays employing various excitation techniques including microstrip line, dielectric image guide, and microstrip branchline [2, 4].

The earliest design described previously used EM coupling serial dielectric image guide feeding for a 12-element DRA array [63]. EM coupling serial feeding has been achieved with the aid of a microstrip line feeding, which showed good radiation characteristics as well as manufacturing advantage of a printable design [67]. In addition, a waveguide has been investigated for the EM coupling, in a 30-element linear DRA array based on composite right/left transmission line [68].

Direct microstripline serial feeding has also been used for an 8-pair of rectangular DRAs where the pairing technique has been proposed to overcome the narrow band issue related to the microstrip line series feeding [69]. Microstrip branch line feeding is a multilayer hybrid feeding system that allows to harness the advantages of both series and parallel microstrip line array feeding. This has been demonstrated in a multi-segment DRA, MSDRA, array case, where an array of a 10 MSDRA elements has achieved a 15.4 dBi X-band gain, with an efficiency of 66% and a 3-dB gain bandwidth of 17% [70]. The designs to be investigated this Chapter are parallel microstrip line fed-aperture DRA arrays.

2.5.2.2 Planar DRA Arrays

This is a research topic that is yet to be expanded and explored with the need to implement more designs. This is a result of the analysis, design and fabrication complexity of planar

arrays generally, and the DRAs planar arrays specifically. However, the available literature offers promising results [4, 5] as this kind of arrays offer a narrow beamwidth in conjunction with a high gain in both planes that provides what is known as a pencil-beam pattern, which provides a narrow beamwidth useful for end-to-end communications application [5]. On the other hand, with a proper arrangement of elements and/or feed, either a linear or circular polarisation can be generated [2, 4, 5].

Planar DRA arrays with linear polarisation have been achieved in couple of configurations such as a 2×2 element probe-fed cylindrical DRA array [71]. In addition, another 2×2 element cylindrical DRA array with a microstrip line aperture coupling has been reported, where it has been demonstrated that both planes beamwidths have reduced from 75° to 54° and 148° to 49° for H-plane and E-plane, respectively. Further, the front/back ratio increased by 50% from 14 dBi to 21 dBi [72]. Additionally, another 2×2 element microstrip line aperture-fed rectangular DRA array has been reported in which an impedance matching bandwidth of 18% has been achieved for the array compared to 10% for a single element, with a gain reaches 11.3 dBi at 7.35 GHz [73].

On the other hand, couple of methods have been employed to achieve circular polarisation using planar DRA arrays. The first method is based on using a properly arranged circularly polarised cylindrical DRA elements such as a 2×2 array that has been feed using branched microstrip line aperture-coupling [74]. This array achieved a 19% impedance matching bandwidth and 16% AR bandwidth compared to 9% and 5.6% for a single CP element, and 8% and 4.5% for a CP array consist of LP elements, respectively. Alternatively, CP DRA array can be designed using a sequential rotation feed for linearly polarised elements to generate a circularly polarised wave [74, 75]. This technique requires the feeding of each element with calculated amplitudes and phases. As a result, a proper feed network needs to be designed that takes into consideration the physically

small available space [4]. However, the available literature involves other techniques to generate circular polarisation with large gain and wide axial ratio bandwidth [2, 4, 5].

5.3.3 Reconfigurable DRA Arrays

There is a limited number of research publications in this topic. However, this research area has been touched recently and started to draw more interest. One of the earliest examples is an investigation of using a digital phase shifter to electronically steer the mainlobe direction of a Multi-Segment DRA (MSDRA) phased planar array that consists of 16 array columns of 20 MSDRA elements [76]. The design employed sixteen digital shifters, 4-bit each, combined with low noise amplifiers within the feed network. This allows an engineer to control each column phase shift to change the main beam direction [4, 5, 76]. Another beam steered DRA phased array has been previously mentioned in this chapter and the previous chapter, with the feed network loaded with MIM varactors. These varactors can be electronically controlled phase shifters to tune the feed, resulting in steering the mainlobe by a range of ±30° [57].

A back-to-back Yagi-Uda five element DRA array has been suggested with beam steering achieved by changing the excitation phase of one of the used two feeds [77]. The array consists of three reflector DRA elements, one in the centre called the common reflector, and two at both ends of the array called parasitic reflectors. Each of the other two DRAs are sandwiched between the common reflector and one of the parasitic reflectors, and each is separated from these reflectors by distances of S_R and S_D, respectively. The latter two are fed and called the driven elements. This array achieved 19% impedance matching bandwidth and 16% AR bandwidth compared to 9% and 5.6% for a single CP element, and 8% and 4.5% for a CP array consisted of LP elements, respectively. Changing the excitation phase for one element only provide a mainbeam steering by up to 67° with a gain of 10 dBi [77].

Two designs have been proposed for a 2-element reconfigurable pattern DRA array for multi-input multi-output (MIMO) applications. The first design suggests allocating each DRA on one of two ground planes that are perpendicular to each other. In the second design, both elements have been allocated on the same ground plane. Both designs activate three modes in each element using RF switches to change the excitation port. The first two ports excite the TE^x and TE^y modes, while the third excites a monopole mode. By controlling each element mode separately, nine different patterns have been achieved using this technique [78, 79].

A sequential rotation fed planar DRA array design has been proposed as a reconfigurable polarisation planar array. The 2×2 microstrip aperture coupled cylindrical DRA array had each element linearly excited with a ±90° phase difference from its neighbouring elements. This results in two elements that excite the horizontal LP, while the other two excite a vertical LP. Excitation arrangements for all the elements lead to both LHCP and RHCP radiation depending on the sequence of phase difference, with axial ratio reaching less than 0.1 dB [80]. Another study has proposed a two slot-fed nonidentical DRA array, with a reconfigurable quad section wideband Wilkinson power divider and reconfigurable stub length. PIN diodes have been suggested to be used to control the impedance of the power divider and stub length, providing a discrete frequency tuning capability in the range as low as ~1.2 GHz up to ~5.3 GHz [81].

2.6 Summary

It has been demonstrated that employing dielectric geometries as a means to excite resonating electromagnetic modes in antennas provide enormous advantages in communication systems. This includes low losses, miniaturised antenna sizes, low costs, and other advantages that overwhelmingly surpass the minor disadvantages.

This chapter has presented the operation concept of basic DRA geometries such as hemispherical, cylindrical as well as rectangular. In addition, a literature review has been conducted that cover some of the key publications in this research topic. The most popular DRA excitation approaches have been reviewed. In addition, the potential advantages of using more complex DRA geometries have been reviewed. Furthermore, a special attention has been given to the topic of reconfigurable DRAs and the key papers in this line have been reviewed.

The theory of antenna arrays has been covered sufficiently, and the DRA linear planar arrays have been discussed as a background for the work presented in Chapter Five. In addition, the past research in the area of reconfigurable DRA arrays have been presented.

In the following chapters, novel reconfigurable DRA designs will be presented. This includes two structures for polarisation reconfiguration in Chapter Three, mode switching design in Chapter Four, Reconfigurable DRA array in Chapter Five, and a study for the ability to use semiconductor plasma in mode switching in Chapter Six.

References

[1] R. D. Richtmyer, "Dielectric Resonators," Journal of Applied Physics, vol. 10, no. 6, pp. 391-398, 1939.

[2] K. M. Luk and K. W. Leung, Dielectric resonator antennas. Research Studies Press, 2003.

[3] R. S. Yaduvanshi and H. Parthasarathy, Rectangular Dielectric Resonator Antennas: Theory and Design. Springer India, 2015.

[4] A. Petosa, Dielectric Resonator Antenna Handbook. Artech House, 2007.

[5] A. Petosa and A. Ittipiboon, "Dielectric Resonator Antennas: A Historical Review and the Current State of the Art," IEEE Antennas and Propagation Magazine, vol. 52, no. 5, pp. 91-116, 2010.

[6] M. Gastine, L. Courtois, and J. L. Dormann, "Electromagnetic Resonances of Free Dielectric Spheres," IEEE Transactions on Microwave Theory and Techniques, vol. 15, no. 12, pp. 694-700, 1967.

[7] S. Long, M. McAllister, and S. Liang, "The resonant cylindrical dielectric cavity antenna," IEEE Transactions on Antennas and Propagation, vol. 31, no. 3, pp. 406-412, 1983.

[8] Y. Hung Yuet, "Natural Resonant Frequencies of Microwave Dielectric Resonators (Correspondence)," IEEE Transactions on Microwave Theory and Techniques, vol. 13, no. 2, pp. 256-256, 1965.

[9] J. C. Sethares and S. J. Naumann, "Design of Microwave Dielectric Resonators," IEEE Transactions on Microwave Theory and Techniques, vol. 14, no. 1, pp. 2-7, 1966.

[10] A. Okaya and L. F. Barash, "The Dielectric Microwave Resonator," Proceedings of the IRE, vol. 50, no. 10, pp. 2081-2092, 1962.

[11] R. K. Mongia and A. Ittipiboon, "Theoretical and experimental investigations on rectangular dielectric resonator antennas," IEEE Transactions on Antennas and Propagation, vol. 45, no. 9, pp. 1348-1356, 1997.

[12] K. L. Wong, N. C. Chen, and H. T. Chen, "Analysis of a hemispherical dielectric resonator antenna with an airgap," IEEE Microwave and Guided Wave Letters, vol. 3, no. 10, pp. 355-357, 1993.

[13] D. Guha and Y. M. M. Antar, "New Half-Hemispherical Dielectric Resonator Antenna for Broadband Monopole-Type Radiation," IEEE Transactions on Antennas and Propagation, vol. 54, no. 12, pp. 3621-3628, 2006.

[14] R. K. Mongia, "Half-split dielectric resonator placed on metallic plane for antenna applications," Electronics Letters, vol. 25, no. 7, pp. 462-464, 1989.

[15] R. K. Mongia, A. Ittipiboon, Y. M. M. Antar, P. Bhartia, and M. Cuhaci, "A half-split cylindrical dielectric resonator antenna using slot-coupling," IEEE Microwave and Guided Wave Letters, vol. 3, no. 2, pp. 38-39, 1993.

[16] R. K. Chaudhary, K. V. Srivastava, and A. Biswas, "A Concentric three-layer half-split cylindrical dielectric resonator antenna for wideband applications," in Electromagnetic Theory (EMTS), Proceedings of 2013 URSI International Symposium on, 2013, pp. 664-667.

[17] R. K. Mongia, A. Ittipiboon, P. Bhartia, and M. Cuhaci, "Electric-monopole antenna using a dielectric ring resonator," Electronics Letters, vol. 29, no. 17, pp. 1530-1531, 1993.

[18] A. A. Kishk, "An elliptic dielectric resonator antenna designed for circular polarization with single feed," Microwave and Optical Technology Letters, vol. 37, no. 6, pp. 454-456, 2003.

[19] A. Ittipiboon, A. Petosa, D. Roscoe, and M. Cuhaci, "An investigation of a novel

broadband dielectric resonator antenna," in Antennas and Propagation Society International Symposium, 1996. AP-S. Digest, 1996, vol. 3, pp. 2038-2041 vol.3.

[20] M. Haneishi and H. Takazawa, "Broadband circularly polarised planar array composed of a pair of dielectric resonator antennas," Electronics Letters, vol. 21, no. 10, pp. 437-438, 1985.

[21] A. Petosa, A. Ittipiboon, Y. M. M. Antar, D. Roscoe, and M. Cuhaci, "Recent advances in dielectric-resonator antenna technology," IEEE Antennas and Propagation Magazine, vol. 40, no. 3, pp. 35-48, 1998.

[22] A. A. Kishk, "Tetrahedron and triangular dielectric resonator antenna with wideband performance," in Antennas and Propagation Society International Symposium, 2002. IEEE, 2002, vol. 4, pp. 462-465 vol.4.

[23] M. Lapierre, Y. M. M. Antar, A. Ittipiboon, and A. Petosa, "A wideband monopole antenna using dielectric resonator loading," in Antennas and Propagation Society International Symposium, 2003. IEEE, 2003, vol. 3, pp. 16-19 vol.3.

[24] L. Yoonjae, Y. Junho, and R. Mittra, "A dual frequency circularly polarized antenna design using a combination of DRA and microstrip patch," in Antennas and Propagation Society International Symposium, 2003. IEEE, 2003, vol. 4, pp. 122-125 vol.4.

[25] A. A. Kishk, A. Ittipiboon, Y. M. M. Antar, and M. Cuhaci, "Dielectric resonator antennas fed by a slot in the ground plane of a microstripline," in Antennas and Propagation, 1993., Eighth International Conference on, 1993, pp. 540-543 vol.1.

[26] K. W. Leung, "Circularly polarized dielectric resonator antenna excited by a shorted annular slot with a backing cavity," IEEE Transactions on Antennas and Propagation, vol. 52, no. 10, pp. 2765-2770, 2004.

[27] R. Bancroft, Microstrip and printed antenna design. The Institution of Engineering

and Technology, 2009.

[28] A. Ittipiboon, R. K. Mongia, Y. M. M. Antar, P. Bhartia, and M. Cuhaci, "Aperture fed rectangular and triangular dielectric resonators for use as magnetic dipole antennas," Electronics Letters, vol. 29, no. 23, pp. 2001-2002, 1993.

[29] D. M. Pozar, "Microstrip antennas," Proceedings of the IEEE, vol. 80, no. 1, pp. 79-91, 1992.

[30] K. W. Leung, W. C. Wong, K. M. Luk, and E. K. N. Yung, "Annular slot-coupled dielectric resonator antenna," Electronics Letters, vol. 34, no. 13, pp. 1275-1277, 1998.

[31] H. Morishita, K. Hirasawa, and K. Fujimoto, "Analysis of a cavity-backed annular slot antenna with one point shorted," IEEE Transactions on Antennas and Propagation, vol. 39, no. 10, pp. 1472-1478, 1991.

[32] K. W. Leung and S. K. Mok, "Circularly polarised dielectric resonator antenna excited by perturbed annular slot with backing cavity," Electronics Letters, vol. 37, no. 15, pp. 934-936, 2001.

[33] M. W. McAllister, S. A. Long, and G. L. Conway, "Rectangular dielectric resonator antenna," Electronics Letters, vol. 19, no. 6, pp. 218-219, 1983.

[34] G. Drossos, Z. Wu, and L. E. Davis, "Linear arrays consisting of four probe-fed cylindrical dielectric resonator antennas," Microwave and Optical Technology Letters, vol. 18, no. 6, pp. 367-370, 1998.

[35] Z. N. Chen, K. W. Leung, K. M. Luk, and E. K. N. Yung, "Effect of parasitic disk on a coaxial probe-fed dielectric resonator antenna," Microwave and Optical Technology Letters, vol. 15, no. 3, pp. 166-168, 1997.

[36] K. M. Luk, M. T. Lee, K. W. Leung, and E. K. N. Yung, "Technique for improving coupling between microstripline and dielectric resonator antenna," Electronics

Letters, vol. 35, no. 5, pp. 357-358, 1999.

[37] G. P. Junker, A. A. Kishk, A. W. Glisson, and D. Kajfez, "Effect of an air gap around the coaxial probe exciting a cylindrical dielectric resonator antenna," Electronics Letters, vol. 30, no. 3, pp. 177-178, 1994.

[38] L. Kwok Wa, "Conformal strip excitation of dielectric resonator antenna," IEEE Transactions on Antennas and Propagation, vol. 48, no. 6, pp. 961-967, 2000.

[39] H. K. Ng and K. W. Leung, "Circular-polarized hemispherical dielectric resonator antenna excited by dual conformal-strip," in Antennas and Propagation Society International Symposium, 2002. IEEE, 2002, vol. 3, pp. 442-445 vol.3.

[40] S. K. Khamas, "Circularly Polarized Dielectric Resonator Antenna Excited by a Conformal Wire," IEEE Antennas and Wireless Propagation Letters, vol. 7, pp. 240-242, 2008.

[41] R. A. Kranenburg and S. A. Long, "Microstrip transmission line excitation of dielectric resonator antennas," Electronics Letters, vol. 24, no. 18, pp. 1156-1157, 1988.

[42] A. Petosa, R. K. Mongia, M. Cuhaci, and J. S. Wight, "Magnetically tunable ferrite resonator antenna," Electronics Letters, vol. 30, no. 13, pp. 1021-1022, 1994.

[43] A. Petosa, R. K. Mongia, A. Ittipiboon, and J. S. Wight, "Switchable LP/CP ferrite disk resonator antenna," Electronics Letters, vol. 31, no. 3, pp. 148-149, 1995.

[44] G. Drossos, Z. Wu, and L. E. Davis, "Switchable cylindrical dielectric resonator antenna," Electronics Letters, vol. 32, no. 10, pp. 862-864, 1996.

[45] Z. Li, C. Wu, and J. Litva, "Adjustable frequency dielectric resonator antenna," Electronics Letters, vol. 32, no. 7, pp. 606-607, 1996.

[46] S. P. Kingsley and S. G. O. Keefe, "Beam steering and monopulse processing of probe-fed dielectric resonator antennas," IEE Proceedings - Radar, Sonar and

Navigation, vol. 146, no. 3, pp. 121-125, 1999.

[47] S. P. Kingsley and S. G. O'keefe, "Steerable-beam multiple-feed dielectric resonator antenna," ed: Google Patents, 2002.

[48] S. P. Kingsley and S. G. O'keefe, "Dielectric resonator antenna array with steerable elements," ed: Google Patents, 2004.

[49] S. P. Kingsley and S. G. O'keefe, "Steerable-beam multiple-feed dielectric resonator antenna," ed: Google Patents, 2005.

[50] H. Fayad and P. Record, "Wideband Dielectric Resonator Antenna with Reconfigurable Radiation Pattern," in Second NASA/ESA Conference on Adaptive Hardware and Systems (AHS 2007), 2007, pp. 3-6.

[51] H. Fayad and P. Record, "Experimental investigation on new steerable dielectric resonator antenna," Electronics Letters, vol. 43, no. 19, pp. 1009-1010, 2007.

[52] A. Petosa and S. Thirakoune, "Frequency tunable rectangular dielectric resonator antenna," in 2009 IEEE Antennas and Propagation Society International Symposium, 2009, pp. 1-4.

[53] J. Desjardins, D. A. McNamara, S. Thirakoune, and A. Petosa, "Electronically Frequency-Reconfigurable Rectangular Dielectric Resonator Antennas," IEEE Transactions on Antennas and Propagation, vol. 60, no. 6, pp. 2997-3002, 2012.

[54] S. G. O. Keefe and S. P. Kingsley, "Tunability of Liquid Dielectric Resonator Antennas," IEEE Antennas and Wireless Propagation Letters, vol. 6, pp. 533-536, 2007.

[55] T. Apperley and M. Okoniewski, "A frequency reconfigurable dielectric resonator antenna using controllable air gaps," in The 8th European Conference on Antennas and Propagation (EuCAP 2014), 2014, pp. 2923-2926.

[56] L. Zhong, J. S. Hong, and H. C. Zhou, "A Novel Pattern-Reconfigurable

Cylindrical Dielectric Resonator Antenna With Enhanced Gain," IEEE Antennas and Wireless Propagation Letters, vol. 15, pp. 1253-1256, 2016.

[57] M. Nikfalazar et al., "Steerable Dielectric Resonator Phased-Array Antenna Based on Inkjet-Printed Tunable Phase Shifter With BST Metal-Insulator-Metal Varactors," IEEE Antennas and Wireless Propagation Letters, vol. 15, pp. 877-880, 2016.

[58] C. A. Balanis, Antenna Theory: Analysis and Design. Wiley-Interscience, 2005.

[59] R. L. Haupt, Antenna arrays: a computational approach. John Wiley & Sons, 2010.

[60] L. H. Randy, "Array Factor Analysis," in Antenna Arrays:A Computational Approach: Wiley-IEEE Press, 2010, pp. 45-114.

[61] M. T. Ma, Theory and application of antenna arrays. Wiley, 1974.

[62] H. Unz, "Linear Arrays with arbitrarily distributed elements," IRE Transactions on Antennas and Propagation, vol. 8, no. 2, pp. 222-223, 1960.

[63] M. T. Birand and R. V. Gelsthorpe, "Experimental millimetric array using dielectric radiators fed by means of dielectric waveguide," Electronics Letters, vol. 17, no. 18, pp. 633-635, 1981.

[64] A. Petosa and S. Thirakoune, "Linear array of dielectric resonator antennas optimized using a genetic algorithm for low-sidelobe applications," in Microwave Conference, 2000 Asia-Pacific, 2000, pp. 21-24.

[65] K. Y. Chow, K. W. Leung, K. M. Luk, and E. K. N. Yung, "Cylindrical dielectric resonator antenna array," Electronics Letters, vol. 31, no. 18, pp. 1536-1537, 1995.

[66] G. Drossos, Z. Wu, and L. Davis, "Two-element broadside arrays using cylindrical dielectric resonator antennas," Microwave and Optical Technology Letters, vol. 11, no. 6, pp. 342-345, 1996.

[67] A. Petosa, R. K. Mongia, A. Ittipiboon, and J. S. Wight, "Investigation of various

feed structures for linear arrays of dielectric resonator antennas," in Antennas and Propagation Society International Symposium, 1995. AP-S. Digest, 1995, vol. 4, pp. 1982-1985 vol.4.

[68] T. Ueda, N. Michishita, M. Akiyama, and T. Itoh, "Dielectric-Resonator-Based Composite Right/Left-Handed Transmission Lines and Their Application to Leaky Wave Antenna," IEEE Transactions on Microwave Theory and Techniques, vol. 56, no. 10, pp. 2259-2269, 2008.

[69] A. Petosa, A. Ittipiboon, M. Cuhaci, and R. Larose, "Bandwidth improvement for a microstrip-fed series array of dielectric resonator antennas," Electronics Letters, vol. 32, no. 7, pp. 608-609, 1996.

[70] A. Petosa, R. Larose, A. Ittipiboon, and M. Cuhaci, "Microstrip-fed array of multisegment dielectric resonator antennas," IEE Proceedings - Microwaves, Antennas and Propagation, vol. 144, no. 6, pp. 472-476, 1997.

[71] G. Drossos, Z. Wu, and L. E. Davis, "Four-element planar arrays employing probe-fed cylindrical dielectric resonator antennas," Microwave and Optical Technology Letters, vol. 18, no. 5, pp. 315-319, 1998.

[72] K. W. Leung, H. Y. Lo, K. M. Luk, and E. K. N. Yung, "Two-dimensional cylindrical dielectric resonator antenna array," Electronics Letters, vol. 34, no. 13, pp. 1283-1285, 1998.

[73] G. D. Loos and Y. M. M. Antar, "Investigation of a novel aperture-coupled dielectric resonator antenna subarray," in Antennas and Propagation Society International Symposium, 1994. AP-S. Digest, 1994, vol. 3, pp. 1510-1513 vol.3.

[74] K. Pang, H. Lo, K. Leung, K. Luk, and E. Yung, "Circularly polarized dielectric resonator antenna subarrays," Microwave and Optical Technology Letters, vol. 27, no. 6, pp. 377-379, 2000.

[75] A. Petosa, A. Ittipiboon, and M. Cuhaci, "Array of circular-polarised cross dielectric resonator antennas," Electronics Letters, vol. 32, no. 19, pp. 1742-1743, 1996.

[76] A. Petosa, R. Larose, A. Ittipiboon, and M. Cuhaci, "Low profile phased array of dielectric resonator antennas," in Phased Array Systems and Technology, 1996., IEEE International Symposium on, 1996, pp. 182-185.

[77] V. Davids and R. Lehmensiek, "A beam steerable back-to-back Yagi-Uda dielectric resonator antenna array," in 2016 10th European Conference on Antennas and Propagation (EuCAP), 2016, pp. 1-4.

[78] I. Shoaib, X. Chen, and Z. Ying, "A pattern reconfigurable dielectric resonator antenna array for adaptive MIMO systems," in Antennas and Propagation Conference (LAPC), 2011 Loughborough, 2011, pp. 1-4.

[79] Y. Li, I. Shoaib, S. Wang, X. Chen, and Z. Ying, "A pattern reconfigurable DRA array for MIMO applications," in Microwave Technology & Computational Electromagnetics (ICMTCE), 2011 IEEE International Conference on, 2011, pp. 301-304.

[80] R. Kumari, S. K. Behera, and S. K. Sharma, "Aperture coupled wideband dielectric resonator antenna array with polarization reconfiguration," in Applied Electromagnetics Conference (AEMC), 2013 IEEE, 2013, pp. 1-2.

[81] B. Dwivedy and S. K. Behera, "Frequency reconfigurable DRA array using wideband Wilkinson's approach," in Communication Technologies (GCCT), 2015 Global Conference on, 2015, pp. 655-658.

Chapter Three

Polarisation Reconfigurable Dielectric Resonator Antennas

3.1 Introduction

As mentioned in Chapter one, the radiated wave's polarisation depends on the antenna's current flow direction [1]. Additionally, it has been mentioned in Chapter 2 that most of the dielectric resonator geometries can be excited to generate both linear and/or circular polarisations. In this chapter, two antenna configurations are studied to be the base for the proposed polarisation reconfiguration techniques to be proposed. Furthermore, a prototype of the second antenna has been built and measured to validate the theoretical results.

3.2 Polarisation

A traveling plane wave can be classified as either linearly, elliptically, or circularly polarised [2]. In the case of a linear polarisation, the electric field oscillates in a perpendicular axis to that of the travelling wave. For example, Figure 3.1 illustrates a wave travelling in the *z*-axis direction, with an E-field component that oscillates along the *y*-axis. The electric field can be *x* or *y* directed.

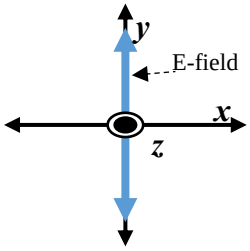

Figure 3.1 Linear Polarisation Along the *y*-Axis

The elliptical polarisation radiation is illustrated in Figure 3.2, where it can be noticed that the wave oscillates around the travelling axis in an elliptic path. As a result, there will be two electric field components that can be expressed as [2]:

$$E_x = E_1 sin(\omega t - \beta z) \tag{3.1}$$

$$E_y = E_2 sin(\omega t - \beta z + \delta) \tag{3.2}$$

where E_1 and E_2 refer to the amplitudes of the x and y components, respectively, and δ is the time-phase angle between these two components. This result in the following vector field equation [2]

$$\boldsymbol{E} = \hat{\boldsymbol{x}} E_1 sin(\omega t - \beta z) + \hat{\boldsymbol{y}} \boldsymbol{E_2} \sin(\omega t - \beta z + \delta) \tag{3.3}$$

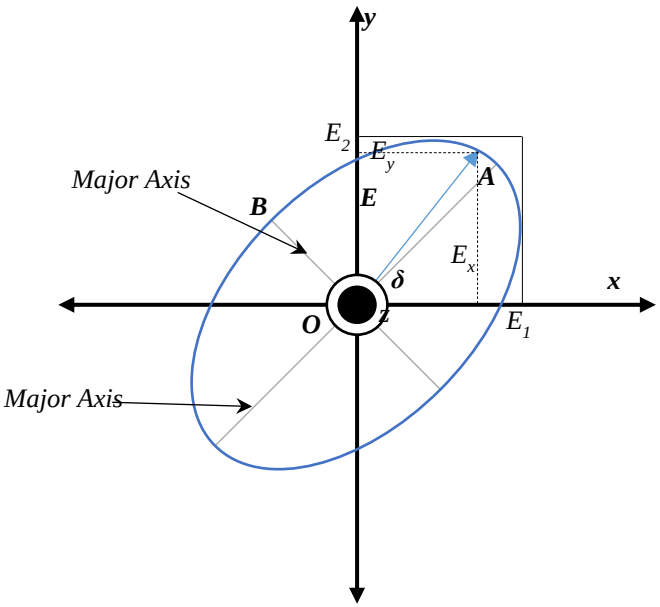

Figure 3.2 Elliptical Polarisation

The axial ratio, ***AR***, defines the relationship between the major and semi-major axes, or between ***OA*** and ***OB*** as shown in Figure 3.2, and can be calculated as [2]

$$AR = \frac{OA}{OB} \tag{3.4}$$

It should be noted that AR ranges from 1 to infinity, which corresponds to pure circular and linear polarisations, respectively. It should be noted that these are special cases of the elliptical polarisation. For example, there is only one electric field component when AR reaches infinity, which corresponds to the linear polarisation case. On the other hand, when AR=1, both ellipse axes have the same amplitude, which corresponds to a pure circular polarisation radiation [2] in which $E_1 = E_2$, and $\delta = \pm 90°$.

The other important characteristics of the elliptical/ circular polarisation is the rotation direction. For instance, if the rotation is in a clockwise direction, the polarisation is classified as a right hand circular polarization (RHCP). On the other hand, left hand circular polarisation (LHCP) radiation is accomplished for the counter clockwise rotation [3].

3.3 Reconfigurable Circular Polarisation using Hemispherical DRA

Figure 3.3 illustrates a configuration of an annular-fed hemispherical DRA that can be used to generate linearly polarised electric field radiation. However, it can be manipulated to generate a circular radiation polarisation by exciting the DRA using an annular slot that is short circuited at an angle of 90° from the feed point [4]. Following a CP DRA design of [4], a modification is proposed to achieve the polarisation reconfigurability by creating the desired short-circuit on the slot using a forward biased PIN diode. Furthermore, an additional PIN diode has been added at an angular distance of 180° from the first counterpart. This configuration results in four possible scenarios; both PIN diodes are OFF, two cases in which one PIN diode is OFF and the other is ON, and a final case in which both PIN diodes are ON, or forwarded biased. In principle, the first case is equivalent to that of a normal annular slot coupled linearly polarised DRA, with the

expectation of some ignorable distortion from the insertion of the PIN diodes materials. Similarly, linear polarisation is expected from the last case in which both diodes are switched ON. However, the real reconfigurability is expected when only one PIN diode is switched ON, where a circular polarisation is generated. In this case the polarization sense can be switched from left to right handed depending on which diode is activated. Further, the diodes will be identified as right and left hand diodes, i.e. RD and LD, respectively. This is based on their position with respect to the feed point. In this model, the circuit equivalent of the PIN diode has been used to represent both of the OFF and ON diodes' states. The parameters have been chosen as those of the BAR50-02V PIN diode data sheet Shown in Appendix B [5].

It should be noted that the employed design parameters are based on those given in [4]; DRA radius of a=12.5 mm, dielectric constant of ε_r = 9.6, slot radius and width of b = 7.37 mm and w= 1.14 mm, respectively, and a backing cavity radius of c = 25 mm. The backing cavity, which is a hemispherical shell, is used to eliminate the backside radiation, and its size must be chosen carefully to avoid affecting the resonance impedance bandwidth [6, 7]. The fundamental TE_{111} mode has been excited, and according to equations (2.2) and (2.4), the expected resonance frequency is 3.68 GHz. Figure 3.4 shows the field distribution inside the DRA for the *x*-z, *y*-z, and *x*-*y* planes determined using CST Microwave Studio. Field distributions are as to be expected for the TE_{111} mode, where the hemispherical DRA is behaving like a horizontal magnetic dipole, considering that the imaginary dipole is laying alongside the *x*-axis.

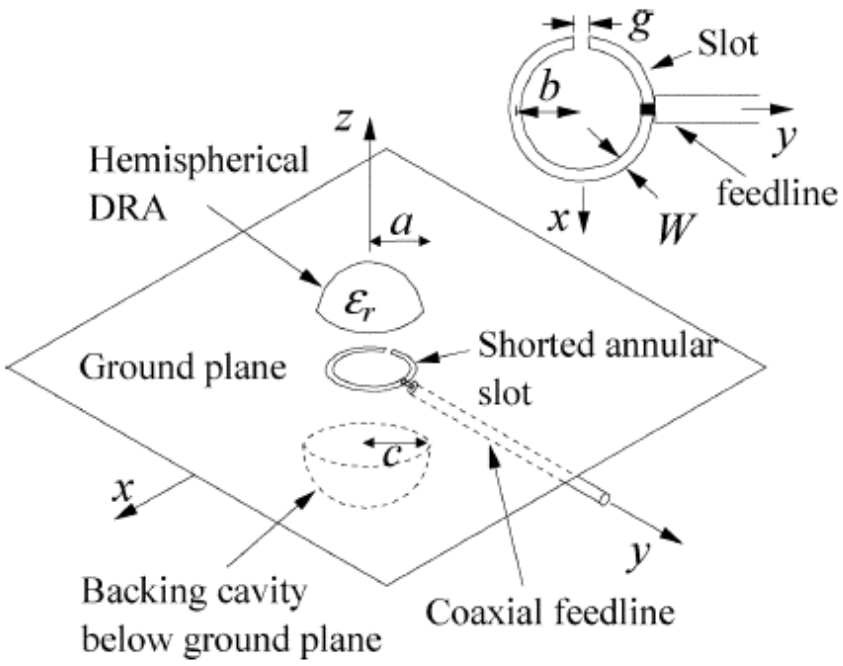

(a)

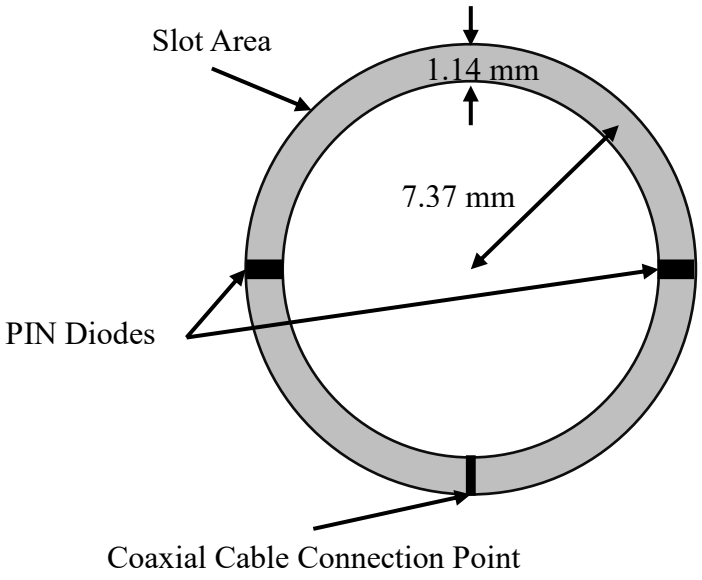

(b)

Figure 3.3 Shorted Annular Slot Fed Hemispherical DRA with a Backing Cavity (a) Antenna Diagram [4] and (b) Slot Area with the Proposed PIN Diodes Locations

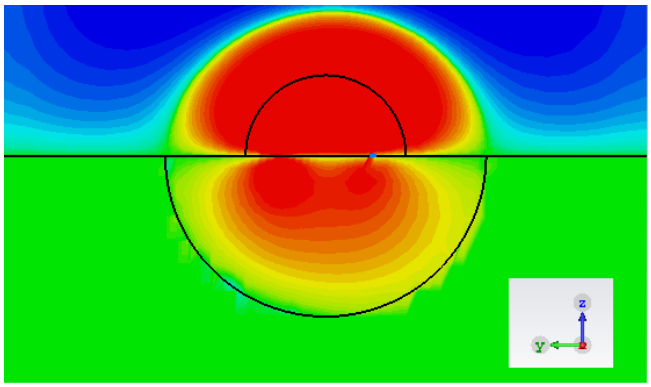

(a) *y-z* plane E-field distribution

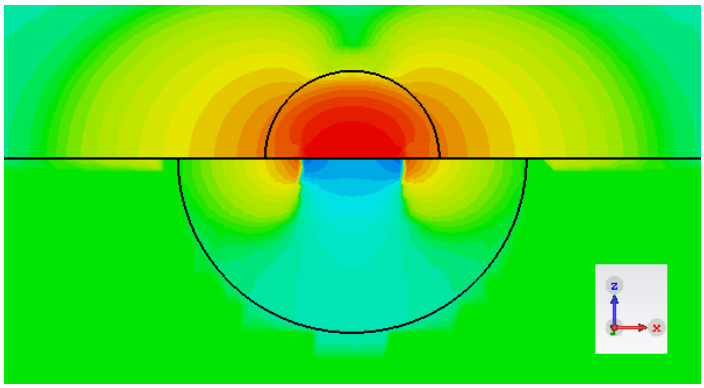

(b) *x-z* plane H-field distribution

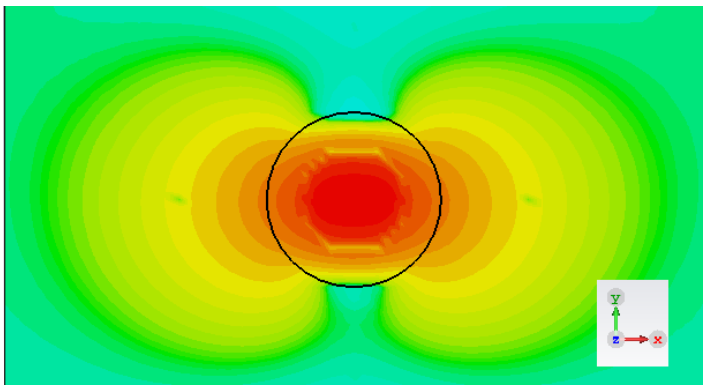

(c) *x-y* plane H-field distribution

Figure 3.4 Field distribution in the Hemispherical DRA at 3.9 GHz

Using CST Microwave Studio 2015, the antenna has been simulated at the absence of any diodes, and a resonance frequency for the TE_{111} mode has been achieved at 3.93 GHz compared to a theoretical figure of 3.66 GHz. As illustrated in Figure 3.5, the fundamental mode has been excited with an impedance matching bandwidth of 9.45% that has been achieved in conjunction with an axial ratio of more than 40 dB, which corresponds to the expected linearly polarised radiation. The E-plane and H-plane radiation patterns are shown in Figure 3.6, which radiation pattern are similar to the broadside patterns expected from TE_{111} mode. It should be noted that two equivalent models have been used to represent the diodes; the first is based on employing metallic strips to short circuit the slot, i.e. the ON state, while a PIN diode equivalent circuit has been used in the second model. In addition, four cases need to be considered in the first model; two when both of the diodes are in the same state, ON or OFF, at the same time, and two when the diodes are in different states, i.e. one is ON and the other is OFF.

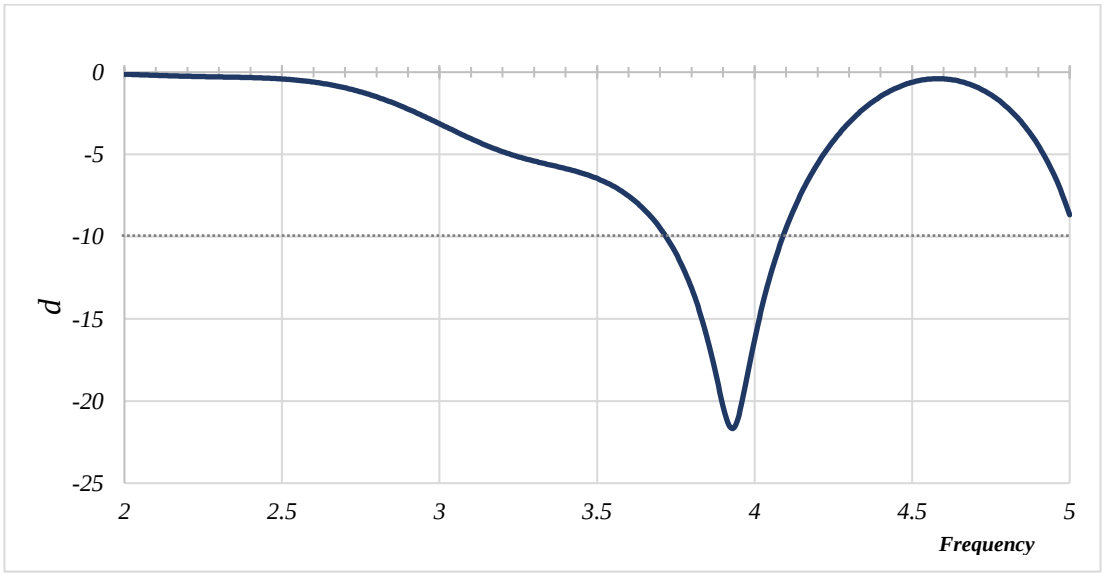

Figure 3.5 Reflection Coefficient for the Annular Slot-Fed Hemispherical DRA

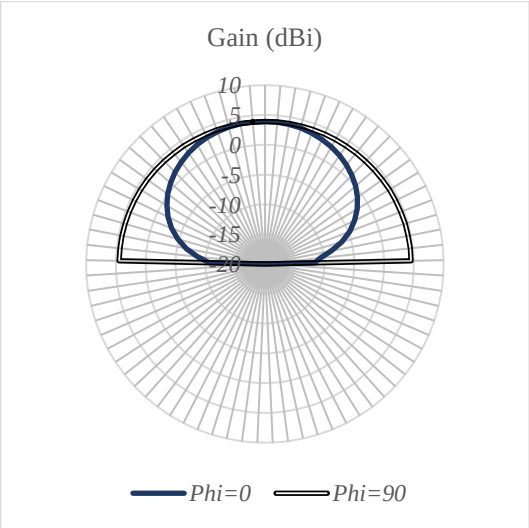

Figure 3.6 Far Field Radiation Pattern for the Annular Slot-Fed Hemispherical DRA (E_θ)

The reflection coefficients for the four cases are illustrated in Figure 3.7, where it can be observed that a resonance frequency of ~3.8 GHz has been achieved that corresponds to the excitation of the fundamental TE_{111} mode. The shift from the 3.93 GHz to 3.8 GHz is likely to be associated with the used material to model the PIN diodes in the simulations, where a perfect electric conductor (PEC) was used instead of copper in the original design, and hence affecting the current and field distributions. On the other hand, case four, in which both diodes are ON, shows another active bandwidth around a centre frequency of 2.78 GHz with a rather narrow impedance matching bandwidth of ~1%. This band probably exists due to an impedance condition that can be related to the annular slot natural frequency or the backing cavity resonance effect, since the operating frequency is approximately 25% less than the dominant mode frequency [7]. In addition, Figure 3.8 illustrates the axial ratio for the second and third cases over a frequency range of 3.3-4 GHz, where it can be noticed that a 3dB AR bandwidth of 1.7% has been achieved with an AR minimum point at 3.57 GHz. Furthermore, Figures 3.9 and 3.10 illustrate comparisons between the E_R and E_L components for both LHCP and RHCP at 3.57 GHz.

From these results, it can be noticed that E_L is larger than E_R when the RD is switched ON, which corresponds to the case of LHCP radiation, and the opposite is true as illustrated in Figure 3.10. Table 3.1 presents a comparison between the four cases in terms of resonance frequency, bandwidth, polarisation, and minimum axial ratio.

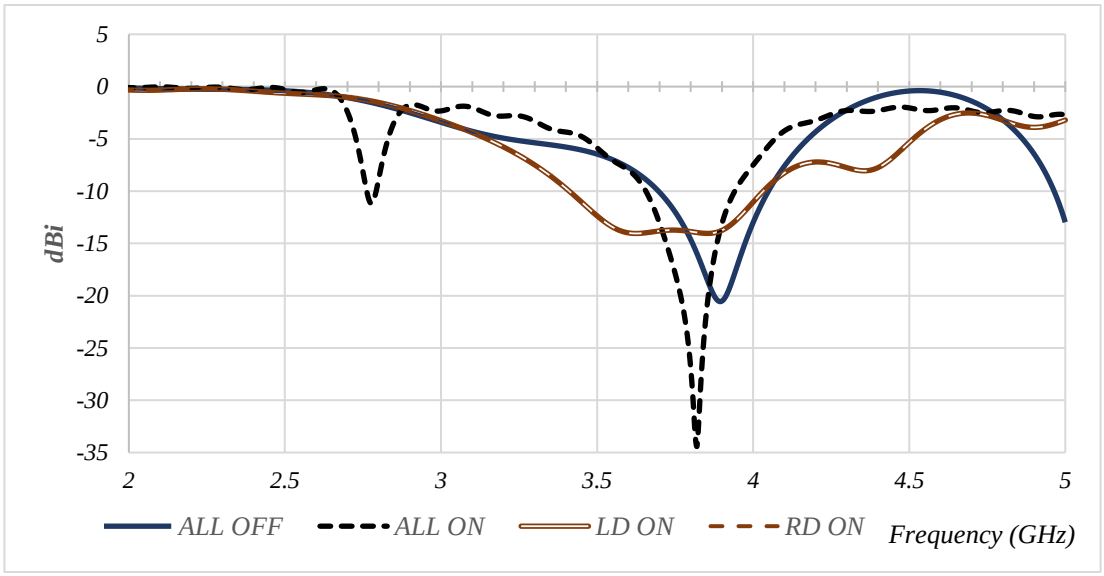

Figure 3.7 Reflection Coefficient (dB) vs Frequency for Reconfigurable Annular Slot-Fed Hemispherical DRA - Model 1

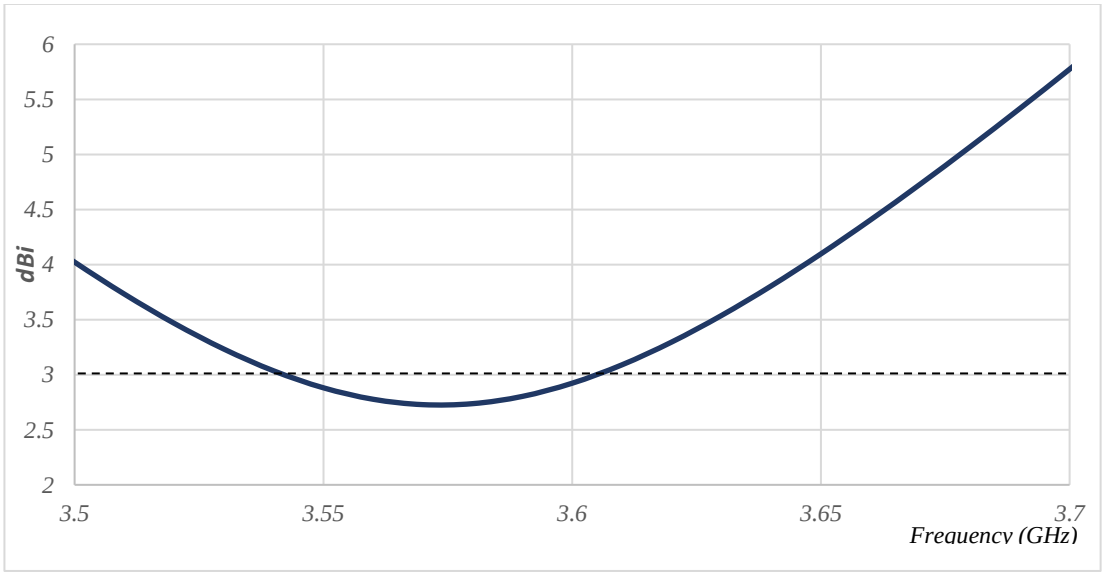

Figure 3.8 Axial Ratio for a Reconfigurable Annular Slot-Fed Hemispherical DRA - Model 1

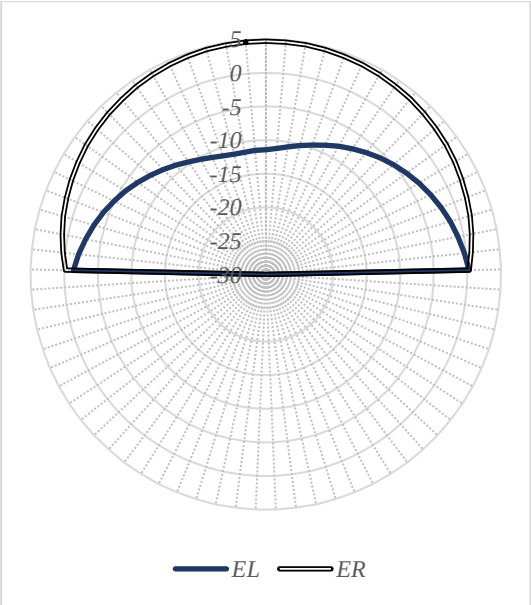

Figure 3.9 EL vs ER (dB) at 3.57 GHz for LHCP, φ=0°-Model 1 (E_θ)

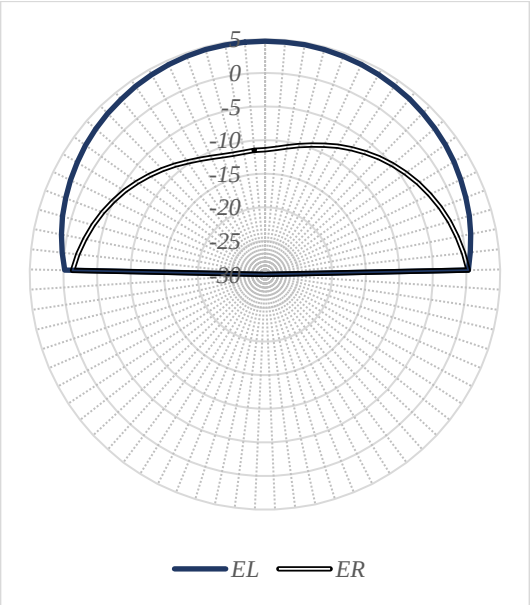

Figure 3.10 EL vs ER (dB) at 3.57 GHz for RHCP, φ=0°- Model 1 (E_θ)

Table 3.1 Comparison for the Four Cases for a Reconfigurable Annular Slot-Fed Hemispherical DRA - Model 1

Properties \ Cases	Diodes OFF	Diodes ON	RD ON	LD ON
Central Frequency (GHz)	3.9	3.82	3.625	3.625
Impedance Bandwidth %	9.04	7.46	17.1	17.1
Polarisation	LP	LP	LHCP	RHCP
Lowest Axial Ratio (dB)	N/A	N/A	2.72	2.72
Lowest Axial Ratio Frequency (GHz)	N/A	N/A	3.57	3.57
Axial Ratio Bandwidth %	N/A	N/A	1.7	1.7

Using the second equivalent circuit model which is shown in Figure 1.2, the ON state parameters have been chosen as R_{ON} = 10 Ω, and L = 1 nH, while the corresponding OFF state parameters are R_{OFF} = 5 kΩ, C_{OFF} = 0.15 pF, and L = 1 nH [5]. The reflection coefficients for the four cases are shown in Figure 3.11, which are similar to those presented in Figure 3.8 using model 1. However, using the diodes equivalent circuits have provided an additional resonance frequency point at ~1.1GHz, which can be attributed to impedance matching and the annular slot and/or the backing cavity natural resonance frequencies as mentioned earlier. Actually, the multi-resonances can be useful for implementing dual band antenna, since two resonances have considerably wide bandwidths. Figure 3.12 presents the axial ratio for the RD ON and LD ON cases, where it can be noticed that a minimum AR of 3.42 dB has been achieved at 3.24 GHz, which indicates an unsatisfactory circular polarisation. In order to address this point, a revised design is suggested in which the slot dimensions have been changed to b = 7.5 mm and w = 1.2 mm in order to improve the CP bandwidth. The reflection coefficients for the four cases are illustrated in Figure 3.13 where it can be noticed that an improved impedance bandwidths has been achieved except for the case where both diodes are OFF. The axial ratios for the second and third cases are presented in Figure 3.14 over a frequency range of 3.15-3.3 GHz, where it can be noticed that an AR bandwidth of ~1.38% has been achieved with a minimum AR point at 3.22 GHz. It should be noted that this is less than the 1.7% achieved in the metallic short model case which can be attributed to the imperfect non-pure resistive impedance characteristics of the PIN diode. Figures 3.15 and 3.16 show the comparison between E_R and E_L for both LHCP and RHCP at 3.22 GHz. A summary of this model data is presented in Table 3.2.

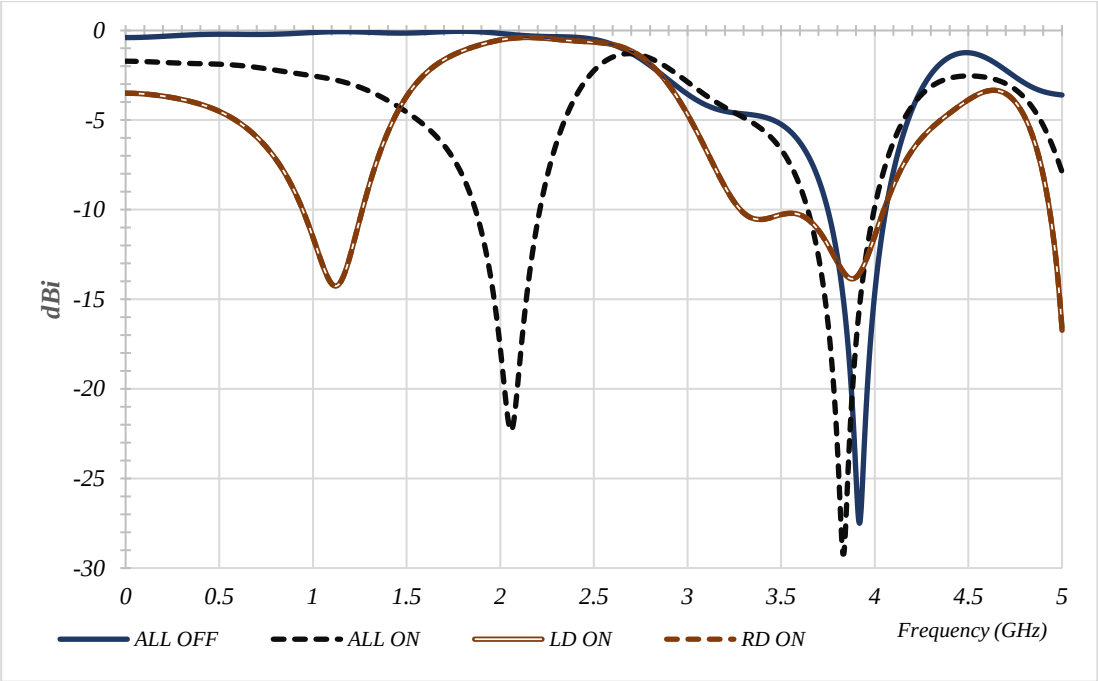

Figure 3.11 Reflection Coefficient (dB) for Reconfigurable Annular Slot-Fed Hemispherical DRA - Model 2

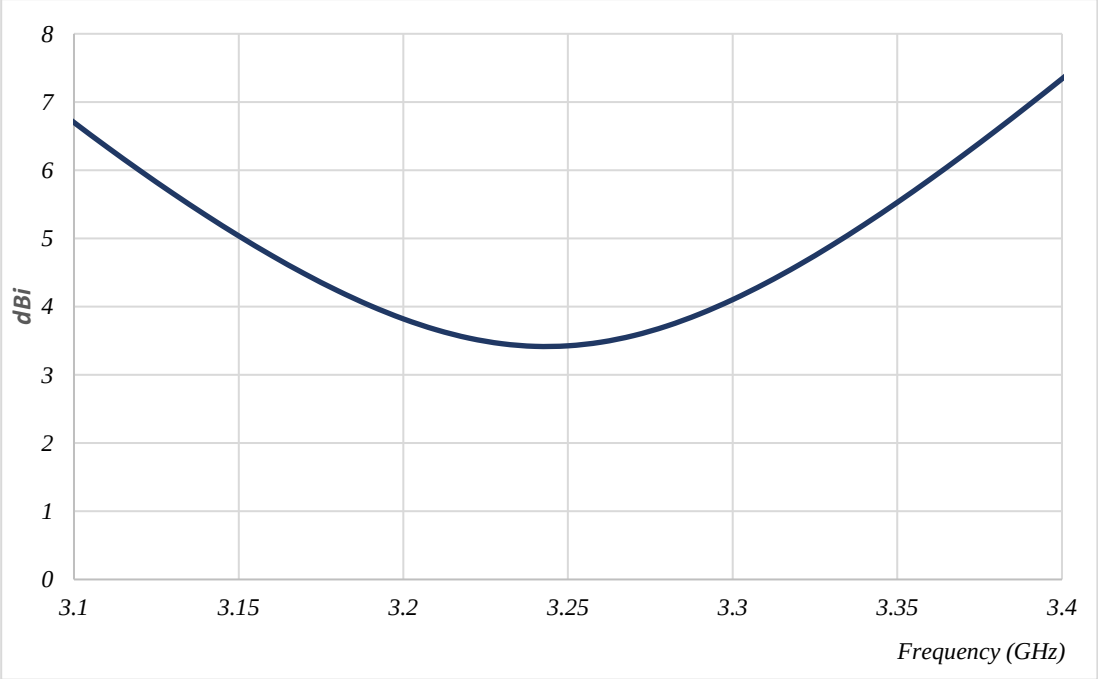

Figure 3.12 Axial Ratio (dB) for Reconfigurable Annular Slot-Fed Hemispherical DRA - Model 2

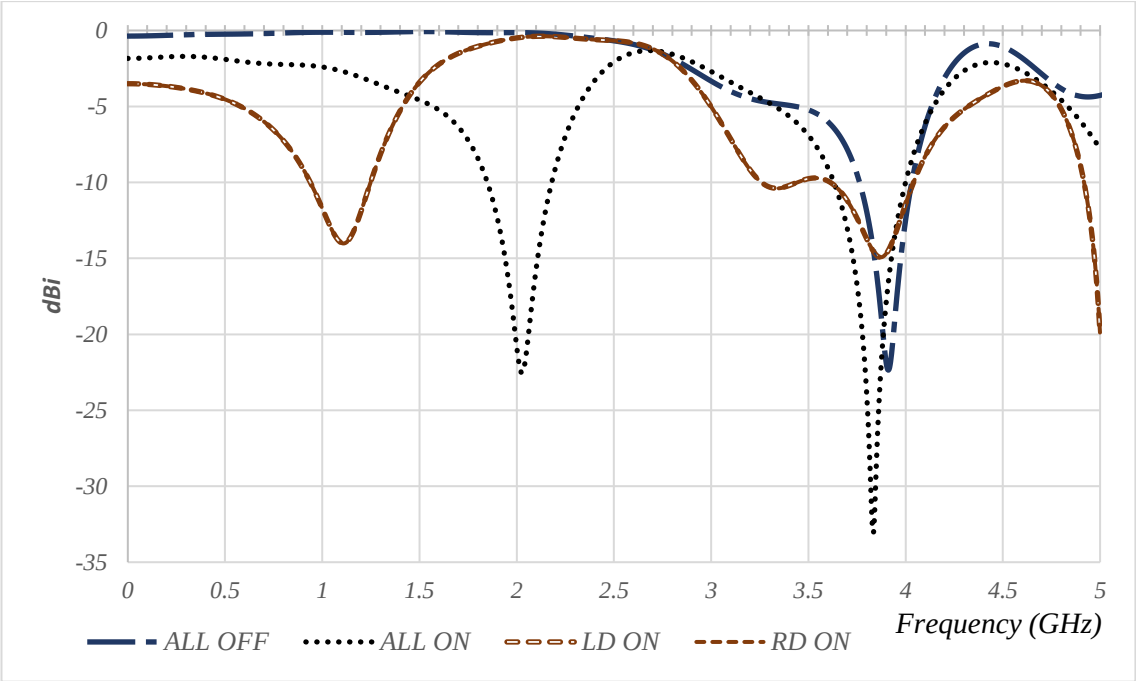

Figure 3.13 Reflection Coefficient (dB) vs Frequency for Reconfigurable Annular Slot-Fed Hemispherical DRA with Revised Dimensions- Model 2

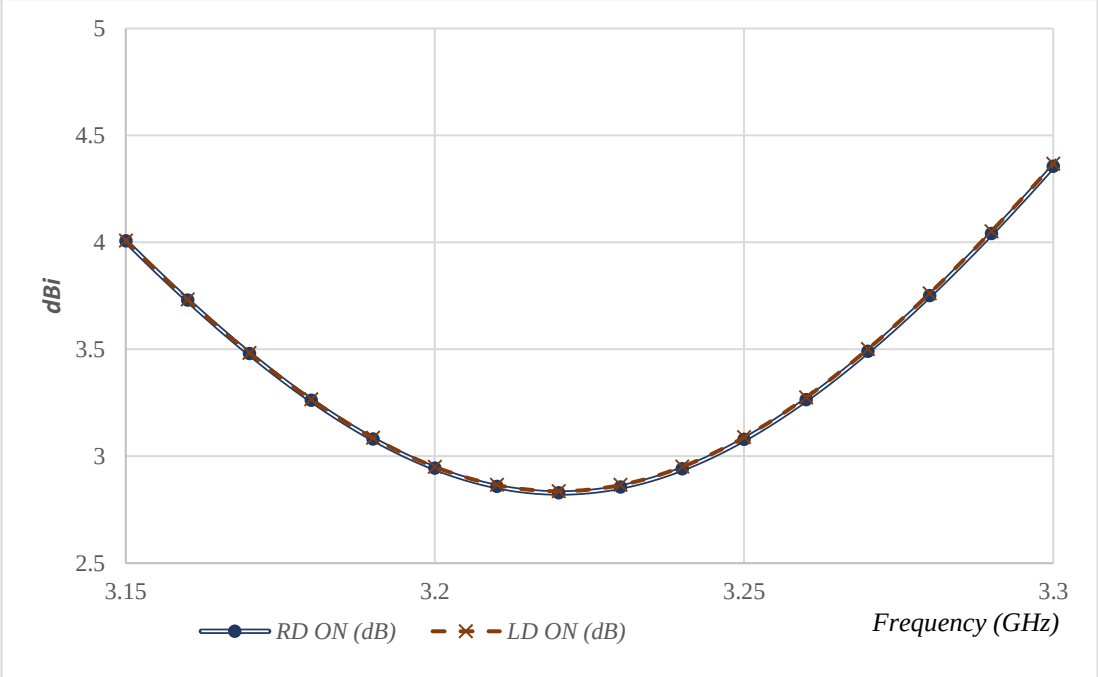

Figure 3.14 Axial Ratio (dB) for Reconfigurable Annular Slot-Fed Hemispherical DRA with Revised Dimensions - Model 2

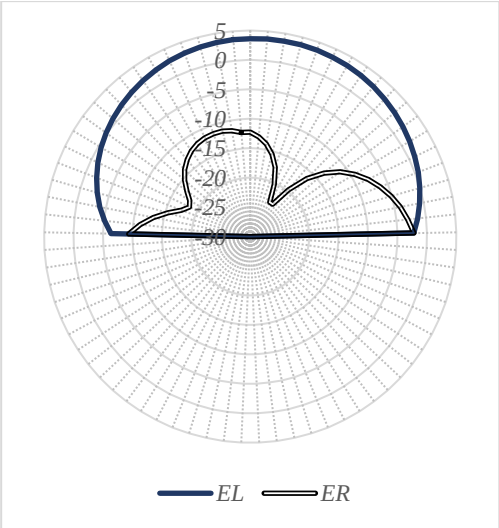

Figure 3.15 EL vs ER (dB) at 3.22 GHz for LHCP, φ=0°-Model 2 (E_θ)

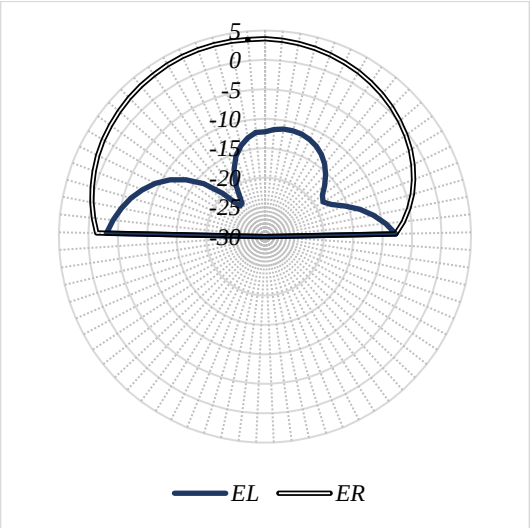

Figure 3.16 EL vs ER (dB) at 3.22 GHz for RHCP, φ=0°-Model 2 (E_θ)

Table 3.2 Comparison for the Four Cases for the Four Cases for Reconfigurable Annular Slot-Fed Hemispherical DRA - Model 2

Properties \ Cases	Diodes OFF	Diodes ON	RD ON	LD ON
Central Frequency (GHz)	3.91	3.835	3.87	3.87
Impedance Bandwidth %	6.86	9.6	20.25	20.2
Polarisation	LP	LP	LHCP	RHCP
Lowest Axial Ratio (dB)	N/A	N/A	1.384	1.386
Lowest Axial Ratio Frequency (GHz)	N/A	N/A	3.22	3.22
Axial Ratio Bandwidth %	N/A	N/A	1.43	1.4

As mentioned earlier, there are two linear polarisation cases that exist when both diodes are switched ON or OFF at the same time. When both diodes are OFF then a full annular slot is achieved. On the other hand, when both diodes are ON, there are two half slots; the first is driven and the second is parasitic. As a result, different results are achieved

between the two LP antenna configurations. However, good impedance matching bandwidth has been attained in both cases, with frequency tuning taking place due to the aforementioned change in the feed.

On the other two cases, turning only one PIN diode ON will affect the slot's current flow direction, which changes the circular polarisation sense. For example, a right hand circular polarisation radiation can be achieved by tuning the left-hand side diode ON, and vice versa. The reflection coefficient results of the CP cases demonstrate improvement in the impedance bandwidth over that of the LP cases. The presented results of this section demonstrate the possibility of a achieving a hemispherical DRA with a reconfigurable polarization.

3.4 Reconfigurable Polarisation Dual CP Bands Notched Rectangular DRA

Inserting an air gap in the DRA is a well-known approach to create what is known as a notched DRA [8]. The main advantage of such a DRA is the improvement in the impedance matching bandwidth over the solid counterpart. This is a result of decreasing the effective permittivity of the DRA owing to the introduction of the airgap [8], which has been demonstrated for a hollow hemispherical DRA as well as a ring DRA [9]. Increasing the airgap dimensions with respect to the total DRA size reduces the stored energy and hence the Q-factor. In addition, creating a hole in the DRA increases the resonance frequency by a factor that depends on the air gap size [9]. Furthermore, it has been demonstrated that a properly positioned parasitic strip with proper dimensions provides circular polarisation radiation [10]. The same technique has been proposed in a recent study in Sheffield [11], which represents the basis of the reconfigurable notched rectangular DRA design presented in this section.

Figure 3.17 illustrates the proposed configuration with the optimized dimensions shown in Figure 3.17 (b). Using the same dimensions of a rigid RDRA, the $TE_{\delta 11}$ mode has been excited at 3.1 GHz. On the other hand, it is expected that inserting the air gap will result in a higher resonance frequency for the TE_{111} mode due to the reduction in the effective permittivity, which is calculated using the CST Studio Eigen Mode Solver as 3.4 GHz for the TE_{111} mode in comparison with 2.81 GHz for Rigid RDRA. The shift from the resonance of the calculated modes in the measured antenna is always expected due to the design impedance matching. The reflection coefficients are illustrated in Figure 3.18 for the solid and hollow DRA, which demonstrate an improvement in the impedance bandwidth of the notched RDRA due to the decrease in the Q-factor, with a slight increment in the central frequency. Table 3.3 presents numerical data that compares the performance of the antennas. Figure 3.19 presents the far-field radiation pattern for both rigid RDRA and notched RDRA at 3.1 GHz 3.43 GHz, respectively. It can be noticed that the radiation patterns are similar to each other owing to the excitation of the fundamental mode in both cases. In addition, the two antennas offer respective gains of 4.18 and 4.52 dBi, respectively.

It is a well-known fact that a CP radiation can be achieved by placing a parasitic strip on one of the DRA surfaces. The position and size of the parasitic strip should be optimized in order to excite two orthogonal nearly-degenerate modes that are needed for circular polarisation. Therefore, a hallow DRA with a parasitic strip will be considered next. The simulated reflection coefficient for the notched rectangular DRA with, and without, the parasitic strip is presented in Figure 3.20, where it can be noticed that an impedance bandwidth of 26.56% has been achieved by adding a parasitic strip to the configuration with a resonance frequency at 4.06 GHz. The TE_{111} and TE_{121} modes have been excited as a result of adding the parasitic strip with respective resonance frequencies of 4.03 and

5.07 GHz. The axial ratio is illustrated in Figure 3.21, where it can be observed that there are two AR minimal frequency points at 4.03 and 5.07 GHz that correspond to the excitation of the TE_{111} and TE_{121} modes. The 3dB AR bandwidth of the first and second bands are 6.1% and 0.97%, respectively. The radiation patterns at the two AR minimal frequency points are illustrated in Figure 3.22, where it can be noticed that the first and second CP bands have provided RHCP and LHCP, respectively, with corresponding gains of 5.25 and 4.94 dBi. The TE_{111} mode field distribution is presented in Figure 3.23 at a frequency of 4.07 GHz.

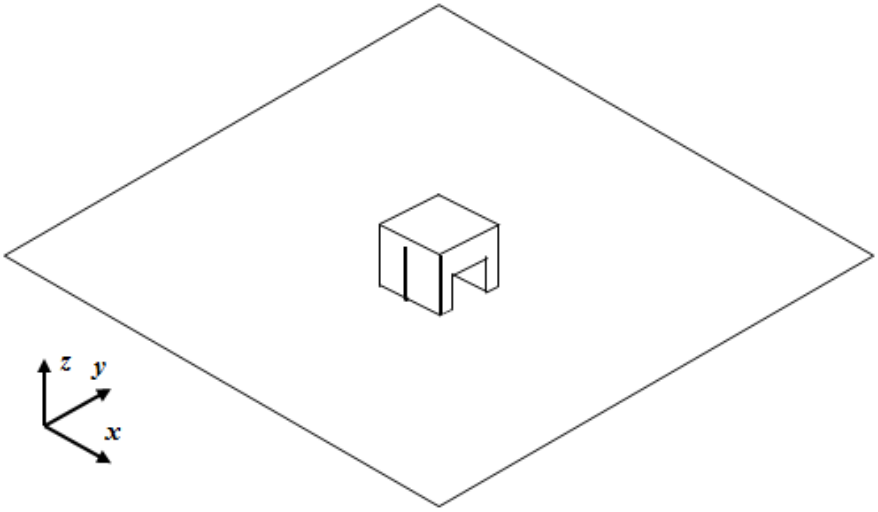

(a)

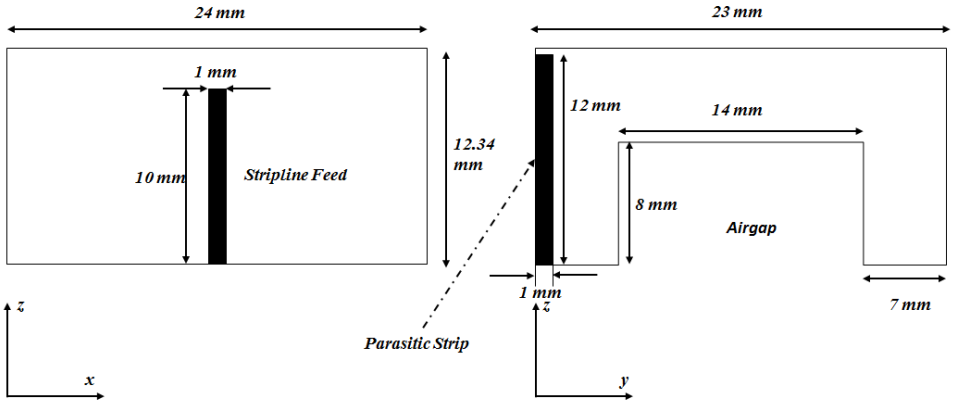

(b)

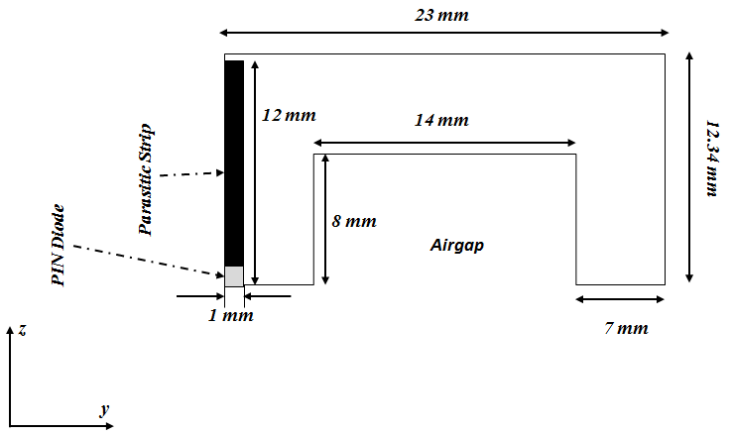

(c)

Figure 3.17 Notched Rectangular DRA with Parasitic Strip (a) General View, (b) Dimensions with Front and Side Views, and (c) Side View for Reconfigurable Parasitic Strip with PIN Diode.

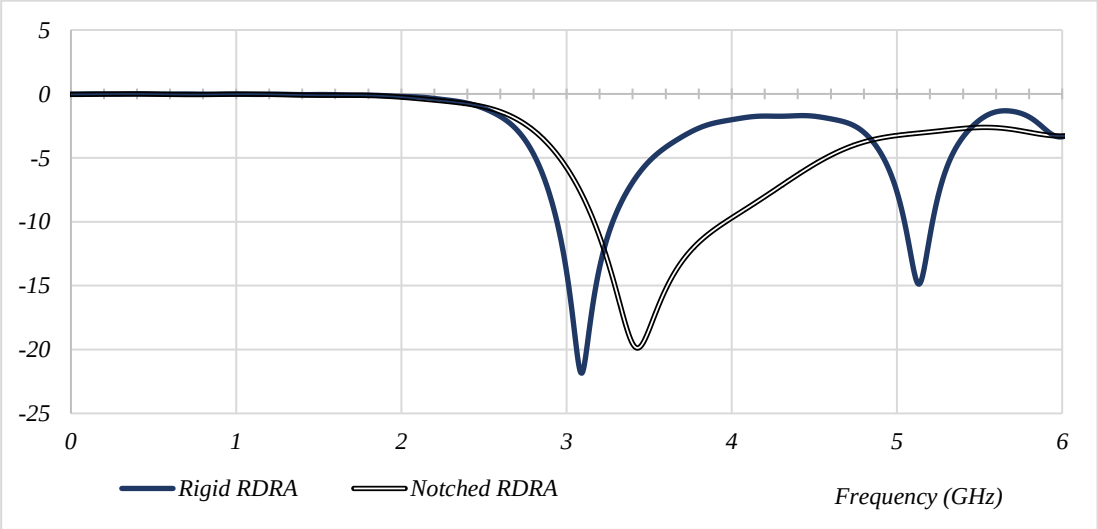

Figure 3.18 Simulation Results for Reflection Coefficients for Rigid vs Notched RDRA

Table 3.3 Rigid vs Notched RDRA

Properties \ Cases	Rigid RDRA	Notched RDRA
Central Frequency (GHz)	3.1	3.43
Impedance Bandwidth %	10.9	21.3
Radiation Efficiency	97.4	98.2

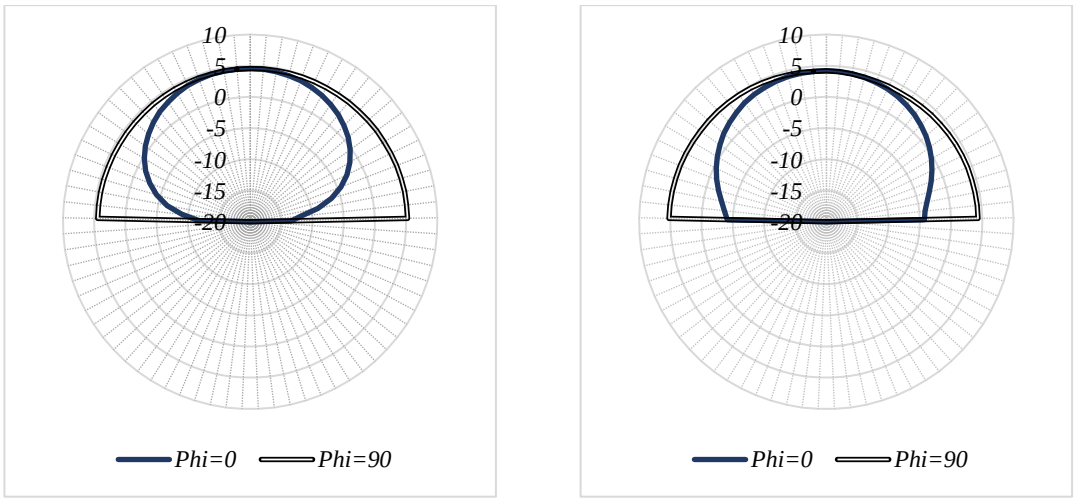

(a) Rigid RDRA at 3.1 GHz (b) Notched RDRA at 3.43 GHz

Figure 3.19 Far-Field Radiation Patterns for Rigid vs Notched RDRA

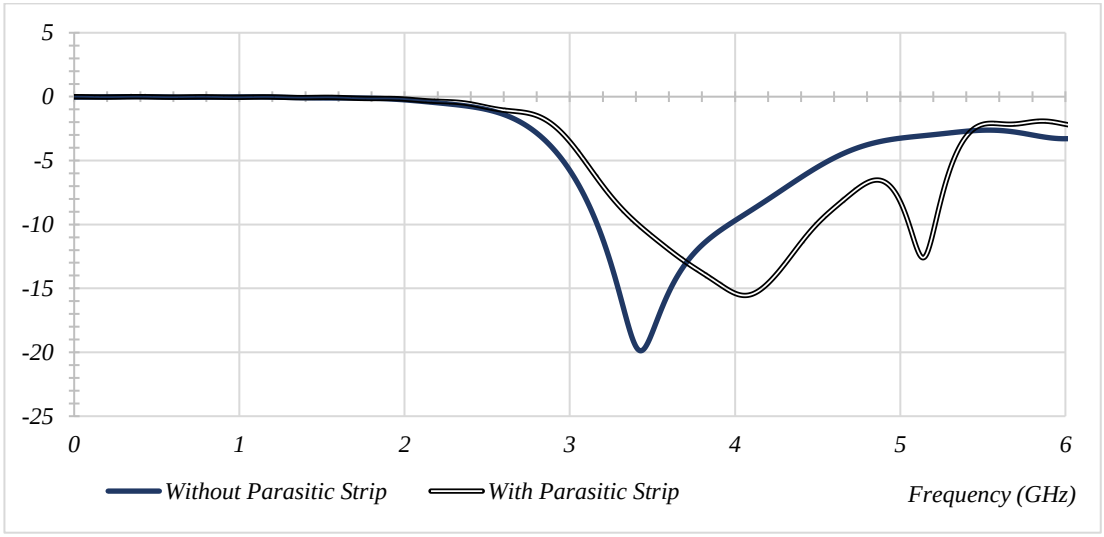

Figure 3.20 Reflection Coefficients for a Notched DRA with and without Parasitic Strip

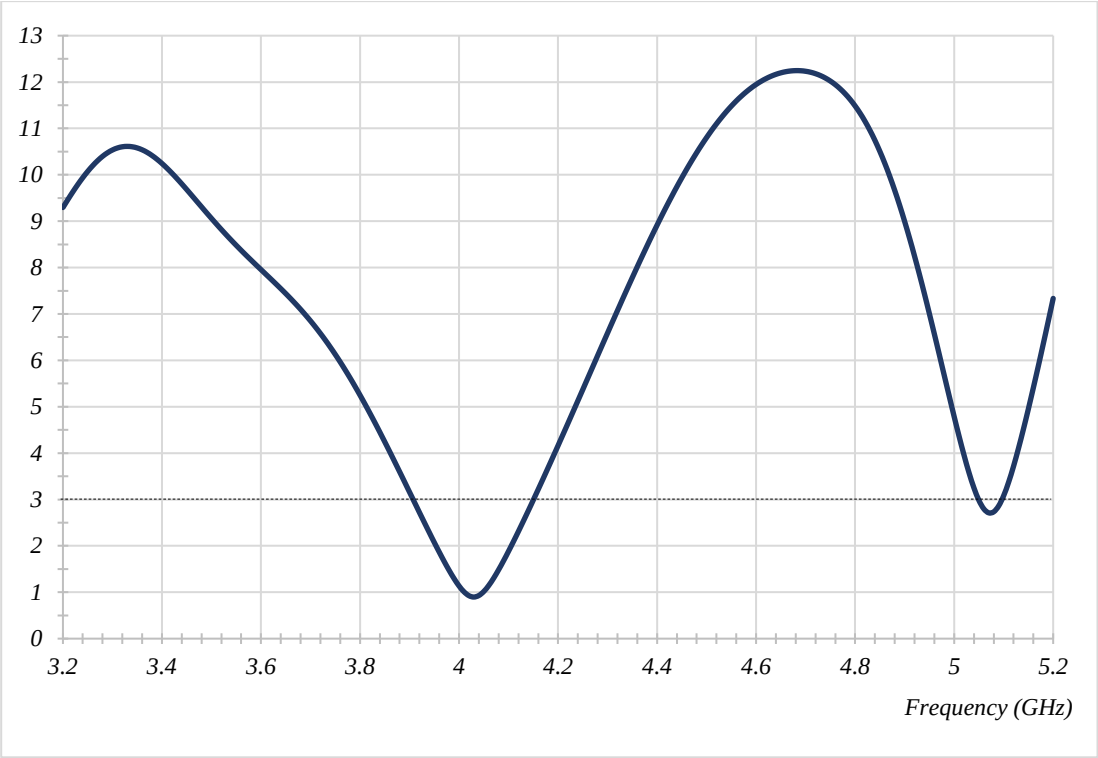

Figure 3.21 Axial Ratio for Parasitic Strip Case

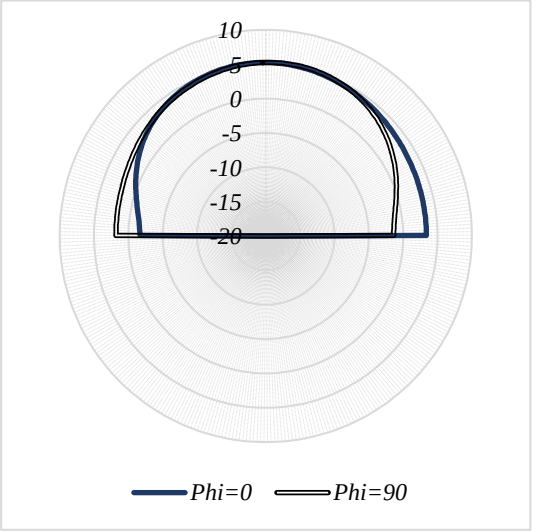

(a) 4.03 GHz

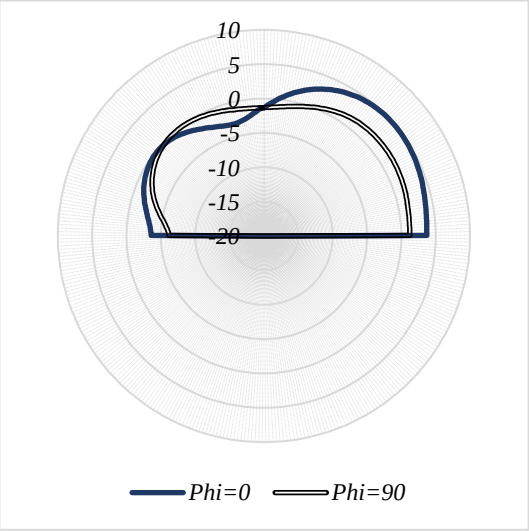

(b) 5.07 GHz

Figure 3.22 Radiation Patterns for Frequencies at which Axial Ratios are Minimal

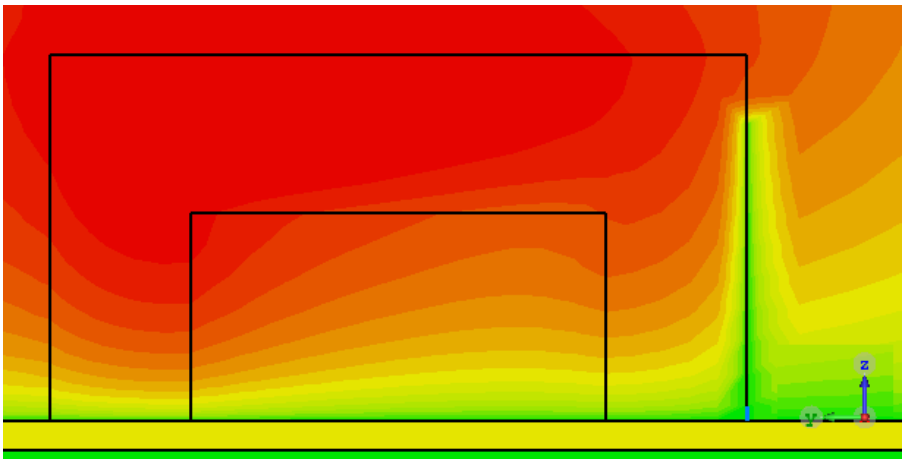

(a) *yz* Plane

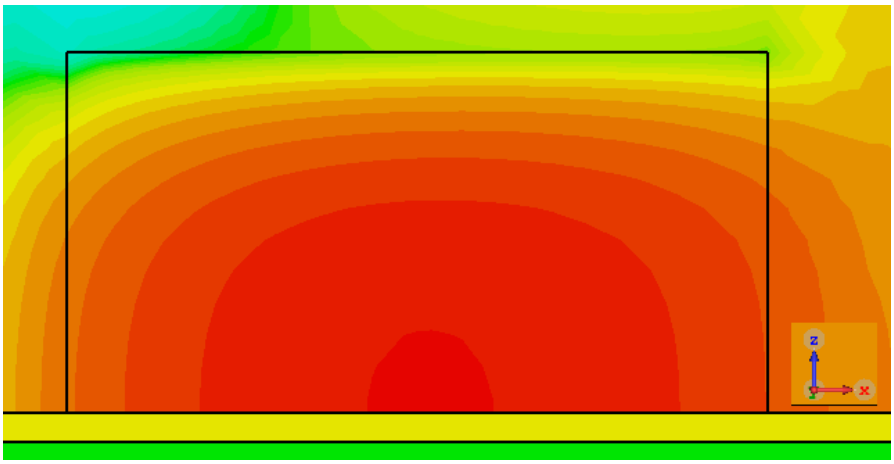

(b) *xz* Plane

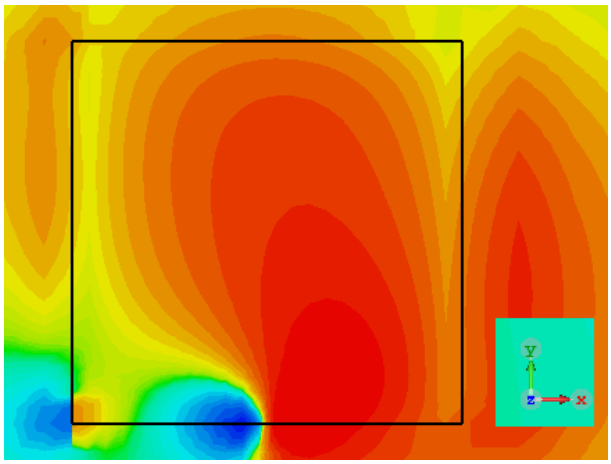

(c) *xy* Plane

Figure 3.23 E-field Distribution in the Notched RDRA at 4.03 GHz

It should be noted that if there is a gap between the ground plane and the parasitic strip, then the effect of the latter will be negligible, which results in a loss of the circular polarisation. This has been proven by measurements as it will be shown in the next section. Using the last remark, it is possible to propose a DRA with a reconfigurable polarisation by replacing a short segment length at the bottom of the parasitic strip by a PIN diode to connect/ disconnect the strip from the ground plane in order to switch between LP and CP the polarisations. Furthermore, it is possible to use two reconfigurable parasitic strips that are located on opposite DRA sides to generate three polarisation types; LP, LHCP, and RHCP.

For the first case of a notched RDRA with a reconfigurable parasitic strip, the PIN model used in the previous section has been employed. Figure 3.24 (a) illustrates the reflection coefficient for both PIN OFF and ON states, which shows good similarity to the results of Figure 3.20. In addition, Figure 3.24 (b) shows the axial ratio for the PIN ON state, which is similar to that of Figure 3.21, but with different values.

Figure 3.24 (a) shows considerable similarity with the results of Figure 3.20, with the resonance frequency for the PIN OFF case at 3.45 GHz and a 21.25% impedance bandwidth compared to 3.43 GHz and 21.3% in the case of the notched RDRA without a parasitic strip. The small shift in the resonance frequency and the impedance bandwidth is due to the presence of the parasitic strip that is disconnected from the ground plane. On the other hand, the main change in the PIN OFF case compared to the case of total absence of parasitic strip is in the resonance frequency that has been changed from 4.07 GHz to 3.95 GHz However, the impedance matching bandwidths is almost the same in both case, e.g. 26.56% compared to 27.14%. This proves that the PIN diode has minimal effect on the impedance characteristics. Nevertheless, the simulations demonstrate more noticeable effect on the CP bands bandwidth, with the first mode AR bandwidth reduced from 6.1%

to 3.87% with the same centre frequency at the same 4.07 GHz, and the second CP band has been completely lost. To solve this issue, the length of the parasitic strip has been changed, and it has been noticed that reducing the length to 8 mm increases the impedance bandwidth up to 34.29% with a centre frequency of 3.83 GHz. The new parasitic strip length provides a first AR minima at 4.32 GHz with a CP bandwidth of ~5% and a second CP bandwidth of 4% around a centre frequency of 5.26 GHz. This has been achieved with negligible changes in the reflection coefficients of the PIN OFF case, which assert the concluded fact of the minimal effect of a parasitic strip that is disconnected from the ground plane. Figure 3.25 shows the results for the revised design.

For the second case of a notched RDRA with two reconfigurable parasitic strips, the reflection coefficients are presented in Figure 3.26 (a) for the two cases when both diodes are either OFF or ON at the same time, and another two cases with only one diode is ON. These results demonstrate a change from the single parasitic strip case, where it is evident that there is an increase in the impedance bandwidth from 11.85% in the all OFF linear polarisation case to 30.54% for the two CP polarization cases. In addition, the results demonstrate the absence of the impedance matching bandwidth for the LP case when all the PIN diodes are ON, which can be explained using the superposition theory in electric circuit analogy, where both parasitic strips that are placed on opposite sides of the DRA are producing the same effects on the radiation but in opposite directions, which means that these strips are cancelling the effects of each other.

Figure 3.26 (b) illustrates three 3dB AR bands, with centre frequencies at 3.67 GHz, 4.51 GHz, and 5.6 GHz and CP bandwidths of 5.13%, 2.54%, and 1.27%, respectively. For the LD ON case the respective polarisations of the three bands are RHCP, LHCP, and RHCP. The reduction in the second CP bandwidth and the creation of the third CP bandwidth shows the effect of using multiple parasitic strips, even though not attached to

the ground plane. In addition, the third CP bandwidth does not share frequency range with any impedance matching bandwidth. Figure 3.27 illustrates the E_R and E_L radiation patterns for case for the three bands in the RD ON, which have the exact same values for the LD ON case, but with reversed directions. The respective gains for the three frequencies are 3.95 dBi, 2.29 dBi, and -4.99 dBi with radiation efficiencies of 84.25%, 66.1%, and 47.92%, respectively.

The radiation efficiencies and the gains for both the second and third CP bandwidths have been reduced due to impedance matching, since the both CP bandwidth with a centre frequencies at 4.51 GHz and 5.6 GHz do not lay within any impedance matching frequency band, hence, it should be ignored. In addition, both radiation patterns at these frequencies have main lobe directed away from $\varphi=0°$, $\theta=90°$ point, producing an elliptical polarisation with high axial ratios at their respective main lobe direction angles. This results in obtaining single CP band dielectric resonator antenna, which less than what is expected. Nonetheless, this design still allows generating both RHCP and LHCP.

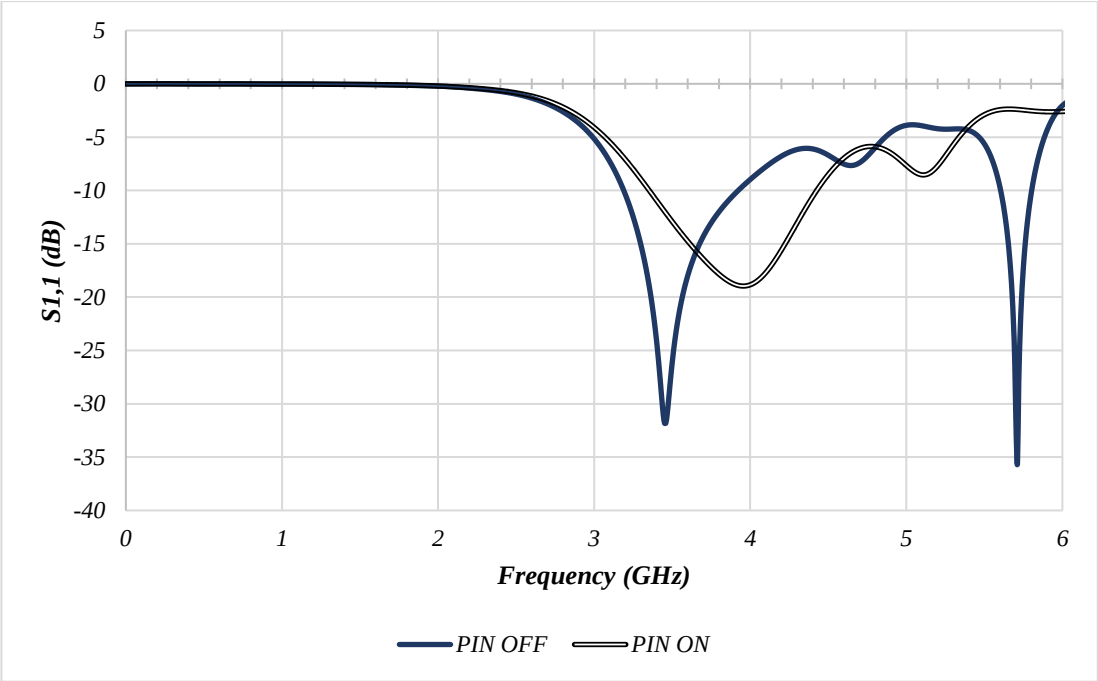

(a)

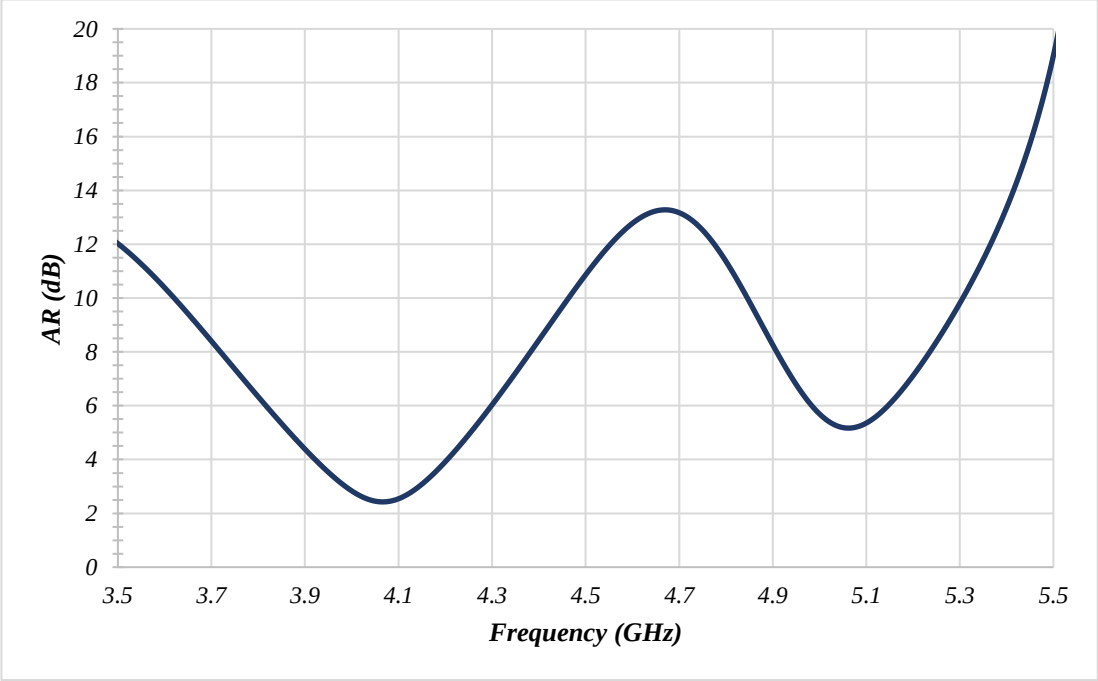

(b)

Figure 3.24 Simulation Results for Notched RDRA with Reconfigurable Parasitic Strip (a) Reflection Coefficients with and without Parasitic Strip and (b) Axial Ratio for PIN ON Case

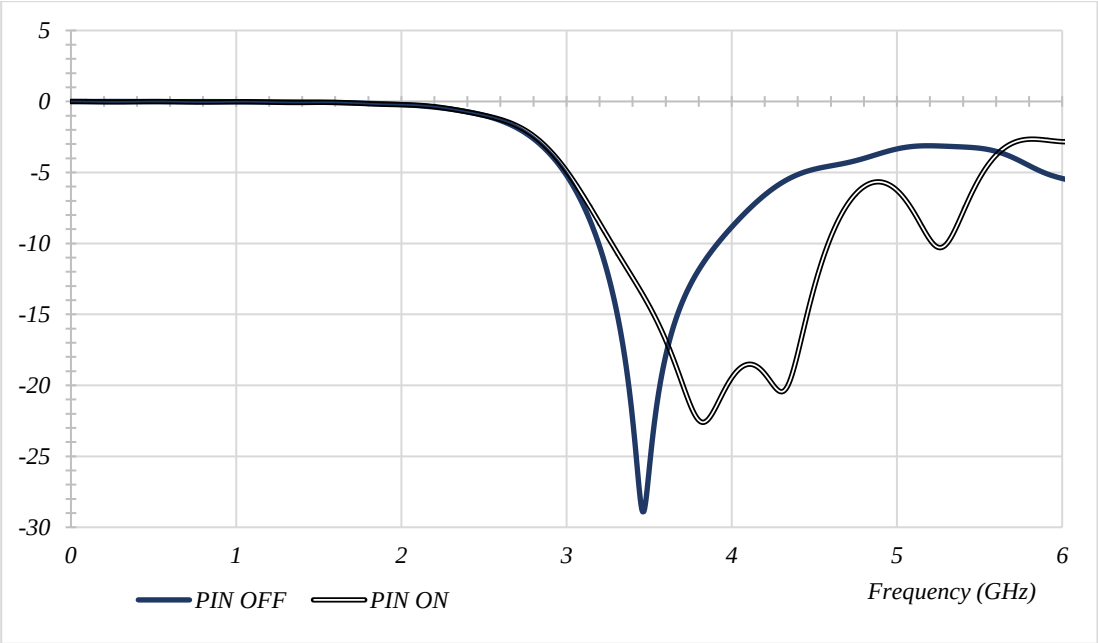

(a)

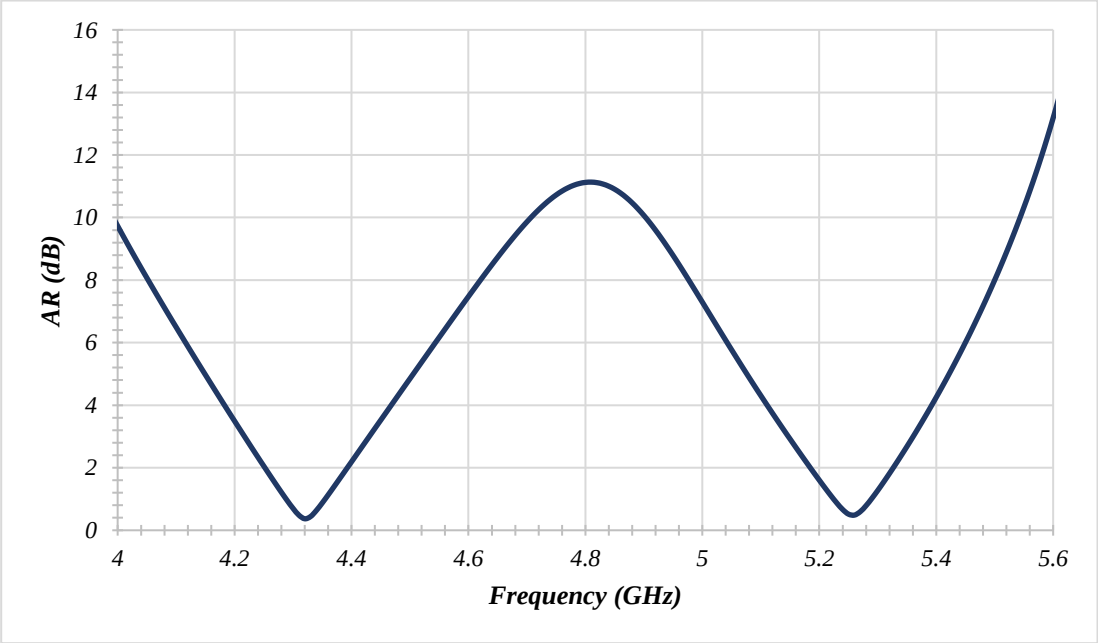

(b)

Figure 3.25 Simulation Results for Notched RDRA with Revised Length for the Reconfigurable Parasitic Strip (a) Reflection Coefficients with and without Parasitic Strip and (b) Axial Ratio for PIN ON Case

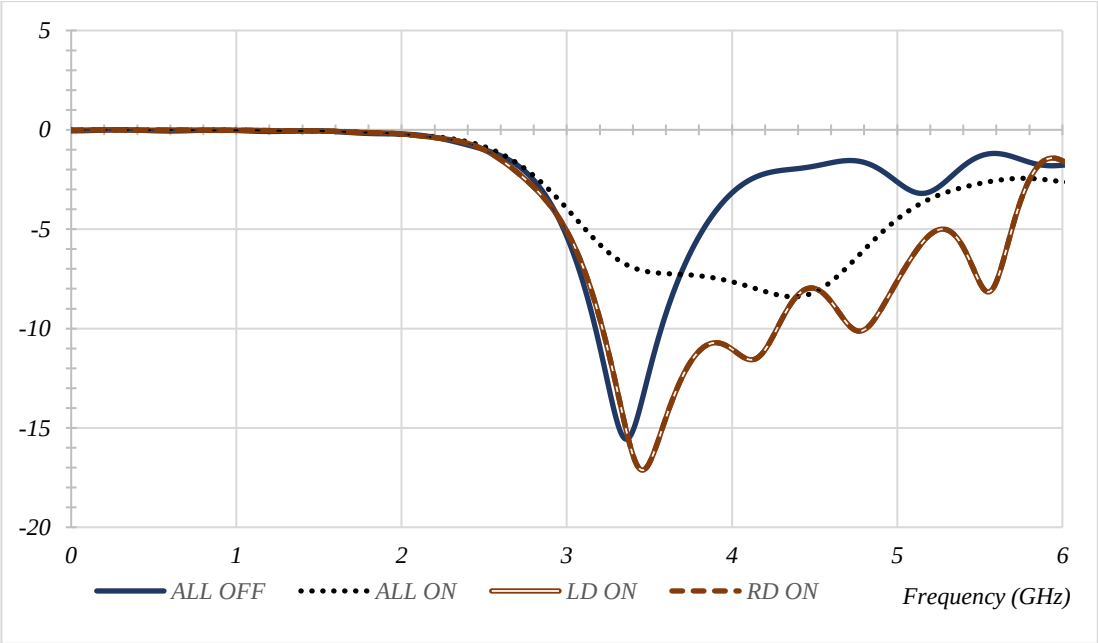

(a)

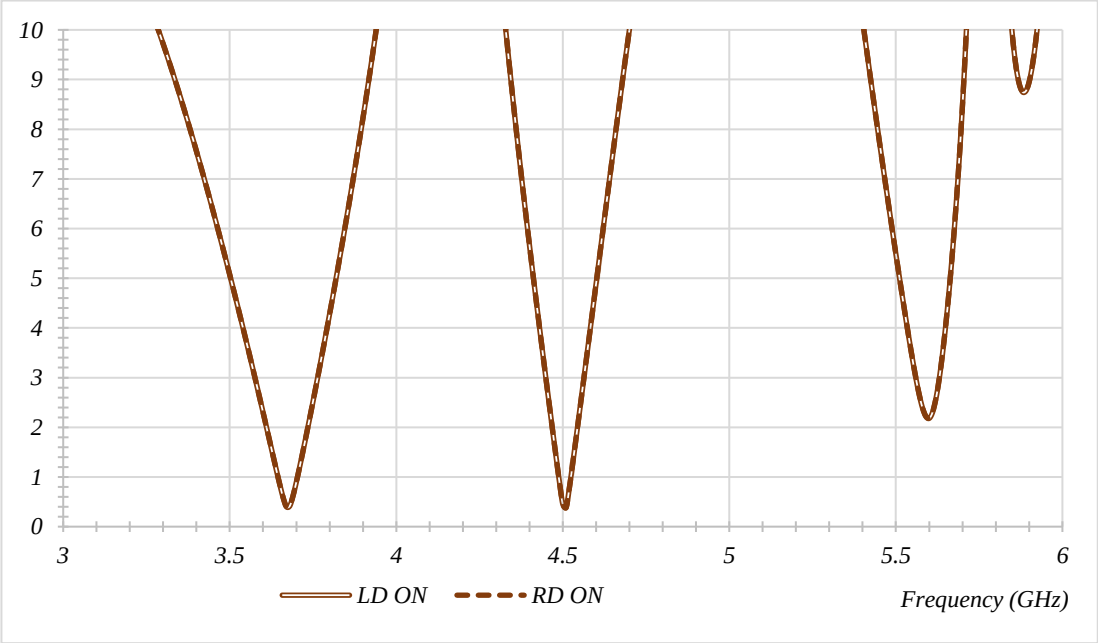

(b)

Figure 3.26 Simulation Results for Notched RDRA with Two Reconfigurable Parasitic Strip (a) Reflection Coefficients and (b) Axial Ratios

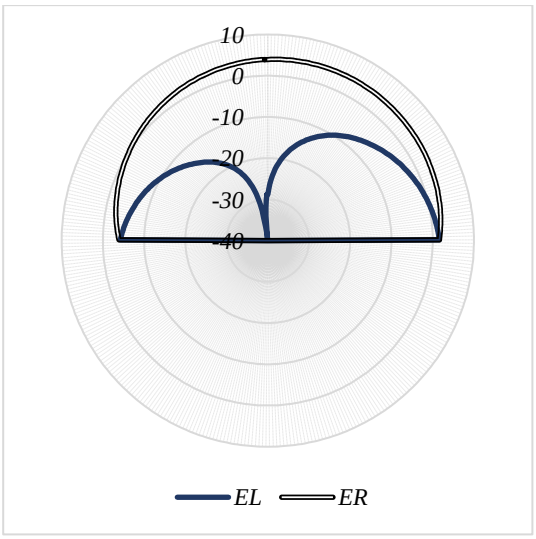

(a) 3.67 GHz

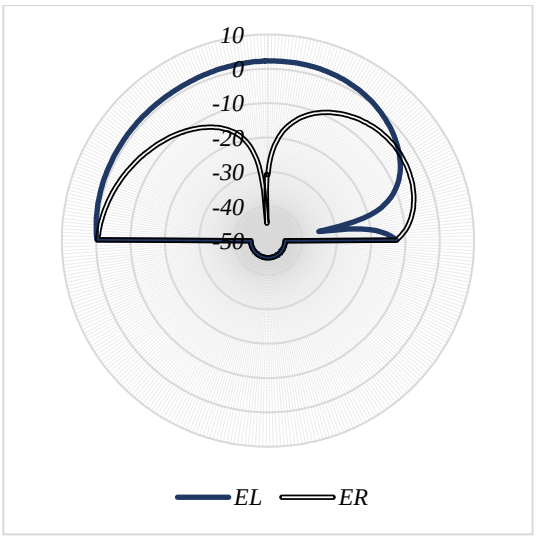

(b) 4.51 GHz

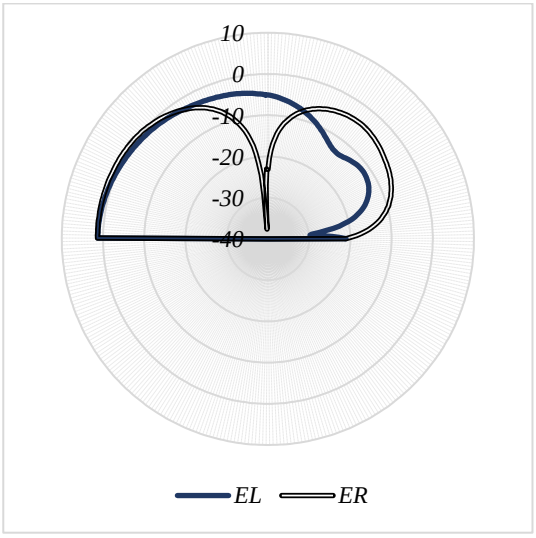

(c) 5.6 GHz

Figure 3.27 E_L vs E_R for the Three CP Bands (E_θ)

3.4.1 Measured Results:

A prototype of the notched DRA has been manufactured by T-Ceram using Alumina with a dielectric constant of 9.8 as illustrated in Figure 3.28 (a). It should be noted that the DRA has been fabricated with a precision of 5%. Adhesive backed Copper tape has been employed to create both of the fed and parasitic strips that have been placed on two of the DRA faces as shown in Figure 3.28 (b). The DRA has been placed on a 30×30 cm^2 Aluminum ground plane with a thickness of 1.5 mm. It is well known that placing the DRA on the metallic ground plane is usually associated with air gaps that alter the DRA performance. However, the effects of these gaps have been be minimized using a double side adhesive backed copper tape to attach the DRA to the ground plane as proposed in [7]. The DRA has been fed using an SMA connector that is connected in one end to the fed strip and in the other to the Agilent Technologies' E5071B vector network analyzer thorough a 50 Ω coaxial cable. The calibration has been carried out using the Agilent's 85052D calibration kit.

Figure 3.29 (a) illustrates the reflection coefficients for the notched RDRA with and without the parasitic strip, where it can be noticed that a wider bandwidth has been achieved at the presence of the parasitic strip owing to the excitation of a second DRA mode. Comparison between the simulated and measured return losses is illustrated in Figure 3.29 (b), where it can be noticed that a close agreement has been achieved between the two set of results with discrepancies that can be attributed to experimental and fabricates tolerances as well as due to using a finite ground plane. For example, the resonance frequency at the absence of the parasitic strip has been measured as ~3.7 GHz compared to a simulated counterpart of 3.43 GHz. Furthermore, the measured impedance bandwidth is ~15% compared to a simulated bandwidth of ~11%. On the other hand, the measured and simulated resonance frequencies for a DRA with a parasitic strip are 3.95

and 4.05 GHz, respectively, with respective impedance bandwidths of ~29.7% and 28%. Two AR bands have been achieved with this prototype, the first at 4.5 GHz and the second at 5.5 GHz, with bandwidths of 8% and 1.2% respectively, compared to the simulated data of 4.03 GHz and 5.07 GHz for the AR bands central frequencies in conjunction with AR bandwidths of 6.1% and 1% respectively. It can be noticed from these results the there is a difference of ~10% between the measured and simulated AR minimal point frequencies. In addition, the measured AR band width of the first band is considerably wider than the simulated counterpart. These discrepancies can be attributed to a number of reason such as a small geometrical difference in the prototype compared to the simulated DRA as well as the sensitivity of these frequency points to the parasitic strip length that has been cut manually. Furthermore, the prototype has been manufactured using Alumina, with a 5% tolerance in the dielectric constants that can affect the final results. The measured and simulated E_L and E_R patterns are illustrated in Fig. 3.29 (f) where with closed agreement for both AR bands, and small differences owing to the aforementioned reasons.

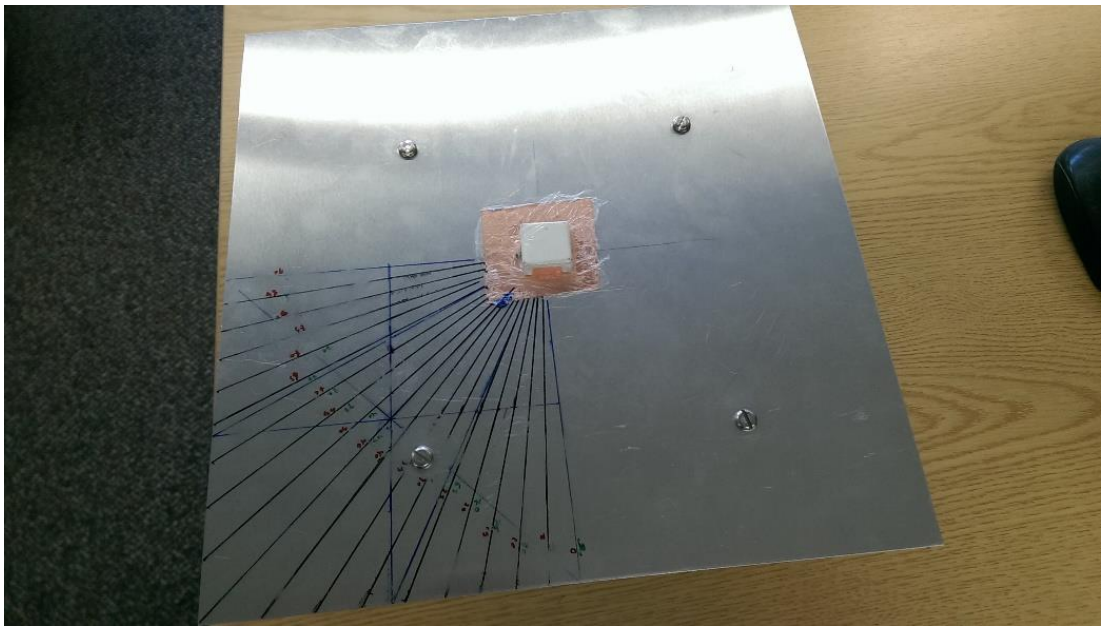

(a)

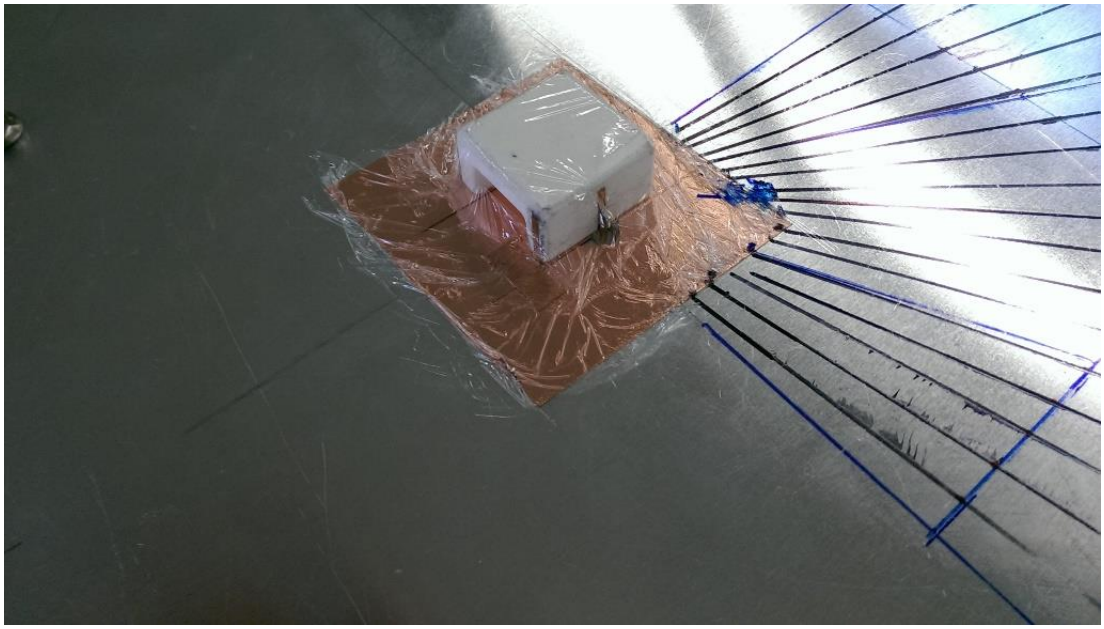

(b)

Figure 3.28 Notched RDRA (a) General View, (b) View over the Dielectric Resonator Antenna Showing Strip Feed and Parasitic Strip

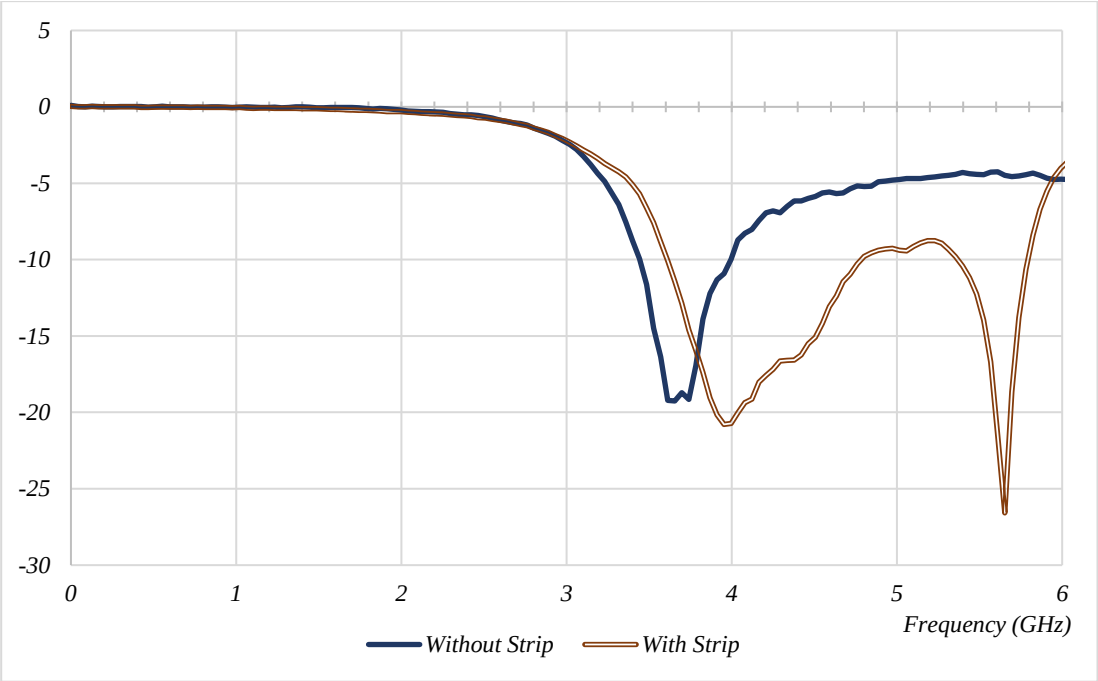

(a) Measured Reflection Coefficients

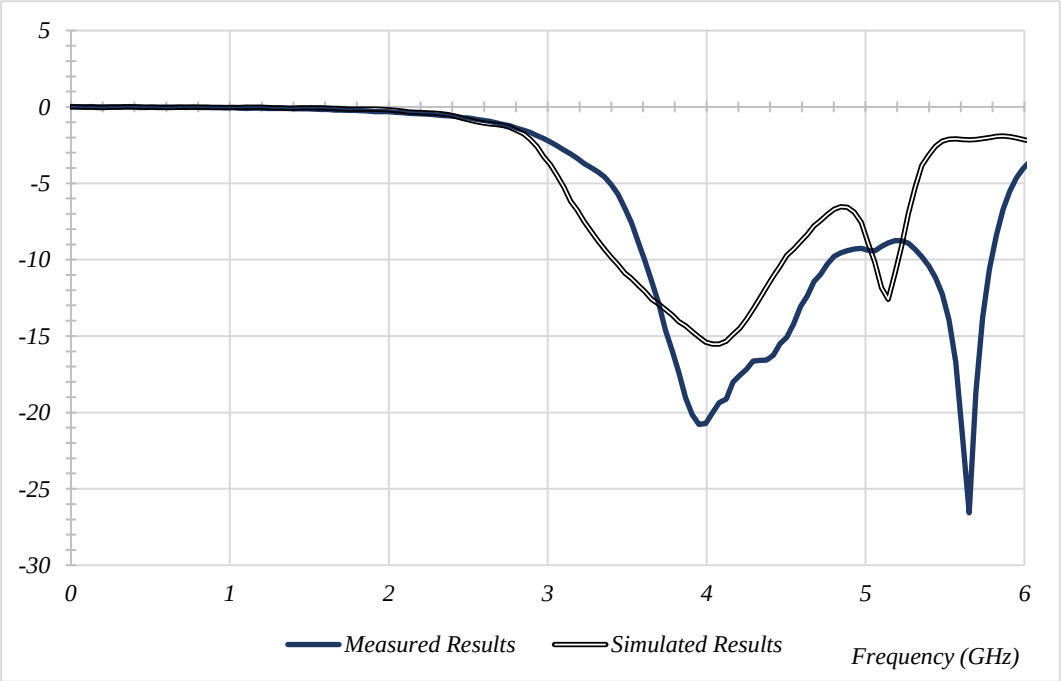

(b) Measured vs Simulated Reflection Coefficients for Notched RDRA with Parasitic Strip

Figure 3.29 Measured and Simulated Results for Notched RDRA with and without Parasitic Strip

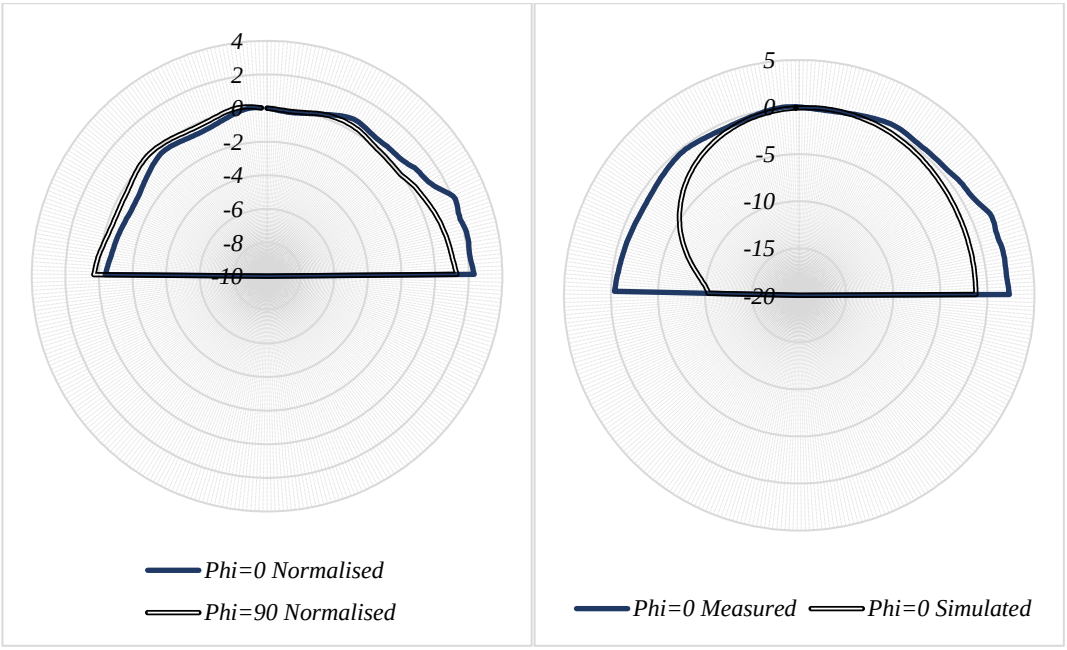

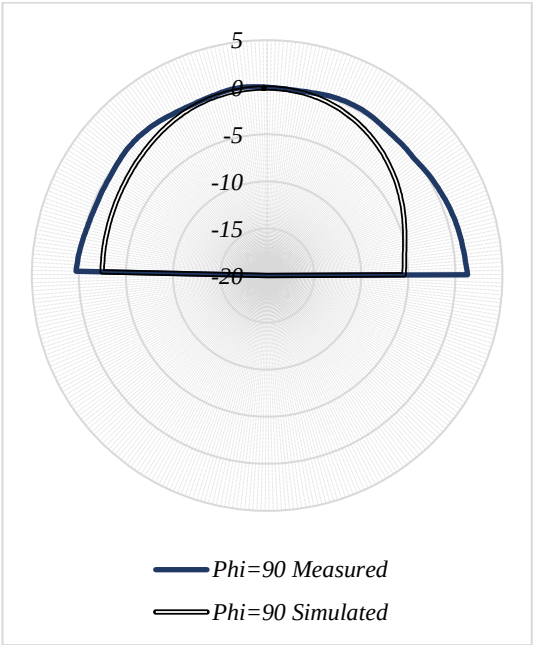

(c) Normalised Radiation Pattern at 3.9 GHz with Comparison to the Simulated Normalised Pattern

Figure 3.29 Continued

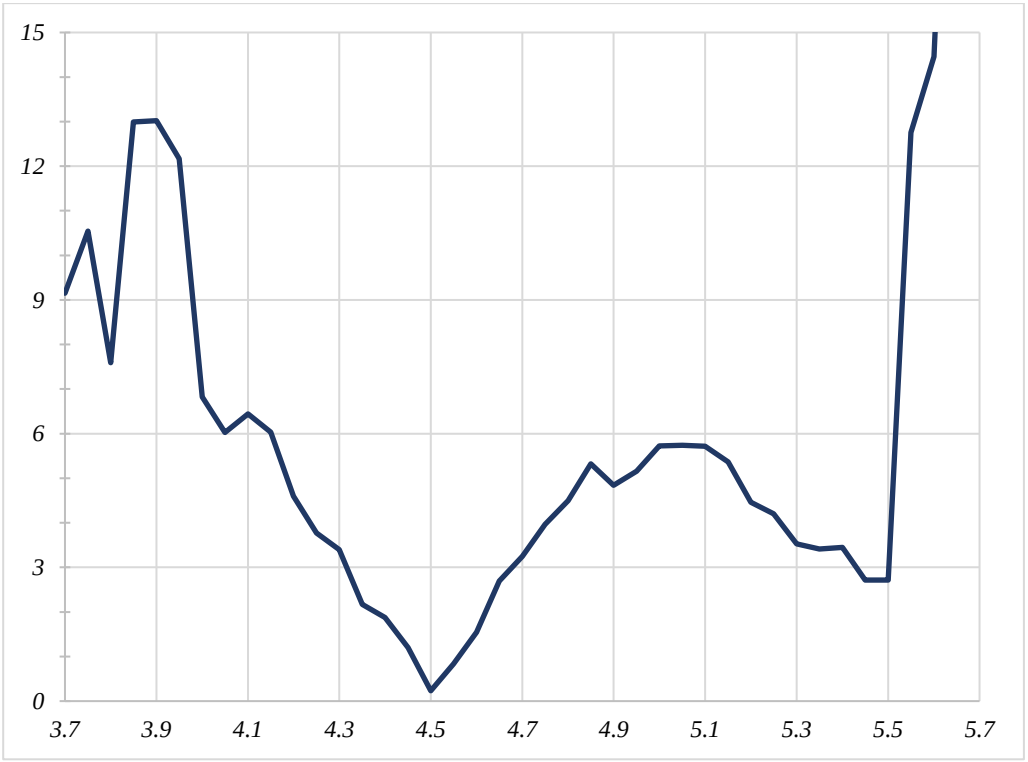

(d) Measured Axial Ratio

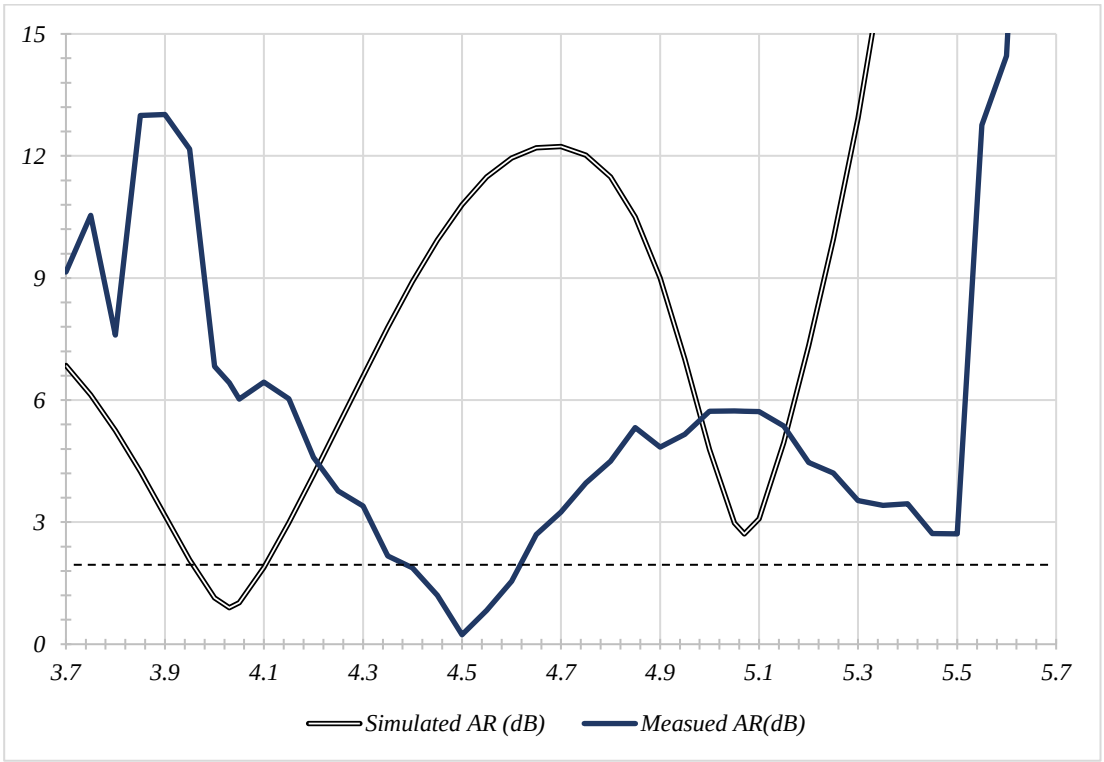

(e) Measured vs Simulated Axial Ratio

Figure 3.29 Continued

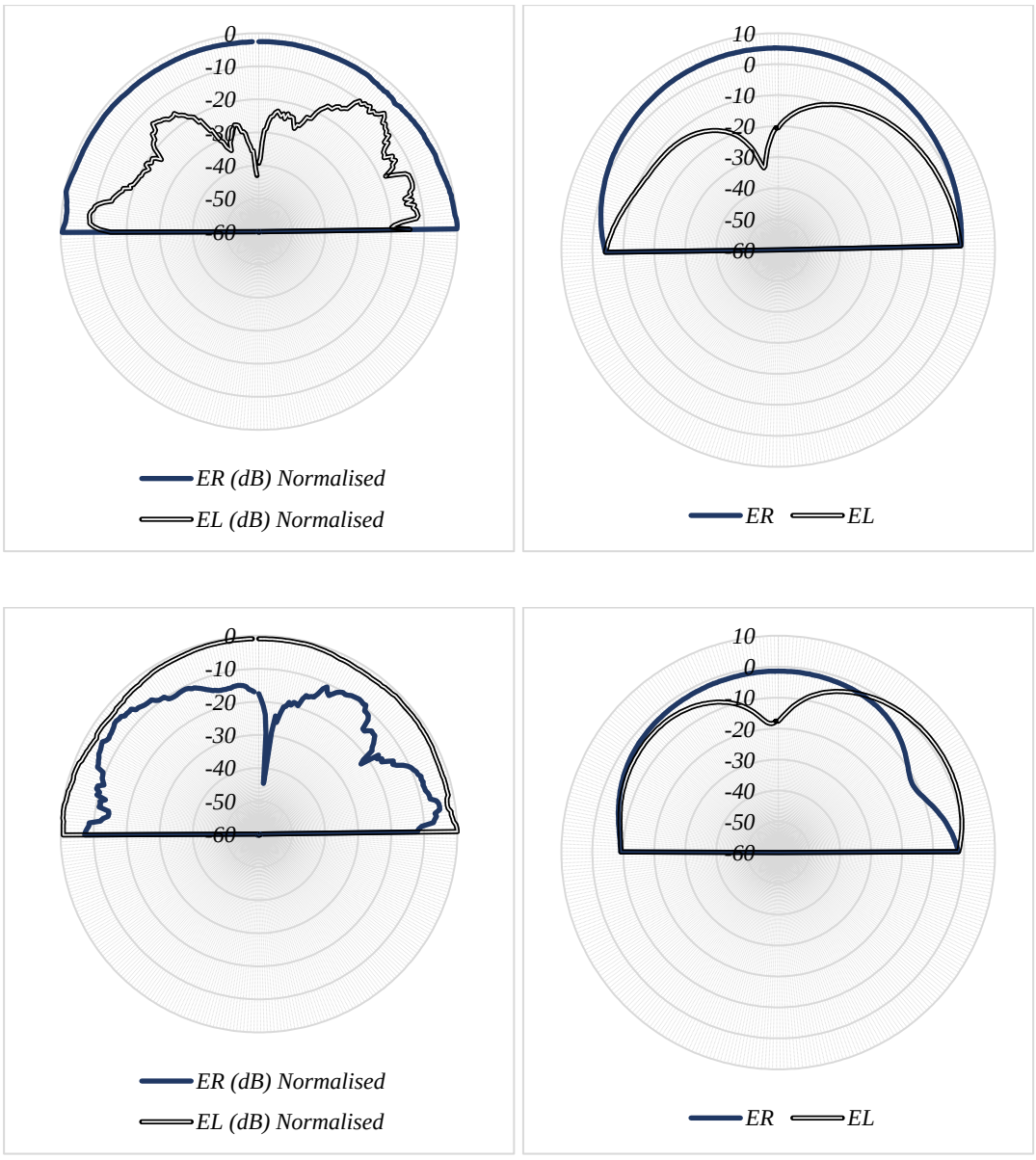

(f) ER vs EL Normalised Measured at 4.5 GHz (Top Left) vs Simulated at 4.03 GHz (Top Right) and Measured at 5.5 GHz (Bottom Left) vs Simulated at 5.07 GHz (Bottom Right)

Figure 3.29 Continued

3.5 Conclusion

In this chapter, the possibility of obtaining an antenna with a polarisation reconfigurability has been demonstrated using conventional DRA. Two designs have been considered, the first is focused on using an annular slot-fed hemispherical DRA. The slot incorporates two PIN diodes that have been located at angles of ±90° with respect to the feed point. In theory, four cases can be achieved from this configuration that have been confirmed through CST simulations. These include two linear polarisation cases when both PINs are either ON or OFF at the same time. In addition, two circular polarisation cases of RHCP and LHCP can be achieved by turning ON either the left or right PIN diode, respectively, with the expected AR bandwidth of 1.4% in both cases.

The second design is based on using a notched RDRA with a parasitic, where it has been demonstrated that disconnecting the parasitic strip from the ground plane provides results identical to those for a configuration without a parasitic strip. This has paved the way to the design of a dual band CP antenna with a reconfigurable polarisation using two parasitic strips that are placed on two opposite DRA sides. As a result, two reconfigurably polarised antenna designs have been proposed on this basis. The first design utilizes a single parasitic strip with a PIN diode to control the contact between the strip and the ground plane, while the second is utilizes two parasitic strips on opposite sides of the DRA that are connected to the ground plane using PIN diodes. While the first will provides a single case of either LHCP or RHCP for each band, the second design facilitates controlling the polarisation sense by activating one parasitic strip at a time. A prototype of a conventional notched DRA has been built and measured with a single parasitic strip. Reasonable agreement has been achieved between measured and simulated data with the possibility of achieving a dual circular polarisation bands.

References

[1] J. T. Bernhard, "Reconfigurable Multifunction Antennas: Next Steps fot the Future," in Microwave, Antenna, Propagation and EMC Technologies for Wireless Communications, 2007 International Symposium on, 2007, pp. K2- 1-K2- 4.

[2] K. Fleisch and J. Kraus, "Electromagnetics with applications," New York: McGraw-Hill, 1999.

[3] C. A. Balanis, Antenna Theory: Analysis and Design: Wiley-Interscience, 2005.

[4] K. W. Leung, "Circularly polarized dielectric resonator antenna excited by a shorted annular slot with a backing cavity," IEEE Transactions on Antennas and Propagation, vol. 52, pp. 2765-2770, 2004.

[5] "http://www.infineon.com/dgdl/Infineon-BAR50SERIES-DS-v01_01-en.pdf?fileId=db3a304314dca3890114fea7dd410a92."

[6] K. K. So and K. W. Leung, "Annular-slot-excited dielectric resonator antenna with a backing cavity," in Antennas and Propagation Society International Symposium, 2002. IEEE, 2002, pp. 470-473 vol.4.

[7] K. Y. Chow, K. W. Leung, K. M. Luk, and E. K. N. Yung, "Input impedance of the slot-fed dielectric resonator antenna with/without a backing cavity," IEEE Transactions on Antennas and Propagation, vol. 49, pp. 307-309, 2001.

[8] A. Petosa, Dielectric Resonator Antenna Handbook: Artech House, 2007.

[9] A. Ittipiboon, A. Petosa, D. Roscoe, and M. Cuhaci, "An investigation of a novel broadband dielectric resonator antenna," in Antennas and Propagation Society International Symposium, 1996. AP-S. Digest, 1996, pp. 2038-2041 vol.3.

[10] L. Bin and L. Kwok Wa, "Strip-fed rectangular dielectric resonator antennas with/without a parasitic patch," IEEE Transactions on Antennas and Propagation,

vol. 53, pp. 2200-2207, 2005.

[11] Z. Qi, "'Design and Measurements of a Wideband Dielectric Resonator Antenna," Master dissertation, Department of Electronic and Electrical Engineering, the University of Sheffield, 2015.

Chapter Four

Frequency/Mode Reconfigurable Dielectric Resonator Antennas

4.1 Introduction

It is well-known that changing the relative location of the antenna feed changes the radiation characteristics, and eventually the resonance frequency and bandwidth as this may change the excited mode [1]. This concept has been utilized originally for impedance tuning and matching, and hence frequency tuning [2]. In principle, this can be employed to reconfigure an aperture-coupled DRA that is excited using multiple slots with a single slot active at a time. Furthermore, DRA modes have different resonance frequencies, and hence, it is expected that this technique will lead to reconfiguring the operating resonance mode.

4.2 Modes Generation in a Rectangular DRA Using Feed-Aperture Shifting

As has been described in Chapter 2, the common aperture-fed RDRA consists of a microstripline beneath a thin dielectric substrate that is covered by a slotted metallic ground plane with a rectangular DRA positioned above the slot. The latter is positioned at the centre of the lower DRA face, as illustrated in Figure 4.1. The resonance frequencies for each RDRA mode can be calculated as [1-3]

$$f_{lmn} = \frac{c}{2\sqrt{\varepsilon_r}}\sqrt{\frac{l^2}{d^2} + \frac{m^2}{w^2} + \frac{n^2}{b^2}} \qquad (4.1)$$

where c is the speed of light, ε_r is the DRA dielectric constant, $b=2h$, d, w and h are the DRA dimensions, l, m, and n are constants related to the order of a particular TE resonance mode.

As discussed in Chapter two, for a slot coupled RDRA, the slot acts as a horizontal short magnetic dipole, and for a slot parallel to the x-axis, it is expected that the activated modes are $TE_{\delta nm}$, where δ is the fraction of the field's half cycle variation that is calculated as $\delta = k_x/(\pi/d)$, and the dominant field components are H_x, E_y, E_z [2].

The RDRA dimensions have been chosen as d = 8 mm, w = 12 mm, and h = 5.5 mm, with a dielectric constant of ε_r = 20 [1]. The used substrate is FR-4, with ε_r = 4.3, and with an area of 10×10 cm^2 as well as a 1.6 mm thickness. This differs from the original design, where the substrate has a dielectric constant ε_r = 3.38 and 0.5 mm thickness. This change has been brought by materials availability. In addition, the slot length and the stub length had been changed in the new design due to substrate change [1]. In the aforementioned design, two slot positions have been investigated, central with respect to the DRA lower face, and offset position from the centre of the DRA. The offset led to pushing up the impedance matching bandwidth from a centre frequency of ~5 GHz to ~6.4 GHz [1]. This frequency shift is considered to be useful for TE mode tuning, due to the fact that both frequencies are operating different modes.

Using equation (4.1), the expected resonance frequencies for the $TE_{\delta 11}$, $TE_{\delta 21}$, and $TE_{\delta 31}$ modes are 4.1 GHz, 6.4 GHz, and 8.9 GHz, respectively. CST Microwave Studio® Eigen Solver has also been used to calculate the modes' resonance frequencies by assuming magnetic walls boundary conditions on all the RDRA sides except the lower face where an electric wall has been assumed to take account of the ground plane presence. The Eigen mode solver has provided resonance frequencies of 4.1 GHz, 6.36 GHz, and 8.9 GHz,

respectively, which shows extremely low error margin between the two calculation methods.

According to simulations, an 8 mm long and 1 mm wide slot should be suitable for efficient coupling of the DRA to the feeding microstrip line that is located at the centre of the substrate and has a 1.2 mm width as well as a 5-mm stub length. The configuration has been simulated using CST Microwave Studio® in order to study the effects of shifting the slot alongside the microstrip line feed. Two cases have been considered; first when the stub length is constant with respect to the slot point of view, and second when the feed line length is constant from the RDRA point of view, i.e. the total length of the microstrip line including the stub is constant. Figures 4.2 and 4.3 illustrate the reflection coefficients of both cases for various slot positions that are determined by a shifting range of P = -4 to P = +4 mm, where P is the shift of the slot from the RDRA centre, respectively. These results clearly demonstrate the effects of different slot locations on the operating frequency and impedance bandwidth, which is expected as a different DRA mode is excited in each case. Additionally, the results illustrate the possibility of designing a reconfigurable DRA.

Since impedance matching bandwidths central frequencies are not always near the DRA resonance frequencies, the TE modes have been checked in some of these frequencies to specify the active resonance modes. Figure 4.4 illustrates few of H-fields at the ground plane level, where it can be noticed that when P=0 mm, there are two resonance frequencies, the first at 4.4 GHz, which corresponds to the $TE_{\delta 11}$ mode. However, despite the fact that the second of 6.45 GHz is close to that of the $TE_{\delta 21}$ mode, the H-field distribution shows similar characteristics to the $TE_{\delta 11}$ field distribution. This is can be attributed to the fact that in $TE_{\delta 21}$, H_x=0 at x=0, but since slot is located at x=0, this cannot be feasible, hence this mode cannot be excited when the slot is at the DRA centre. On the

other hand, this resonance can be caused by the slot's self-resonance. On the other hand, when *P*=-1 mm there are three impedance matching bandwidths, 4.4 GHz, 6.4 GHz, and 7.3 GHz. While the field distribution at 4.4 GHz shows the expected $TE_{\delta 11}$ mode modal field. The field distribution of the 6.4 GHz frequency band illustrates the general shape of the $TE_{\delta 21}$ mode. In addition, the third band lay between $TE_{\delta 21}$ and $TE_{\delta 31}$ modes resonance frequencies, hence the H-field distribution at 7.3 GHz is similar to that of the $TE_{\delta 21}$ mode. However, this resonance can be cause by slot's self-resonance.

In the next two sections, two designs are proposed; the first involves a single central slot with only two operations, antenna ON and antenna OFF, and the second incorporates dual slots with only one of the active, i.e. feed the RDRA, at a time. Prototypes of these design have been built and measured. In addition, a triple slots-fed RDRA has been investigated.

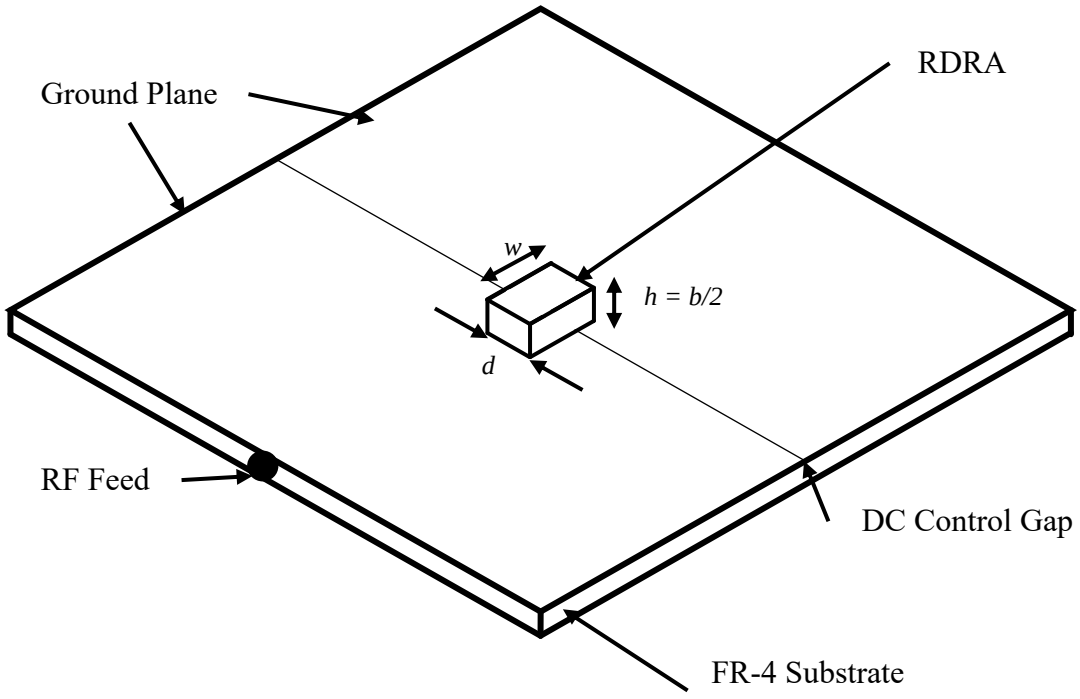

(a) General View

Figure 4.1 Antenna Diagram

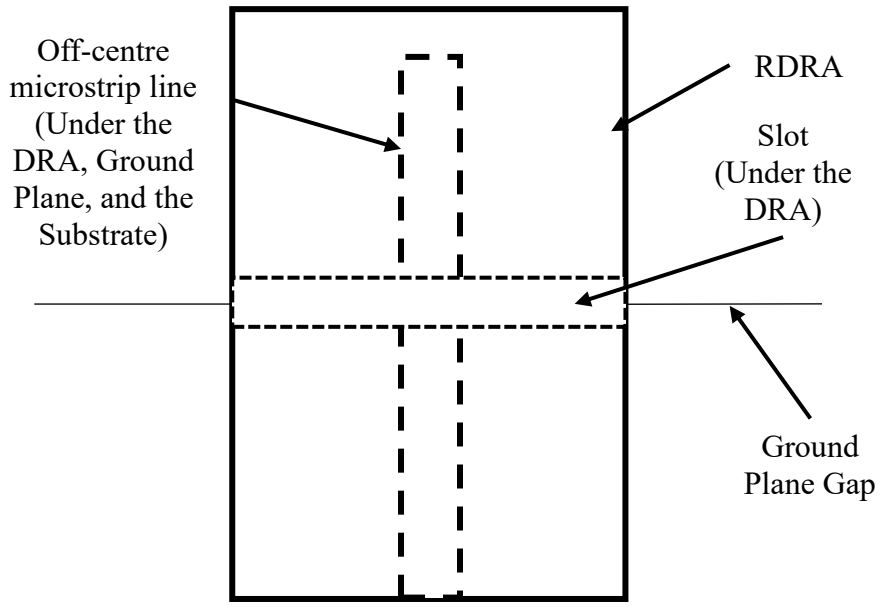

(b) DRA Area Top View and

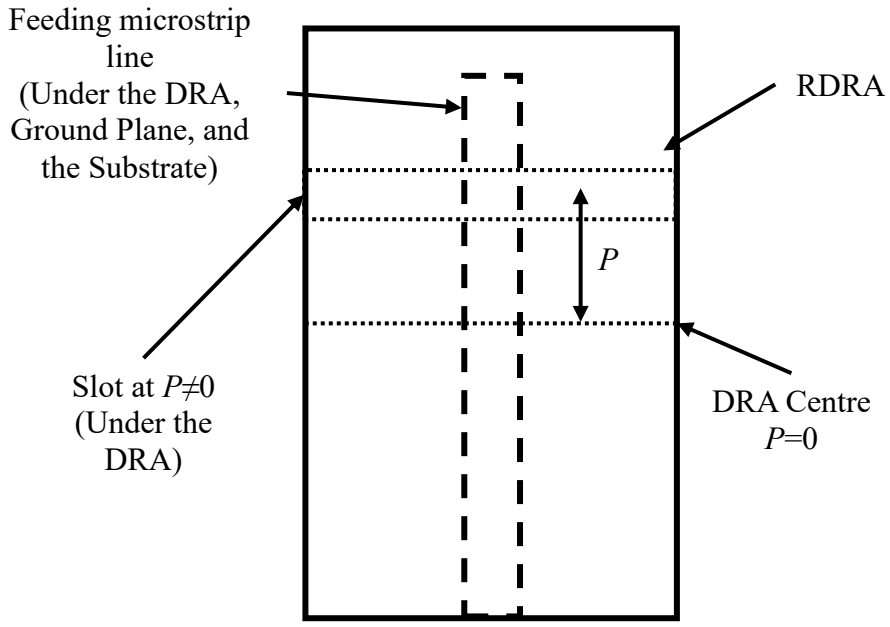

(c) DRA Area Top View Illustrating the Slot at Position $P \neq 0$

Figure 4.1 Continued

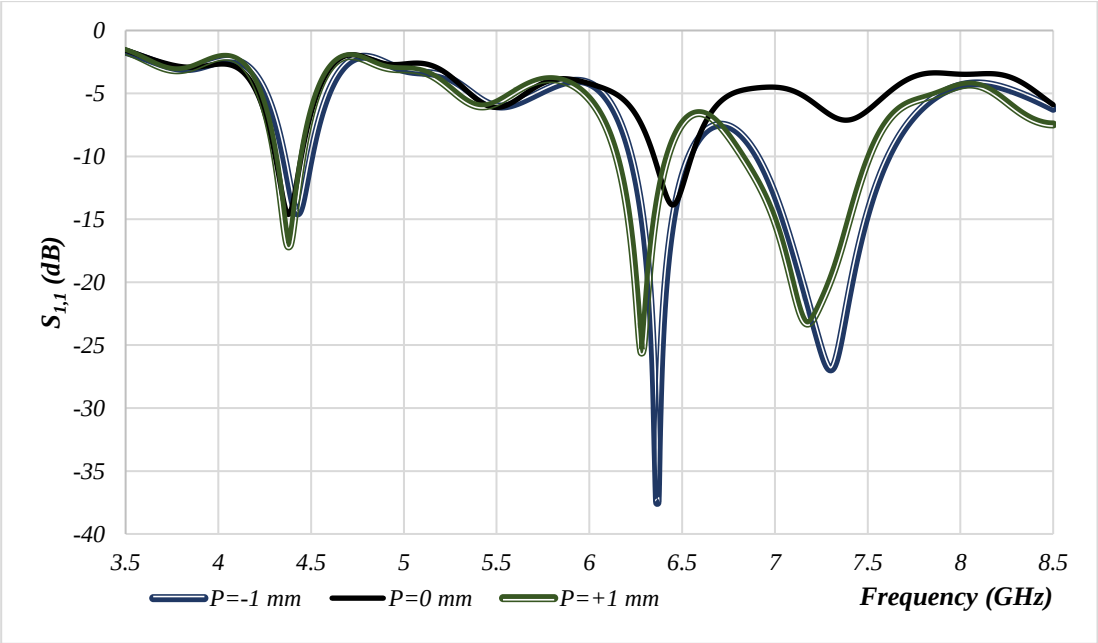

(a)

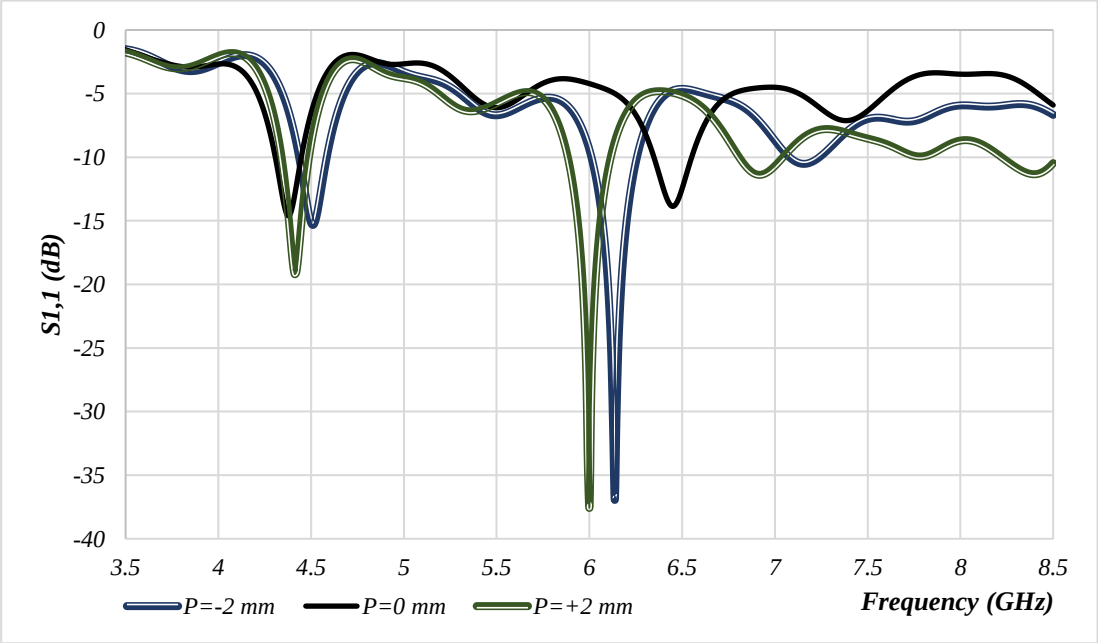

(b)

Figure 4.2 Effect of Shifting the Slot Position (*P*) with Respect to the DRA Centre with a Constant Stub Length (a) *P*=±1 mm, (b) *P*=±2 mm, (c) *P*=±3 mm, and (d) *P*=±4 mm

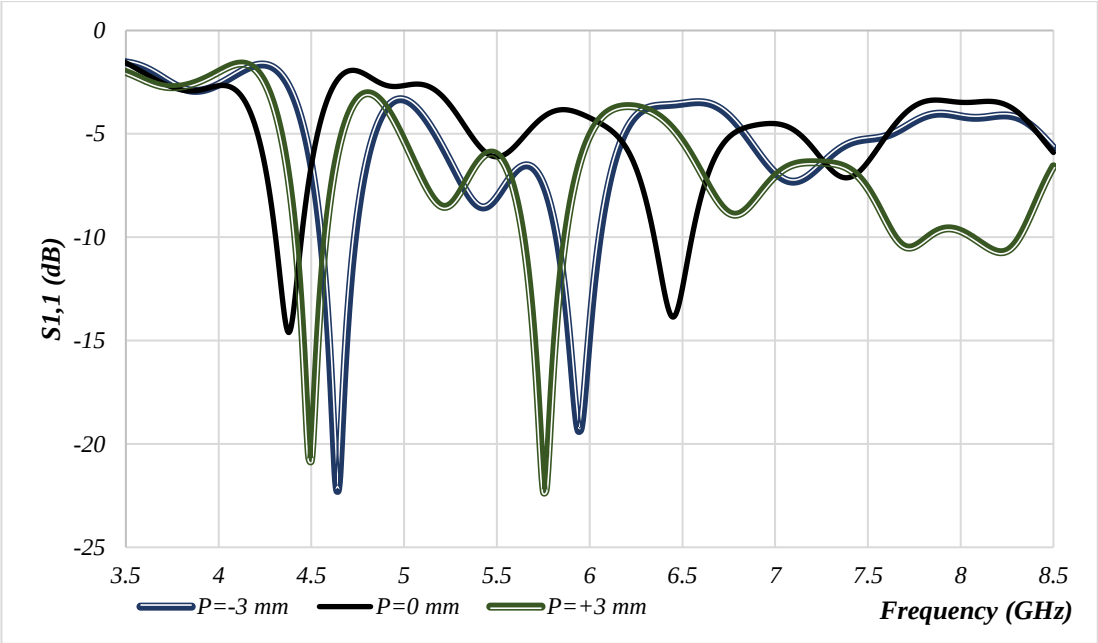

(c)

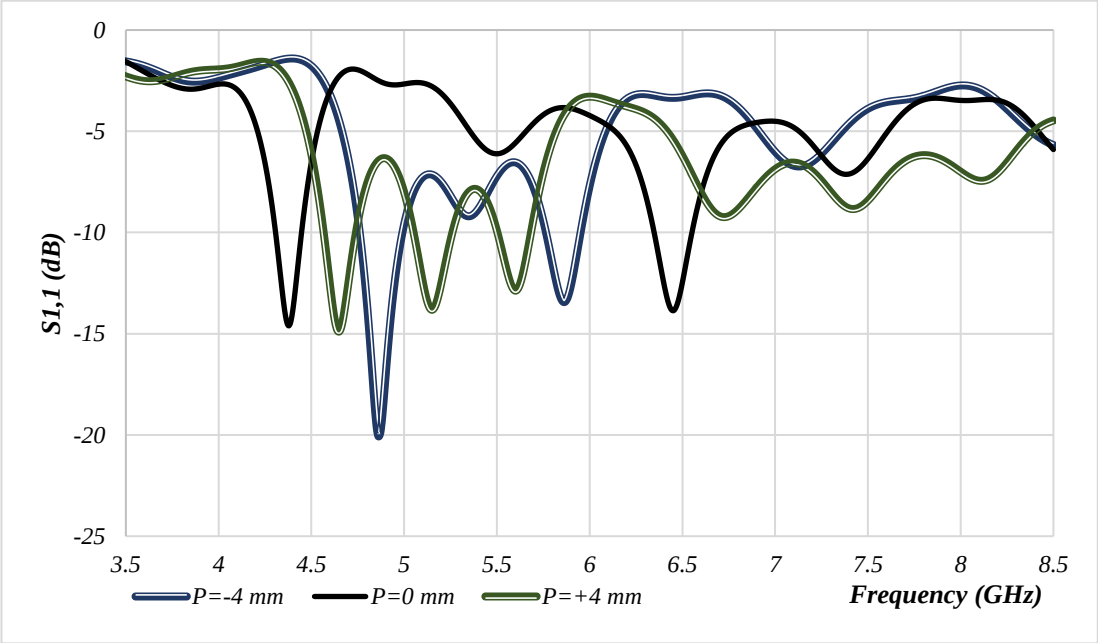

(d)

Figure 4.2 Continued

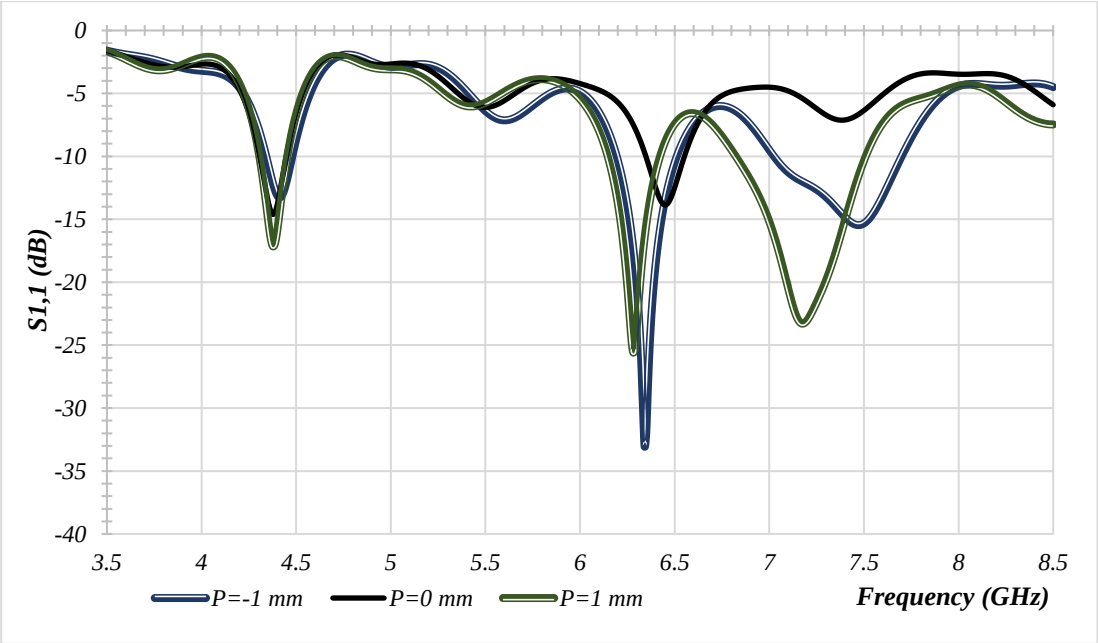

(a)

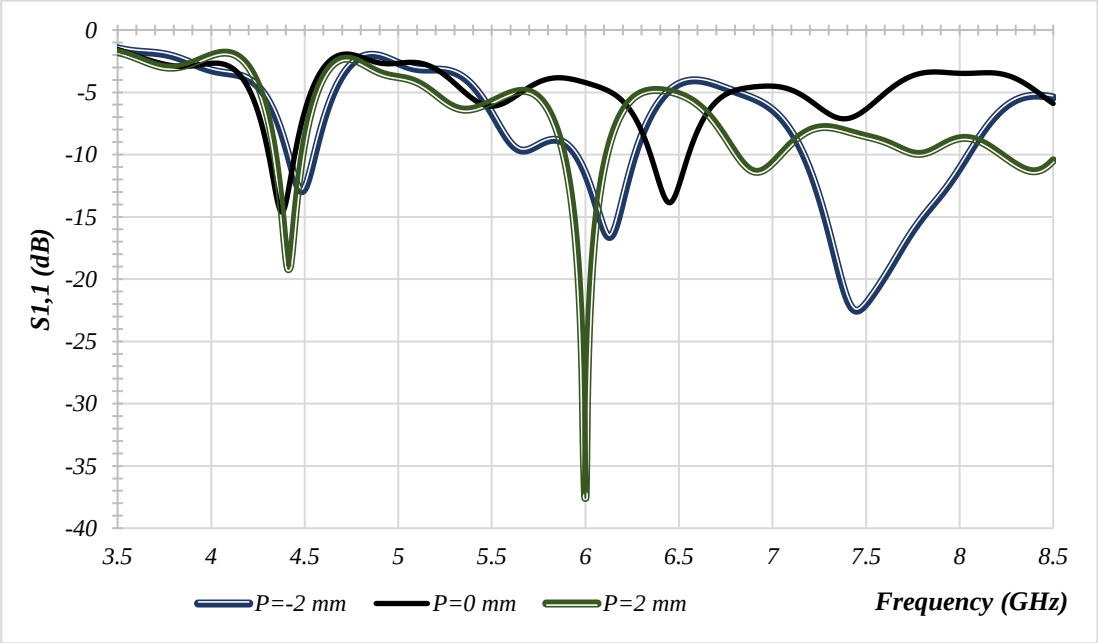

(b)

Figure 4.3 Effect of Shifting the Slot Position (*P*) with Respect to the DRA Centre with a Constant Total Microstrip Line Length (a) *P*=±1 mm, (b) *P*=±2 mm, (c) *P*=±3 mm, and (d) *P*=±4 mm

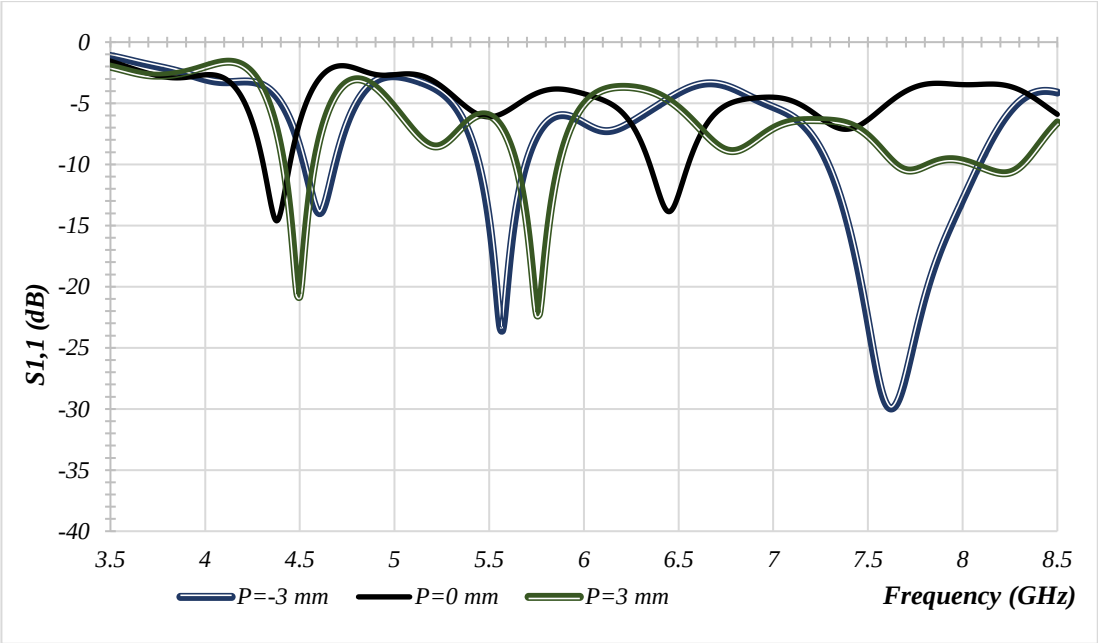

(c)

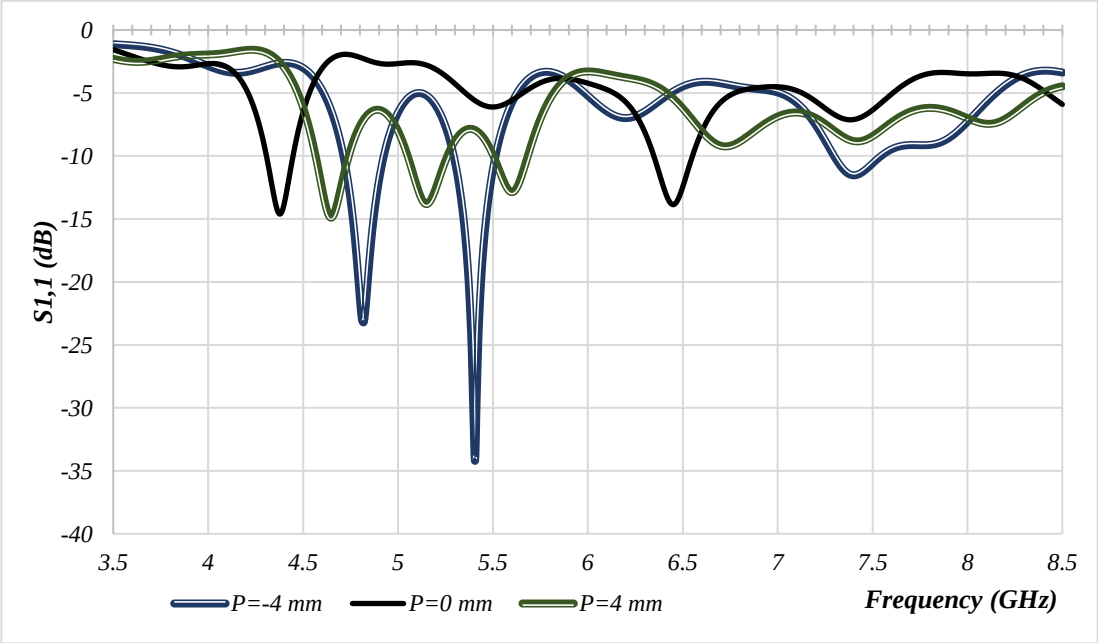

(d)

Figure 4.3 Continued

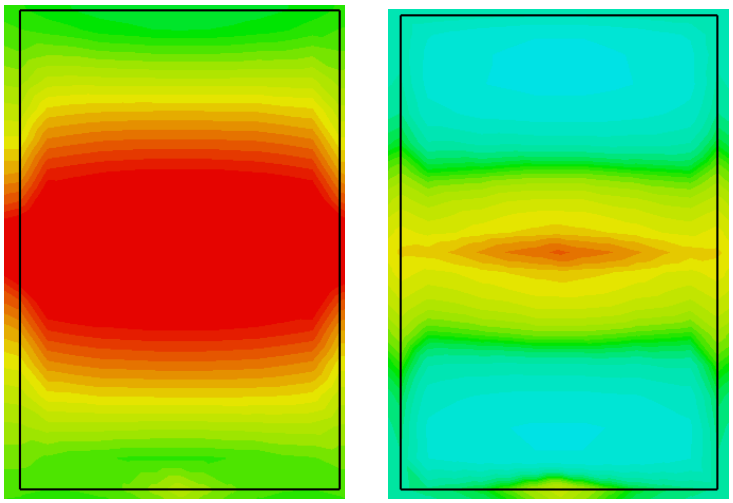

(a) $TE_{\delta 11}$ at 4.4 GHz (Left) and $TE_{\delta 21}$ at 6.45 GHz (Right)

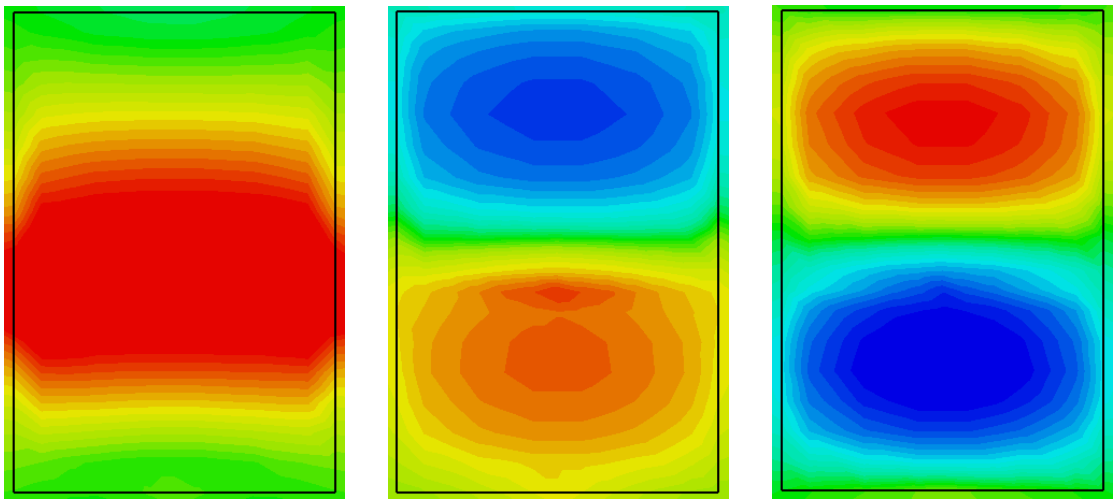

(b) $TE_{\delta 11}$ at 4.4 GHz (Left), $TE_{\delta 21}$ at 6.4 GHz (Centre), and 7.3 GHz (Right)

Figure 4.4 Effect of Shifting the Slot Position (*P*) with Respect to the DRA centre on H-Field distributions for (a) *P* = 0 mm, and (b) *P* = -1 mm

4.3 Reconfigurable Single Slot-Fed RDRA

In this model, the RDRA reconfigurability concept is demonstrated by turning the antenna radiation ON/OFF through controlling the slot in which a PIN diode is inserted. Turning the diode ON will electrically short circuit the slot, which results in a negligible electric field inside it. However, it is expected that the PIN diode material, the needed gap to accommodate the diode, and the DC bias will affect the impedance bandwidth, resonance frequency, as well as the radiation pattern.

Figure 4.3 presents the rectangular DRA design in addition to a picture of the built prototype. Since the relative location of the input feed affects the input impedance, the off-centre microstripline feed has been employed in order to improve the impedance bandwidth [4]. The employed dimensions are: Ground plane and substrate area of 10×10 cm^2, substrate thickness of 1.6 mm, 8 mm long and 1 mm wide feeding slot. The RDRA is made of E-20 compound provided by T-Ceram with ε_r = 20 [5], and dimensions of 12×8×5.5 mm^3 with an error tolerance of ±5%. The microstripline width has been chosen as 1.2 mm. It has been noticed throughout CST simulations that the impedance bandwidth can be improved using a 5-mm stub as well as a 2.4 mm shift in the microstrip line position from the slot centre. In addition, a BAR50-02V PIN diode has been employed, and its parameters have been used to represent the diode's equivalent circuit in the simulations [6]. The ground plane has been divided into two equal halves, from the middle alongside the slot, in order to create the required isolation to connect the DC biasing. The gap between the two ground plane halves must be kept as small as possible, typically < 0.3mm, in order to minimize any disturbance to the antenna characteristics. Furthermore, two capacitors have been added on both sides of the gap to directly connect these two halves from the RF/Microwave perspective and minimize the gap effect while the DC bias isolation is maintained. The capacitors have been chosen as 1 μF each, and

it has been proven via simulations and measurements that these capacitors are useful to decrease the effects of the gaps when the ratio of gap to slot width increases, but less important when this ratio decreases. It has been noticed that a centrally located diode has a minimum impact on the DRA characteristics when the slot is fed by an off-center strip line. This is expected to some extent as the diode needs to be placed at the point of a maximum coupling between the slot and the off-centre feeding strip. Therefore, an additional diode has been incorporated inside the slot and placed above the feeding strip as shown in Figure 4.3 (a). The DC feed consists of two 1.5 V batteries that are connected in series, a variable resistor, and two inductors serving as RF chocks to eliminate the flow of the microwave signal's current through the DC biasing circuity and hence effectively disconnect the DC lines from the antenna as shown in Figure 4.3 (b). The variable resistor has been fixed at 10 Ω to drive a 200 mA current that is needed to turn both diodes ON in order to short circuit the slot.

As mentioned in the previous Chapter, air gaps between the DRA and the ground plane have been minimised using adhesive backed double sided copper tape [7, 8]. In addition, a cling film layer has been used to hold the DRA firmly to the ground plane, which further reduces the potential air gaps. The reflection coefficients are illustrated in Figure 4.4 where the absence of a DRA excited mode can be noticed at frequencies lower than 7 GHz when the PIN diode is ON. However, this statement is no longer valid at higher frequencies due to the limitation of the PIN diode frequency range which has a maximum of 6 GHz according to the manufacturer's data sheet [6]. On the other hand, when the diode is in the OFF state, the respective measured and simulated impedance bandwidths are 12.46% and 11.3% with corresponding resonance frequencies of 6.1 GHz and 6 GHz. It should be expected that the DRA $TE_{\delta 11}$ mode has been excited at these frequencies since it lays between the $TE_{\delta 11}$ mode and $TE_{\delta 21}$ mode resonance frequencies, along with

a central slot coupling the DRA, which prevents an even order mode from being excited, otherwise, this resonance can be expected to be slot's resonance. In addition, the measured results include a rather narrow impedance bandwidth at a frequency of 4.25 GHz with an impedance bandwidth around 1.1%. This frequency is near the $TE_{\delta 11}$ mode resonance frequency, which can lead to the conclusion of a weakly excited $TE_{\delta 11}$ mode. The results demonstrate a reasonable agreement between simulations and measurements with some differences that may be expected when the DRA is associated an airgap in the aperture coupling area that accommodates the diode [1, 7]. The simulated and measured radiation patterns for the cases of open and shorted slots are shown in Figure 4.5. The comparison shows gain modulations of ~8.1 dBi at 5.99 GHz and ~6.5 dBi at 6.12 GHz for simulations and measurements, respectively. The general shapes of both radiation patterns are similar, but the main beam directions at θ=38 at 5.99 GHz and θ=55° 6.12 GHz for the simulated and measured results, respectively. The main difference between the measured and simulated radiation patterns is the higher measured back radiation, which can be attributed to the prototype imperfections and measurements error. Figure 4.6 illustrates the simulated E-field and H-Field distribution inside the DRA at 5.99 GHz. Both distributions show the general characteristics of $TE_{\delta 11}$ mode, although not ideal, since this operating frequency is near the $TE_{\delta 21}$ mode resonance frequency. Finally, Table 4.1 compares the simulated and measured data with respect to the central operating frequency, impedance bandwidth, gain, and gain modulation.

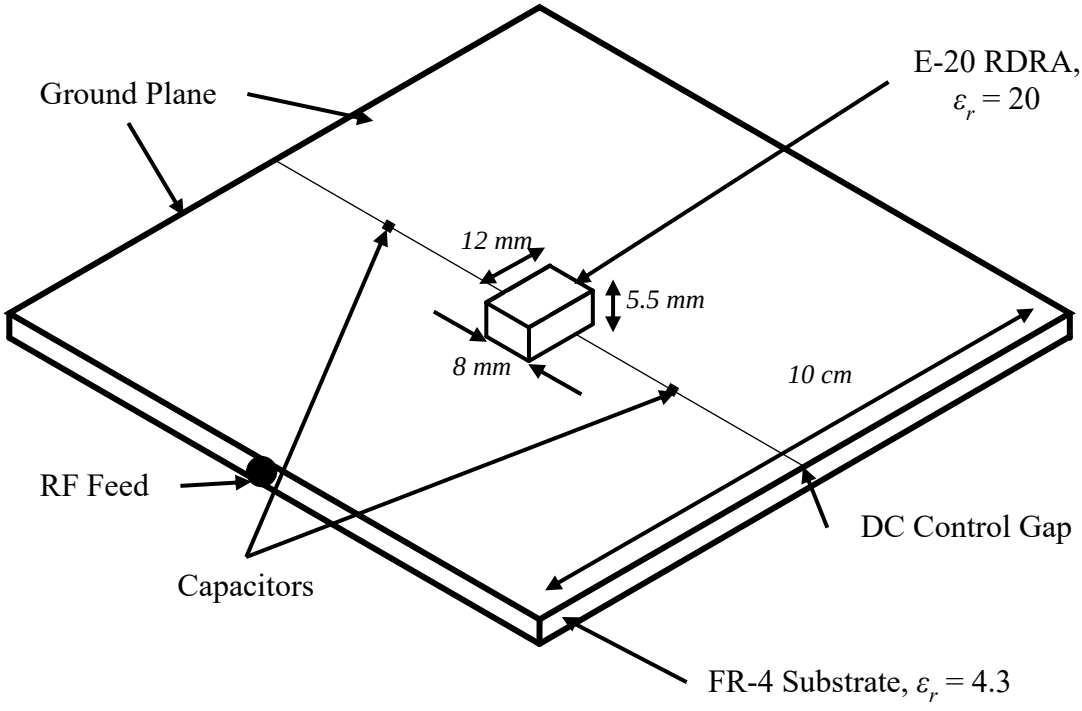

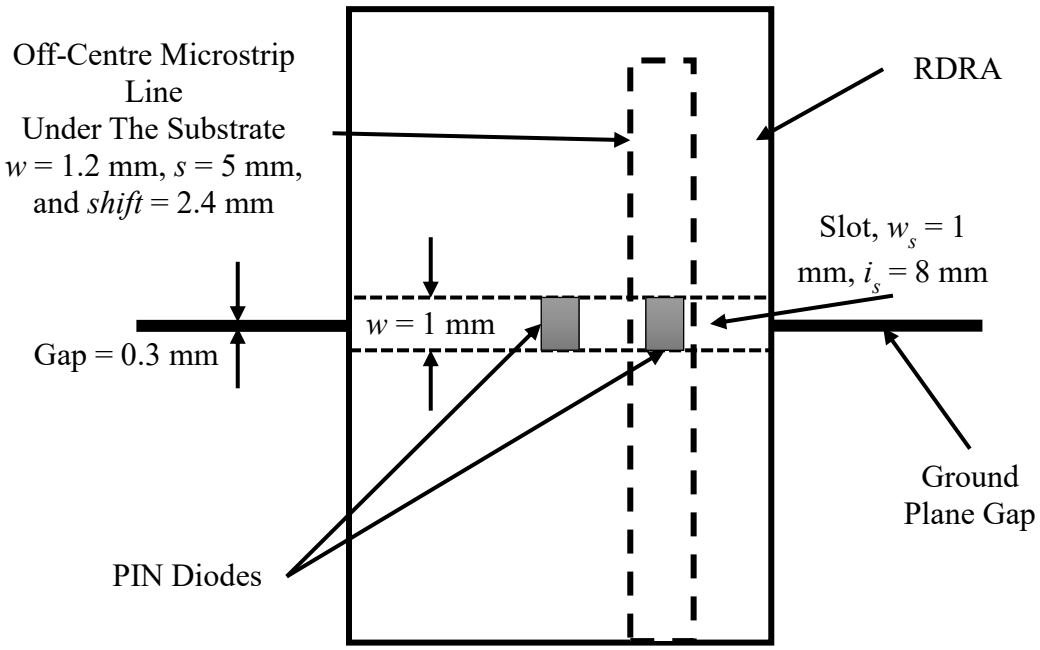

(a)

Figure 4.3 Reconfigurable Aperture Coupled RDRA (a) Antenna Diagram and DRA Area, (b) DC Control Diagram, (c) Built Antenna Prototype Top View and (d) Bottom View of the Feed

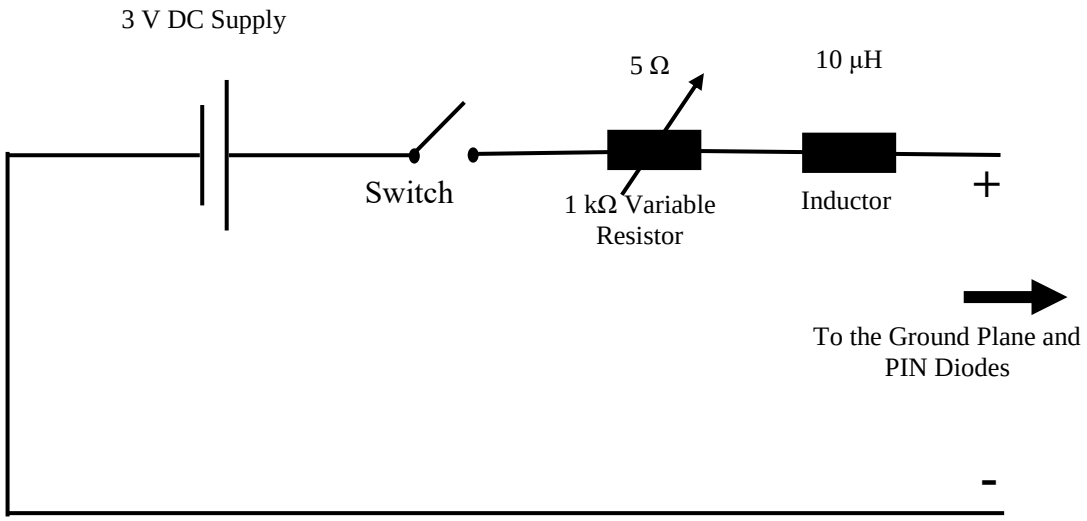

(b)

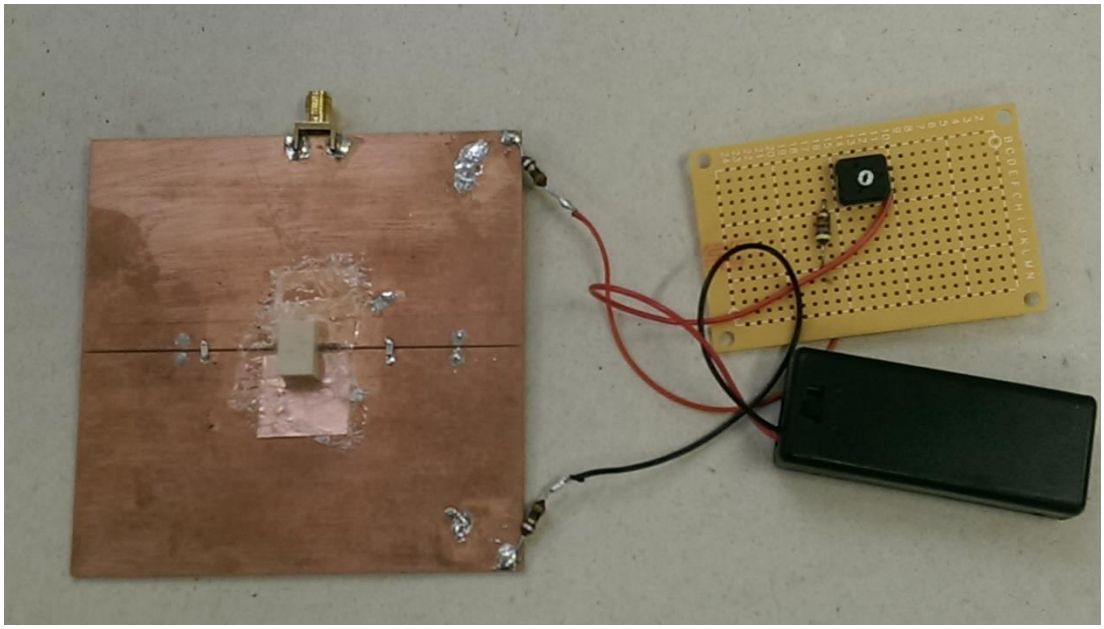

(c)

Figure 4.3 Continued

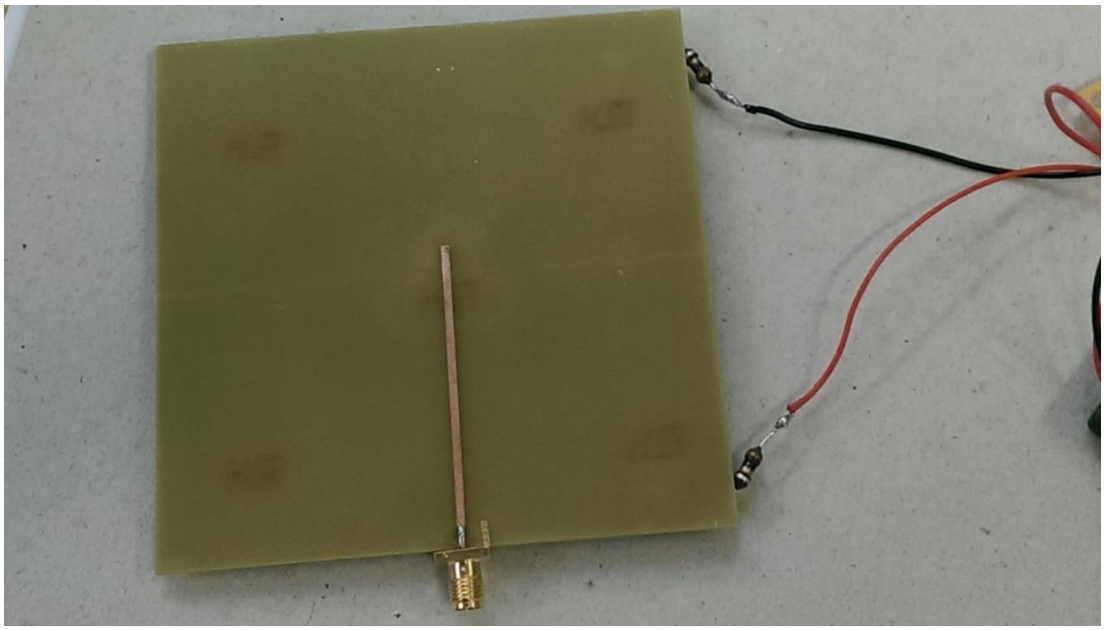

(d)

Figure 4.3 Continued

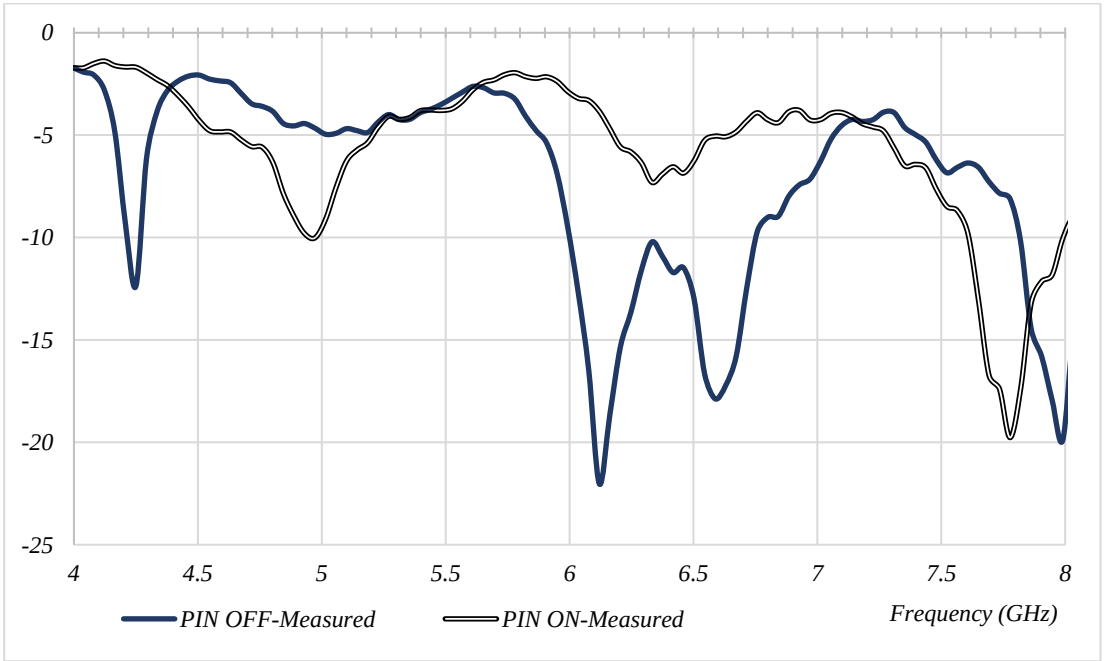

(a) Measured Results

Figure 4.4 Reflection coefficients of a single slot fed RDRA with a PIN diode

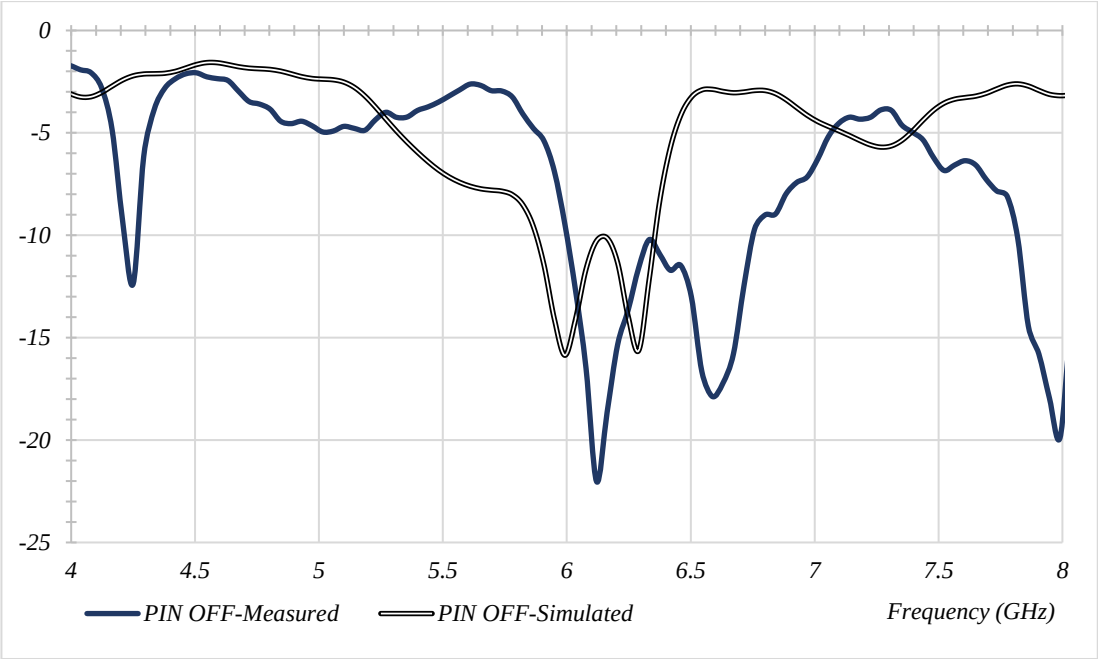

(b) PIN diodes OFF Case Measured vs Simulated

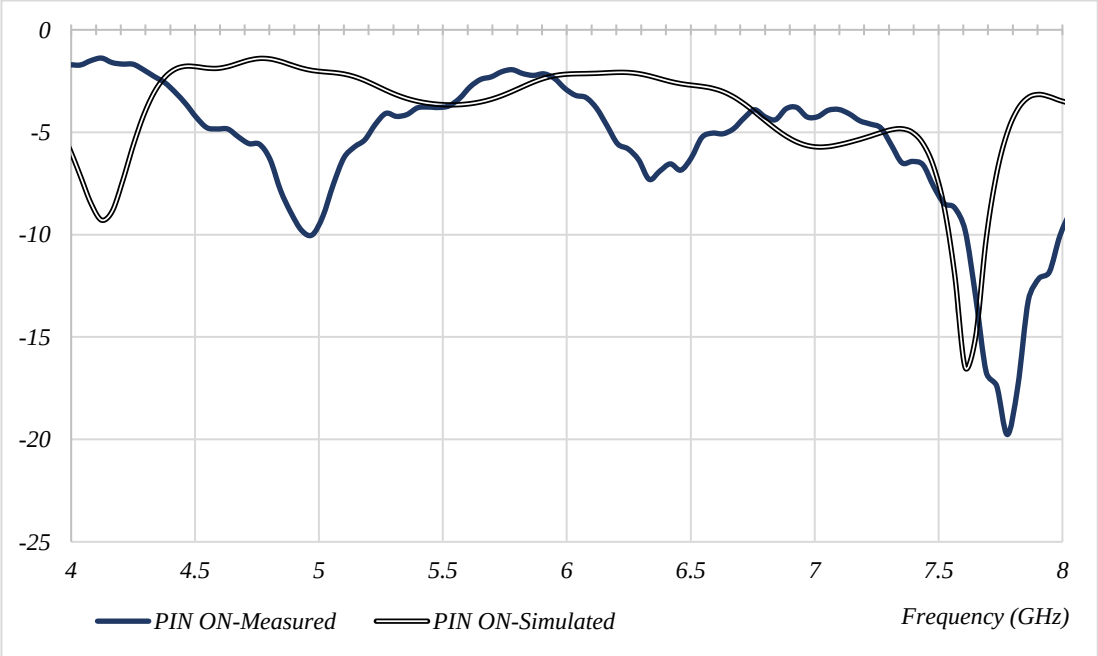

(c) PIN diodes ON Case Measured vs Simulated

Figure 4.4 Continued

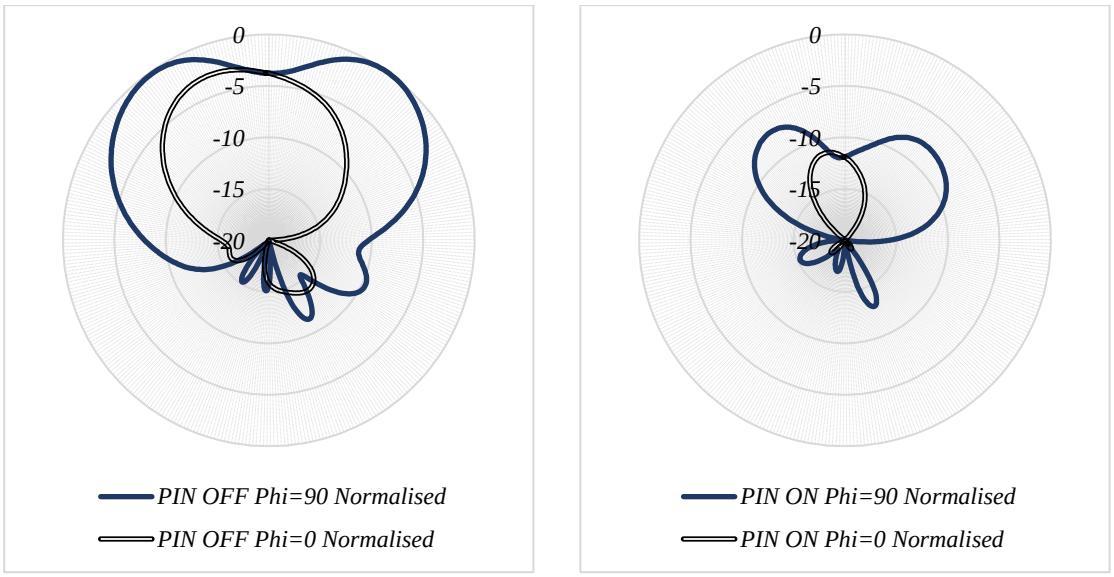

(a) Normalised Simulated at 5.99 GHz

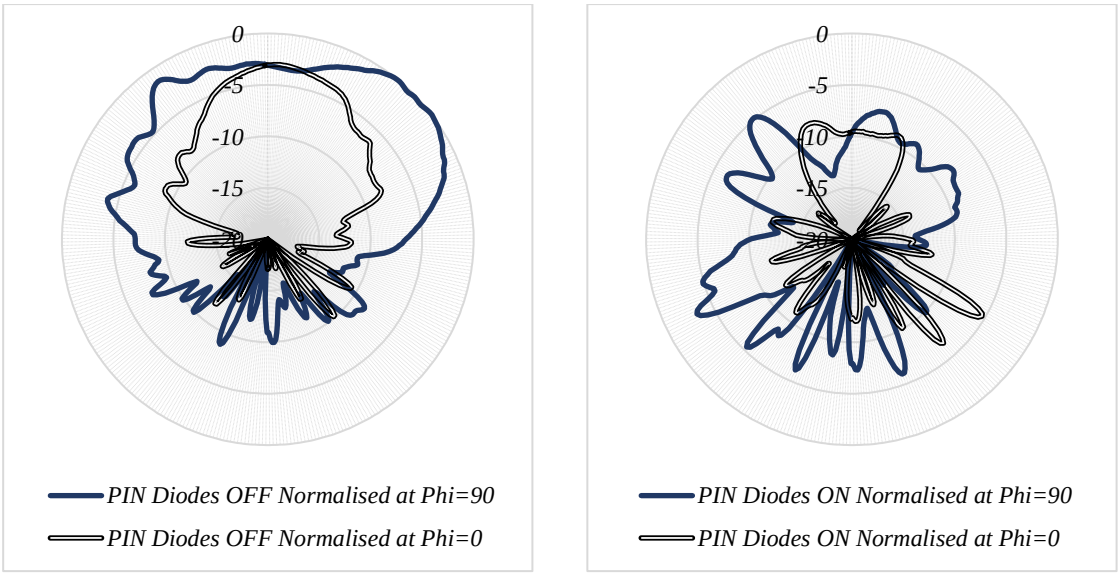

(b) Normalised Measured at 6.12 GHz

Figure 4.5 Radiation patterns of a single slot fed RDRA with a PIN diode Normalised with Respect to Maximum Radiated Power in any Given Direction, for both Co-polar (φ=90º) and Cross-polar (φ=90º)

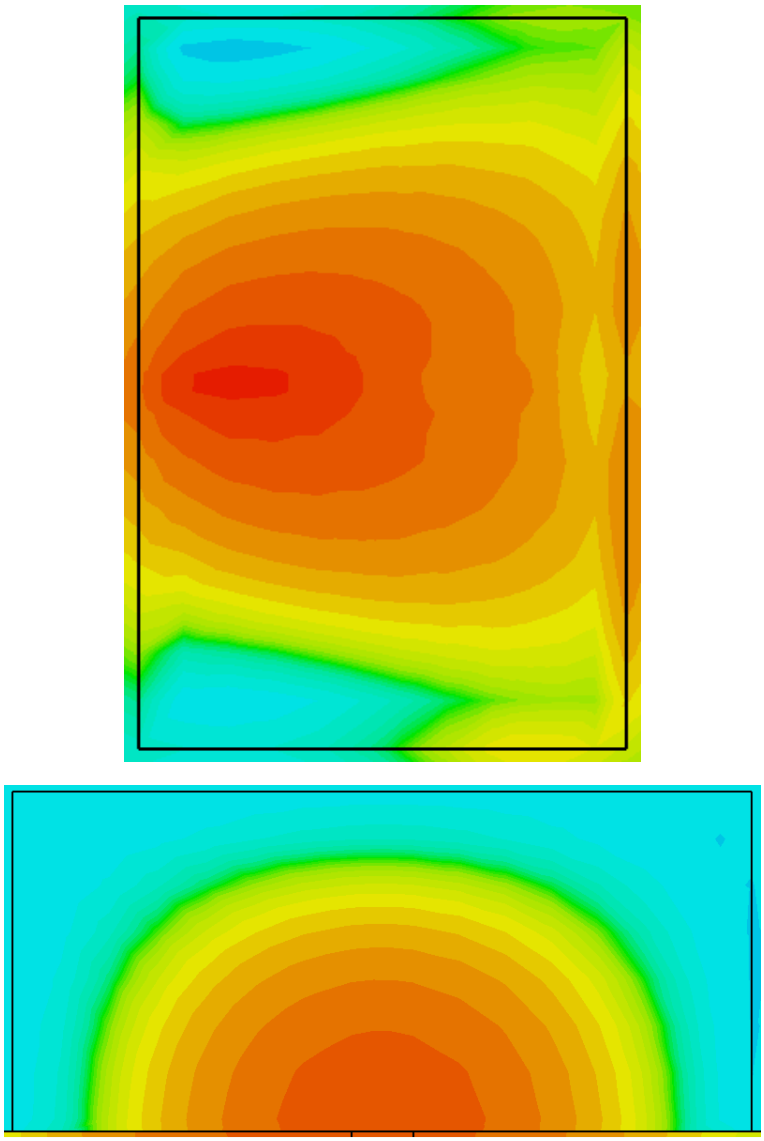

Figure 4.6 H-Field Distribution Top View at *x-y* plane (Top) and Side View *y-z* plane (Bottom) inside the DRA at 5.99 GHz

Table 4.1 Simulated and Measured Results Comparison

Comparison	Measured	Simulated
Central Frequency (GHz)	6.12	5.91
Impedance Bandwidth %	12.25	11.3
Gain at Central Frequency (dB)	3.6	5.35
Gain Modulation (dB)	6.5	8.6

4.4 Reconfigurable Multi-Slot-Fed RDRA

Using the principles discussed in section 4.1, two novel configurations are proposed; dual, and triple-slot fed DRAs as shown in Figures 4.7 and 4.11, respectively. In these two configurations, all the slots are shorted except one at a time that is left open to excite the DRA, i.e. only a single slot at a time operates as a coupling feed-aperture. It is expected that switching the feeding aperture will change the impedance characteristics of the antenna in a similar way to that shown in the example of section 4.1. However, since these short circuits are achieved using PIN diodes that cover the slots partially and they are not as good as a perfect electric conductor, it is expected that there will be some coupling with the short-circuited slots. In addition, an undesired interference is introduced due to the uncovered area of the shorted slots, which impacts the antenna radiation characteristics.

4.4.1 Reconfigurable Dual-Slot Coupled RDRA

Figure 4.7 illustrates the proposed DRA as well as a picture of the built prototype where ground plane and substrate area of 15×15 cm^2 have been used. The thickness of the FR-4 substrate is 0.8 mm, and each slot has a length and width of 16 mm and 1.2 mm, respectively. The first slot has been denoted as Slot-0 since it is positioned at the DRA centre, while the second slot has been denoted as Slot+6, since it is shifted 6 mm from the DRA centre. The microstripline width is 1.2 mm, and using CST optimization, it has been observed that the optimum stub length for both configurations need to be chosen as 11 mm from the first slot position.

The RDRA dimensions have been chosen as 24×16×11 mm^3, and it has been fabricated using the same T-Ceram's E-20 compound employed in the previous prototype [5]. It should be noted that the prototype incorporates a 1 mm width and depth tunnel that is

located in the DRA lower side to accommodate the PIN diodes, which are positioned on the top of the substrate. This technique has been used to minimize the slot's field disturbance owing to inserting the diodes inside the substrate. Furthermore, the original DRA size has been doubled in order to simplify fabrication and increasing the physical separation between the two slots. According to the simulated results, introducing the narrow tunnel has shifted the resonance frequencies of the $TE_{\delta 11}$, $TE_{\delta 21}$, and $TE_{\delta 31}$ modes by only ~1%, and hence its effects on the performance are marginal. Furthermore, doubling the DRA dimensions reduces the resonance frequencies by a factor of two, which is expected for the same dielectric constant. As a result, the simulated resonance frequencies using CST Eigen Mode Solver have been reduced to 2.08 GHz, 3.22 GHz, 4.5 GHz and 4.78 GHz for the $TE_{\delta 11}$, $TE_{\delta 21}$, $TE_{\delta 31}$ and $TE_{\delta 13}$ modes, respectively.

Once more, a BAR50-02V PIN diode has been employed, and its parameters have been used to represents the equivalent circuit in the simulations [6]. The ground plane has been partitioned d into three sections alongside the slots in a similar way to that used in the previous design, with two capacitors placed across each of the 0.2 mm gaps to minimize the effects on the RF/Microwave connection. In addition, three inductors have been used as RF chocks to separate the DC lines from the antenna with respect to the RF/Microwave frequency signal. A couple of inductors have been employed to connect the two positive DC lines with their respective parts of the ground plane and the third connects the negative DC ground to the middle part of the ground plane as shown in Figure 4.7 (b) as well as in the antenna picture of Figure 4.7 (c).

The effects of the parasitic inactive slot have been studied using CST Microwave Studio simulations. Figure 4.8 compares the results of a single slot fed DRA with the case the of a dual-slot fed DRA for both of the Slot-0 and Slot+6 cases when only a single slot is active at a time. In both cases, there are changes such as a lower central frequency in the

Slot-0 case, and a wider impedance bandwidth in the Slot+6 case. The effects on the reflection coefficients are expected due to the change in the impedance characteristics and field distribution as a result of the parasitic slot presence. It should be noted that the off-center stripline feed that has been used with the single slot prototype has been abandoned due to the difficulty of arranging a shift that can service improvement in both cases, or at least provide enhancement in one case without negatively effecting the other case.

The experimental and simulated reflection coefficients are presented in Figure 4.9 with reasonable agreement and some differences that can be attributed to experimental and fabrication tolerances as well as the accuracy of the employed diodes' equivalent circuits. For example, resonance frequencies of 3.06 GHz for Slot-0 ($TE_{\delta 21}$) and 3.8 GHz for Slot+6 ($TE_{\delta 21}$) with impedance bandwidths of 32.6% and 19.8% have been measured, respectively. These results are comparable to the simulated data of 3.2 GHz ($TE_{\delta 21}$), 4.7 GHz ($TE_{\delta 31}$), 32.6% and 25%, respectively. These results show better agreement in the in Slot-0 case compared to that of Slot+6. The simulated data has a wider bandwidth, by almost 25%. In addition, the measured results central frequency is 3.8 GHz, while the simulated results have a minimum point at ~3.9 GHz. Moreover, the $TE_{\delta 13}$ has not been excited in the measured results at 4.7 GHz, a narrow impedance matching bandwidth exists at~ 5.1 GHz. It can be concluded that the measured results have suffered from the imperfection of prototype assembling as well as the minor differences between the simulated model and measured prototype.

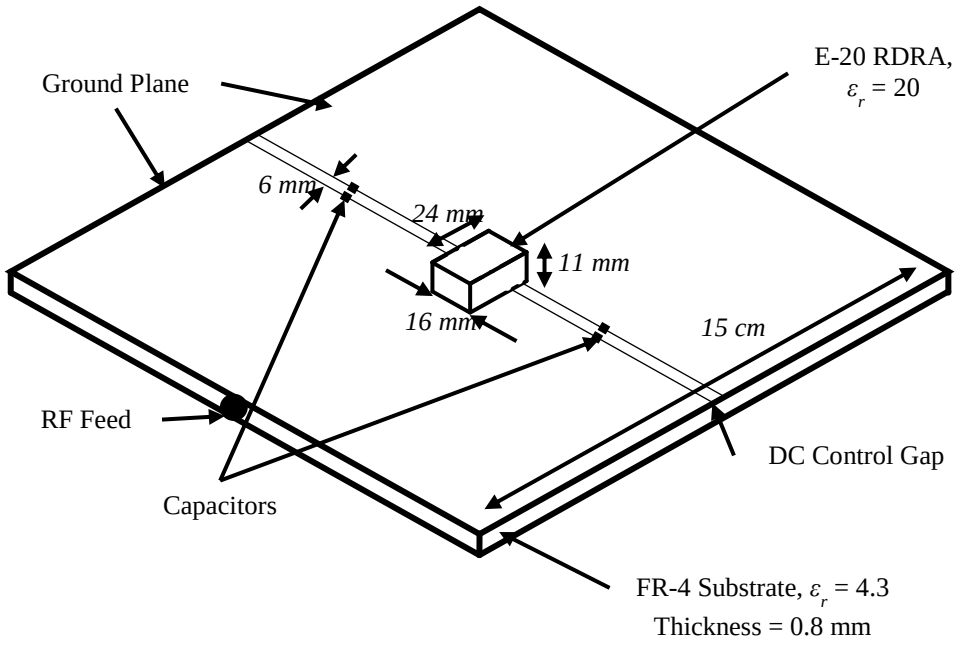

(a)

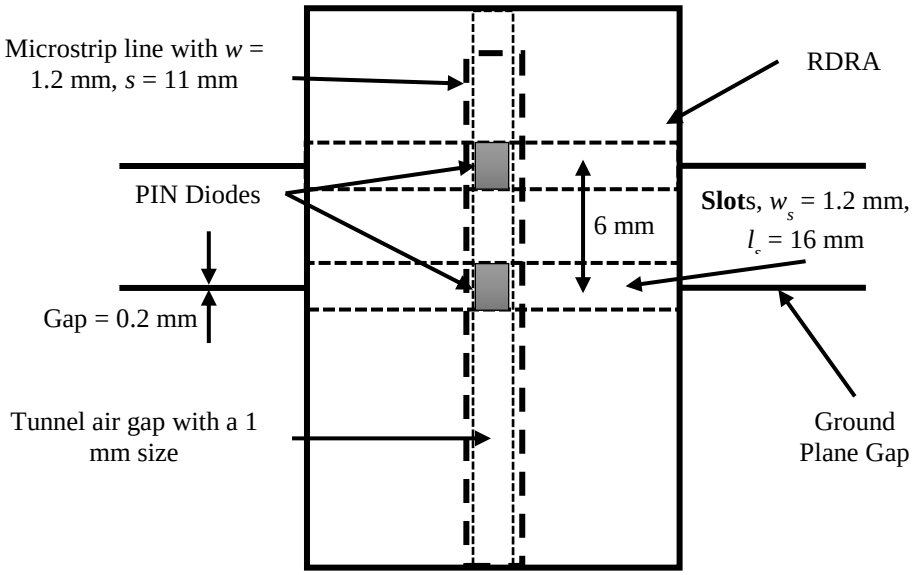

(b)

Figure 4.7 Reconfigurable Two Slots Aperture Coupled RDRA (a) Antenna Diagram, (b) DRA Area Diagram, (c) DC Control Diagram, (d) Built Antenna Prototype Top View and (e) Closer View Pointing the Feeding Slots, and (f) Bottom View of the Feed

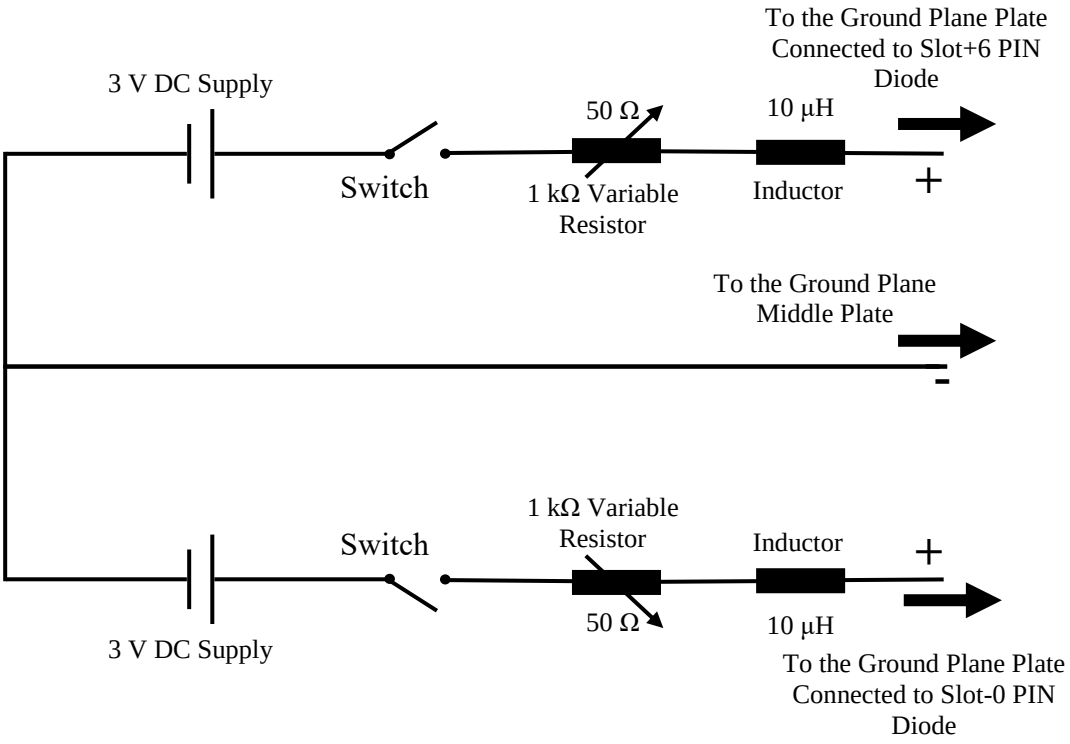

(c)

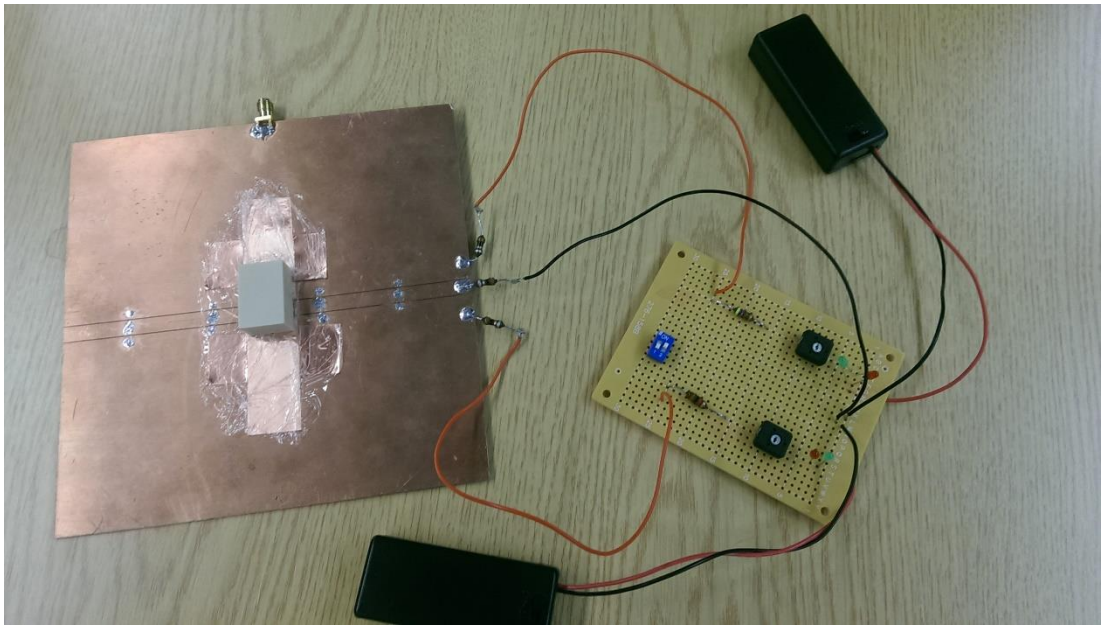

(d)

Figure 4.7 Continued

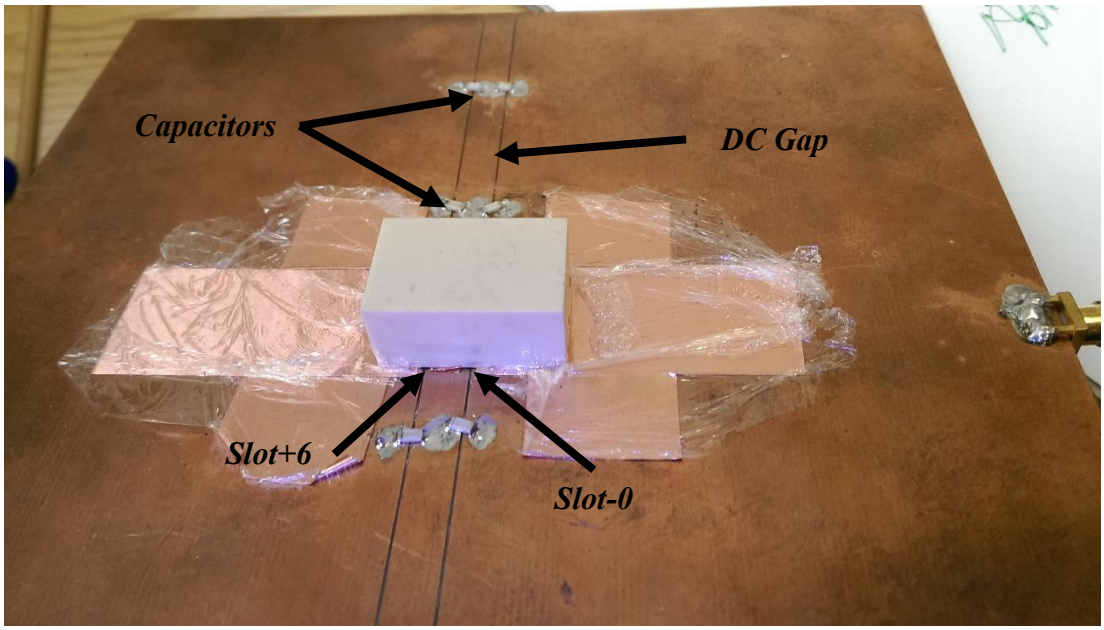

(e)

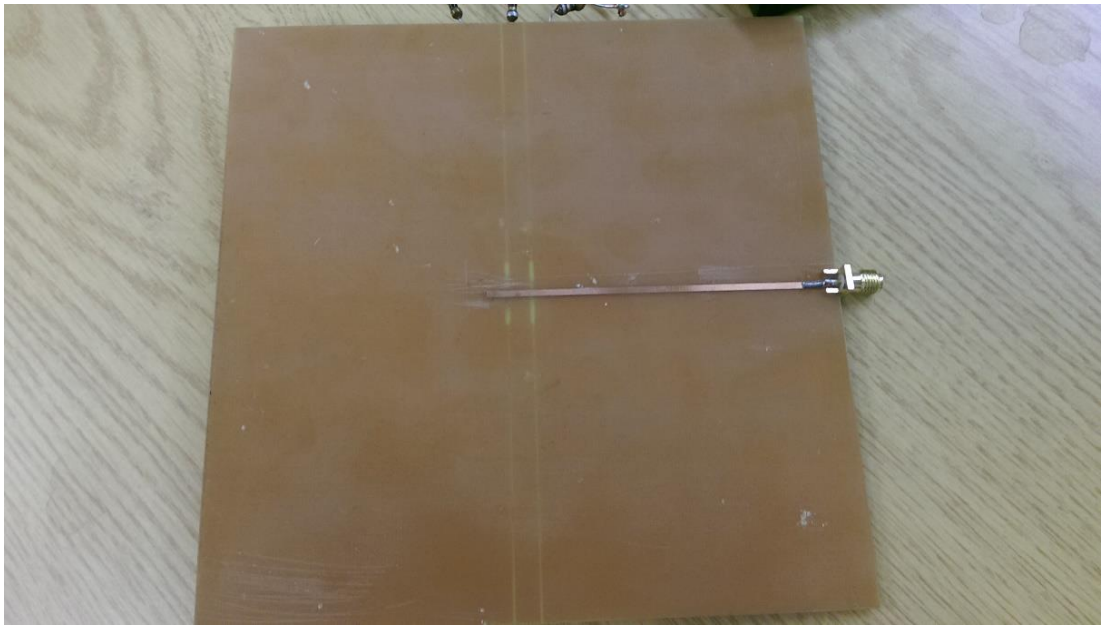

(f)

Figure 4.7 Continued

The resonance frequencies indicate that when Slot-0 is active, the $TE_{\delta 11}$ mode is excited, while the $TE_{\delta 31}$ mode is excited when Slot+6 is activated. However, the measured S_{11} when Slot-0 is active includes a second band that operates in the $TE_{\delta 31}$ mode region, where the measured band has a central frequency of 4.2 GHz with impedance bandwidth of 11.5%, compared to simulated results of 4.4 GHz and 4%. The same criterion appears for Slot+6 case, a second band with central frequency at 5.1 GHz and 2.74% bandwidth has been measured. This band operates at $TE_{\delta 13}$ mode region, which is the same as the simulated band that is centered at 4.7 GHz. This can be expected to be due to the small differences between the simulated and built prototypes that merged both bands of the theoretical results, while they are separated in the measured results due to the shift in the central frequency. Figure 4.10 presents the far-field radiation patterns, where the simulated results show the effects of the parasitic slot on the mainlobe direction, especially in the Slot-0 case. The H-plane pattern indicates a negative bore-sight gain, which may be due to shift in the main beam to 38° as can be noticed in the E-plane pattern, with a gain of 1.36 dBi. In the Slot+6 case, the H-plane field return a satisfactory gain of 4.5 dBi gain at $\theta = 0°$, and a maximum of 5.5 dBi at $\theta = \pm 22°$ with a wide beamwidth of 88.5°. However, the E-plane radiation pattern still shows some distortion due to presence of the parasitic slot. This has been proved by comparing the far field pattern of a dual-slot fed DRA to that of for a single slot-fed DRA at the same frequencies illustrated in Figures 4.10 (a) and (b), with the single slot located at the same position of the activated slot of in the dual-slot configuration. Comparing these results show that in the Slot-0 case at 3.06 GHz the E-plane patterns are almost identical with symmetrical main beams at $\theta = \pm 35°$ in the single slot case compared to asymmetry of ~3.6 dBi in the dual-slot case. Furthermore, similar effects can be noticed for the case when Slot+6 is activated and the patterns are monitored at 3.8 GHz. The measured radiation patterns for Slot-0 at 3.06

GHz has a shift of 47° in the E-plane main beam direction and for Slot+6 a shift of 48° in the opposite direction to that of the Slot-0 case. These results show a close similarity to the simulated data for the E-plane radiation patterns, i.e. φ=90°, however there are noticeable differences in the H-plane patterns that may be attributed to prototype unperfected building and measurements errors. Figure 4.11 compares between the simulated and measured radiation patterns.

Figure 4.12 illustrates H-field distributions for both cases at their respective simulated central frequencies. The results illustrate the expected distribution for both the $TE_{\delta 11}$ and $TE_{\delta 21}$ modes, respectively, accompanied with some distortion to the resultant distribution when compared to the H-field distribution for the same slots but without a parasitic slot. From the Slot-0 case at 3.06 GHz H-field, it can be compared to that of the same DRA without a parasitic slot. Comparing the Slot-0 case at 3.06 GHz, it to a single slot case at the same frequency, it can be noticed that in the single slot case there is a single peak at the centre compared to a shifted peak in the, which demonstrates the effects of the parasitic slot. Finally, Table 4.2 illustrates a comparison between the measured and simulated central operating frequencies, impedance bandwidths and gains. In both case, there is a close agreement between the impedance bandwidths, and a slight shift in the central frequencies for the slot-0 case. The gains are recorded using the main beam of the pattern.

Table 4.2 Simulated and Measured Results Comparison

Comparison	Slot-0		Slot+6	
	Simulated	Measured	Simulated	Measured
Central Frequency (GHz)	3.2	3.06	4.667	3.8
Impedance Bandwidth %	32.58	32.6	25.1	19.76
Gain	1.36	3.9	5.49	5.3

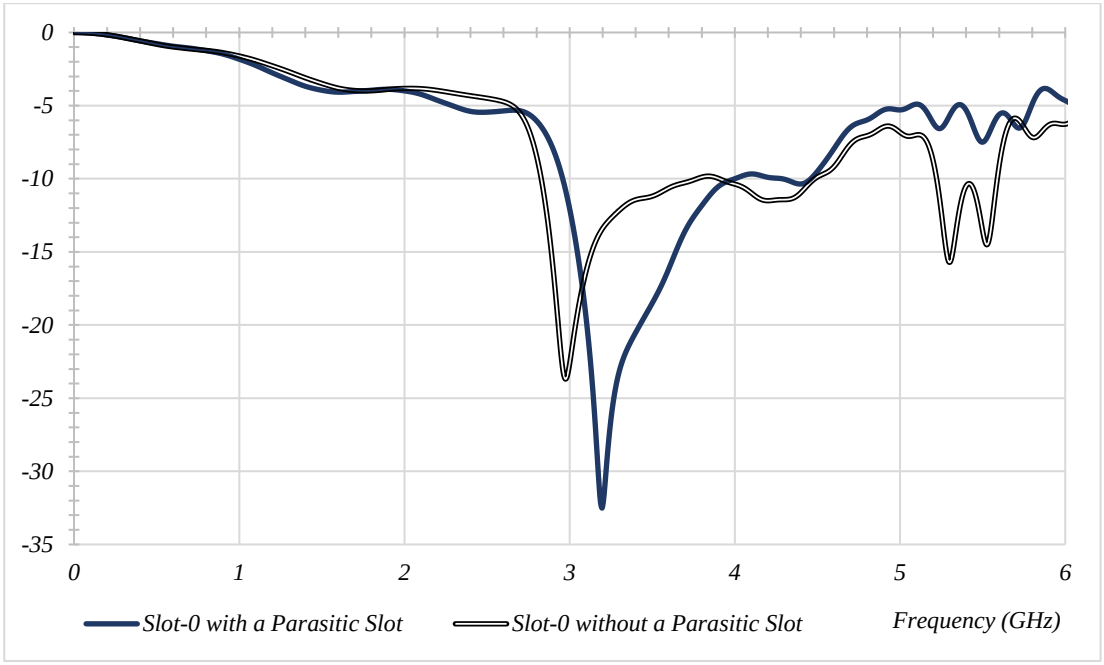

(a) Slot-0

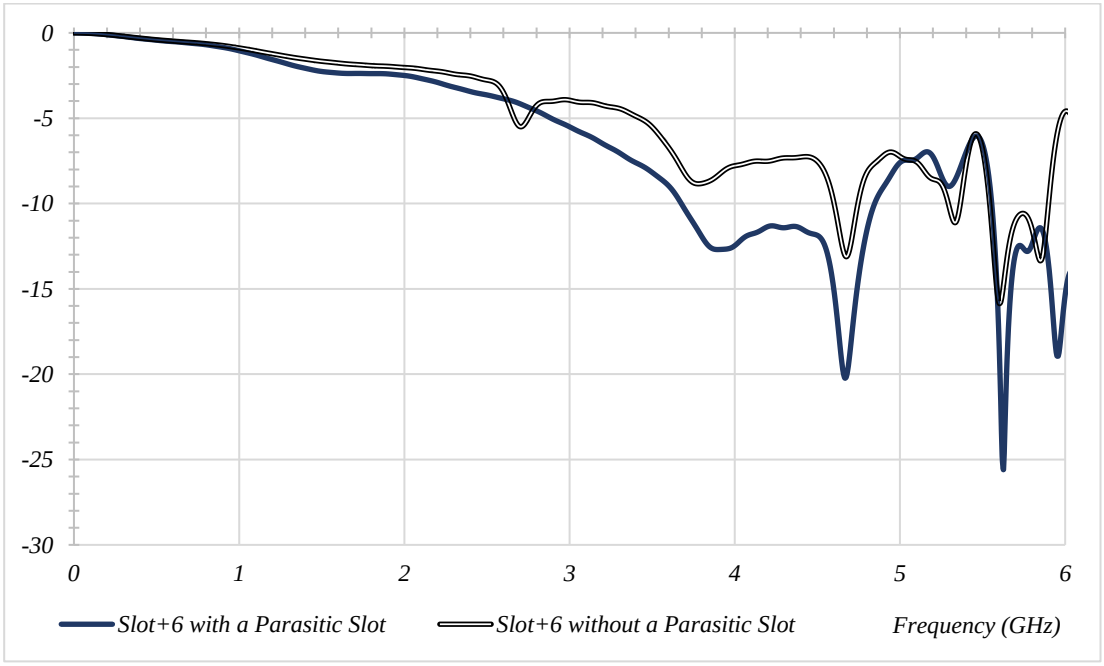

(b) Slot+6

Figure 4.8 Reflection Coefficients for Aperture Coupled DRA with and without a Parasitic Slot

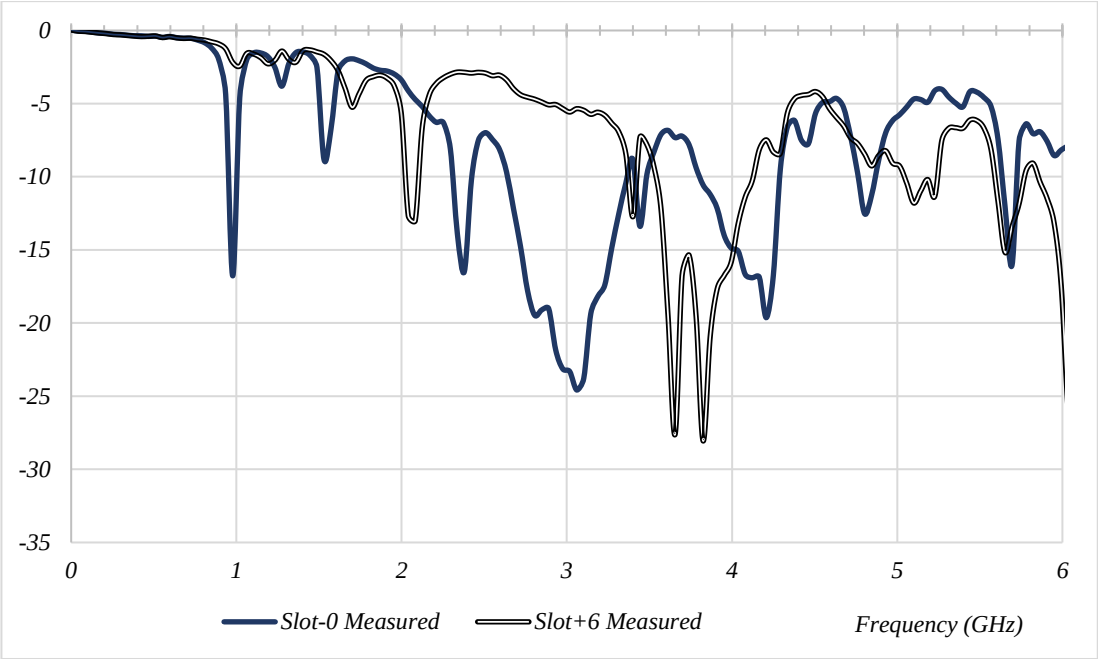

(a) Measured Results

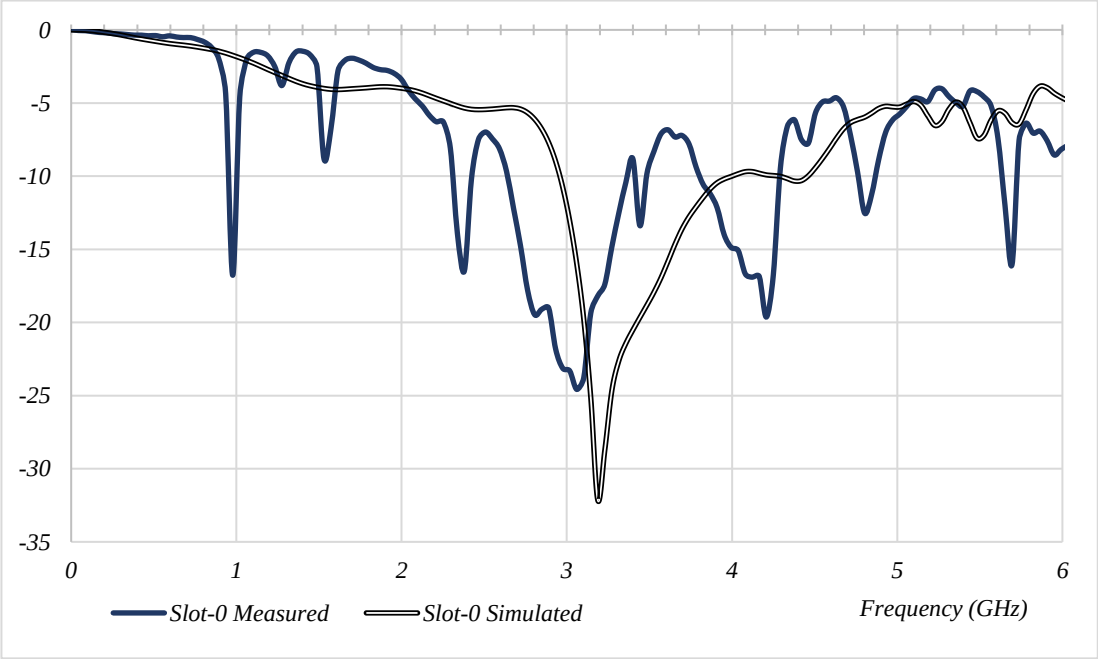

(b) Slot-0 is Active and Slot+6 is Shorted

Figure 4.9 Measured and simulated reflection coefficients of a dual-slot fed RDRA

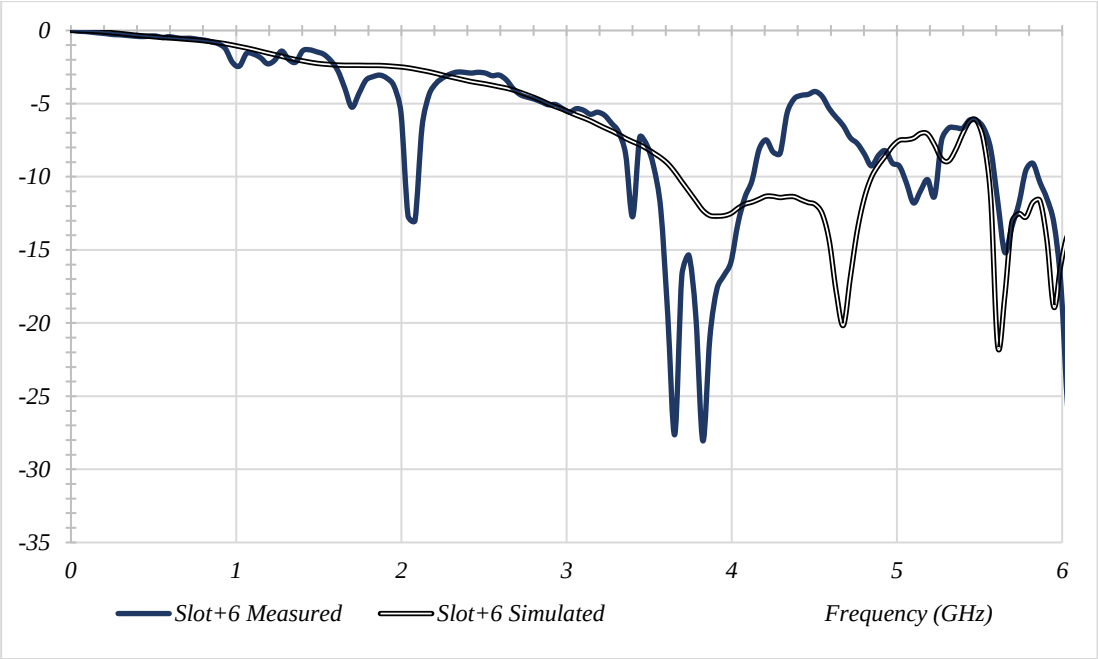

(c) Slot+6 is Active and Slot-0 is Shorted

Figure 4.9 Continued

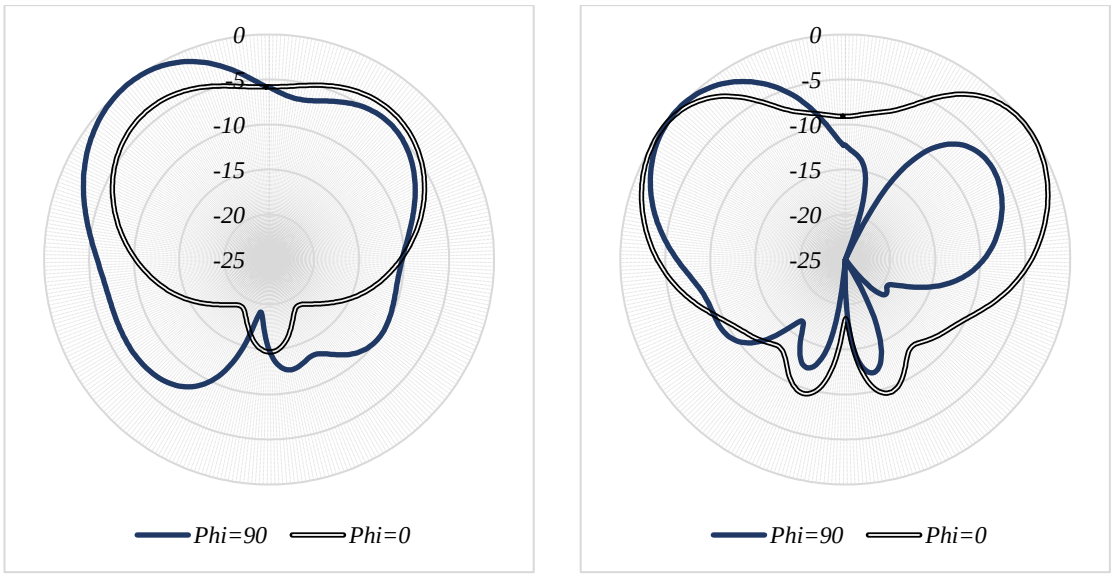

(a) Normalised Simulated Radiation Patterns at 3.06 GHz for Slot-0 (left) and 3.8 GHz for Slot+6 (right)

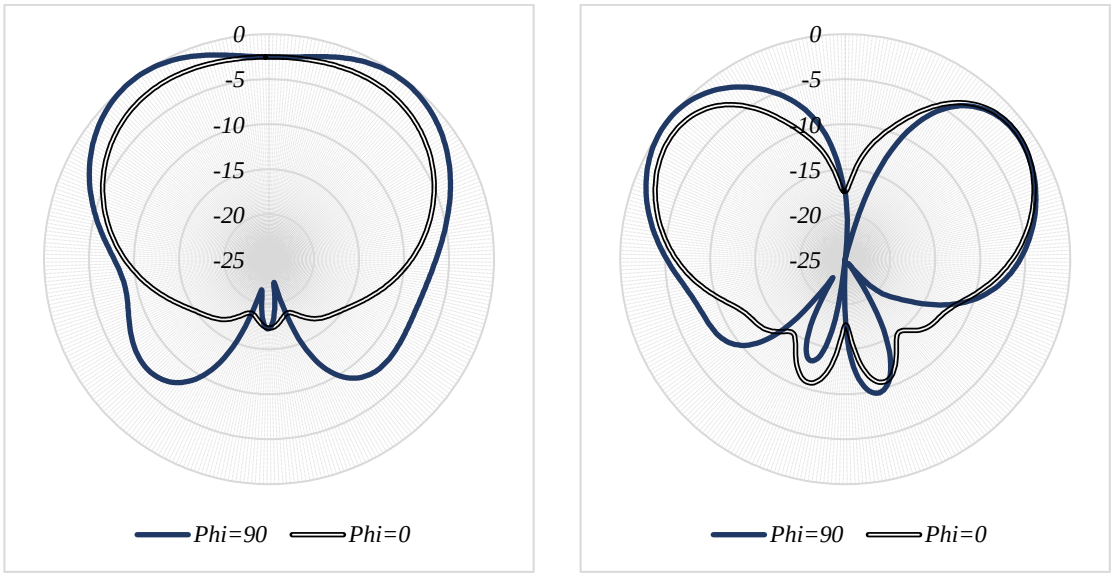

(b) Normalised Simulated Radiation Patterns for the Single Slot Case located at Slot-0 position (left) and at 3.8 GHz for the position Slot+6 (right)

Figure 4.10 Simulated Radiation Patterns for a Dual-Slot Fed RDRA vs Single Slot Fed RDRA Case

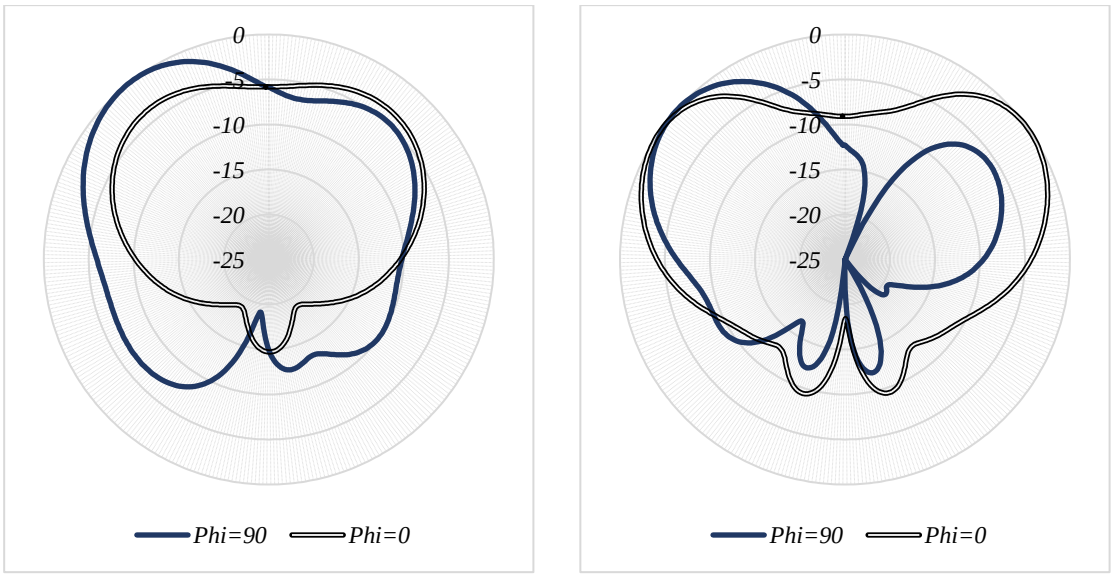

(a) Normalised Simulated Radiation Patterns at 3.06 GHz for Slot-0 (left) and 3.8 GHz for Slot+6 (right)

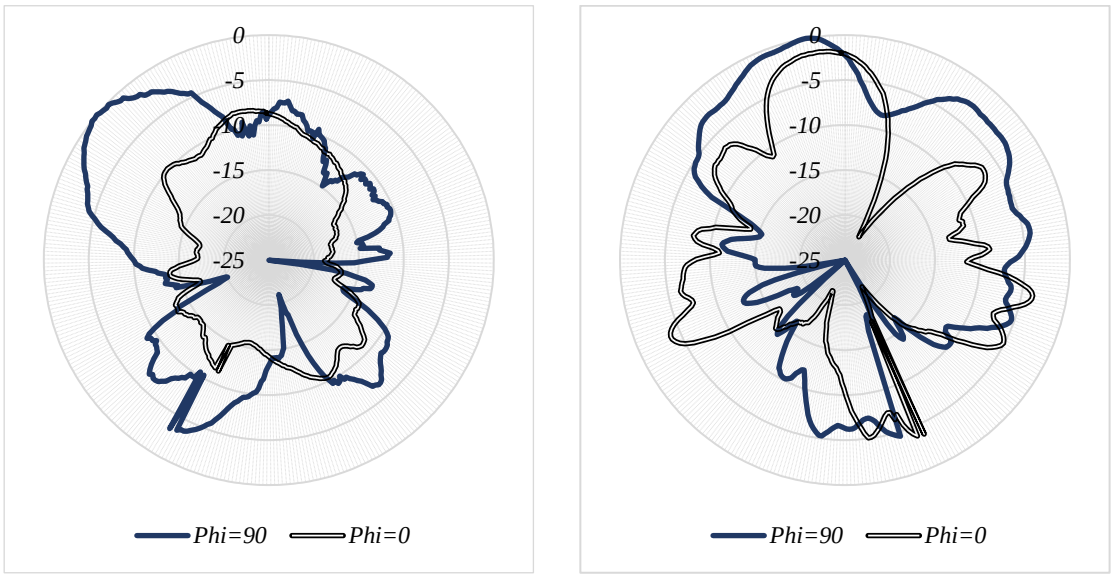

(b) Normalised Measured Radiation Patterns for Patterns for 3.06 GHz for Slot-0 (left) and 3.8 GHz for Slot+6 (right)

Figure 4.11 Radiation Patterns of a Dual-Slot Fed RDRA Simulated vs Measured

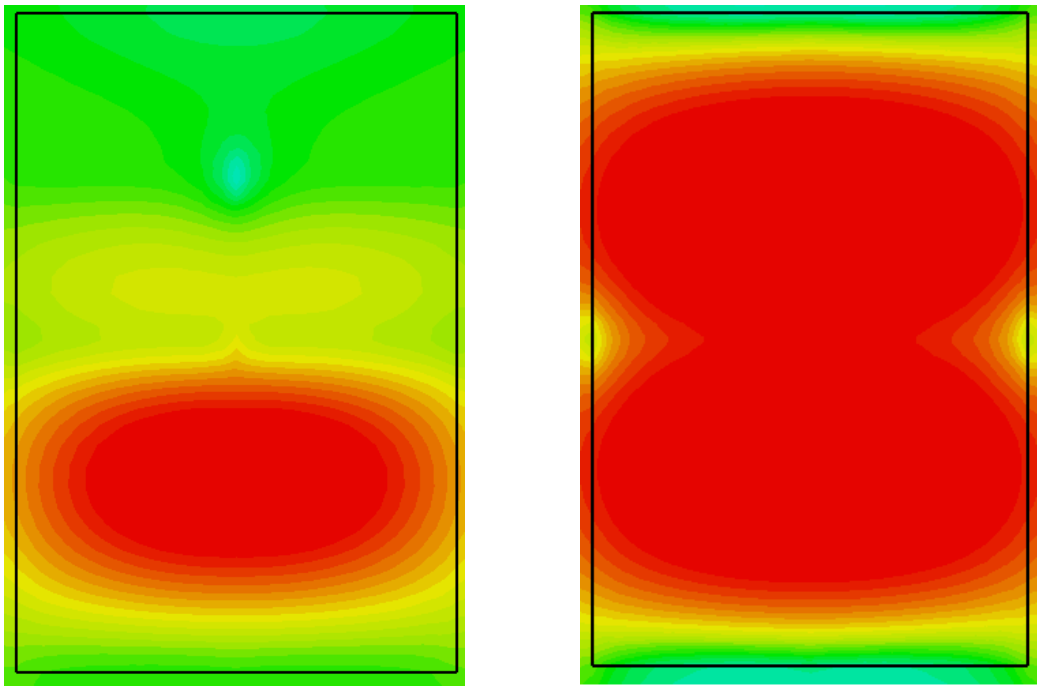

(a)

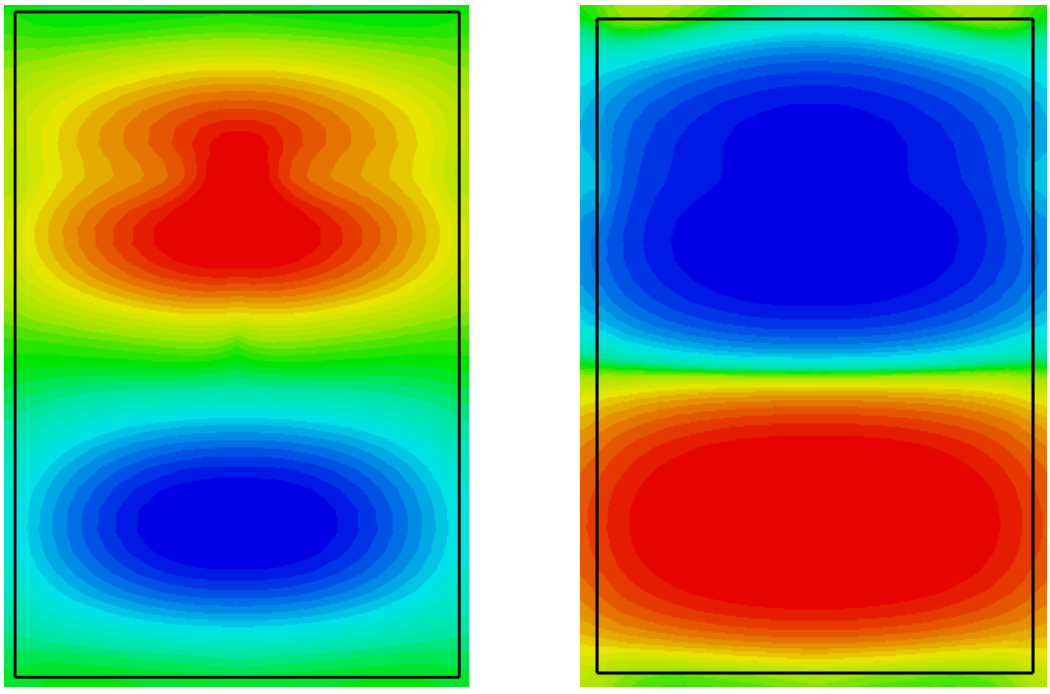

(b)

Figure 4.12 H-Field Distribution Above the Tunnel Air Gap Level (a) for Slot-0 at 3.06 GHz for 2-Slots case (Left) and Single Slot Case (Right), and (b) for Slot+6 at 3.8 GHz for 2-Slots case (Left) and Single Slot Case (Left)

4.4.2 Reconfigurable Triple-Slot Fed RDRA

This is a more complicated configuration as it is a challenging task to keep the same feeding dimensions for the three slots without compromising the impedance matching bandwidth for each case. In addition, distortion due to the exposed areas from the parasitic slots deteriorates the interference efficiency. This means, if the DRA used in the single slot case to be used in the triple-slot configuration, the overall exposed area of the two inactive slots is 16 mm^2 compared to a lower DRA face area of 96 mm^2. Furthermore, considering the 8 mm^2 area of the active slot as well as the area of the imperfect conducting PIN diodes the shielded ground plane area is reduced by ~20% compared to the single slot case. However, this limitation can be minimized by using a larger DRA dimensions, which results in the excitation of higher order modes. In addition, it has been noticed that the antenna reconfiguration response can be improved by reducing the ground plane gaps to 0.1 mm.

The proposed final design is illustrated in Figure 4.13, which consists of three slots, Slot-0 at the centre of the DRA, Slot-6 shifted 6 mm closer to the feed point, and Slot+6 that is shifted 6 mm towards the other DRA end. The size of all the slots is 1.2×16 mm^2, with a PIN diode at the centre of each slot. Once more, 0.1 mm wide gaps that are parallel to the slots have been incorporated to support the diodes' DC biasing. The microstrip line has a width of w = 1.2 mm, and a stub length of s = 14 mm.

Using CST Studio simulation, the reflection coefficients are illustrated in Figure 4.14, in which Slot-0 and Slot-6 excite the $TE_{\delta 11}$ mode and Slot+6 excites the $TE_{\delta 21}$ mode. Furthermore, Slot-6 excites two additional modes; $TE_{\delta 31}$ and $TE_{\delta 13}$ that have respective resonance frequencies of 4.51 GHz and 4.78 GHz. Slot-0 coupling results illustrates two main bands; the first has a central frequency at ~3 GHz and the second at 4.48 GHz, with

respective impedance bandwidths of 10.8 % and 11.9 %. The first band is associated with the $TE_{\delta 11}$ mode, while the second can be associated with the $TE_{\delta 21}$ mode, although the H-field distribution for the second case shows some deformation due to the two parasitic slots and the proximity to the $TE_{\delta 31}$ and $TE_{\delta 13}$ modes resonance frequencies. The distortion pattern has been noticed also in all the frequencies around this band in the other slots excitation cases. In addition, another band exists at a central frequency of 6.23 GHz and field distribution of $TE_{\delta 41}$ mode. The last two cases show that it is possible to generate even TE modes with centre slot excitation when parasitic slots are presented. However, these generated modes will always suffer from deformation due to the same parasitic slots.

When the DRA is excited using Slot-6, an impedance bandwidth of 5.8% has been achieved with a centre frequency of ~2.5 GHz that corresponds to the $TE_{\delta 11}$ mode. However, the field distribution shows some distortion in the centre field peak. In addition, a second impedance matching bandwidth of 7.1% is achieved with a centre frequency of 4.4 GHz that corresponds to the $TE_{\delta 31}$ mode, but also with some distortion in the modal field distribution. Finally, exciting the DRA using Slot+6 provides an impedance bandwidth of ~12% at a centre frequency at 4.1 GHz, which is close to that of the $TE_{\delta 21}$ mode, and a second narrow bandwidth of 2% around 5.7 GHz, which indicates the excitation of the higher order $TE_{\delta 23}$ mode. Figure 4.15 illustrate the radiation pattern at the central frequency of each case. It can be noticed that in some cases the radiation pattern returns a negative gain in the H-plane (Phi=0), but the E-plane (Phi=90) returns a higher gain with a shifted main beam to 64°. This is a result of the effect of the parasitic slots, which act as weak feeding due to the imperfect PIN diodes isolation. In addition, a stronger back-lobes can be observed that can be attributed to the exposed DRA sections owing to the presence of two partially short circuited slots in each case. Figure 4.16

illustrates the H-field distributions at the central frequencies for every band discussed in this section. The field distributions agree with the defined modes. In addition, these results show the disturbances in fields' distribution which causes the distortion in the E-plane radiation patterns.

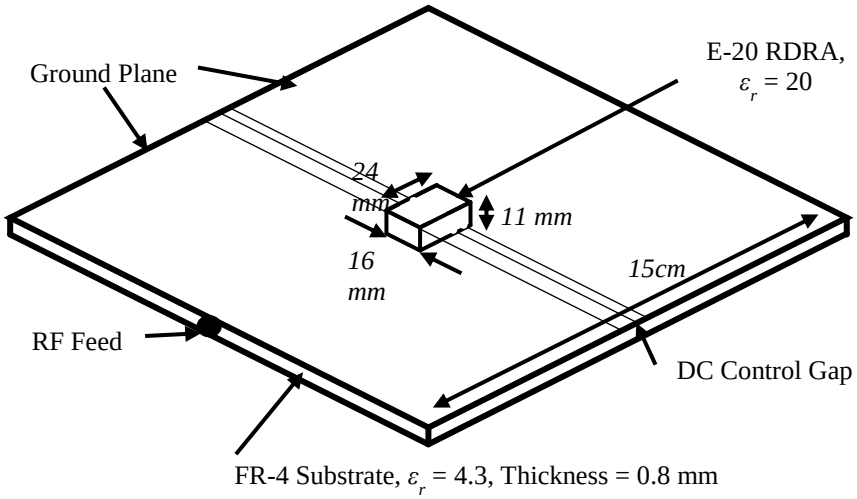

(a) General View

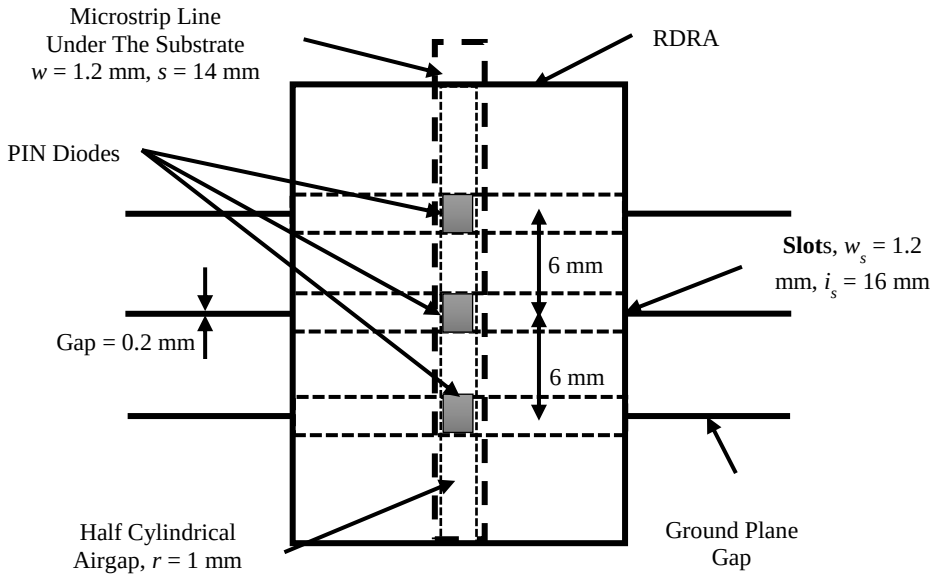

(b) DRA and Slots Area

Figure 4.13 Reconfigurable Three Slots Coupled RDRA

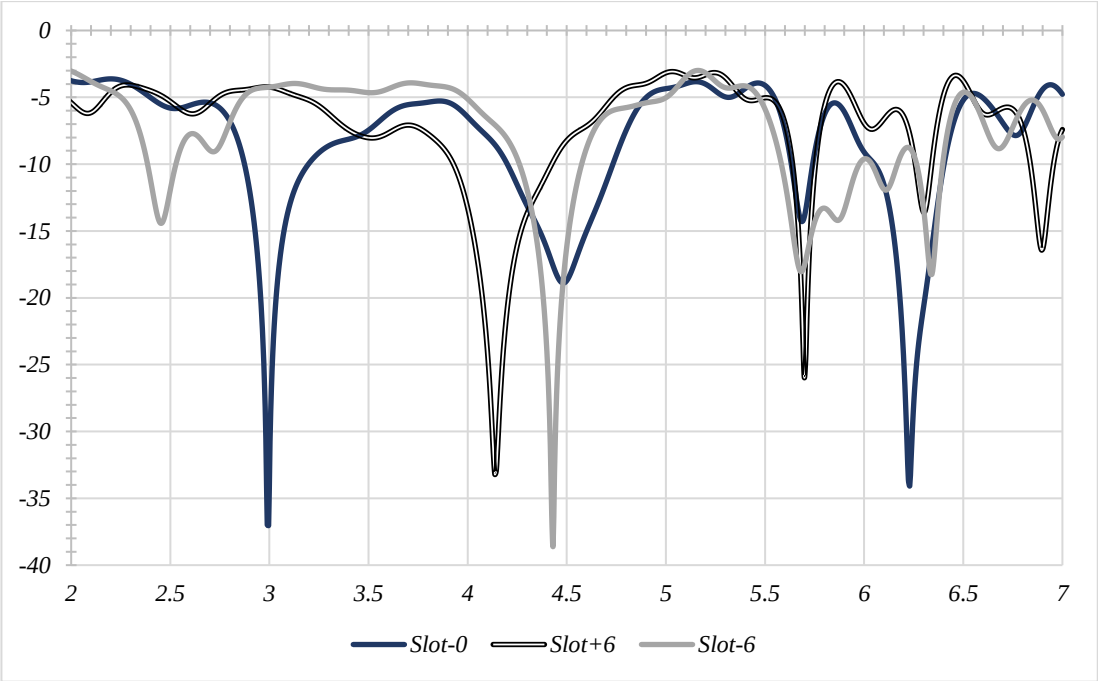

(a) Reflection Coefficients with parasitic Slots

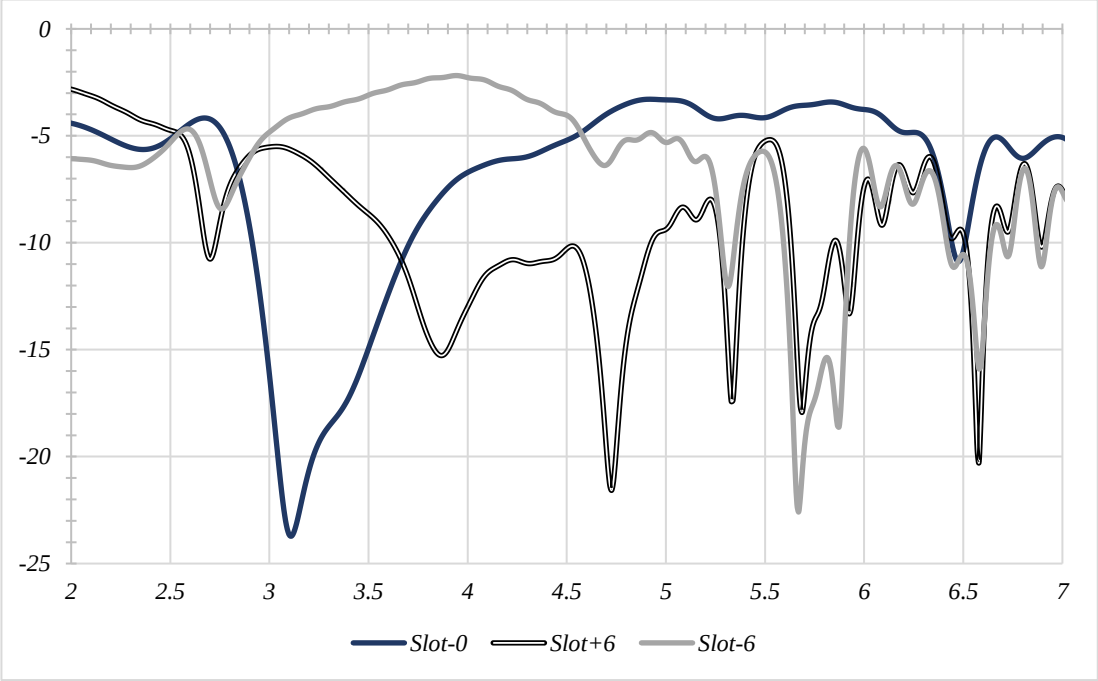

(b) Reflection Coefficients without parasitic Slots

Figure 4.14 Reflection Coefficients for the Reconfigurable Three Slots Coupled RDRA Compared to Single Slot Fed RDRA with the Same Position of the Active Slot

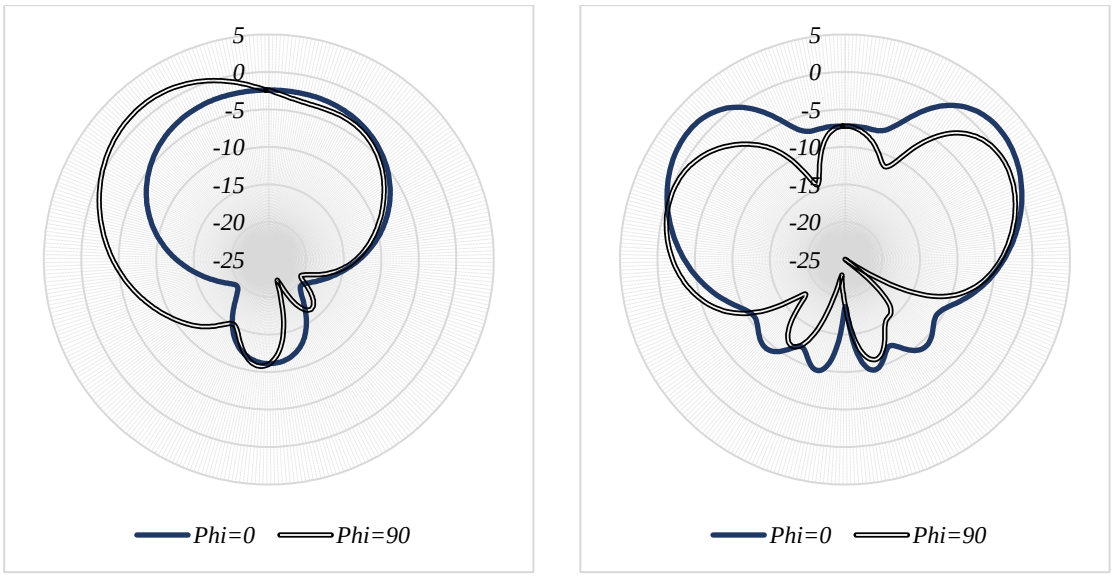

(a)

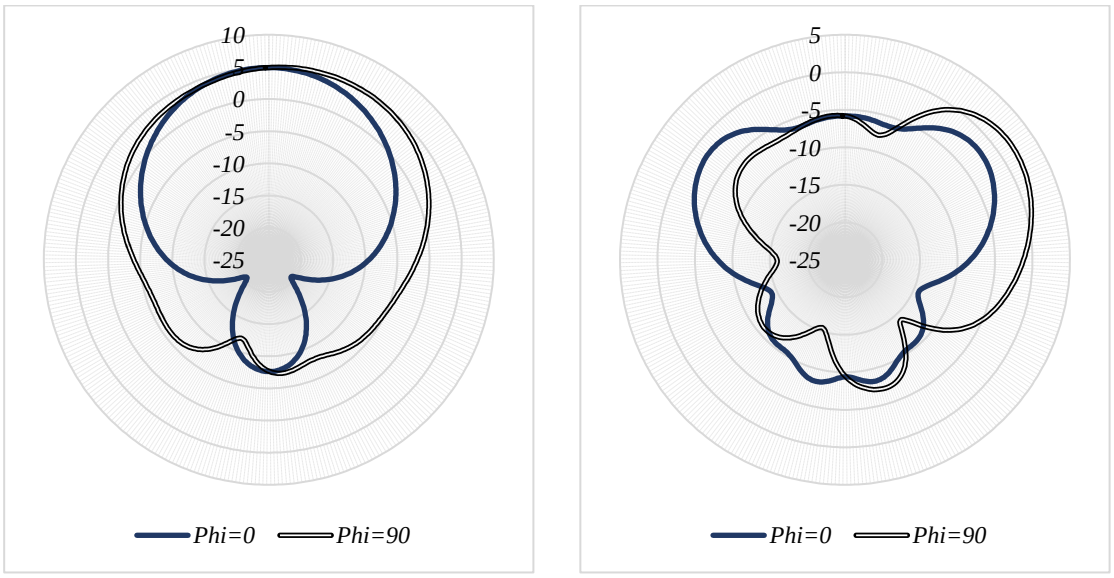

(b)

Figure 4.15 Simulated Radiation Patterns for Reconfigurable Three Slots Coupled RDRA for (a) Slot-0 at 3 GHz (Left) and 4.48 GHz (Right), (b) Slot-6 at 2.5 GHz (Left) and 4.4 GHz (Right), and (c) Slot+6 at 4.4 GHz (Left) and 5.7 GHz (Right)

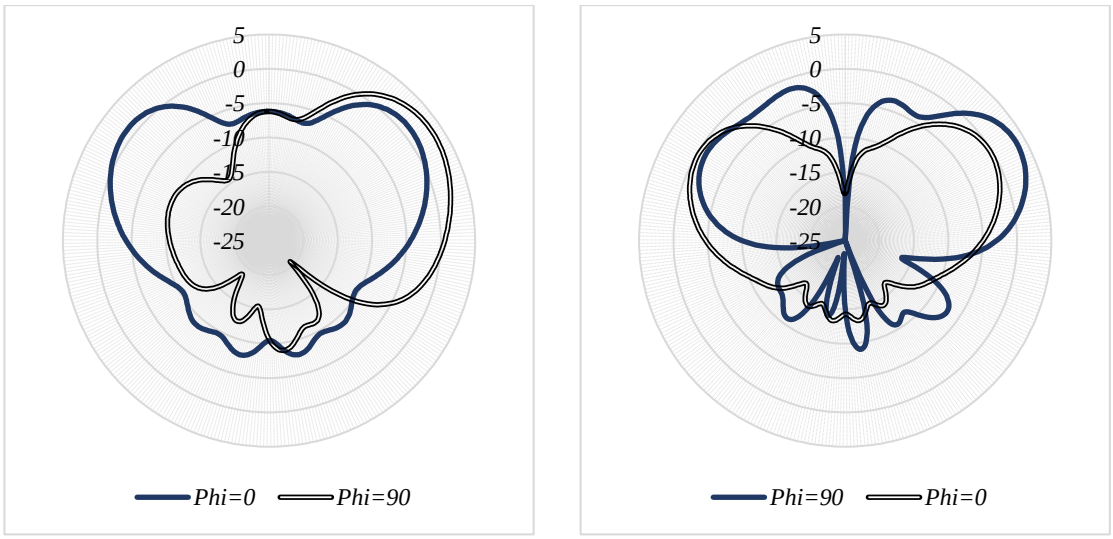

(c)

Figure 4.15 Continued

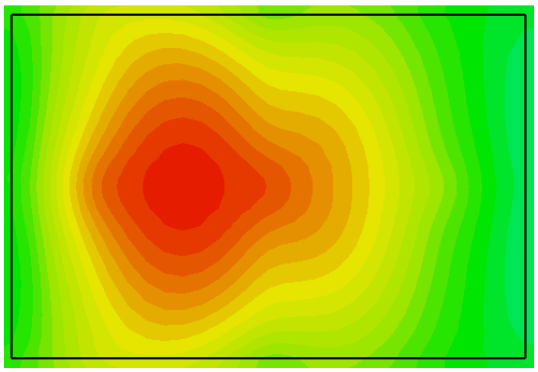

(a) H-Field Distribution for Slot-0 at 3.0 GHz ($TE_{\delta 11}$)

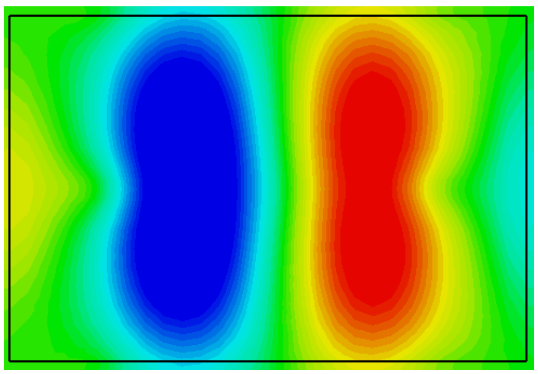

(b) H-Field Distribution for Slot-0 at 4.48 GHz ($TE_{\delta 21}$)

Figure 4.16 Expected H-Field Distributions

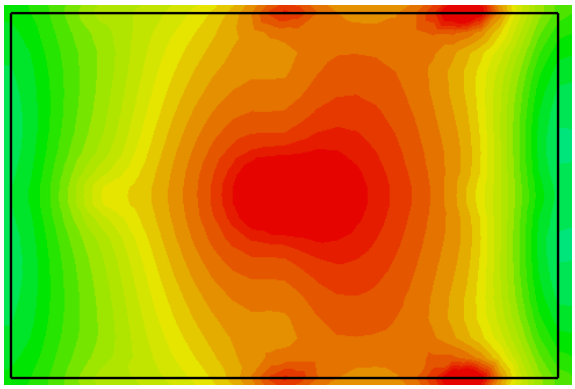

(c) H-Field Distribution for Slot-6 at 2.5 GHz ($TE_{\delta 11}$)

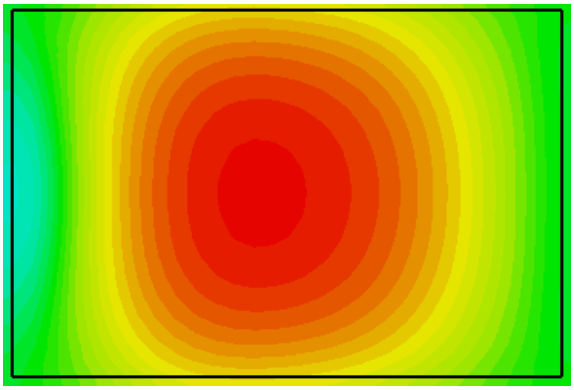

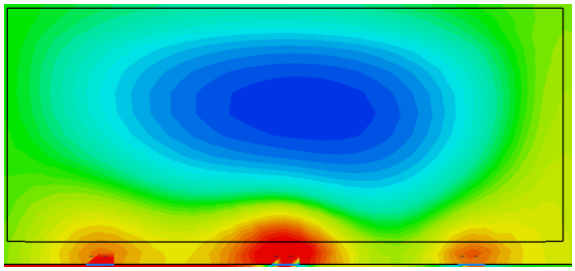

(d) H-Field Distribution parallel to *xy* plane (Above) and *yz* plane (Below) for Slot-6 at 4.43 GHz ($TE_{\delta 13}$)

Figure 4.16 Continued

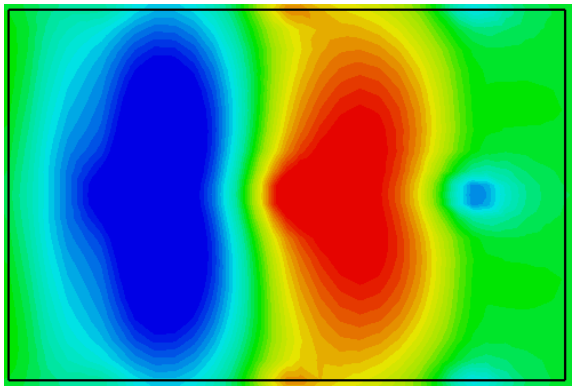

(c) H-Field Distribution for Slot+6 at 4.1 GHz ($TE_{\delta 21}$)

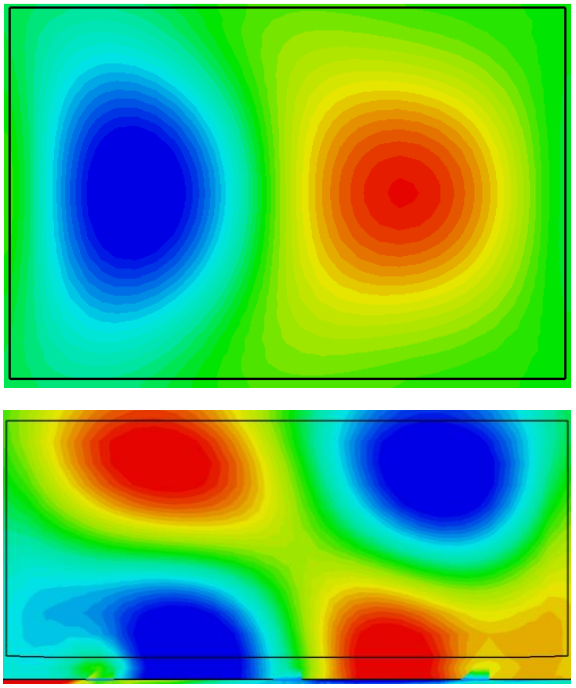

(d) H-Field Distribution parallel to *xy* plane (Above) and *yz* plane (Below) for Slot+6 at 5.7 GHz ($TE_{\delta 23}$)

Figure 4.16 Continued

4.5 Conclusions

In this chapter, the possibility of controlling the operation band and the excited TE mode of the RDRA has been investigated. The first step was to implement a simple switch ON/OFF DRA antenna by using a PIN diode to open / short the coupling slot aperture. While the concept was proven, a few issues have been raised during the building and measurements process. The first is the insertion of the PIN diode inside the substrate, which adds an airgap to the configuration in addition to the distortion of the waves and current inside the slot. The second issue is concerned with the achieved impedance bandwidth, especially the offset microstrip line feed. During the measurements, it has been noticed that using a PIN diode placed at the slot's centre is insufficient for the total elimination of the active band. Therefore, another PIN diode has been added, hence, an additional drilled hole with further field disturbance. The third issue is concerned with the use of the correct PIN diode type. According to the data sheets, the used device works properly up to 6 GHz [6], and although two PIN diodes have successfully been eliminated, the bands at a frequency of more than 6.5 GHz require an extra DC current supply to be provided.

In order to avoid the problems occurred during the first model testing, a physically larger DRA has been employed for the multiple-slot DRA configurations with every dimension doubled to halve the operating frequency. In addition, a shallow notch has been created at the DRA bottom side to accommodate the PIN diodes, hence avoiding any disturbances to the substrate and the slot area. These solutions proved to improve the expected results and performance. On the other hand, using a multiple aperture coupling technique with a single active slot leads to the issue of unideal shortening of the passive slots and the uncovered areas that affect the DRA-ground plane side interference and, hence, the antenna efficiency. Furthermore, it has been observed that the more apertures used, the more difficult it becomes to control all the slots using a single feed. Finally, despite all

the issues that faced the research in this direction, it is safe to say that this technique is viable, and can lead to excellent results of a frequency reconfigurable dielectric resonator antenna, with the measured results demonstrate reasonable agreement with simulations.

References

[1] K. M. Luk and K. W. Leung, Dielectric resonator antennas: Research Studies Press, 2003.

[2] A. Petosa, Dielectric Resonator Antenna Handbook: Artech House, 2007.

[3] R. S. Yaduvanshi and H. Parthasarathy, Rectangular Dielectric Resonator Antennas: Theory and Design: Springer India, 2015.

[4] D. M. Pozar, "Microstrip antennas," Proceedings of the IEEE, vol. 80, pp. 79-91, 1992.

[5] T-Ceram, "http://t-ceram.com/dielectric-resonators.htm."

[6] "http://www.infineon.com/dgdl/Infineon-BAR50SERIES-DS-v01_01-en.pdf?fileId=db3a304314dca3890114fea7dd410a92."

[7] G. P. Junker, A. A. Kishk, A. W. Glisson, and D. Kajfez, "Effect of fabrication imperfections for ground-plane-backed dielectric-resonator antennas," IEEE Antennas and Propagation Magazine, vol. 37, pp. 40-47, 1995.

[8] K. Y. Chow, K. W. Leung, K. M. Luk, and E. K. N. Yung, "Input impedance of the slot-fed dielectric resonator antenna with/without a backing cavity," IEEE Transactions on Antennas and Propagation, vol. 49, pp. 307-309, 2001.

Chapter Five

DRA Linear Arrays Reconfigurability

5.1 Introduction

Dielectric resonator antenna arrays have been reported as early as 1981 [1]. Since then, numerous studies have been published in this topic including research on linear arrays to enhance the radiation pattern and gain, or arrays arranged to generate circular polarisation [2, 3]. In this Chapter, the focus is to study the linear arrays' reconfigurability, and the challenges that accompany the design process, especially with managing the impedance matching and bandwidth as well as radiation pattern. It is expected that the most affected characteristic is the radiation pattern in terms of the beam width and main lobe direction. However, owing to mutual coupling, a shift in the operation frequency is expected.

5.2 Reconfigurable DRA Arrays Designs

In line with other array types, the DRA array radiation depends on the parameters mentioned earlier in this chapter. A couple of configurations will be investigated in this chapter; two and four element parallel fed DRA arrays. In both cases, the elements are uniformly excited when all of them are activated and uniformly spaced in the case of a four-element array. The investigated designs are based on those presented in Chapter 4. This includes the single slot and dual slots configurations.

5.2.1 Two Elements Array

Figure 5.1 (a) illustrates a two-element parallel array of microstrip line slot–fed DRAs. As explained earlier, each element is fed through a switchable rectangular slot aperture, and each slot is switchable separately. This configuration provides four operation

scenarios; a standard array of two active elements, two cases with only one element is active, and finally a case when the two antennas are switched off, which can be excluded but included for comparison purposes. These cases will be denoted as: 2-DRA Array, Left DRA, Right DRA, Array-OFF.

In theory, the 2-DRA Array case can be classified as a uniform 2-element DRA array. On the other hand, Left DRA and Right DRA cases can be analysed firstly by assuming the turned OFF element to act as a totally non-radiating parasitic dielectric element. Secondly, the switched OFF element is excited with a finite amplitude but with a uniform phase since in real cases the PIN diodes mostly operate as attenuators i.e. $A_1 \neq A_2 \neq 0$, alongside the assumption of ignorable mutual coupling. Finally, mutual coupling is to be considered for a more accurate array factor and total radiation pattern estimation.

The dimensions of each element are based on the design of the reconfigurable single slot fed RDRA investigated in Chapter 4, i.e. 12×8×5.5 mm^3, with ε_r = 20. Each element is coupled with a centrally located rectangular slot aperture of 8 mm length and 1 mm. The used FR-4 substrate has a thickness of 1.6 mm and an area of 15×15 cm^2. The microstrip line is 2.4 mm wide and connected to the RF source from one end and divided into two 1.2 mm branches as shown in Figure 5.1 (a) with each branch centrally feed a single DRA element using a stub length of s = 7 mm. In order to accommodate the DC supply for both PIN diodes, two gaps have been inserted in the ground plane as illustrated in Figure 5.4 (a). A separation distance of $\lambda_g/2$ has been use in order to minimise the mutual coupling [2].

An initial design has been proposed with separation distance of 17 mm. A conventional 2-DRA array has been simulated first and then compared with a reconfigurable model that contains both ground plane DC gaps and PIN diodes equivalent models. The resulted

comparison shown a major change in reflection coefficients and reduction in the gains at the assumed central frequency at 4.3 GHz as shown in Figure 5.1 (b-c). This can be associated with the effect of both the PIN diodes and the parasitic gaps [4]. Hence, it has been suggested to change the separation distance to accommodate the these effects. CST Microwave Studio have been used to find the required dimensions for an efficient design to reach better reconfiguration properties with good radiation efficiency. This change will affect the remaining three reconfigurable designs.

A parameter sweep has been carried out using CST Microwave Studio to improve the total efficiency and gain, and the results suggest an optimum separation distance of ~30 mm, with a central frequency of 5.63 GHz. However, the best total efficiency has been around 5.7 GHz. This is different from the initial suggested operating frequency of 4.3 GHz. Figure 5.1 (d) presents the simulated reflection coefficients for the four cases, where it can be observed that the fully operational 2-DRA array offers the best performance with a central frequency at 5.6 GHz and impedance bandwidth of 11.6% compared to a single DRA operating frequency and bandwidth of 5.64 GHz, 8%, respectively. It should be noted that the central frequency of 5.6 GHz corresponds to that of the $TE_{\delta 11}$ resonance mode. On the other hand, the Left DRA and Right DRA cases offer a slightly lower impedance matching bandwidth of 8.8%in conjunction with a marginal shift in the central frequency to 5.73 GHz. Finally, the Array-OFF case shows almost no impedance bandwidth as expected, with a low total efficiency and gain. Figure 5.1 (e) shows the H-plane radiation patterns for the four cases at 5.7 GHz. These results demonstrate that the antenna can be used as a basic reconfigurable beam direction antenna since the beam is steered in the active element direction, with a beam steering range of ±15°. Although this range is small, it can be useful for minor direction tuning applications. In addition, since this design is only preliminary, further optimisation can lead to a wider steering angle.

While the 2-DRA Array offers a broadside gain of 4.83 dBi, activating a single DRAprovides a steered beam with a gain of 3.14 dBi at 5.7 GHz. However, the maximum gain is 3.94 dBi at θ=53° and φ=250°,290°, which is a steering of ±20 away from φ=270° plane. This is can be attributed to the presence of the PIN diode in the deactivated element that is far from an ideal short circuit and also affect the excitation phase, which results in a nonuniform excitation in both amplitude and phase. In addition, it is expcted that the impedance balance from the feed point is affected, which alters the current disribution. Moreover, the effect of the mutual coupling radiation can effect radiation patterncharacteristics. On the other hand, the Aray-OFF case shows a low gain of -0.9 dBi, with the main lobe direction at 0°.

Table 5.1 presents a summary of the radiation characteristics for the considered array configurations when each DRA element is fed using a single slot. It should be noticed that the low total efficiencies are due to the fact this design has been considered as an initial design to prove the concept, and it must not be considered as a final design for practical considerations. The total efficiency can be improved by applying changing to the microstrip line. This criterion is a reoccurring fact in the following designs.

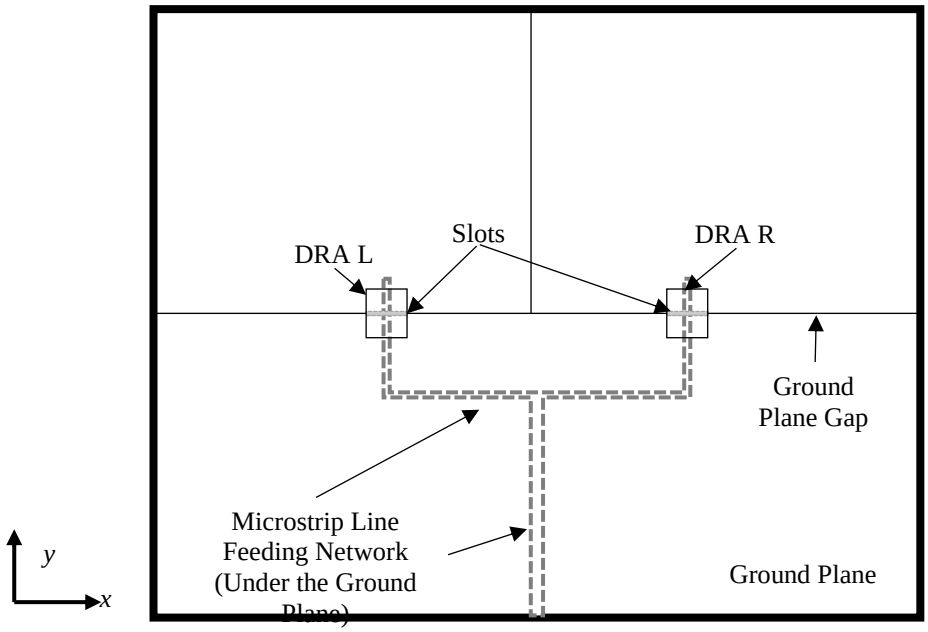

(a)

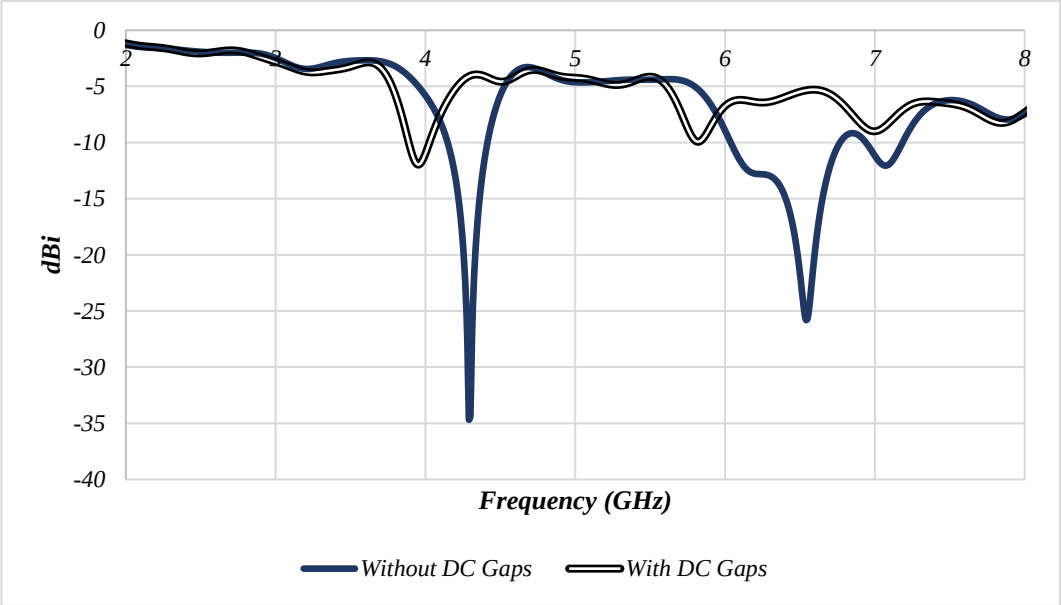

(b)

Figure 5.1 Reconfigurable Single Slot Fed 2-DRA Array (a) Antenna Diagram (Top View), (b) Reflection Coefficients for the initial design, and (c) Radiation Patterns for the initial design at 4.3 GHz, (d) Reflection Coefficients the final design, and (e) Radiation Patterns at 5.6 GHz

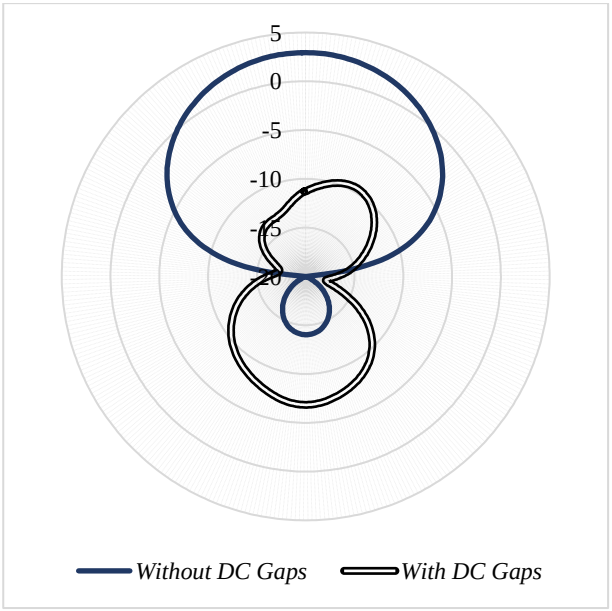

(c)

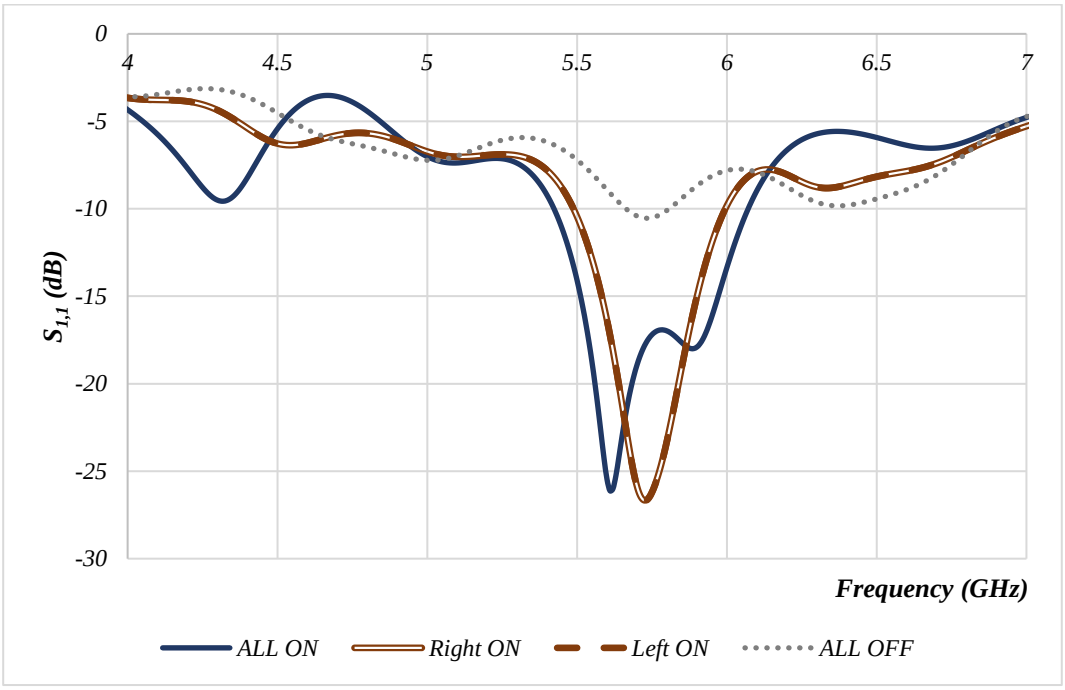

(d)

Figure 5.1 Continued

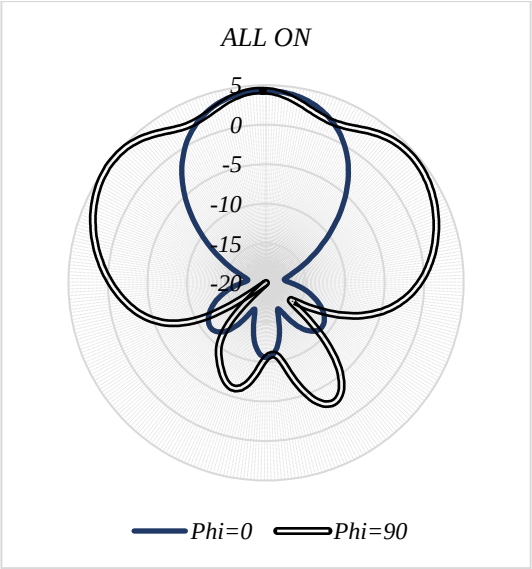

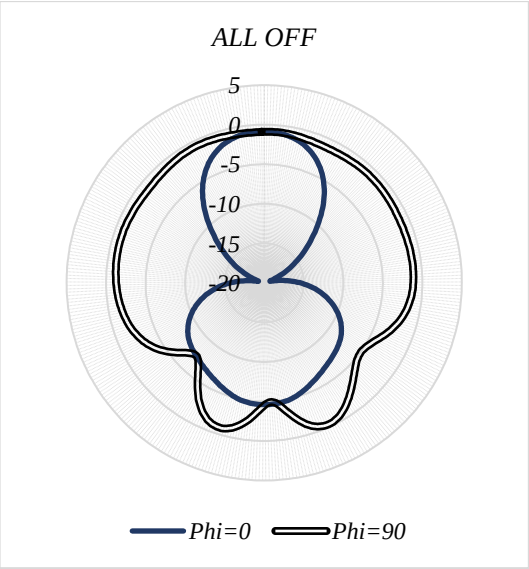

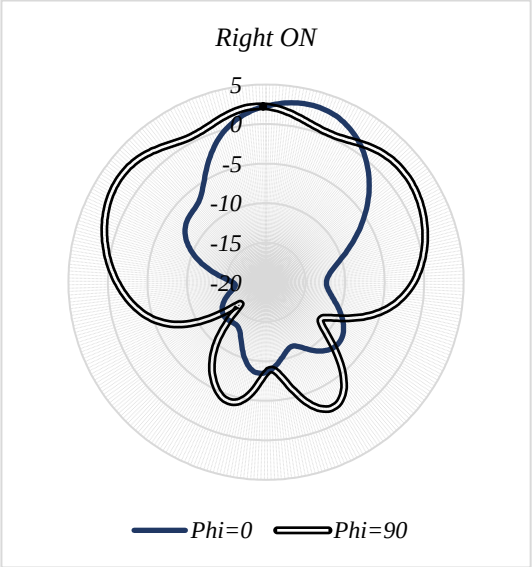

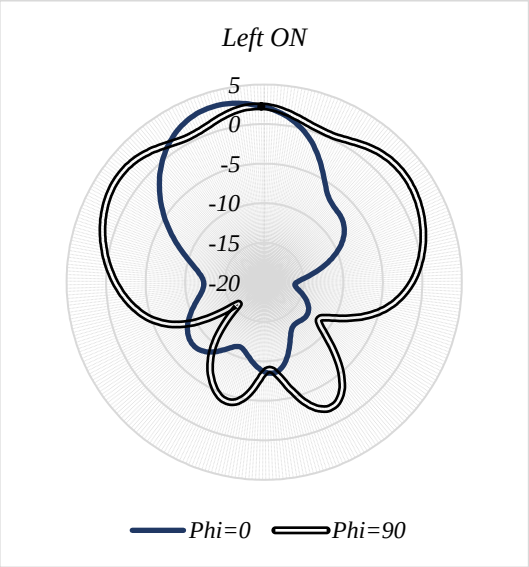

(e)

Figure 5.1 Continued

Table 5.1 Reconfigurable Single Slot Fed 2-DRA Array Characteristics with Radiation Pattern Characteristics at 5.7 GHz

Characteristics	2-DRA Array	Right DRA	Left DRA	Array-OFF
Operating Frequency	5.61	5.73	5.73	5.73
Impedance Bandwidth %	11.6	8.8	8.8	2.5
Angular Beamwidth at φ=0°	50.9°	51.8°	51.8°	53°
Main Beam Direction at φ=0°	0°	15°	-15°	0°
Total Efficiency %	57.7	52.1	52.1	32.6
Maximum Gain (dBi)	4.83	3.94	3.94	-0.91
Maximum Gain (dBi) (θ, φ)	51°, 270°	52°, 290°	52°, 250°	0°, 0°

Next, the dual-slot coupled DRA suggested in Chapter 4 is employed in the two-element array as shown in Figure 5.2 (a). In theory, this configuration offer 16 possible scenarios. However, since each element will be fed by a single slot, two cases are excluded. Analysing these combinations can be more sophisticated compared to the previous prototype, since the extra parasitic slots make the perfect short circuit a less valid assumption. On top of that, it is fair to expect that the mutual coupling will be effected by these parasitic slots. Figure 5.2 (b) presents a range of reflection coefficients for the valid cases. Each case has been denoted according to the active slots with respect to their activated elements, with *R* and *L* denote the right and left DRAs, respectively, (0) for the central slot, (6) for the off-centre slot6, and *n* for the non-activated DRA. For example, *R*0*L*0 represents the case when both right and left DRAs are excited with their respective Slot-0, *R*6*L*0 refers to the case when the right DRA is excited using Slot+6 and the left DRA is fed using Slot-0, and *RnL*6 denote the case when both slots of the right DRA are

shorted while the left DRA is excited using Slot-6. Since only a single slot is to be activated, 8 combinations are to be examined for beam steering purposes.

Based on the original design presented in Chapter 4, a CST Microwave Studio model has been built for the proposed 2-DRA array. The DRA dimensions are 24×16×11 mm^3, with a 1 mm wide half cylindrical air tunnel in the centre of the lower face along the longest dimension. Dual identical slots are used with each DRA with the dimensions of 16×1.2 mm^2. The feed network consists of a 2.4 mm wide microstrip line that has been divided equally into two parallel 1.2 mm with branches each feed one DRA, with a stub of 11 mm beyond the DRA centre. The separation between the array elements has been chosen as 55 mm, which corresponds to 0.59 λ_0, 0.66 λ_0, and 0.90 λ_0, at 3.2 GHz, 3.6 GHz, and 4.9 GHz, respectively. This compare to the modes' resonance frequencies of 3.2 GHz, 3.8 GHz, and 4.7 GHz established in the model in Chapter 4. The increase in the separation distance is because of the doubling of the DRA dimensions, hence the decrease in the TE modes resonance frequency, thus the increase of the wavelength. Using the above dimensions, the eight cases listed in Table 5.2 have been simulated. Figure 5.2 (b) illustrates the reflection coefficients where it can be observed that three active bands stood out in the eight cases; the first is over a range of 3.0-3.3 GHz with an impedance matching bandwidth of 10 to 11.8%. It should be noted that the 3.2 GHz operating frequency corresponds to that of the $TE_{\delta 21}$ resonance mode. The second is around 3.6 GHz, with impedance matching bandwidth around 6%, which is again in line with that of the $TE_{\delta 21}$ mode field distribution characteristics. The third band has a shifted central frequency from 4.82-4.95 GHz, with a narrow impedance matching bandwidth of ~5%, which is in line with the $TE_{\delta 13}$ resonance mode. Compared to the single DRA, it can be observed that the gain and efficiency have been studied and the results at 3.2 GHz demonstrate maximum gains of 5.3-6.7 dBi, with a main beam direction shifted by 42°-44° from the

z-axis in the opposite direction to Slot+6, but with low efficiency around 55-60%, which is due to the fact that the design is less optimised for operating at this frequency. The radiation pattern at 3.6 GHz has a gain 4.3-4.8 dBi, with same maximum diversion direction at an angle range of θ=51°-54°. However, in his case the total efficiency rise to more than 90%. In the previous two frequencies, the radiation pattern does not steer more than ±2° from the *z*-axis in the φ=0° plane. On the other hand, provide more degree of steering in both θ and φ directions, as it can be noticed from Figure 5.2 (c-f) and Table 5.2. However, the gain range is low as 2.2-2.9 dBi, with a moderate total efficiency around 70%.

From the previous description and the listed results in Figure 5.5 and Table 5.2, it is clear that there is not too much space for reconfiguration for both the two bands, except for some minor band tuning and gain control. However, the third band shows a higher central frequency tuning, where the shift in the band is clear, and the beam steering agility is acceptable. Therefore, it offers a good prospect for design improvements in terms of central frequency tuning and beam steering agility. This can be improved by considering the spacing between the elements with respect to 4.9 GHz.

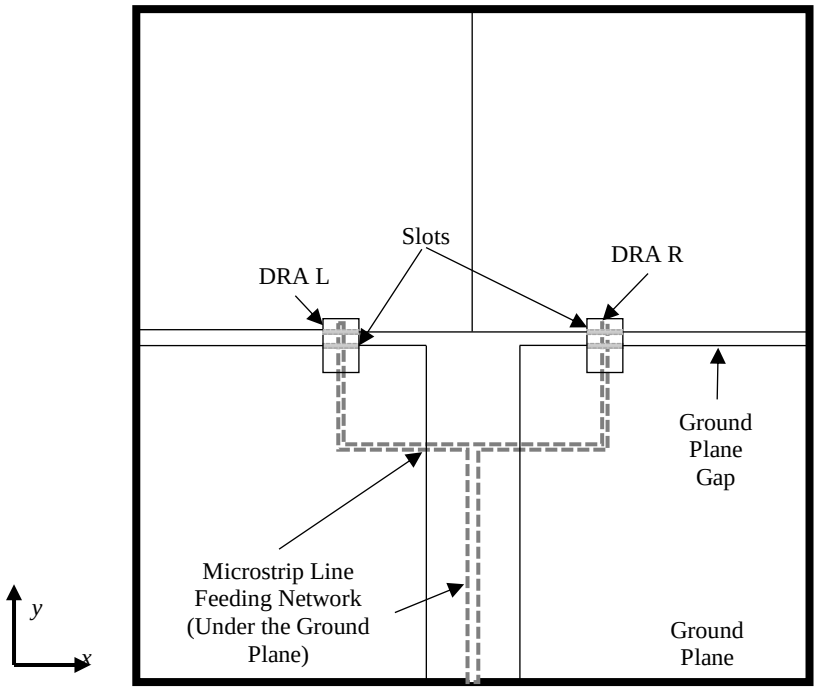

(a)

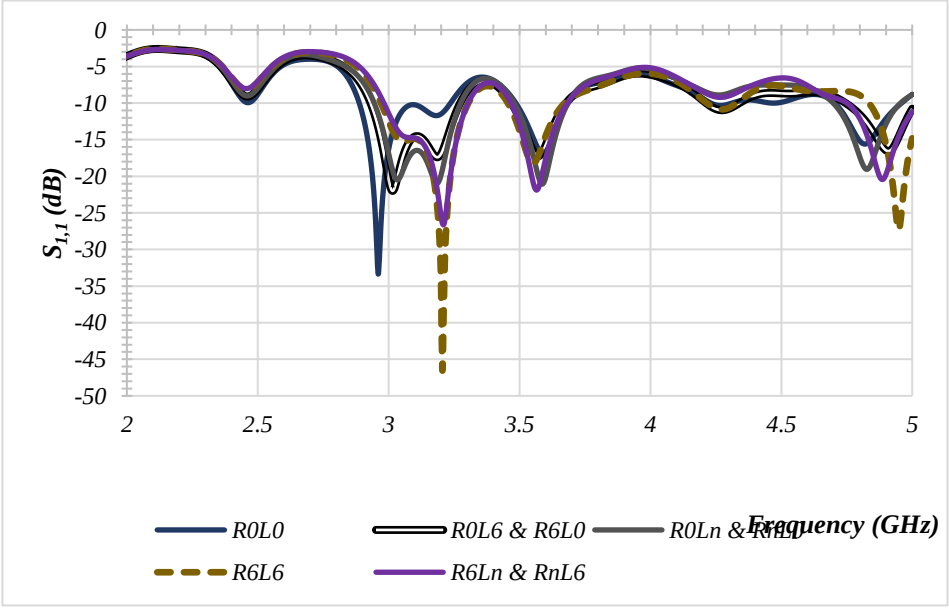

(b)

Figure 5.2 2-Slot 2-DRA Parallel Fed Array (a) Antenna Diagram, (b) Reflection Coefficients, and (c-e) Simulated Radiation Patterns at φ=0° (Left) and at φ=90° (Right) for 3.2 GHz, 3.6 GHz, and 4.9 GHz, Respectively, and Beam Steering at φ=0° at 4.9 GHz for (f) (Bottom)

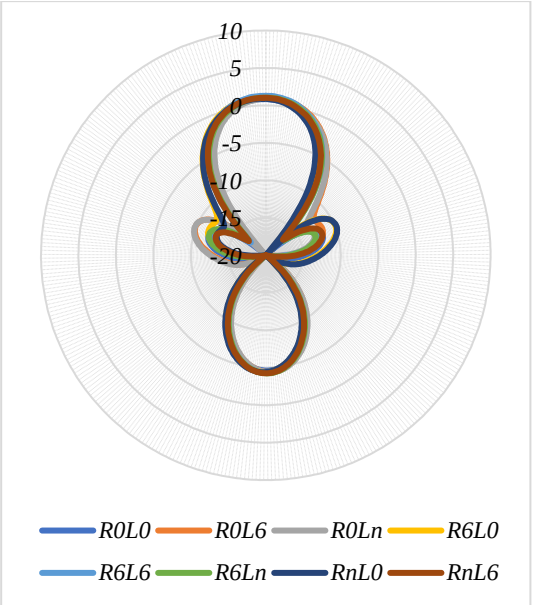

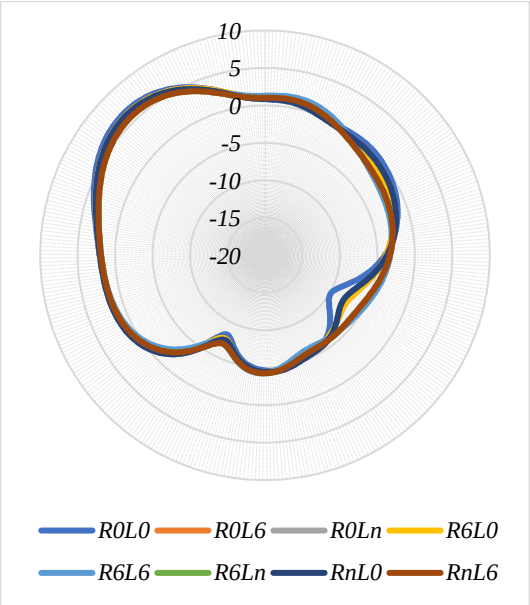

(c)

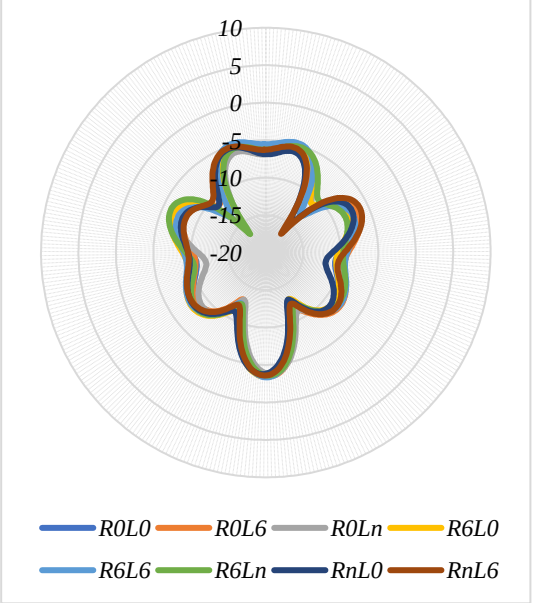

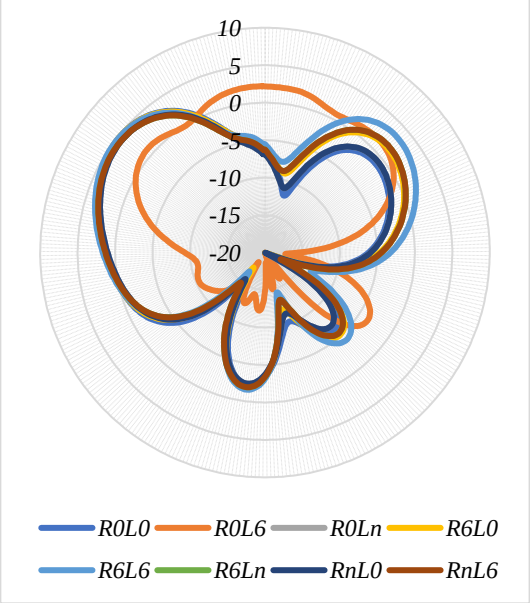

(d)

Figure 5.2 Continued

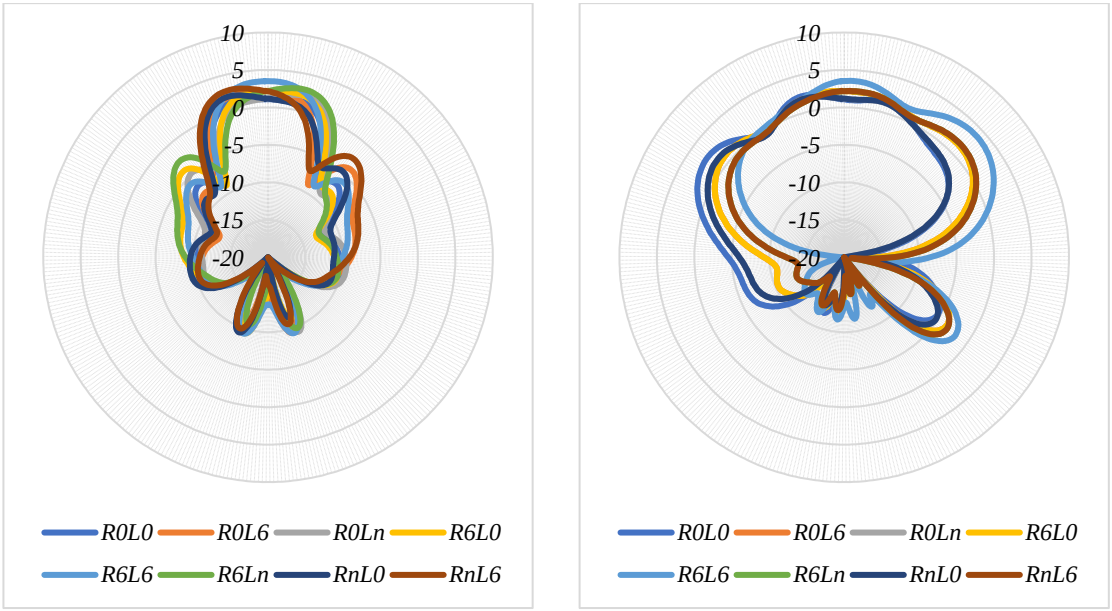

(e)

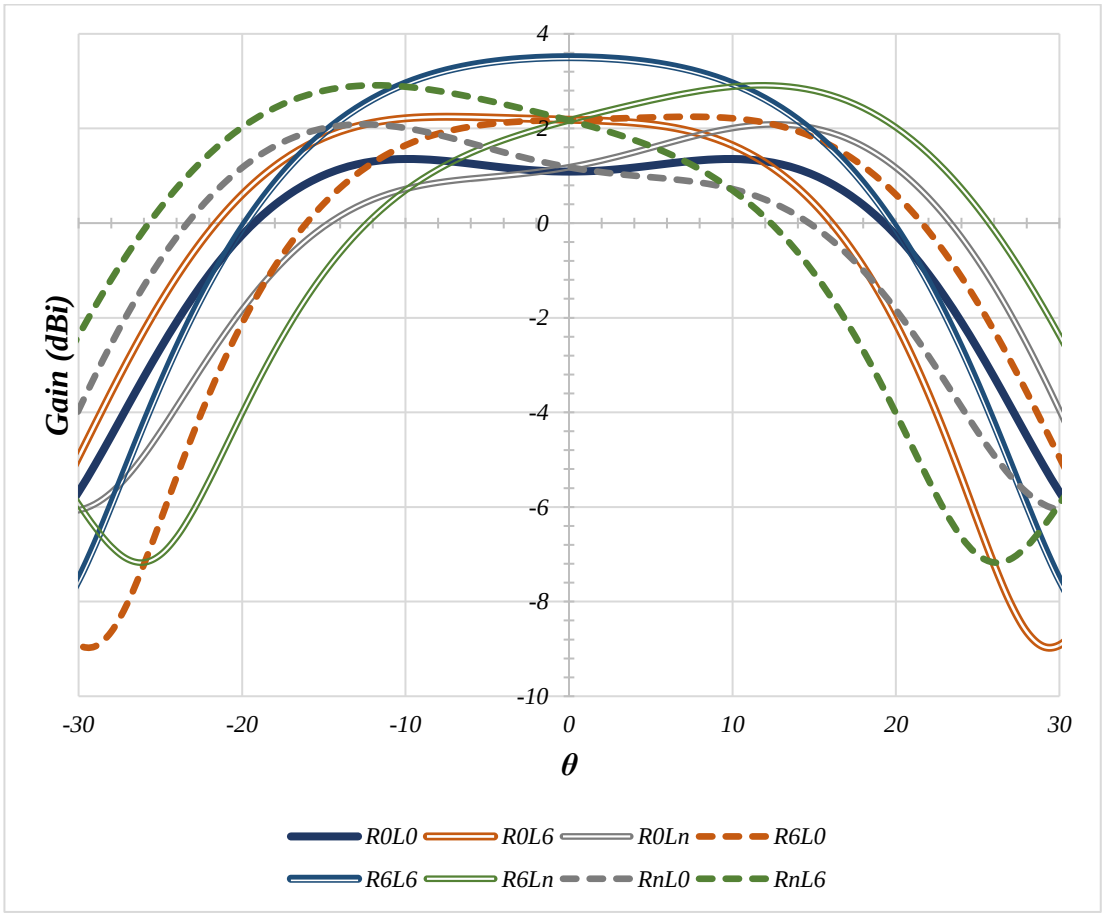

(f)

Figure 5.2 Continued

Table 5.2 Radiation properties of the array configuration of Figure 5.5(a)

Band	3.2 GHz					3.6 GHz					4.9 GHz				
Case	Beamwidth φ= 0°	Beamwidth φ= 90°	φ Max	θ Max	Max Gain	Beamwidth φ= 0°	Beamwidth φ= 90°	φ Max	θ Max	Max Gain	Beamwidth φ= 0°	Beamwidth φ= 90°	φ Max	θ Max	Max Gain
R0L0	43.7	54.2	270	44	6.72	NG	55.0	270	51	4.78	46.3	41.3	270	53	2.58
R0L6	43.8	56.9	271	43	6.34	NG	56.2	267	52	4.84	40.9	126	204	7	2.26
R0Ln	44.0	56.7	272	43	6.31	NG	57.2	271	52	4.30	43.0	110	327	13	2.17
R6L0	43.8	56.9	269	43	6.34	NG	56.2	273	52	4.84	40.9	126	336	7	2.26
R6L6	43.9	60.8	270	42	5.80	NG	56.9	270	54	4.84	37.5	91.3	90	48	3.94
R6Ln	43.9	60.9	271	43	5.72	NG	58.4	275	53	4.41	38.5	116	8	12	2.92
RnL0	44.0	56.7	268	43	6.31	NG	57.2	269	52	4.30	43.0	110	213	13	2.17
RnL6	43.9	60.9	269	43	5.72	NG	58.4	265	53	4.41	38.5	116	352	12	2.92

**NG = Negative Gain*

5.4.2 Four Elements DRA Array

In this array, each element is excited using a single slot as shown in Figure 5.3 (a). There are 16 expected cases, hence a binary denotation has been used to represent each case, where "1" represents a radiating element and "0" is a switched OFF element, with the most and least significant bits represent the most left and right DRAs, respectively. For example, the symbol "1000" means only first element is ON, while "0101" means the second and fourth elements are ON and the rest are OFF. Ideally, the design of a single slot 2-DRA array can be extended to a single slot 4-DRA array. However, adding extra elements means additional mutual coupling and extra parasitic elements. In addition, more PIN diodes are needed which means additional DC gaps need to be introduced in the ground plane. These parameters are expected to affect the array radiation characteristics, which means a revised design is needed. In addition, the size of the ground plane has been enlarged to 20×15 cm^2.

CST Microwave Studio has been used to simulate an initial design, then parameter sweeping has been initialised to decide the best combination of the elements separation distance (d) and microstrip lines stub length (s) for multi-band reconfiguration. The same DRAs and slots dimensions of the previous section have been used. The feed network consists of a 4.8 mm wide microstrip line that has been equally divided into two parallel 2.4 mm strips, which are subsequently divided into two branches each, with a final four parallel branches width of 1.2 mm and a stub length of 6 mm from the Slot-0 centre. The separation between two adjacent elements is 25 mm, which equals to $0.467\lambda_0$ at 5.6 GHz, to achieve a better balance for the impedance matching bandwidth and the beam steering agility. The separation distance is different from the two elements array is due to increase in the number of the elements, hence the increase in the mutual coupling, which requires changes in the separation distance.

The reflection coefficients for the 16 cases are illustrated in Figure 5.3 (b). Since there are cases with the reversed activation order with respect to another case, such as 0101 and 1010, these cases have the same reflection coefficients, hence only 10 data plots are required. In all cases, there are three main impedance matching bands; a narrow band at ~ 3.8 GHz, a slightly wider band at ~4.5 GHz, and a third wide band that ranges from ~5.3 to 6 GHz. The first band has a low total efficiency with a negative gains and with a lower centre frequency compared to the dominant $TE_{\delta 11}$ mode resonance frequency (4.1 GHz), it can be expected that this band occurred due to the equivalent circuit network of the antenna has the required values to have impedance matching from the RF input point of view, or due to the slot' self-resonance, which as a length of 8 mm which is approximately equals to $(\lambda_0/\varepsilon_r^{0.5})/2$ at 3.8 GHz. On the other hand, the second has a higher total efficiency of ~70 %, but with a broadside gain of -4 dBi, and a back-lobe gain of 2 dBi. This may have occurred due to the fact this design focused on the matching at 5.6 GHz rather than 4.5 GHz in line with both the single DRA and the 2-elements DRA models which have resonance frequencies around 5.6 GHz, which led to deteriorating mutual coupling. On the other hand, the third band, which has the field distribution characteristics of $TE_{\delta 11}$ resonance mode, has an acceptable total efficiency at 5.6 GHz with a maximum gains range of 6.1 dBi for the full array, case 1111, to ~4 dBi in some single activated cases. However, in the φ=0° plane, the maximum gain is ranging from 4.8 dBi to negative values in the same cases, since the pattern at φ=90°has two higher gain points shifted away from the *z*-axis. In addition, the total efficiencies deteriorate along with the decrease of the activated elements number.

Table A.1 presents a comparison for few of the array radiation characteristics for the 16 cases at 5.6 GHz, since in all cases this frequency range offers highest gain and total efficiencies. In the table, each case has been subject to a validity test, where in the case

of a very low total efficiency, the row is shown in a grey background. Figure 5.3 (c) presents the beam agility in the φ=0° plane, i.e. the H-plane. It can be noticed from this Figure, and from the Table, that there is a narrow main-lobe steering in the range of ±10°. On the other hand, Figure 5.3 (d) shows the effect of the number of the active elements on the array gain by observing the radiation pattern from the φ=90° plane, i.e. the E-plane. In addition, there is a reconfigurability in the angular beam-width range of 26.2° up to 41.3°. Moreover, Table 5.3 shows that the maximum of the radiation patterns are not in the broadside direction. However, this is independent of the beam steering and it is due to the fact that the wide beam at φ=90° has two or three maximum gain points with one of the side points slightly higher than the other on the other side of the graph and both are higher than the one along the *z*-axis due to the increase in the number of elements and the effect of the ground plane gaps.

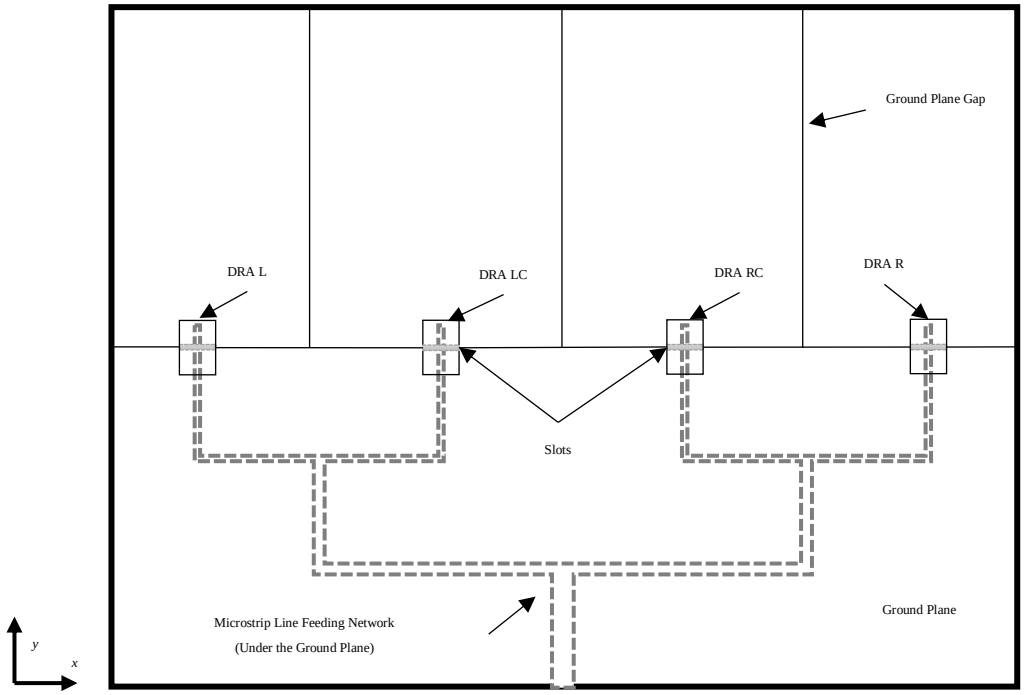

(a)

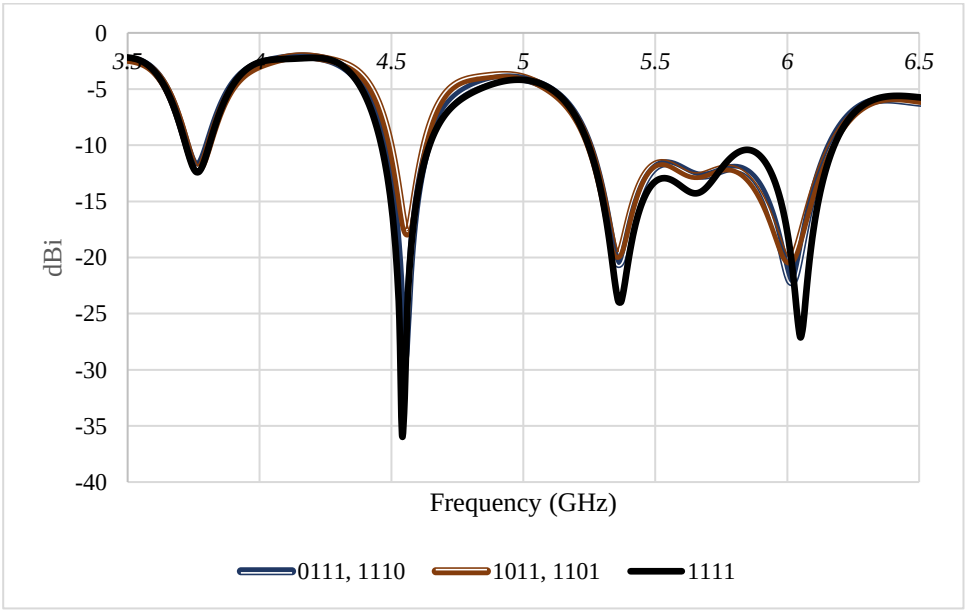

(b)

Figure 5.3 Single-Slot 4-DRA Parallel Fed Array (a) Antenna Diagram, (b) Reflection Coefficients, (c) φ=90° Plane Radiation Patterns Showing Beam Steering Agility at 5.6 GHz and (d) Radiation Patterns at 5.6 GHz at φ=90° Plane.

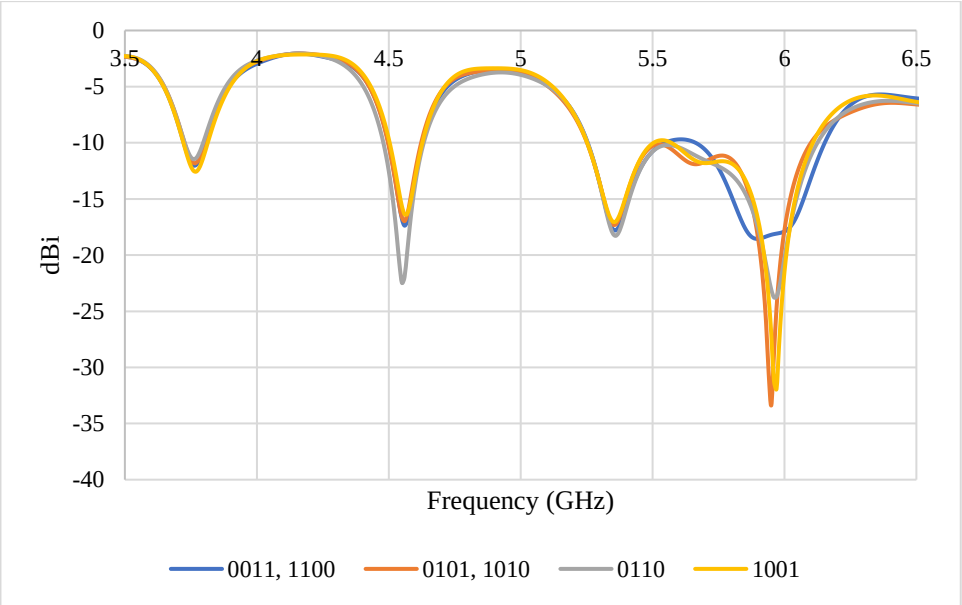

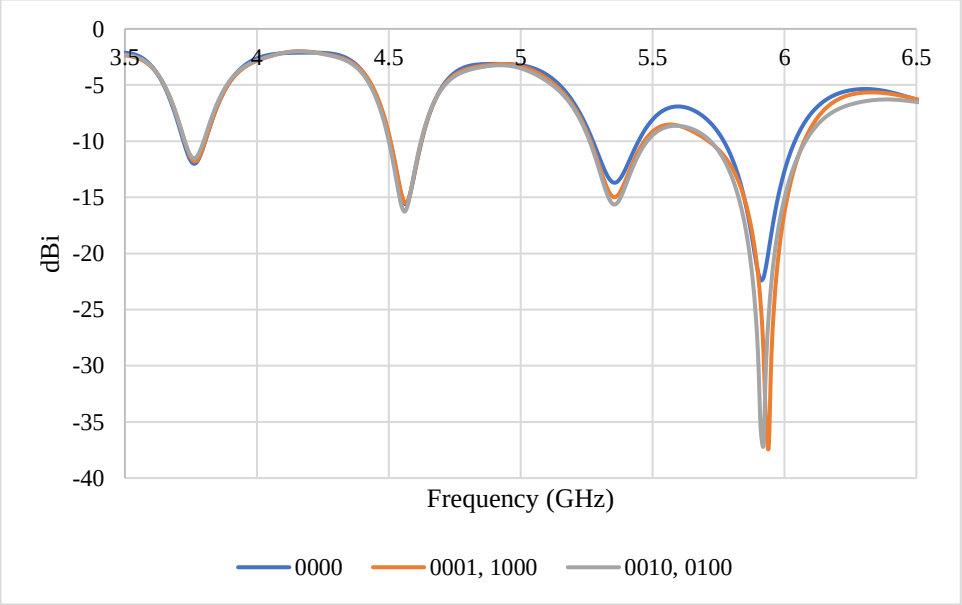

(b) Continued

Figure 5.3 Continued

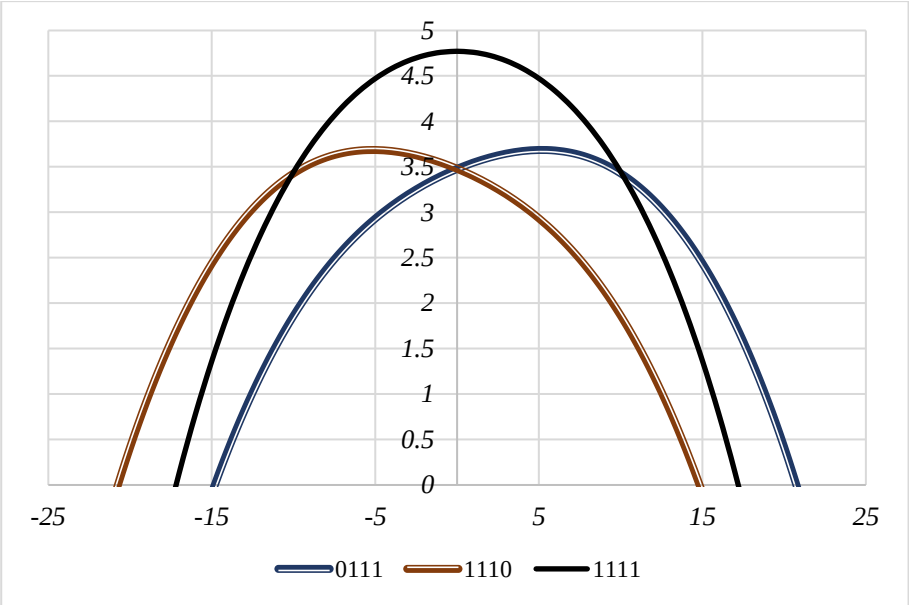

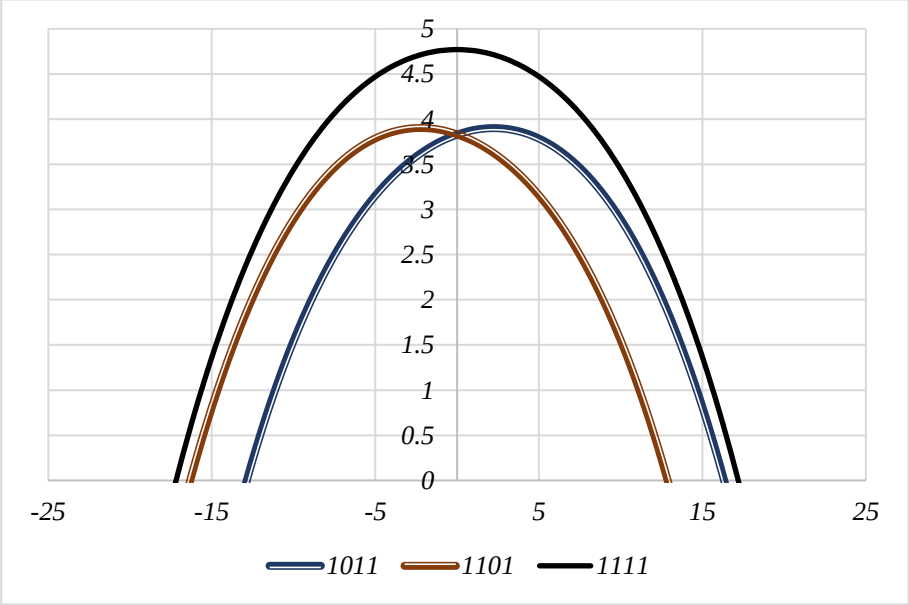

(c)

Figure 5.3 Continued

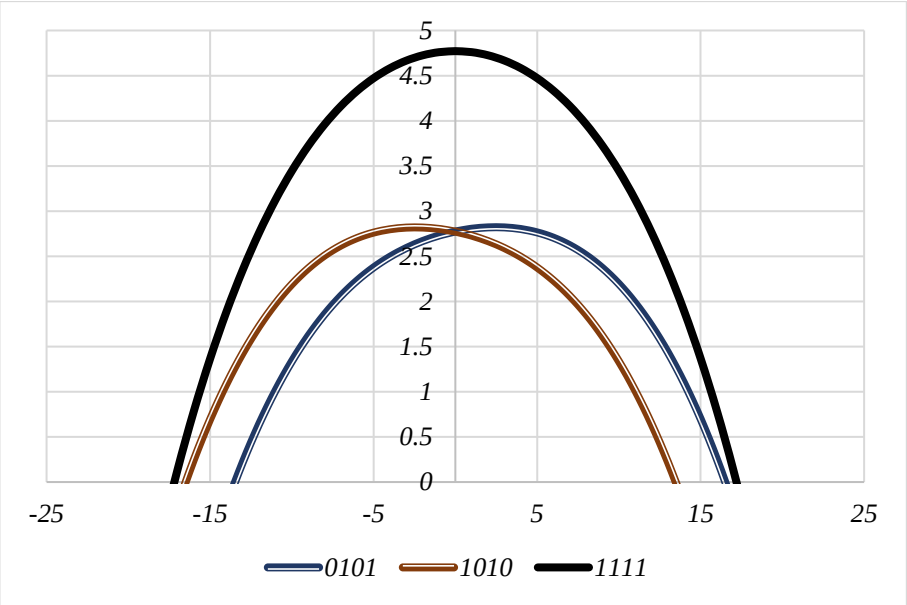

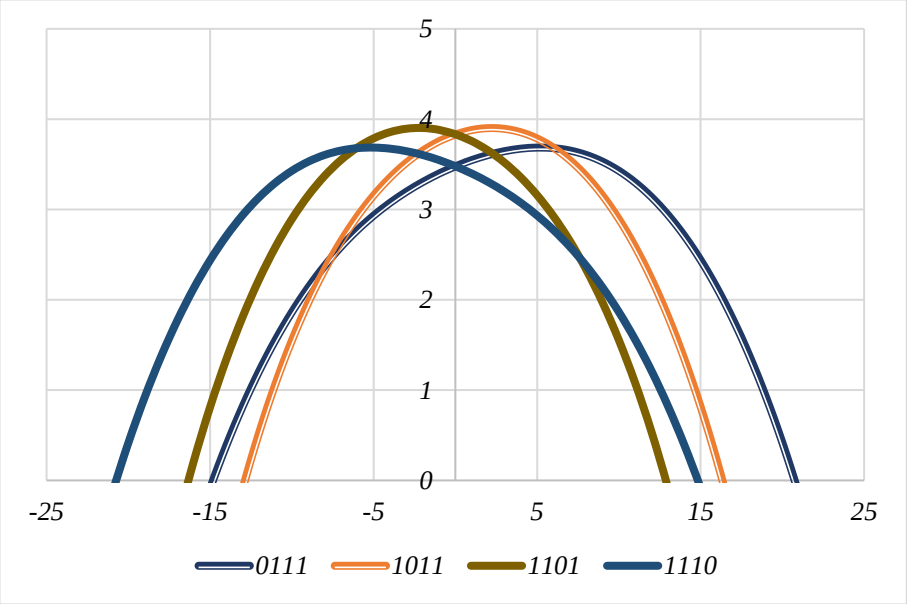

(c) Continued

Figure 5.3 Continue

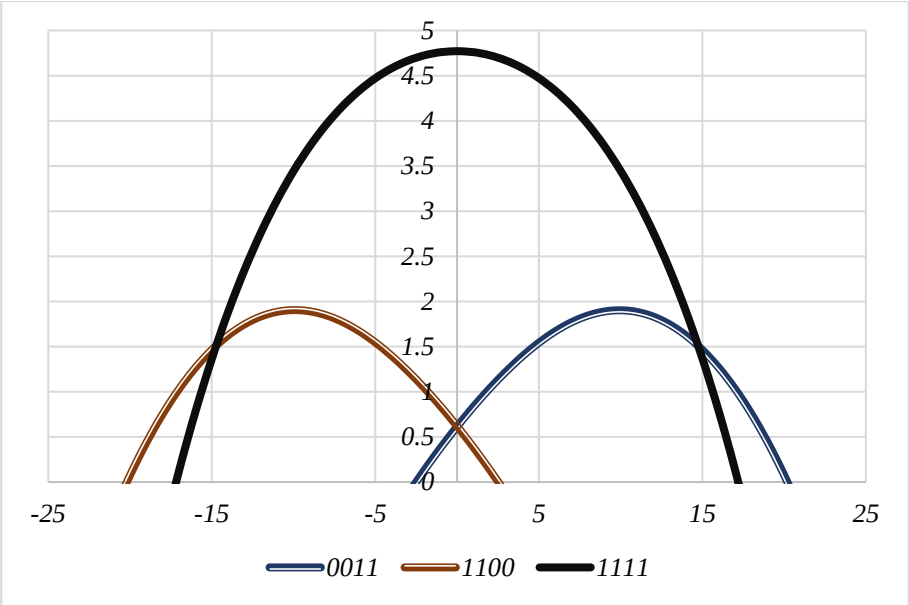

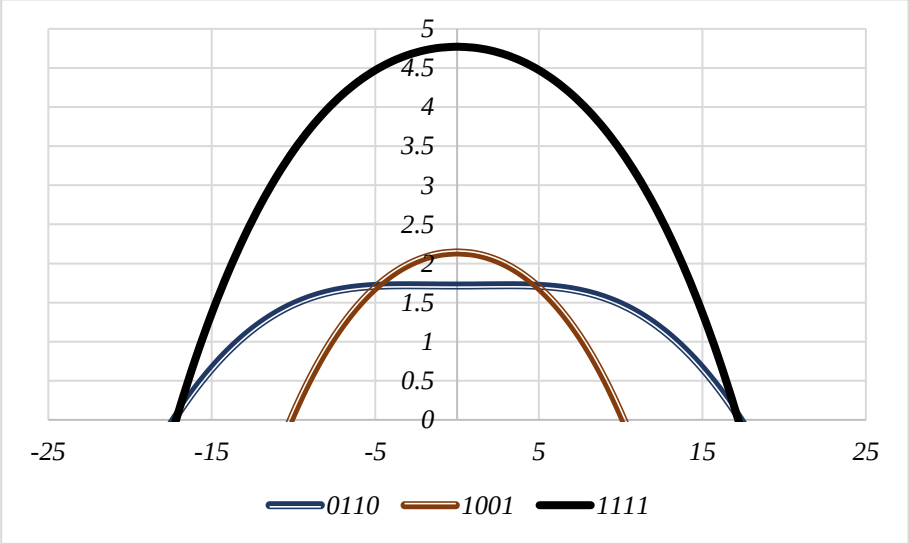

(c) Continued

Figure 5.3 Continue

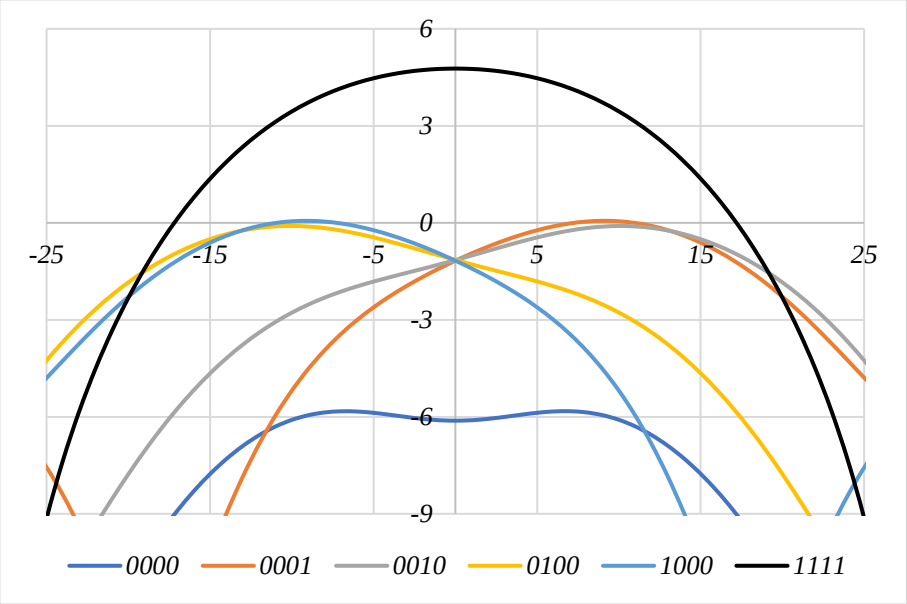

(c) Continued

Figure 5.3 Continue

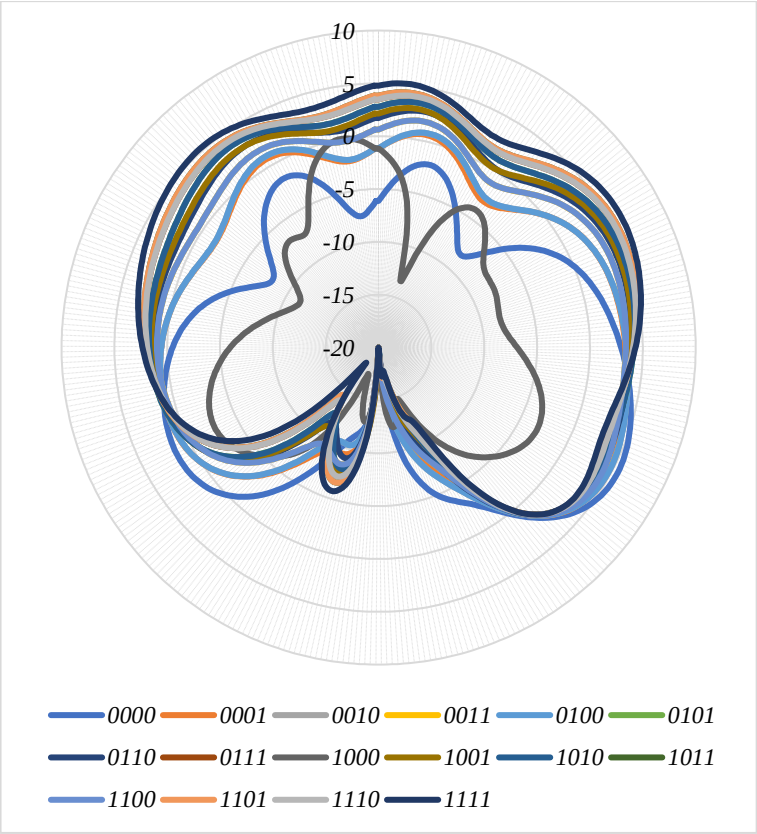

(d)

Figure 5.3 Continue

The same procedure followed for a dual-slot two elements array can be applied for the four elements array. For each DRA element, there are 3 cases Slot-0 (0), Slot+6 (6), and inactive (*n*). This means that there are 3^4, 81, cases. However, using the earlier mentioned mirror reversibility concept, only 45 cases need to be examined. Figure 5.4 (a) illustrates the array diagram, where it can be noticed that with the increase of the reconfigurable apertures, there is a notable increase in the ground plane DC biasing gaps. In addition to the effect on the antenna characteristics, there is an extra need for a DC control circuity. This can increase the effects on the antenna performance considerably if no extra attention is given. Moreover, capacitances that have been used in earlier designs were eliminated

from this model to avoid the extensive use of extra passive elements, which can add extra distortion to the array system characteristics. The DRA elements and slot dimensions are the same as those used earlier. For simplicity, the four DRAs, denoted from right to left as DRA R, DRA RC, DRA LC, and DRA L. CST Microwave Studio has been used to optimise the design for multiband reconfigurability alongside beam steering agility. The final model has each branch terminated with an 11 mm stub from the Slot-0 centre, and the distance between two adjacent elements centres is 44 mm. This change in the spacing has been introduced to accommodate the increase in the number of DRA elements, slots, and the round plane gaps.

Figure 5.4 (b) illustrates the reflection coefficients, where it can be noticed that four main impedance matching bands are obtained. The first is around a central frequency of 2.8 GHz which corresponds to the $TE_{\delta 11}$ mode, with a bandwidth ranges from ~4to 10%. The second band extends from 3 to 3.45 GHz, which corresponds to the $TE_{\delta 21}$ mode. This band is diminished in some cases, or it can be wide enough to be connected to the first band producing an even wider impedance matching bandwidth of 20-26%. The third band is around a centre frequency of ~4.2 GHz which corresponds to $TE_{\delta 21}$ mode, and it is a narrow band of less than 3% so that it can be diminished too in some cases. The last case is around a centre frequency of 4.6 GHz, which corresponds to $TE_{\delta 31}$ mode, with a narrow impedance matching bandwidth range from 2.9-3.5%. Table A.2 compares the radiation characteristics for all possible sequences, with the mirrored sequences followed by the (*) sign to indicate a reverse φ=0° plane beam direction. It can be noticed that the best total efficiencies and gains are normally obtained by activating as much elements as possible, especially with Slot-0 activation. In addition, a narrow beam steering range of ±9° has been obtained in the φ=0° plane. However, in this case the beam steering can be more into (φ, θ) as shown in Table A.3.

Table A.3 lists the beam-widths at the φ= 0° and φ=90° plane, and the maximum gain and beam (φ, θ) direction at 2.8, 3.4, 4.2, and 4.6 GHz. Each frequency corresponds one of the described four bands above. in addition, the table shows the range of beam-widths at both of the φ= 0°and φ=90°plane, which decreases with the increase of the operating frequency alongside the increase in gain as it should be expected from higher order modes [5]. However, in most cases, the gain at 4.2 GHz is higher than the one associated to 4.6 GHz, which can be expected to due to either the different levels of mutual coupling at the different frequencies [2, 6], or due to the fact that at higher TE modes the magnetic fields can overlap, which causes distortion to the radiated field and possible reduction in the gain [5]. In addition, these sequences allow beam steering in the two-dimensional space, with some patterns are narrower and more directional than others. This allows a more steering freedom for applications that require antennas with more accuracy in transmission/receiving directions especially for the narrow beam-width applications.

The four cases of reconfiguration can be summarised as following:

- Band 2.8 GHz: There is some change in the beam-width at φ=0° from 33° up to 51.6°, and less obvious change in the beam-width at φ=90°, unless all DRAs have their (Slot-0) shorted, which leads to reduce the beam-width from a range of wide beam-width of 117°-141° to an average beam-width around 70° with the main beam shifted away from *z*-axis. In addition, the gain ranges from around 5.8-2.3 dBi with at least one active (Slot-0), and a low range around 2-1.45 dBi in case of shorted Slot-0. The first case can be useful for gain control, which can be used to control the radiating range since the beam-width allows small maneuvering for beam steering, even though with the fact there is Right/Left beam steering at the φ=0° plane. The efficiencies are dependent on the number of active slots in particular the central slot, Slot-0, for each DRA. The range of total efficiencies

can usually span from 50-85%, however, it reaches 95% for (0066) and (6600) sequences, and 98% for (6666) sequence.

- Band 3.2 GHz: Beside the θ= ~±40° Right/Left beam reconfiguration, there a marginal beam steering in this directional beam case. However, the gain can be reconfigured in the range 5.2-2.7 dBi, which can be useful for range control cases.
- Band 4.2 GHz: There are marginal changes in the beam-width and maximum gain. The only change is the maximum gain direction at θ, which gives a beam steering of Right/Left 51°-56°. The efficiencies have a wide span from around 99% to lower than 50%.
- Band 4.6 GHz: In this case, the Right/Left steering is in the range of θ=±4°to 6°, which does not allow too much steering with a beam-width around 22°-24°. However, this frequency has a beam steering capability range around φ=221°-320°, with beam-width averages of 22.2° and 37.5° in the φ=0° and φ=90° planes, respectively. In addition, the φ=90° plane pattern has a side-lobe beam around 60° away from the main-lobe with a gain peak of ~ 0.5-1 dBi lower that the maximum gain. The total radiation for this frequency range is usually lower than other three cases, where the overall total efficiencies are in the range of 50-55%.

Although the results demonstrate low gains and total efficiencies, the overall concept has been proven. The main issues that have to be dealt with in the future to improve the array's performance are the elements' spacing, mutual coupling, parasitic slots, and the ground plane's DC control gaps. The first two issue need distance between the elements to be optimised to agree as much as possible for the four frequencies. For example, the spacing in this model is 44 mm, which corresponds to $0.41\lambda_0$, $0.47\lambda_0$, $0.62\lambda_0$, and $0.67\lambda_0$ for 2.8 GHz, 3.2 GHz, 4.2 GHz, and 4.6 GHz, respectively. The parasitic slots need special consideration to minimize their impact on both the efficiency, and radiation pattern.

However, their effects on the beam steering can be turn into useful applications with further planning and optimisation. The last issue is the ground plane gaps, which can be minimized by reducing the gaps size depending on the available fabrication technology. Figure 5.4 (c) compares the radiation patterns for several sequence cases for the four frequencies. These cases illustrate the main radiation characteristics cases that are summarised in Table A.3.

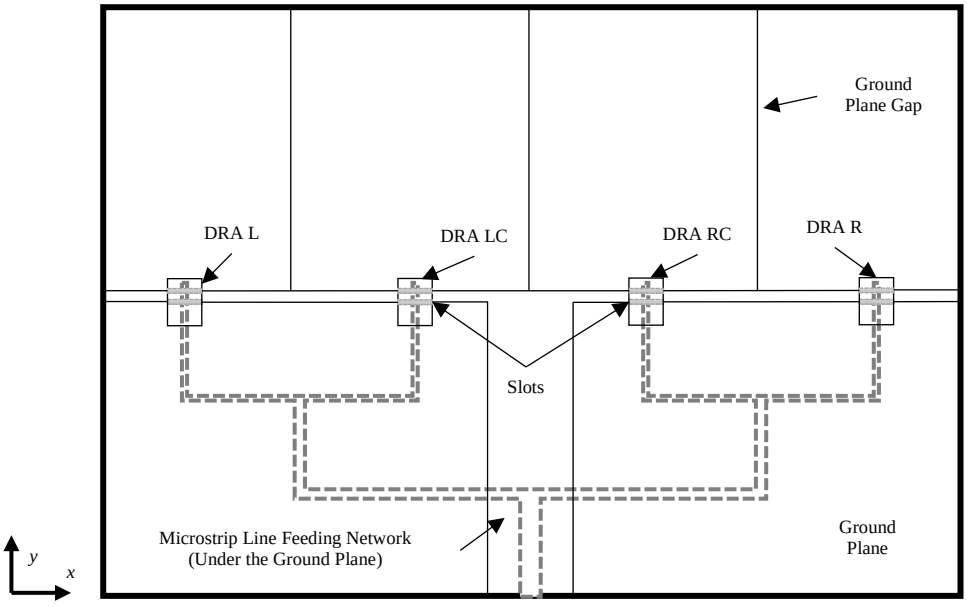

(a)

Figure 5.4 2-Slots 4-DRA Reconfigurable Array (a) Array Diagram Top View, (b) Reflection Coefficients, and (c) Selected Radiation Patterns at φ= 0° (Left), and φ=90° (Right)

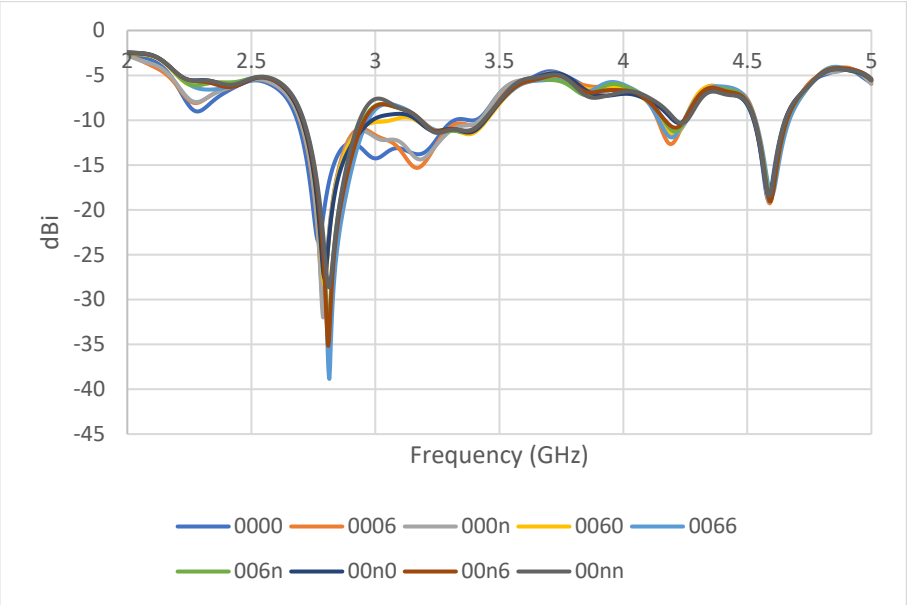

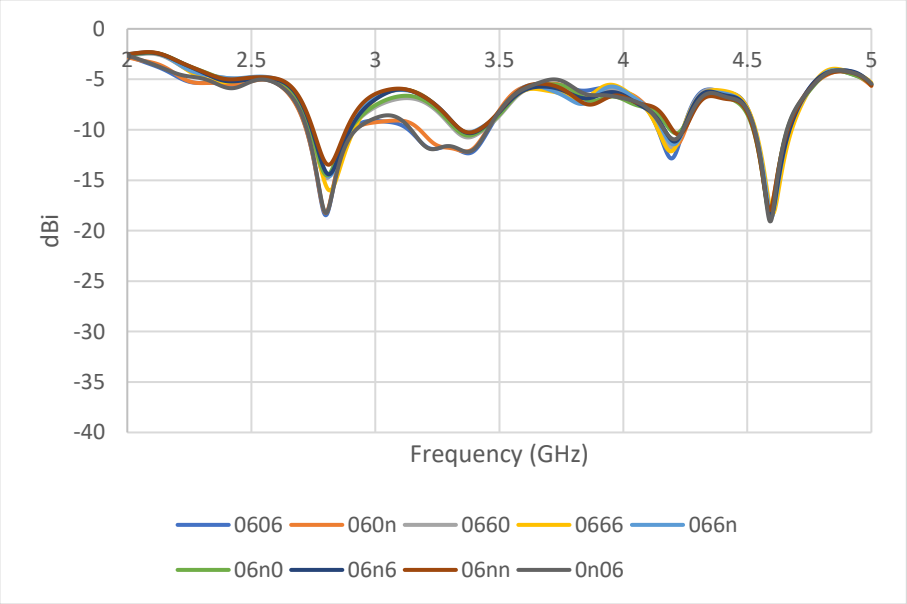

(b)

Figure 5.4 Continued

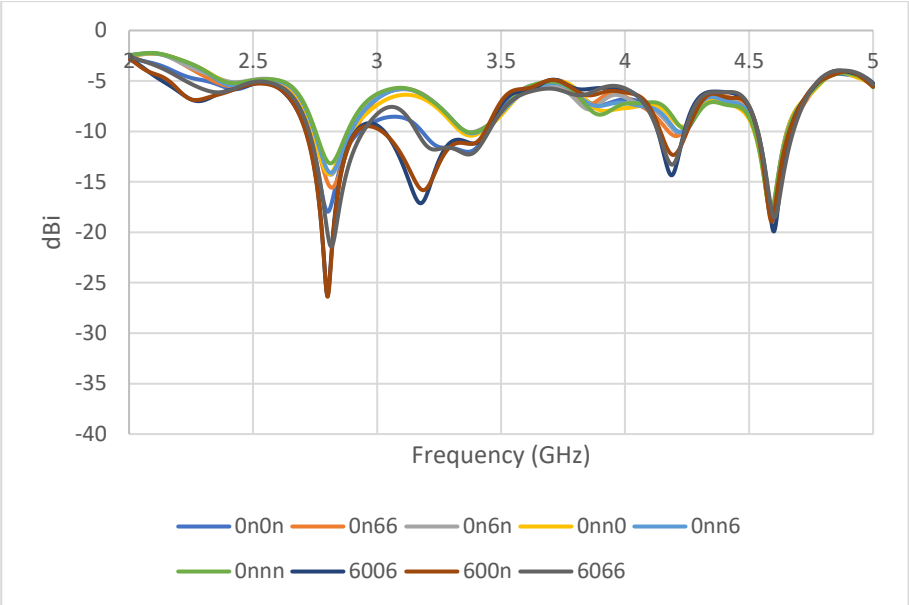

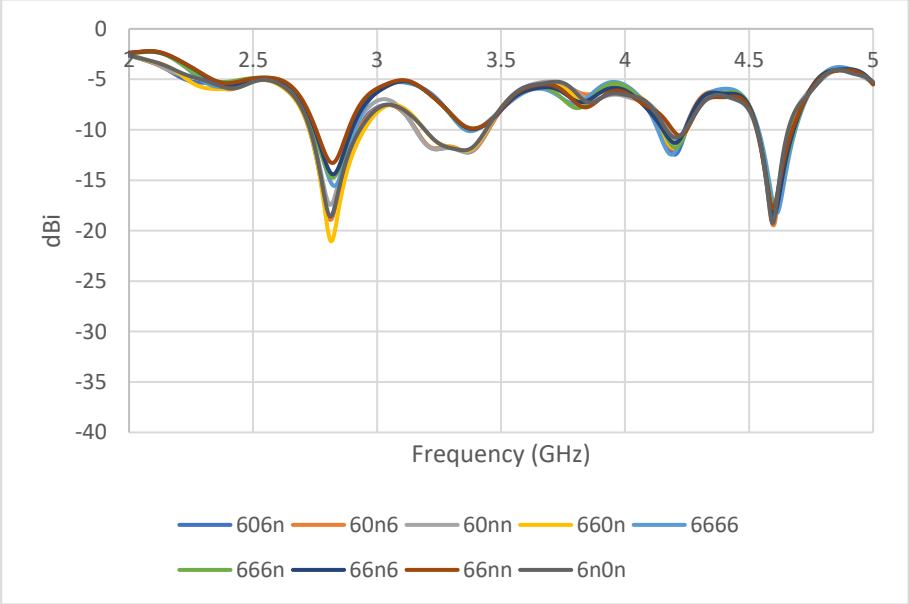

(b)

Figure 5.4 Continued

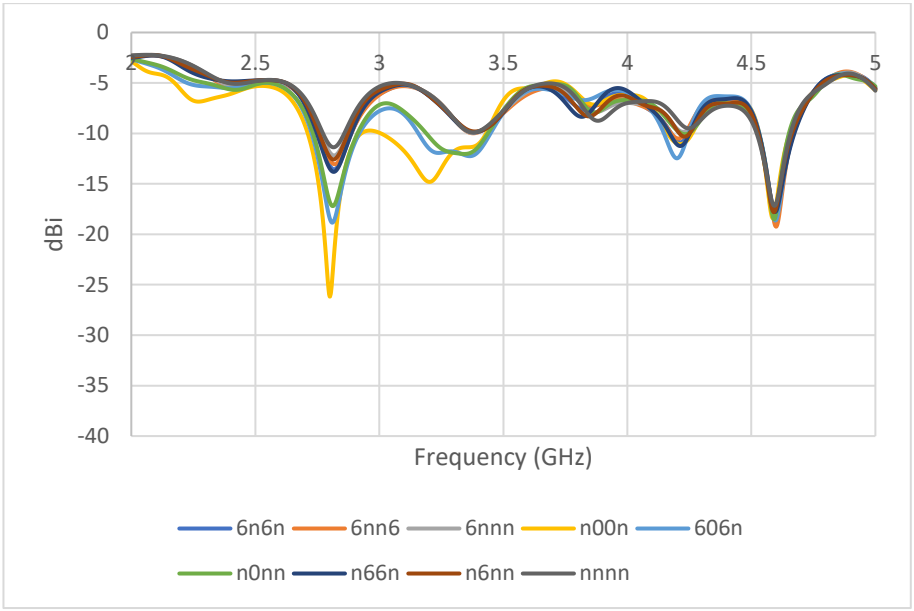

(b) Continued

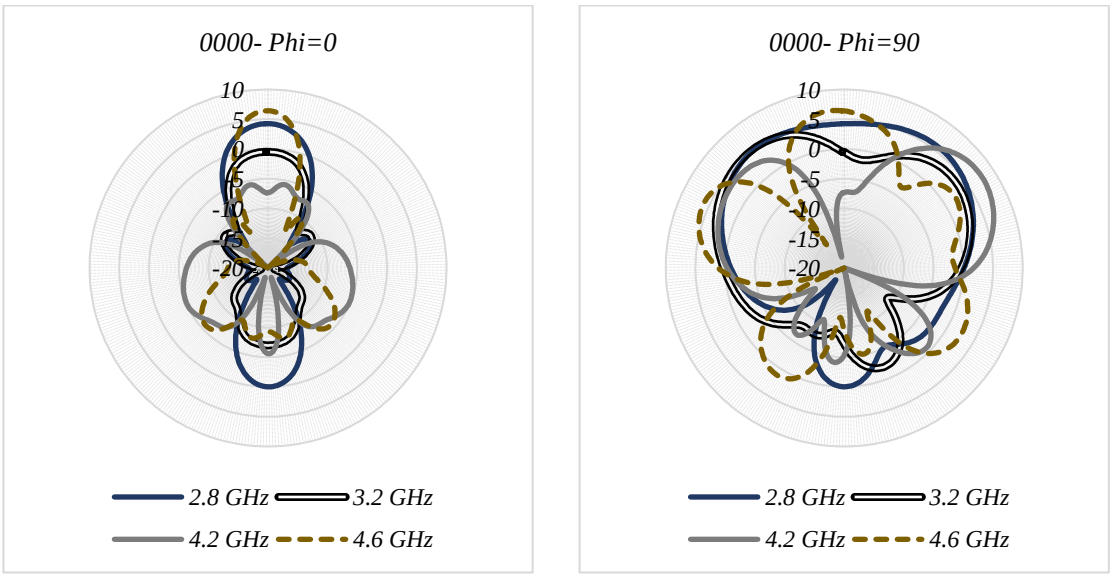

(c)

Figure 5.4 Continued

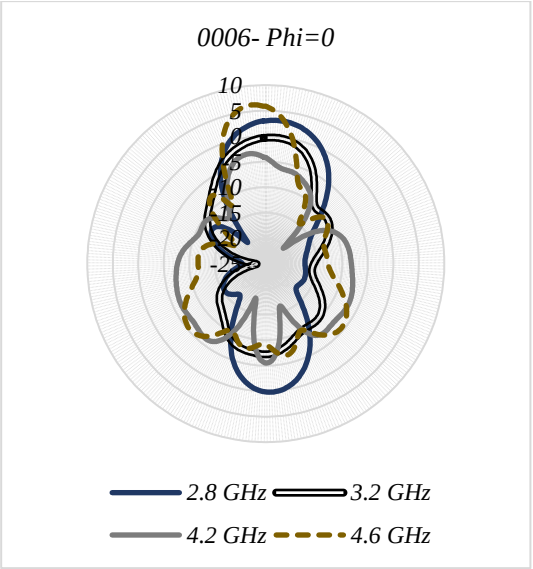

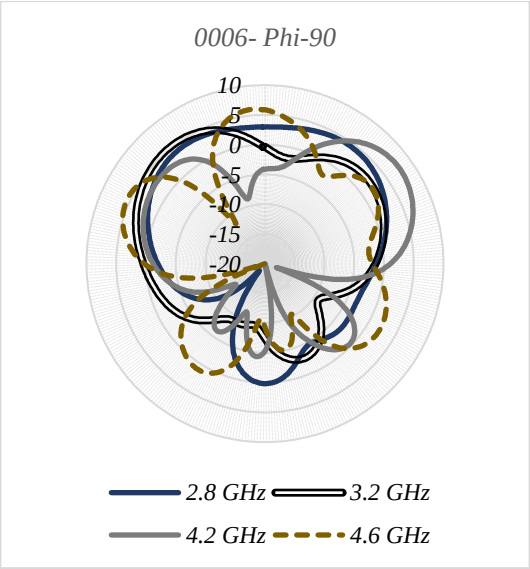

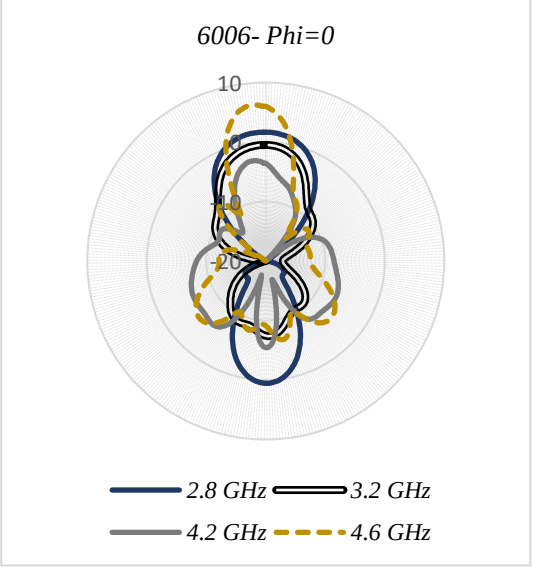

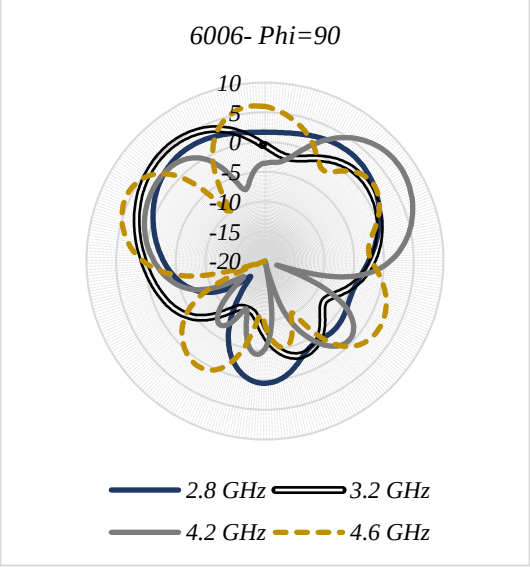

(c) Continued

Figure 5.4 Continued

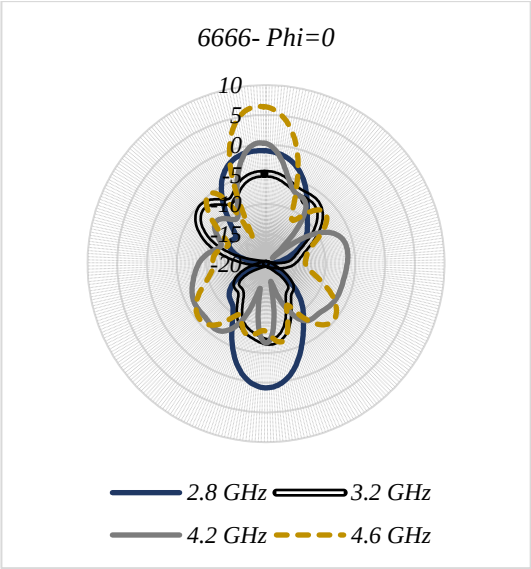

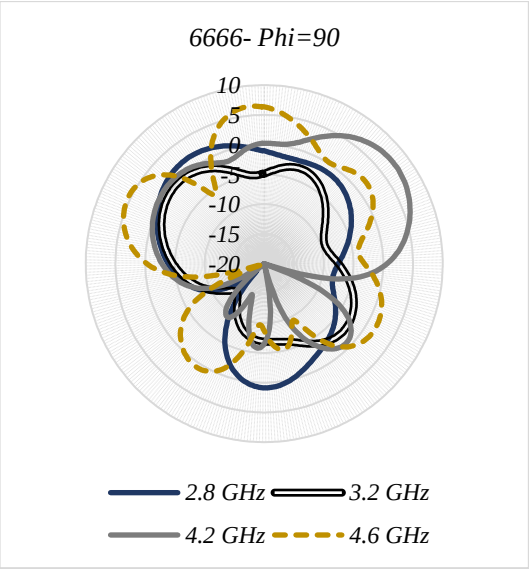

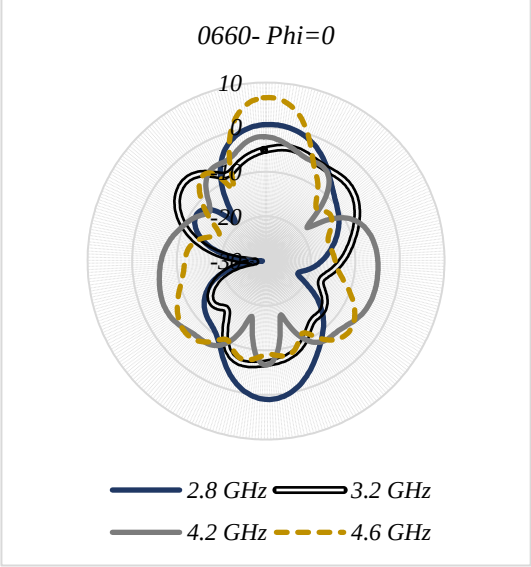

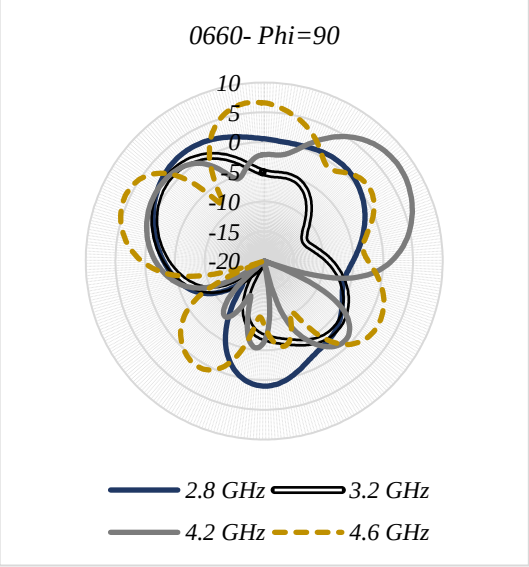

(c) Continued

Figure 5.4 Continued

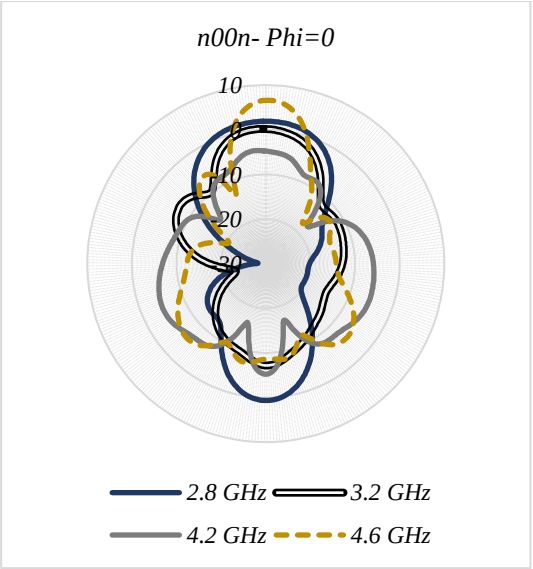

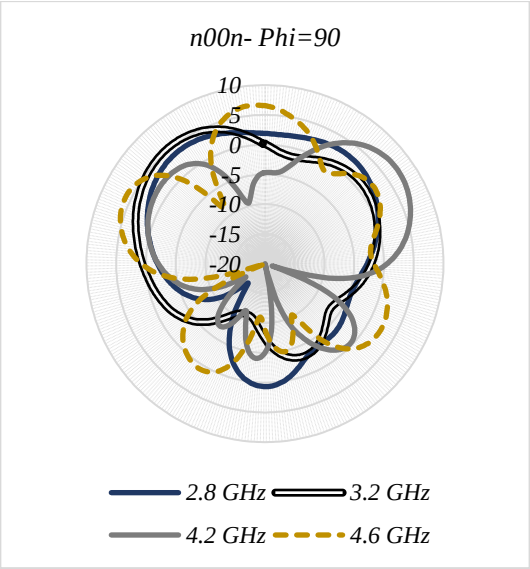

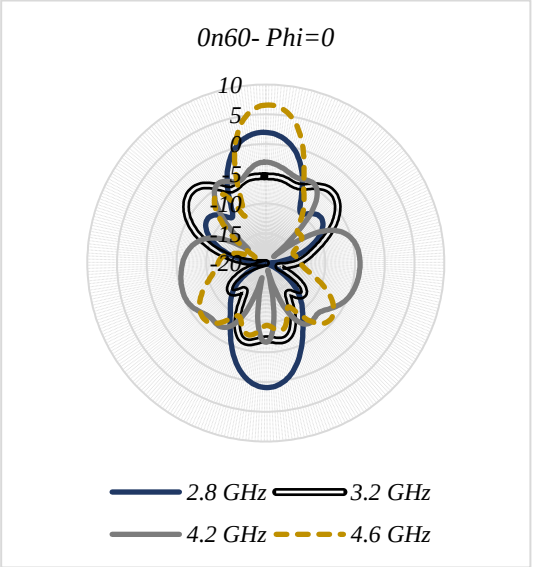

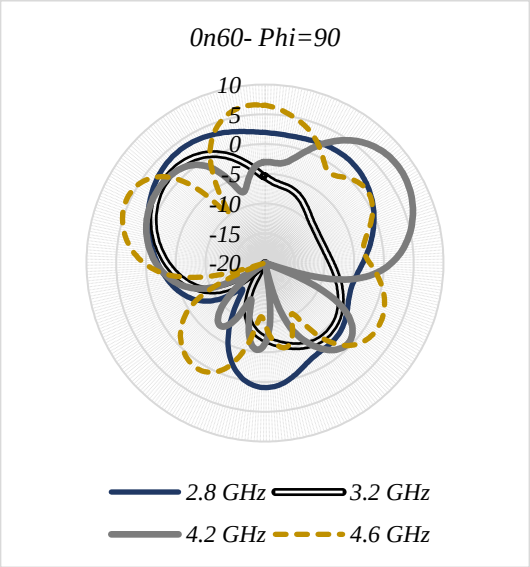

(c) Continued

Figure 5.4 Continued

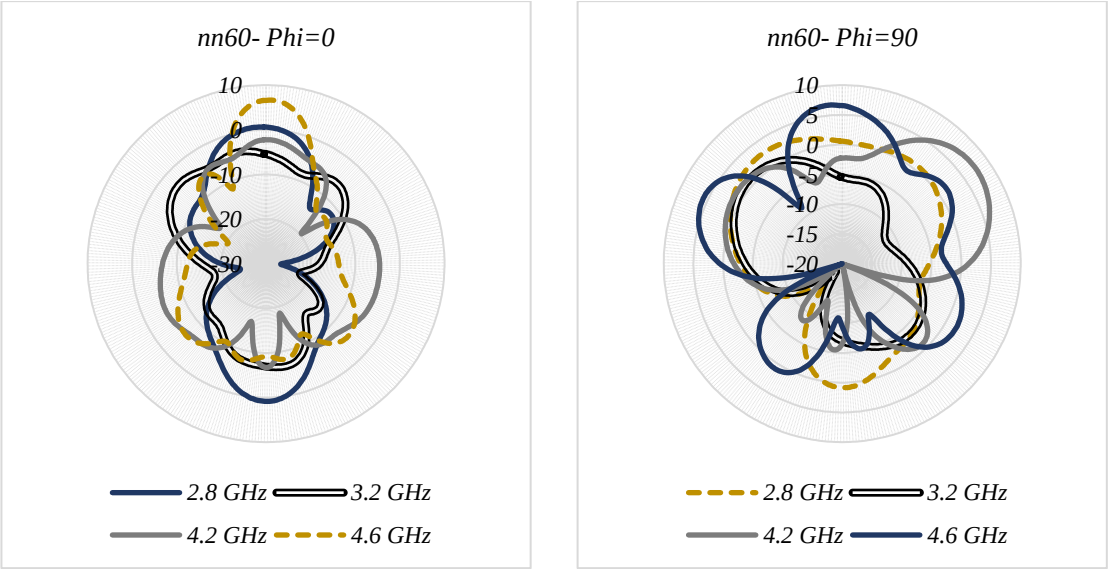

(c) Continued

Figure 5.4 Continued

5.5 Summary

In this chapter, the work in Chapter 4 has been extended to investigate the design of reconfigurable arrays. Four cases have been investigated, these include 2- and 4-elements microstripline slot coupled parallel fed linear DRA arrays, with each case examined using single as well as dual feeding slots. All the considered designs are based on using the H-plane (φ=0°) coupling and use the DRA elements presented in Chapter 4. In the first case, the single-slot two elements array, the four cases of elements' excitation demonstrate little variation in the central operating frequency and impedance matching bandwidth. On the other hand, the beam has been steered at φ=0°, with main-lobe directions of -12°, 0°, and 12°. This design has been expanded to study the dual-slots two elements DRA array. At the first glance, the reflection coefficients demonstrated a good prospect of multiple frequency/radiation pattern reconfigurability. However, the proposed design proved to be mostly viable for beam steering at the band around 4.9 GHz, with beam steering at both φ and θ directions.

Four elements DRA arrays have been considered based on the 2-elements models, with some changes to accommodate the additional mutual coupling due to the increase in the number of radiating elements. In addition, with more elements, a narrower pattern has been obtained in the H-plane, with the single slot case beam steering reduced from ±12° to ±10°. However, the dual-slots four elements DRA array offered a good prospect in both frequency reconfiguring as well as two-dimensional beam steering on a range of frequency bands.

The frequency agility can be observed from comparison of the four active bands, where the first and fourth bands are constantly active with all the array activation arrangements, while the other two can be turned ON/OFF by selecting the appropriate activation sequence. In addition, each band has some degree of impedance bandwidth reconfigurability. Hence, it is possible to exploit this option in the future to design a multiband reconfigurable antenna array.

This chapter study has been limited to simulating linear arrays with up to four elements and up to double-slot feeding. A three-slot model was initially investigated as an ideal model without ground planes gaps and with ideal short circuits instead of the PIN diodes circuit model, which initially had promising results. However, due to the addition of the latter two, the model proved to be somewhat complex and with some difficulty to obtain good results without further investment of time, which was not available. Therefore, this topic has been omitted from this study. Nevertheless, some of the obtained results shown a possibility for further investigation and improve the results. The overall results shown that there is an opportunity for improvement in the investigated models. Although, some results have been below satisfactory in terms of both gain and total efficiency, that was related to the fact that this research is focused on proving the concept rather than obtaining desirable final results. In addition, future investigation can extend to study arrays with

more elements, series and branch-line feeding techniques, reconfigurable planar arrays, and the improvement of the two-dimensional beam steering.

References

[1] M. T. Birand and R. V. Gelsthorpe, "Experimental millimetric array using dielectric radiators fed by means of dielectric waveguide," Electronics Letters, vol. 17, no. 18, pp. 633-635, 1981.

[2] K. M. Luk and K. W. Leung, Dielectric resonator antennas. Research Studies Press, 2003.

[3] A. Petosa and A. Ittipiboon, "Dielectric Resonator Antennas: A Historical Review and the Current State of the Art," IEEE Antennas and Propagation Magazine, vol. 52, no. 5, pp. 91-116, 2010.

[4] H. A. Majid, M. K. A. Rahim, M. R. Hamid, and M. F. Ismail, "A Compact Frequency-Reconfigurable Narrowband Microstrip Slot Antenna," IEEE Antennas and Wireless Propagation Letters, vol. 11, pp. 616-619, 2012.

[5] R. S. Yaduvanshi and H. Parthasarathy, Rectangular Dielectric Resonator Antennas: Theory and Design. Springer India, 2015.

[6] A. Petosa, Dielectric Resonator Antenna Handbook. Artech House, 2007.

Chapter Six

Reconfigurable Semiconductor Plasma Antenna

6.1 Introduction

The original aim of this research is to investigate and build an antenna that employs an active semiconductor device, which injects sufficient charge carriers to create a semiconductor plasma to substitute metallic patches when necessary, and remove it be simply eliminating the charge carriers' supply. This technique was supposed to be used with the prototypes investigated in Chapter 3-5, where classical PIN diodes have been employed to prove the reconfiguration concept.

Owing to the fabrication cost and complexity, the Plasma Island has been created using an AlGaN/GaN HFET block rather than the silicon-based SPIN diodes described in Chapter One. The substrate containing the AlGaN/GaN HFET has been manufactured with the help of Prof Peter Houston and Dr. Kean Boon Lee in the Semiconductor Materials and Devices group at the University of Sheffield. Since the subjects of both silicon SPIN diodes and AlGaN/GaN HFET have been discussed in details in Chapter One, this chapter is focused on comparison between the two devices, design, and results.

6.2 Silicon SPIN Diodes vs AlGaN/GaN HFETs

As explained in Chapter one, semiconductor Plasma Island is based on injecting sufficient number of charge carriers that provide a conducting area of plasma causing the semiconductor to behave in a semi-metallic condition for an RF signal [1]. It has been shown in multiple studies and investigations that silicon is a favourite choice to establish a reliable area charge carrier for plasma islands due to its prolonged carriers' lifetime

compared to other semiconductor materials. This is in conjunction with a suitable size for antenna applications, low cost, adequate mechanical and thermal properties and the well-established high-quality technology [1, 2]. On the other hand, materials such as GaAs require more complex manufacturing alongside higher cost, with limited smaller size and carriers' lifetime [2]. These factors have been decisive for the introduction of silicon SPIN diode to design reconfigurable antennas [3, 4]. However, some materials such as AlGaN/GaN can convey higher charge carriers density than silicon. For example, a silicon SPIN diode offers a carriers density as high as 10^{18} per cm^3, which decreases with longer SPIN diodes [1]. On the other hand, AlGaN/GaN HFET can convey charge carrier's density over 10^{20} carriers per cm^3 [5, 6]. However, SPIN diodes require only terminal connections at both long ends of the diode, while HFETs require three terminals, one must be at the centre. This gives silicon SPIN diodes an extra advantage over the AlGaN/GaN HFETs, where these extra connections mean that some of the reconfigurable surface is covered by metal components. This reduces the reconfigurable area, which is already smaller than that of the silicon SPIN diodes counterpart. In addition, these connections in the narrow area of the HFET can cause an increase in the capacitive reaction in the reconfigurable area. This means, for a specific area, that the required number of AlGaN/GaN HFETs is greater than that for silicon SPIN diodes. Therefore, more connection complexity is introduced and higher capacitive reactions are expected in conjunction with a lower reconfigurable area. However, bulky counterparts such as MESFET and PHEMT have shown that these capacitances are too small to cause major change in the final result [7]. Nevertheless, in principle, AlGaN/GaN HFETs can be used as reconfiguration unit devices for some reconfigurable limited antenna application that need to be tolerant to the expected capacitive effects. In addition, as antennas are getting smaller and more miniaturised, AlGaN/GaN HFETs can be more acceptable as

semiconductor plasma device, due to the low power consumption of the HFETs that are, unlike other FETs, are voltage controlled devices, while SPIN diodes are current controlled devices [7].

6.3 Slot-Fed HFET Reconfigurable DRA

Figure 6.1 (a-e) illustrates the antenna block diagram and photographs. The RDRA is identical to the one used in Section 4.3, i.e. with dimensions of 12×8×5.5 mm^3 and ε_r = 20. The DRA is based on a circular Sapphire substrate which has a dielectric constant ~9.4, with 2" diameter (~5 cm). The thickness of the wafer is ~0.35 mm. The DRA has been fed using a 0.7×8 mm^2 slot with a 1.2 mm wide microstripline that has 9 mm stub. A block of 3 AlGaN/GaN HFETs has been fabricated in the middle of the slot to control the operation. The limit in the wafer's size is related to the availability of the material alongside the antenna total cost. On the other hand, the limit on the number of fabricated HFETs has limited the total supplied current, and hence its heat dissipation, which affects the performance of the Sapphire wafer that has small heat capacity. However, these limits are expected to affect both the gain for the substrate size, and slot shortening capability for the number of the HFETs. The total width of the HFETs block is ~0.1 mm. A 30×30 mm^2 gold ground plane has been printed on the top of the substrate with three 30 μm DC control gaps for the HFETs three terminals; Drain, Source, and Gate. The rest of the substrate has been covered with a copper tape to increase the ground plane area.

Figure 6.2 illustrates the DC characteristics of the fabricated HFETs. Hence, both the Gate and the Drain have been connected to 6 V DC sources (4×1.5 V AAA Batteries) through a series variable resistances and inductances as shown in Figure 6.5 (a). In addition, inductances have been inserted to act as RF chocks. The Drain current at V_{GS} = 0 V is 17 mA. The simulated reflection coefficient is present in Figure 6.3 (a), from

which it can be noticed that turning the HFETs ON cause to kill the impedance matching bandwidth around 4.56 GHz. Figure 6.3 (b) illustrates the simulated radiation pattern for HFETs OFF case with 5.77 dBi gain and 80% radiation efficiency. This band operates near the $TE_{\delta 11}$ resonance mode frequency of 4.1 GHz. On the other hand, turning the HFETs ON results in a reduced gain reduced of ~ -2 dBi with a radiation efficiency of less than 1%.

The measured reflection coefficient is illustrated in Figure 6.3(c) with considerable differences compare to the expected simulated results. There are four biasing cases: V_{DD} and V_{GG} are OFF (Both OFF), V_{DD} is ON and V_{GG} is OFF, V_{DD} OFF and V_{GG} ON, and Both V_{DD} and V_{GG} are ON (Both ON). Except for the last case, the three first cases shown almost identical reflection coefficients, even with change of the Drain current in the second case. Therefore, only the "Both OFF" case is considered. An impedance matching bandwidth has been measured at a centre frequency of 4.1 GHz and a 16.7% bandwidth, which corresponds to the $TE_{\delta 11}$ DRA resonance mode. On the other hand, it can be noticed that the "Both ON" case provided a different type of reconfigurability, where instead of eliminating the main band, two bands have been activated. The first at a centre frequency of 3.1 GHz and 26.7% impedance matching bandwidth, and the second at 4.51 GHz with a 4.9% bandwidth. It can be concluded from these results that although the inserted charges are not sufficient to short out the slot, they caused a change in the field distribution inside the slot, hence changing the antenna response. In addition, a narrow impedance matching bandwidth of ~ 2% exists at 7 GHz for the HFETs OFF, which nearly vanishes for the HFETs ON state with a bandwidth of less than 1%.

Far-field radiation patterns have been measured, and the results have been unsatisfactory for the four measured frequencies. Figure 6.3 (d) illustrates the measured radiation patterns at both the H-plane ($\varphi=0^{o}$) and E-plane ($\varphi=90^{o}$). All the gains are very low in the

negative range in both cases where the HFETs are activated or not. However, in all case it can be noticed that changing the state of the HFETs change the radiation patterns and its gain noticeably. These unsatisfactory results can be related to several factors, such as the required wiring inside the slot, the range of operating frequencies, and to a minimal effect of the small size of the ground plane ($1.4\lambda_0$ at 4.1 GHz).

These results lead to the conclude that the HFETs can be expected to be an excellent candidate for antenna reconfigurability application at a much higher range of frequencies due to its physical characteristics such as skin depth and charge carriers' density. However, these active devices are not suitable to be used for aperture coupled DRA reconfigurability.

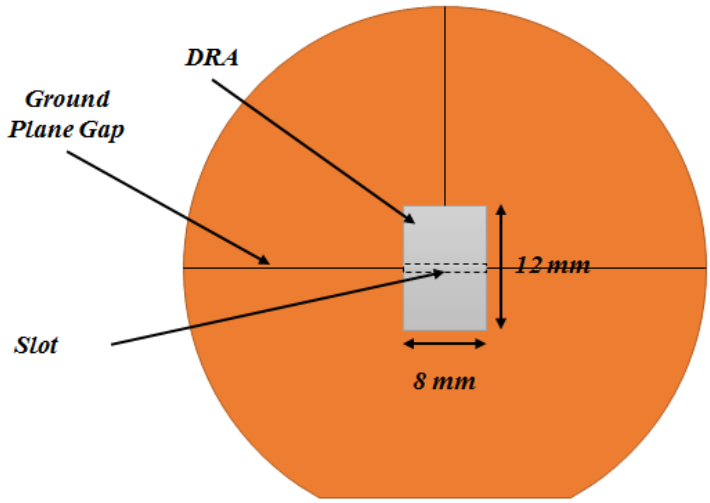

(a)

Figure 6.1 Slot-Fed HFET Reconfigurable DRA (a) Top View Block diagram, (b) Side View Block diagram, (c) General View of the Antenna with DC Control, (d) Top View, and (e) Back View showing the Ground Plane through the Semi-Transparent Substrate

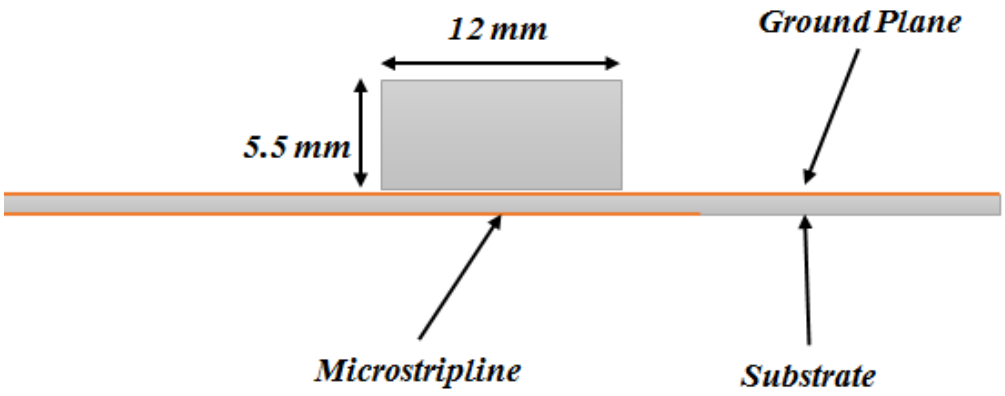

(b)

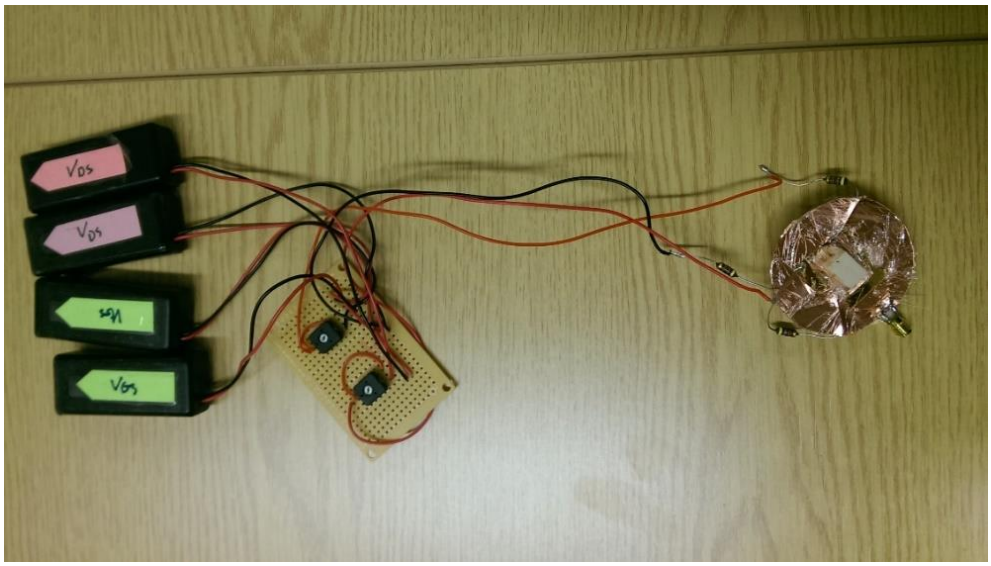

(c)

Figure 6.1 Continued

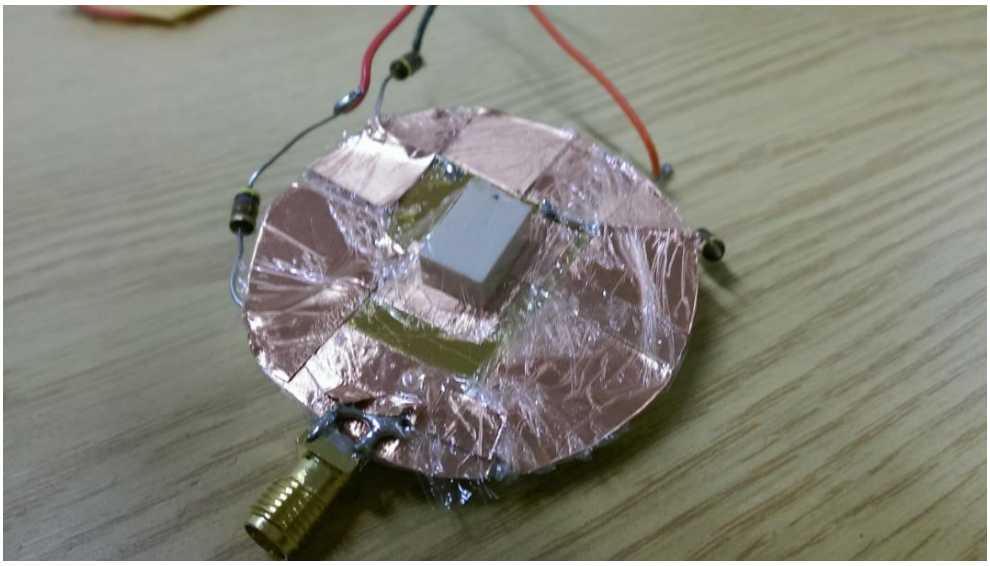

(d)

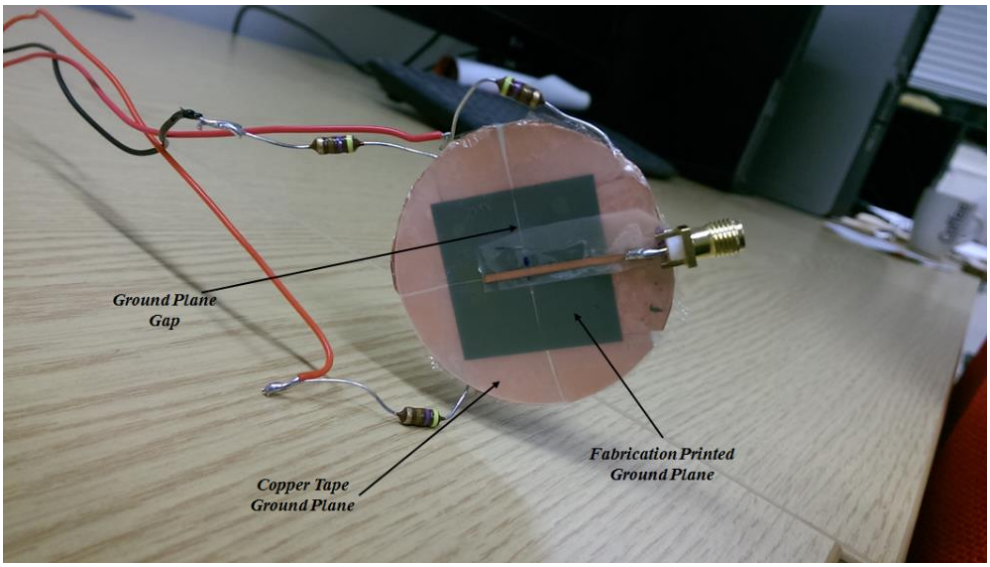

(e)

Figure 6.1 Continued

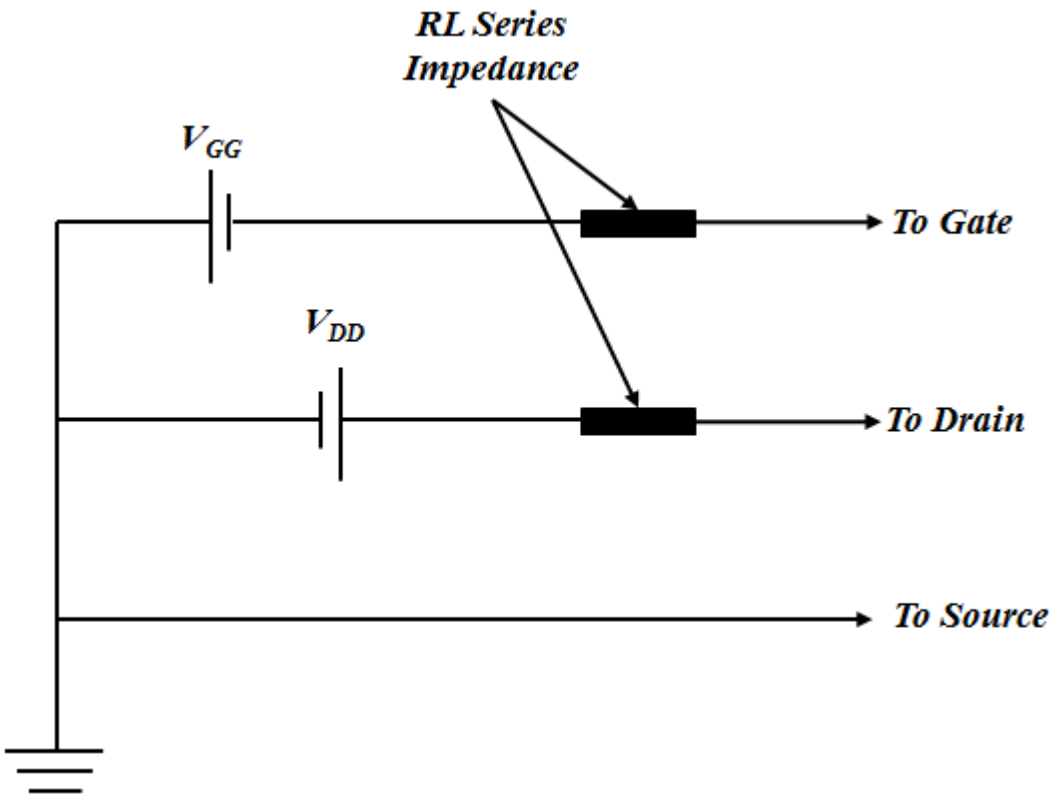
RL Series
Impedance
V_{GG}
V_{DD}
To Gate
To Drain
To Source

(a)

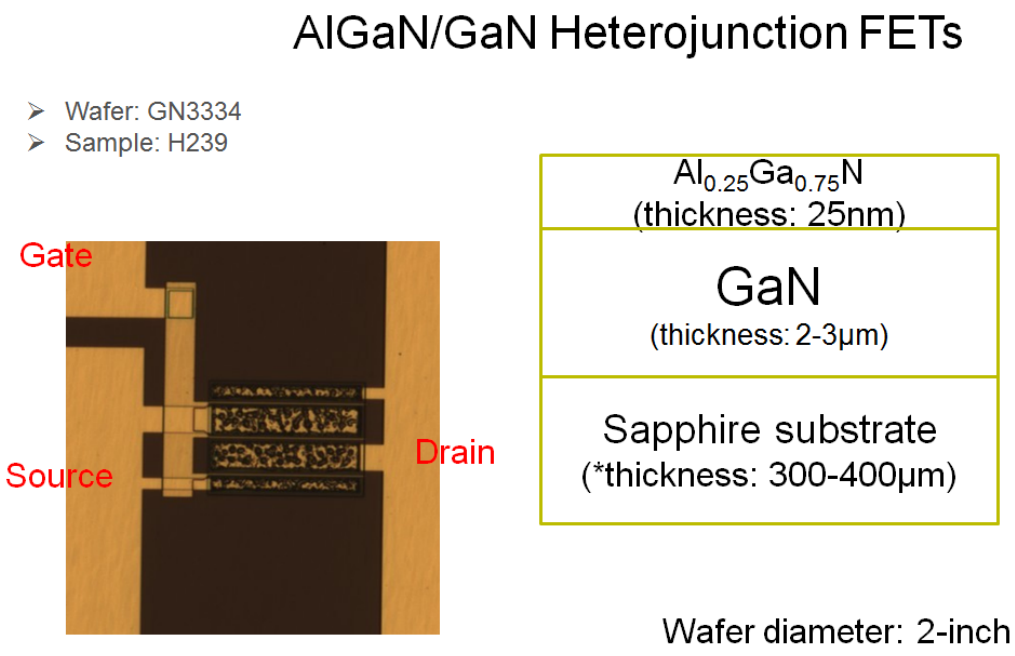
AlGaN/GaN Heterojunction FETs
Wafer: GN3334
Sample: H239
Gate
Source
Drain
$Al_{0.25}Ga_{0.75}N$
(thickness: 25nm)
GaN
(thickness: 2-3μm)
Sapphire substrate
(*thickness: 300-400μm)
Wafer diameter: 2-inch

(b)

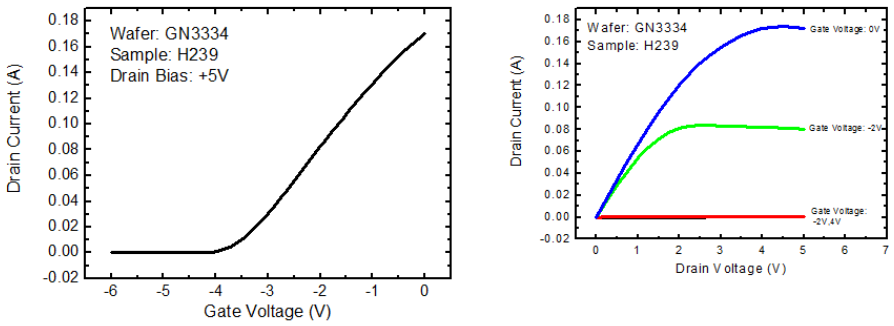

(c)

Figure 6.2 AlGaN/GaN HFET (a) DC Control Circuit Block Diagram, (b) Fabrication Data and Zoomed Photograph*, and (c) DC Characteristics*

* Figure 6.2 (b-c) are courtesy of Dr. Kean Boon Lee, Semiconductor Materials and Devices group at the University of Sheffield

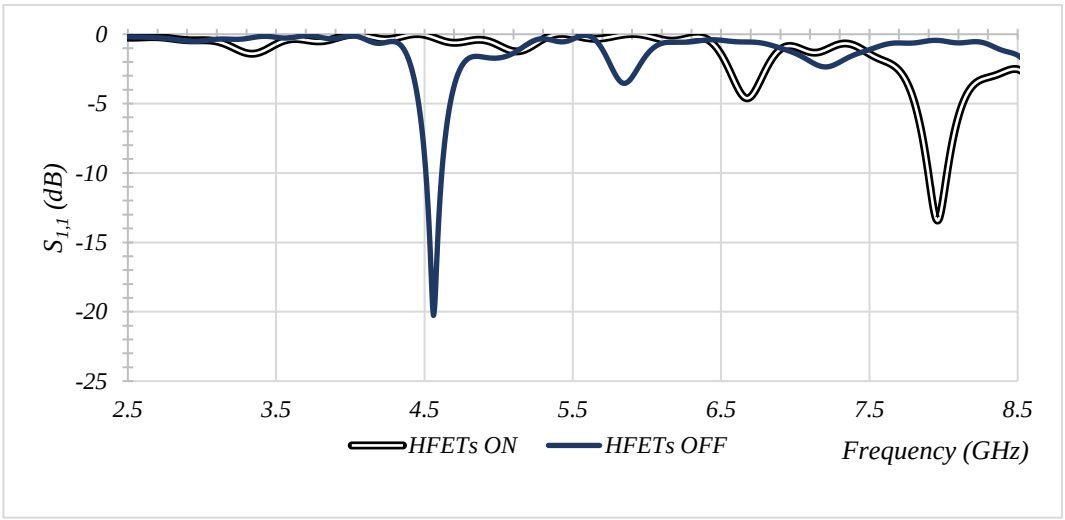

(a)

Figure 6.3 Slot Fed HFET Reconfigurable RDRA (a) Simulated Reflection Coefficients, (b) Simulated Radiation Pattern at 4.56 GHz, (c) Measured Reflection Coefficients, and (d) Measured Radiation Pattern at H-Plane (φ=0°) (Left) and H-Plane (φ=90°) (Right)

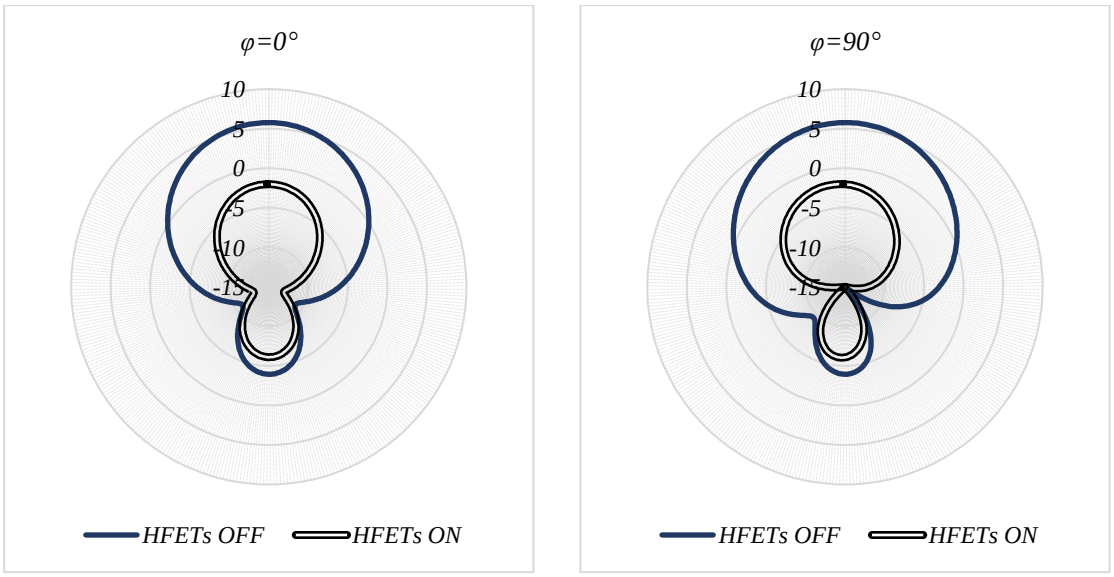

(b) 4.56 GHz

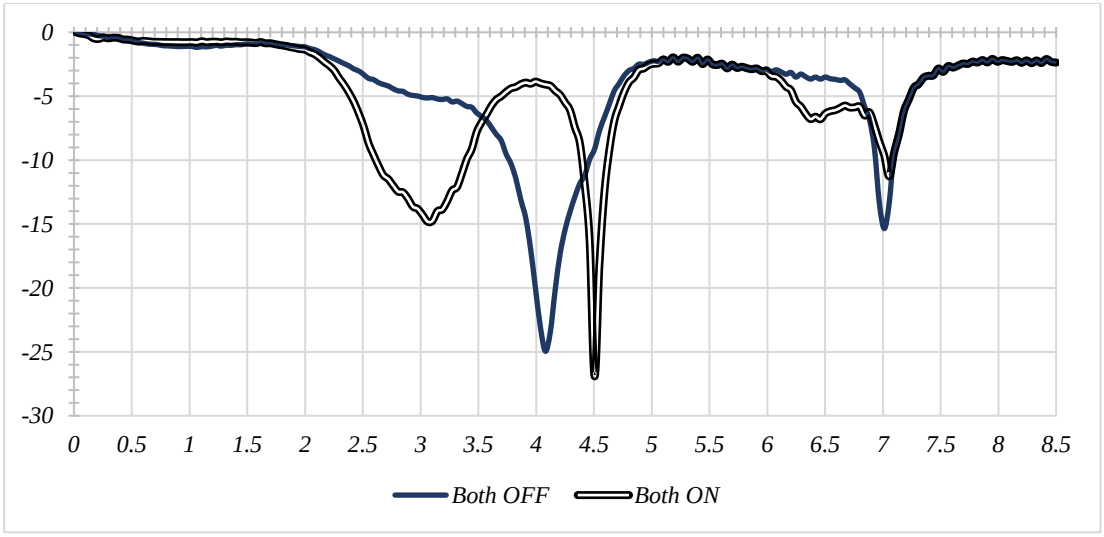

(c)

Figure 6.3 Continued

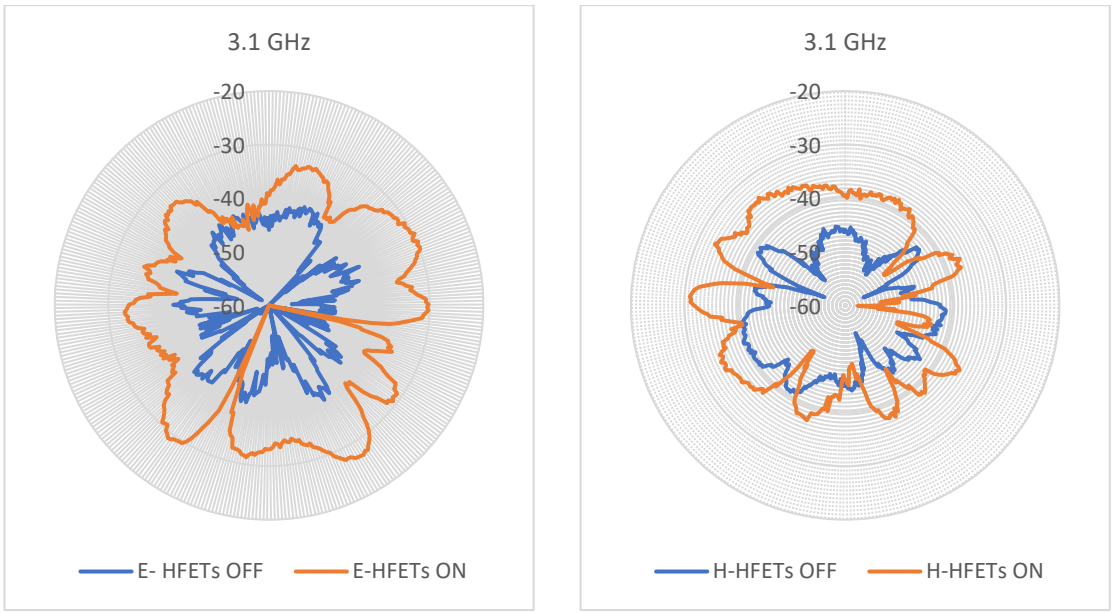

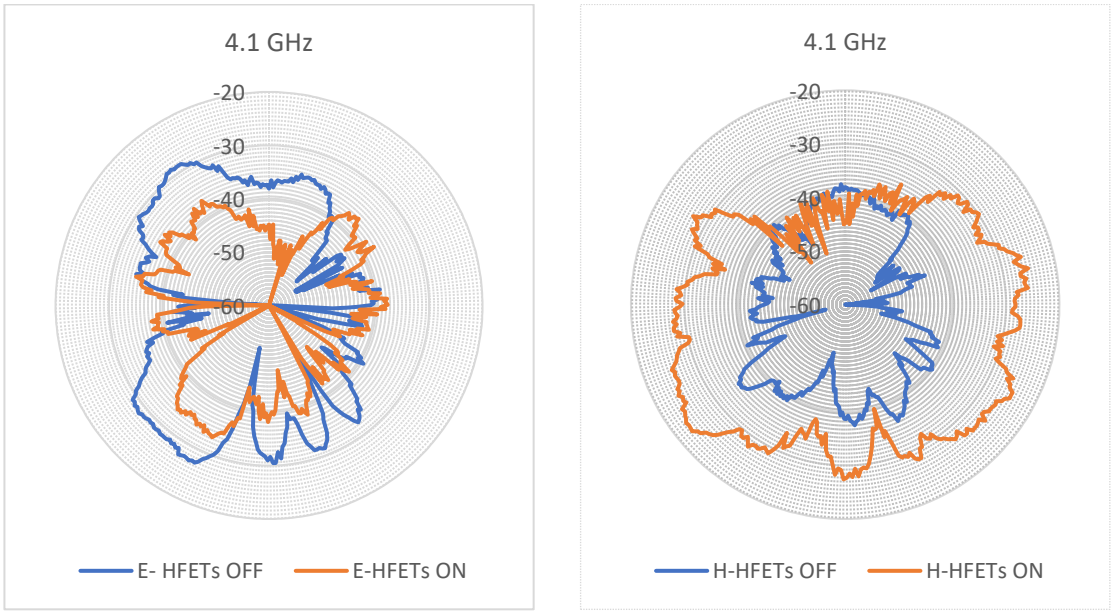

(d)

* ON = Antenna ON, OFF = Antenna OFF

H = H-plane (φ=0º), E = E-plane (φ=90º)

Figure 6.3 Continued

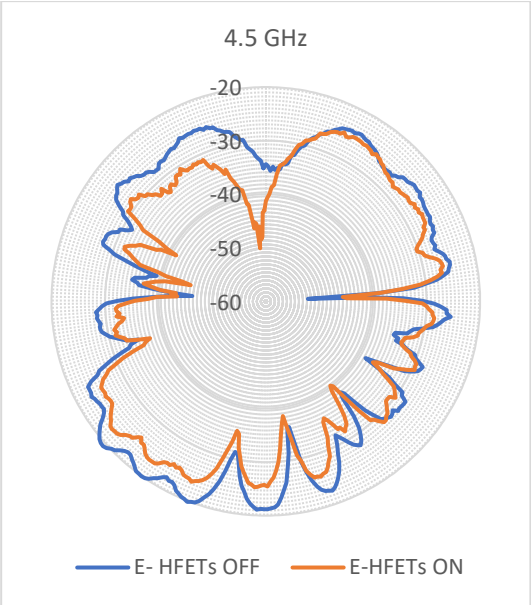

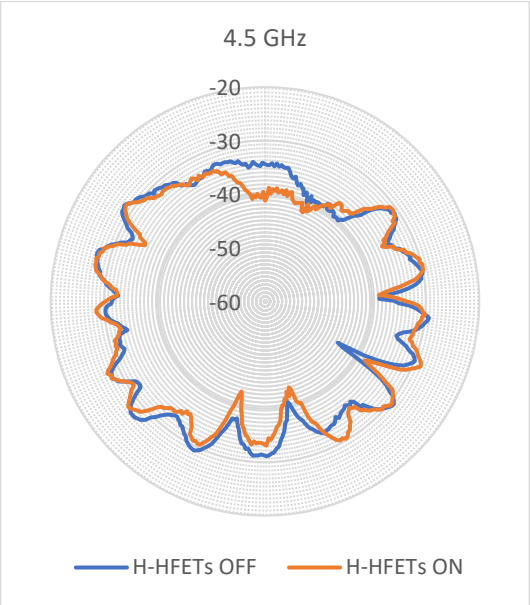

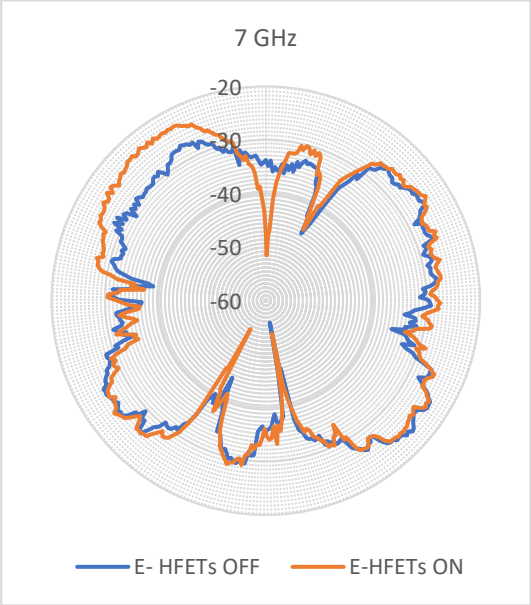

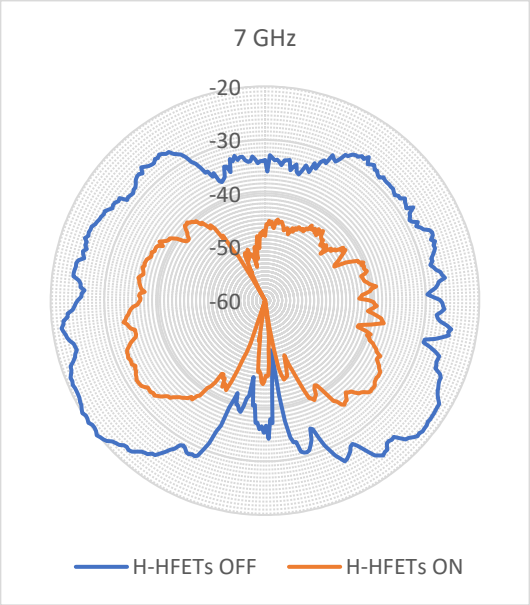

(d) Continued

Figure 6.3 Continued

6.4 Conclusion

Two Semiconductor plasma reconfigurability techniques have been discussed in this chapter for a slot fed RDRA. The first technique is to use the well-established SPIN diodes, while the second is to use HFETs. At a first glance, the main advantage of the semiconductor plasma reconfigurable devices over the bulky semiconductor RF devices is the circuit integration ability, which allows to control the antenna accuracy during fabrication. This can be illustrated by comparing the built models in Chapter 4 against the model shown in Figure 6.1. In addition, this fabrication process offers reduced slots airgap under the DRA drastically, hence reducing the effect on the operating frequency and radiation efficiency.

The shown mixed results, due to some uncertainty about the limited space of the HFETs that convey the plasma islands and its limited thickness. The measured reflection coefficients show a mix of both sides of the theory. In the case of the HFETs disconnected from the control voltages, two bands have been obtained at 4.1 GHz and 7 GHz. These two bands demonstrate different reactions to activating the HFETs voltage controls. The first band suffered from what is appeared as a frequency shift, while the second has been subjected to the expected band deterioration. This can be attributed to the lower frequency limit affected by the skin depth criteria [1, 2]. This limit is expected to increase with the decrease of the charged plasma thickness. Hence, since the plasma island inside an HFETs is much thinner than the one inside a SPIN diode, it is rational to expect it to increase much higher than the 1 GHz lower limit of a SPIN diode [1, 2]. In addition, the far-field results have been very poor. This mainly due to the structure of the HFETs connects that interfere with the role of the aperture coupling for the DRA. Hence, it has been suggested that the HFETs are not the best choice in this reconfiguration technique. However, the

overall results shown that HFETs can be used as an active semiconductor plasma medium in other antenna configurations.

In summary, HFETs can be expected to outperform SPIN diodes at higher frequencies than the. In addition, it is important to consider the size limit and substrate issues, which can be performed easily. The size limit has been introduced to deal with the current heat dissipation problem and its effect on the Sapphire substrate. However, since the HFETs are voltage controlled devices, input current can be expected to be nearly zero. In addition, the substrate can be replaced with a silicon one with a higher heat capacity. Hence, HFET devices are expected to perform better in miniaturised integrated reconfigurable antennas with higher frequency range than the investigated range in this research.

References

[1] A. E. Fathy, A. Rosen, H. S. Owen, F. McGinty, D. J. McGee, G. C. Taylor, et al., "Silicon-based reconfigurable antennas-concepts, analysis, implementation, and feasibility," IEEE Transactions on Microwave Theory and Techniques, vol. 51, pp. 1650-1661, 2003.

[2] Y. Yashchyshyn, K. Derzakowski, and P. Bajurko, "Reconfigurable semiconductor antenna for sub-THz frequencies," in Antennas and Propagation (EuCAP), 2013 7th European Conference on, 2013, pp. 537-540.

[3] G. C. Taylor, A. Rosen, A. E. Fathy, P. K. Swain, and S. M. Perlow, "Surface PIN device," ed: Google Patents, 2003.

[4] G. C. Taylor, S. M. Perlow, A. Rosen, A. E. Fathy, S. Kanamaluru, and M. Esherbiny, "Reconfigurable antenna," ed: Google Patents, 2003.

[5] J. Tirado, J. Sanchez-Rojas, and J. Izpura, "2D simulation of static surface states in AlGaN/GaN HEMT and GaN MESFET devices," Semiconductor science and technology, vol. 20, p. 864, 2005.

[6] Y. Chang, K. Tong, and C. Surya, "Numerical simulation of current–voltage characteristics of AlGaN/GaN HEMTs at high temperatures," Semiconductor science and technology, vol. 20, p. 188, 2005.

[7] R. L. Haupt and M. Lanagan, "Reconfigurable Antennas," IEEE Antennas and Propagation Magazine, vol. 55, pp. 49-61, 2013.

Chapter Seven

Summary, Conclusion and Future Work

7.1 Summary

The research is focused on to investigating reconfigurability of several DRA configurations using semiconductor RF PIN diodes switches in Chapters 3-5, and HFETs as semiconductror plasma devices in Chapter 6. In general, these applied techniques proved to have the required reconfiguration characteristics for polarisation, frequency/mode tuning and beam steering.

7.1.1 Chapter Three Summary

Two polarisation reconfiguration approaches have been investigated. In both models; LP, RHCP, and LHCP radiations have been achieved. In the first configuration a hemispherical DRA that is excited with a reconfigurable annular slot has been considered. Based on the fact that shortening the annular slot at a specific point can lead to CP, instead of LP, radiation, PIN diodes have been employedto short out the slot at 90° angular distance from the feed point. Furthermore, two PIN diodes on opposite sides of the slot have been employed to achieve LP/RHCP/LHCP reconfigurability. An axial ratio of 1.7% has been achieved for the first case compared to 1.4% for the second case, at 3.57 GHz and 3.22 GHz, respectively. In addition, it has been shown that shortening both slot sides generates LP radiation, since this provides a configuration in which th DRA is excited with a couple of C-shaped slots.

The second configuration has been proposeded to achieve polarisation reconfigurability with a dual band CP notched RDRA that incorporates a reconfigurable parasitic strip. The DRA is excitedusing a flat metallic strip placedon one of the rigid DRA side. In addition,

a parasitic strip has been added to one of the notched sides to excite the required circular polaristion radiation. It has been shown that connecting and disconnecting the parasitic strip to the ground plane generates CP and LP radiations, respectively. Hence, two cases have been investigated. In the first a single reconfigurable parasitic strip has been used to gernerate the dual CP radiation,. On the other hand, simulations showed that dual reconfigurable parasitic strips reduce the second AR bandwidth. However, these bands can operate in either LP, RHCP, or LHCP, depending on the PIN diodes activation. Moreover, activating both PIN diodes elemenates the impedance matching bandwidth, since both parasitic strips have similar effect on the field distribbution inside the DRA albiet in opposite direction cuasing the deteroiratation of the total radiation.

7.1.2 Chapter Four Summary

Reconfigurable slot-fed RDAR has been investigated in Chapter 4. Firstly, a single slot-fed reconfigurable DRA has been designed and implemented. This model proved to be valid as expected for the simple ON/OFF operation. However, a couple of points had to be addressed. The first is with respect to the insertion of the PIN diodes inside the substrate and its effect on the field distribution and the interface with the DRA. The second issue is concerned with using off-centre microstripline feed to improve the impedance matching in which an extra PIN diode has been added to force stronger shortening of the slot. Hence, it has been suggested to avoid these issues in the multi-slots-fed DRA. In addition, a third issue has been addressed when the operating frequency band is around 6 GHz, which is close to the used PIN diode upper operating frequency limit. Hence, it is suggested to double the DRA dimensions, which halfed the resonance mode frequency as expected.

The observed issues in the single slot model have been considered in both dual and triple slot-fed DRA designs. The ratio of the DRA to the slots size is critical to the total ground

plane-DRA interface. Hence, in the triple slots model, the slots width has been reduced to improve the interface, hence, the radiation efficiency. On the other hand, the introduction of non-ideally shorted parasitic slots caused some changes in the impedance matching bandwidths, radiation efficiency, and main beam direction. However, both models proved viable for mode reconfiguration as modes such as $TE_{\delta 11}$, $TE_{\delta 21}$, $TE_{\delta 31}$, and $TE_{\delta 13}$ have been excited. However, the existence of the parasitic slots proved to have a distributive effects on the field distribution for each mode due to the interface issue.

7.1.3 Chapter Five Summary

Reconfigurable linear DRA arrays have been investigated in Chapter Five. All the models are based on the single, and dual,-slot fed DRA configurations. Two, and four,-element DRA arrays have been investigated with initial elements separation of $\sim\lambda_0/2$ of the lower operating frequency with a minor change to improve efficiency and/or antenna reconfigrability. A narrow beam steering of ±15° for the two-elements array and ±12° for the four-elements array have been achieved at ~5.7 GHz. In addition, it has been noticed that more elements provide a narrower beam-width in the array axis plane, which agree with theory. In addition, due to the effects of the ground plane gaps, it has been obsereved that the gain has two maxima points at the φ=90° plane at θ =53° when both elements are coupled with active slots. On the other hand, dual slots configuration offer more reconfigurability options. In addition to the promising two-dimensional beam steering, some frequency tuning and reconfigurability have been achieved for a couple of bands in a multiple impedance matching bandwidth antenna array. Three impedance matching bandwidths have been observed in the dual-slot two-elements DRA array at 3.2 GHz, 3.6 GHz, and 4.9 GHz.

Although hese models demonstrated good prospect as multi-purpose reconfigurable arrays, the efficiency and gain are less than satisfactory in several cases, due to the fact

these are preliminary investigation models, and additional time is needed to improve the design. This is especially true for the four-element dual-slot fed DRA array, which represent the most promising model with a wider range of possibilities. In addition, it can be expected that adding more elements can enhance the array reconfigurability choices.

7.1.4 Chapter Six Summary

The main object of this project is investigating a reconfigurable semiconductor plasma antenna using SPIN diodes to create a plasma island. However, due to budget and fabrication issues, an alternative has been introduced in using the GaN/AlGaN HFET investigated in Chapter Six. The fabricated prototype isbased on Chapter Four's single slot-fed DRA design. In addition, Sapphire has been chosen instead of Silicon-On-Insulator (SOI) for the substrate that has a diameter of ~5 cm, which equals to $0.76\lambda_0$ at a 4.56 GHz central frequency. The use of the HFETs as a replacement to the SPIN diodes has partially provid the expected results. Although turning the HFET ON did not completely eleminate the impedance matching bandwidth, it caused some kind of frequency tuning for the reflection coefficients. On the other hand, the HFET ON case shown the expected impedance matching bandwidth vanishing of a non-ideal semi-metallic short inside the slot. This issue is expected due to the limited size of the HFETs surface as well as the very thin skin depth that isinversly related to the lower operating frequency. In addition, far-field results have unsatisfactory with very low negative gain values. This points to the issue of the requied wiring of the HFETs which affects the fild coupling through the aperture where the HFETs exists, which make the HFETs less fit to be used in this particular application. Hence, it is expected that HFETs can perform better in higher frequencies and other antenna types.

7.2 Conclusion and Future Work

In this project, two research directionshave been investigated; reconfigurable DRAs and reconfigurable semiconductor plasma antennas based on GaN/AlGaN HFET, in which both have shown promising results to some extent. The DRA polarisation reconfigurability can be extended into other DRA configurations easily since the introduced models in this research proved excellent prospect in this direction. In addition, reconfigurable slot-fed DRA are efficient in achieving a frequency/mode change. However, there is a limit on the number of reconfigurable slots that can be inserted to feed the DRA. Nevertheless, semiconductor plasma devices can boost this limit to some extent. On the other hand, reconfigurable DRA arrays have demonstrated a good prospect. However, deeper investigations and more improvements are essential in order to achieve viabilility of these designs. GaN/AlGaN HFET is promesing in the design and implementation of reconfigurable semiconductor plasma antennas . Bulky and integrated FETs have been used in numerous reconfigurable antenna designs. Hence, HFETs can be arguably compared and used in the same manner as FETs, which can be paralleled with SPIN and PIN diodes comparison.

In the future, GaN/AlGaN HFET can be created using alternative substrates with a higher heat capacity such as silicon. In addition, the total surface area can be increased since the power consumed and heat dissipated due to turning these devices ON is nearly zero. Moreover, the size of the HFETs and the expected high-frequency limit can be investigated for miniaturised high-frequency reconfigurable antennas. In addition, polarisation reconfigurability can be impoved to enhance the AR bandwidth by make some adjusments to the designs to accommodate the impedance changes due to using the PIN diode. Moreover, the RF switches can be replaced by semiconductor plasma devices. Another protentially useful approach is to consider optically injected semiconductor

plasma devices for both of the configurations that have been investigated in Chapter Three. This is owing to the fact that this approach reduces the wiring noise and effect problem on the polarisation, especially for the parasitic strip technique, where the wires can affect the DRA fields.

Likewise, semiconductor plamsa reconfigurable DRA array can be an interesting area to be investigated. Available semiconductor technology can helpin building massive linear and planar DRA reconfigurable arrays with reconfigurable semiconductor plasma devices that are fabricated on a semiconductor substrate. For example, the configurations studied in Chapter Five can be revised and miniturised for higher frequencies. In addition, these configurations represent the basis for designing large scale reconfigurale DRA palnar arrays based on a semiconductor substrate,. Such arrays can be used for beam steering as well as frequency tuning.

Appendices

Appendix A: Tables

Table A.1 Radiation properties for the array configuration of Figure 5.6 (a) at 5.6 GHz

Case	Central frequency (GHz)	BW %	Angular beamwidth at φ=0°,	main beam direction in the φ=0° plane	Maximum Gain	Maximum Gain Direction (φ, θ)	Efficiency %
0000	5.36, 5.91	3.2, 4.6	NG	NG	5.54	(90, 118)	35.8
0001	5.36, 5.94	3.8, 6.1	NG	NG	4.71	(89, 119)	43.9
0010	5.36, 5.92	4.1, 6.1	NG	NG	4.78	(88, 119)	41.7
0011	5.36, 5.9	5.5, 8.4	28.7	10	4.27	(89, 121)	54.7
0100	5.36, 5.92	4.1, 6.1	NG	NG	4.78	(92, 119)	41.7
0101	5.95	14.3	30.7	2	4.71	(89, 69)	50
0110	5.96	14.6	41.3	3	4.16	(90. 73)	46.7
0111	6.02	15.2	32.8	5	5.22	(87, 65)	51.1
1000	5.36, 5.94	3.8, 6.1	NG	NG	4.71	(91, 119)	43.9
1001	5.97, 5.35	9.0, 4.7	23.4	0	4.33	(90, 70)	50.2
1010	5.95	14.3	30.7	-2	4.71	(91, 69)	50
1011	6.01	15.3	26.2	2	5.42	(88, 64)	52.7
1100	5.36, 5.9	5.5, 8.4	28.7	-10	4.27	(91, 121)	54.7
1101	6.01	15.3	26.2	-2	5.42	(92, 64)	52.7
1110	6.02	15.2	32.8	-5	5.22	(93, 65)	51.1
1111	6.05	15.4	28.4	0	6.08	(0, 62)	54.4

Table A.2 Comparison of the Antenna Array Radiation Characteristics for the Array Excitation Sequences at 2.8 GHz with N/G Stands for Negative Gain

Case	Central frequency (GHz)	BW % in Degrees	Angular beamwidth at φ=0°	θ max at φ=0°	Maximum Gain	Efficiency %
0000	2.77	23	34.7	0	5.76	84.9
0006*	2.79	26.3	40.5	-5	4.63	83.1
000n*	2.79	26	40.9	-6	4.67	82.8
0060*	2.8	13	34.4	-6	4.64	80.0
0066*	2.82	9.4	43.3	-4	3.73	95.5
006n*	2.81	8.7	43.3	-8	3.89	86.6
00n0*	2.8	10.1	34.1	-5	4.56	79.0
00n6*	2.81	8.8	41.6	-6	3.81	84.4
00nn*	2.82	8	43.3	-9	3.64	79.1
0606*	2.8	6.8	40	2	3.61	73.0
060n*	2.8	6.9	40.2	1	3.53	72.8
0660	2.8	5.8	33.7	0	3.84	65.8
0666*	2.82	6.2	39.5	2	2.9	82.0
066n*	2.81	5.6	41.3	-2	2.95	71.2
06n0*	2.81	5.7	33.1	0	3.76	63.1
06n6*	2.82	5.3	40	0	3.06	66.4
06nn*	2.81	4.8	41.3	-3	2.86	59.7
0n06*	2.82	5.3	38.6	0	2.89	63.5
0n0n*	2.81	4.6	40.7	-4	2.59	56.6
0n66*	2.82	6	39.6	2	2.66	79.5
0n6n*	2.82	5.4	40.7	-3	2.85	68.7
0nn0	2.81	5.6	32.5	0	3.66	60.0
0nn6*	2.82	5.3	22.3	0	2.89	63.5
0nnn*	2.81	4.6	35.7	-4	2.59	56.6
6006	2.8	7.2	48.4	0	3.12	78.2
600n*	2.8	7.4	48.8	-1	3.14	77.8
6066*	2.82	7.8	51.8	3	2.38	89.2

606n*	2.81	6.9	52.4	-4	2.67	79.1
60n6*	2.81	7	48.7	1	2.58	76.8
60nn*	2.81	6.3	50.9	-6	2.41	70.3
660n*	2.82	7.9	51.6	-4	2.25	88.9
6666	2.83	5.9	N/G	N/G	1.74	98.2
666n*	2.82	5.4	N/G	N/G	1.82	88.3
66n6*	2.83	5.3	N/G	N/G	1.36	84.1
66nn*	2.82	4.6	N/G	N/G	1.24	76.7
6n0n*	2.81	7.1	48.6	0	2.51	76.9
6n6n*	2.82	4.8	N/G	N/G	1.99	72.1
6nn6	2.82	4.5	N/G	N/G	1.83	67.0
6nnn*	2.82	3.8	N/G	N/G	1.6	59.4
n00n*	2.8	10.4	49.5	0	3.18	77.4
n06n*	2.81	6.9	52.9	-3	2.52	78.9
n0nn*	2.81	6.4	51.3	-5	2.29	70.5
n66n	2.82	4.9	N/G	N/G	1.83	76.3
n6nn*	2.82	4.1	N/G	N/G	1.45	64.4
nnnn	2.82	3.1	N/G	N/G	1.3	51.0

***** The case has a reversed ordered activation combination

Table A.3 Comparison of the Antenna Array Radiation Patterns for the Array Excitation Sequences at the Four Bands with (N/G) Stands for Negative Gain and (N/A) Stands for Not Available within Impedance Matching Bandwidth

Band	2.8					3.2					4.2					4.6				
Case	Beamwidth φ= 0°	Beamwidth φ= 90°	φ Max	θ Max	Max Gain	Beamwidth φ= 0°	Beamwidth φ= 90°	φ Max	θ Max	Max Gain	Beamwidth φ= 0°	Beamwidth φ= 90°	φ Max	θ Max	Max Gain	Beamwidth φ= 0°	Beamwidth φ= 90°	φ Max	θ Max	Max Gain
0000	34.7	135.8	90	37	5.76	N/G	64.5	270	38	5.17	N/G	44.9	90	56	7.76	21.9	39.2	270	4	6.54
0006	40.5	138.6	98	37	4.63	N/G	64.8	271	39	2.25	N/G	45.6	88	55	7.79	22.0	36.0	314	6	6.38
000n	40.9	137.3	98	37	4.67	N/G	65.3	268	38	4.97	N/G	45.4	90	56	7.68	21.7	38.2	275	4	6.62
0060	34.4	140.4	260	34	4.64	N/G	63.6	276	39	3.73	N/G	45.3	89	55	7.78	22.2	37.5	292	4	6.66

9900	43.3	134.8	266	34	3.73	N/G	64.9	276	41	2.95	N/G	46.7	87	54	7.66	21.5	36.6	321	6	7.53
900n	43.3	137.2	258	34	3.89	N/G	64.7	274	41	3.16	N/G	46.3	89	55	7.63	21.9	36.7	298	4	6.71
00n0	34.1	140.8	260	33	4.56	N/G	64.2	274	41	3.87	N/A	N/A	N/A	N/A	N/A	22.1	39.1	270	4	6.68
00n6	41.6	139.0	262	34	3.81	N/G	64.7	276	42	3.24	N/G	47.1	88	55	7.64	22.2	35.9	318	5	6.53
00nn	43.3	141.0	257	34	3.64	N/G	64.7	272	42	3.56	N/A	N/A	N/A	N/A	N/A	22.0	38.1	276	3	6.75
0606	40.0	136.9	276	35	3.61	N/G	64.7	265	41	3.72	N/G	46.4	89	53	7.86	22.4	35.2	297	5	6.42
060n	40.2	137.7	275	34	3.53	N/G	65.8	261	41	3.56	N/G	46.0	91	55	7.77	22.1	36.7	252	4	6.67

0660	33.7	127.7	270	35	3.84	N/A	N/A	N/A	N/A	N/A	N/G	46.0	90	53	7.82	22.8	37.0	270	4	6.85
0666	40.1	117.2	276	36	2.90	N/A	N/A	N/A	N/A	N/A	25.7	47.5	88	52	7.82	22.1	37.3	307	5	7.74
066n	41.5	118.7	269	36	2.95	N/A	N/A	N/A	N/A	N/A	N/G	47.0	90	53	7.76	22.5	36.3	274	4	6.95
06n0	33.1	130.9	271	35	3.76	N/A	N/A	N/A	N/A	N/A	N/G	46.2	91	55	7.67	22.3	38	249	4	6.70
06n6	39.1	123.9	273	36	3.06	N/A	N/A	N/A	N/A	N/A	N/G	47.8	89	53	7.65	22.5	35.7	297	5	6.52
06nn	41.5	127.4	268	35	2.68	N/A	N/A	N/A	N/A	N/A	N/G	47.3	91	55	7.71	22.2	37.2	253	4	6.78
0n06	39.4	138.8	275	34	3.54	N/G	65.2	267	41	3.88	N/G	46.5	88	55	7.72	22.4	36.2	317	5	6.45

0n0n	39.6	139.5	274	34	3.48	N/G	66.1	263	41	3.63	N/A	N/A	N/A	N/A	N/A	21.9	38.5	273	4	6.71
0n66	38.4	123.5	275	35	2.66	N/A	N/A	N/A	N/A	N/A	N/G	47.6	87	54	7.59	21.8	36.9	320	6	7.58
0n6n	40.7	124.2	268	36	2.85	N/A	N/A	N/A	N/A	N/A	N/A	N/A	N/A	N/A	N/A	22.1	37.0	296	4	6.80
0nn0	32.5	133.9	270	34	3.66	N/A	N/A	N/A	N/A	N/A	N/A	N/A	N/A	N/A	N/A	22.3	39.6	270	4	6.74
0nn6	38.5	128.3	272	35	2.89	N/A	N/A	N/A	N/A	N/A	N/A	N/A	N/A	N/A	N/A	22.4	36.6	313	6	6.60
0nnn	34.8	131.3	267	35	2.59	N/A	N/A	N/A	N/A	N/A	N/A	N/A	N/A	N/A	N/A	22.2	38.7	275	4	6.83
6006	48.4	141.9	270	34	3.11	N/G	65.1	270	39	5.32	N/G	46.7	90	53	7.67	23.9	33.8	270	4	5.84

600n	48.8	141.0	90	38	3.14	N/G	65.7	267	39	5.07	N/G	46.1	92	55	7.75	22.0	35.5	225	5	6.44
6006	51.8	131.0	271	36	2.38	N/G	65.7	275	42	2.94	20.7	48.1	90	52	7.66	22.7	35.8	288	4	7.03
606n	52.3	132.1	263	35	2.67	N/G	65.5	272	42	3.15	N/G	47.5	91	53	7.72	22.2	37.4	244	4	6.45
60n6	48.7	134.8	267	35	2.58	N/G	65.4	274	42	3.26	N/G	48.3	90	53	7.43	23.9	34.1	270	4	5.93
60nn	51.0	137.5	261	35	2.41	N/G	65.4	271	42	3.61	N/G	47.6	93	54	7.66	22.5	35.6	226	5	6.56
660n	51.6	132.4	268	35	2.25	N/G	67.6	261	43	2.70	N/G	47.3	93	53	7.67	21.6	36.1	221	6	7.54
6666	N/G	68.8	270	37	1.74	N/A	N/A	N/A	N/A	N/A	21.4	49.9	90	50	7.69	22.0	38.8	270	4	8.16

666n	N/G	69.9	263	37	1.82	N/A	N/A	N/A	N/A	N/A	23.9	48.7	92	51	7.77	22.0	37.0	236	5	7.83
66n6	N/G	72.4	267	37	1.63	N/A	N/A	N/A	N/A	N/A	20.7	49.7	91	52	7.51	22.8	36.2	252	4	7.13
66nn	N/G	77.0	261	36	1.24	N/A	N/A	N/A	N/A	N/A	N/G	49.0	93	53	7.64	21.7	36.5	222	6	7.66
6n0n	48.6	135.7	272	35	2.51	N/G	66.8	262	43	3.03	N/G	47.7	92	54	7.52	22.1	35.6	224	5	6.54
6n6n	N/G	72.1	265	37	1.99	N/A	N/A	N/A	N/A	N/A	22.6	49.0	91	53	7.57	22.3	35.1	244	4	6.62
6nn6	N/G	76.3	270	36	1.83	N/A	N/A	N/A	N/A	N/A	21.2	50.4	90	53	7.24	24.4	34.5	270	4	6.17
6nnn	N/G	122.4	264	36	1.60	N/A	N/A	N/A	N/A	N/A	N/A	N/A	N/A	N/A	N/A	22.7	35.7	227	5	6.75

n00n	49.5	139.7	90	38	3.18	N/G	66.4	270	39	4.73	N/G	45.8	90	56	7.66	21.6	37.7	270	4	6.69
n06n	52.9	133.5	264	35	2.52	N/G	67.2	277	42	2.89	N/G	46.9	89	54	7.64	21.9	35.9	293	4	6.74
n0nn	51.2	138.7	262	35	2.29	N/G	66.5	275	43	3.32	N/A	N/A	N/A	N/A	N/A	21.9	37.7	274	3	6.75
n66n	N/G	69.8	270	37	1.83	N/A	N/A	N/A	N/A	N/A	N/G	48.2	90	52	7.69	22.4	35.6	270	4	7.07
n6nn	N/G	74.7	270	36	1.45	N/A	N/A	N/A	N/A	N/A	N/A	N/A	N/A	N/A	N/A	22.0	36.3	248	4	6.90

Appendix B: Datasheets

B1: Infineon-BAR50SERIES PIN Diodes

Silicon PIN Diodes

- Current-controlled RF resistor for switching and attenuating applications
- Frequency range above 10 MHz up to 6 GHz
- Especially useful as antenna switch in mobile communication
- Very low capacitance at zero volt reverse bias at freuencies above 1 GHz (typ. 0.15 pF)
- Low forward resistance
- Very low harmonic distortion
- Pb-free (RoHS compliant) package
- Qualified according AEC Q101[1)]

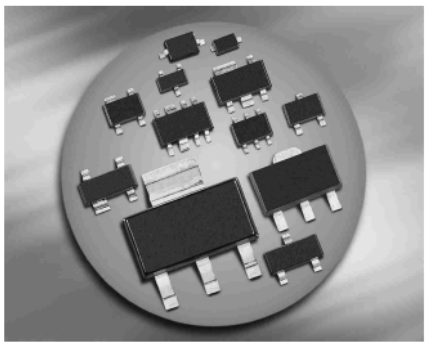

AEC Qualified RoHS

BAR50-02L
BAR50-02V
BAR50-03W

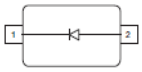

Type	Package	Configuration	L_S(nH)	Marking
BAR50-02L*	TSLP-2-1	single, leadless	0.4	AB
BAR50-02V	SC79	single	0.6	a
BAR50-03W	SOD323	single	1.8	blue A

[1]*BAR50-02L is not qualified according AEC Q101

Maximum Ratings at T_A = 25°C, unless otherwise specified

Parameter	Symbol	Value	Unit
Diode reverse voltage	V_R	50	V
Forward current	I_F	100	mA
Total power dissipation	P_{tot}		mW
BAR50-02L, $T_S \leq$ 130°C		250	
BAR50-02V, $T_S \leq$ 120°C		250	
BAR50-03W, $T_S \leq$ 115°C		250	
Junction temperature	T_j	150	°C
Operating temperature range	T_{op}	-55 ... 125	
Storage temperature	T_{stg}	-55 ... 150	

Thermal Resistance

Parameter	Symbol	Value	Unit
Junction - soldering point[1)]	R_{thJS}		K/W
BAR50-02L		≤ 80	
BAR50-02V		≤ 120	
BAR50-03W		≤ 140	

Electrical Characteristics at T_A = 25°C, unless otherwise specified

Parameter	Symbol	Values			Unit
		min.	typ.	max.	
DC Characteristics					
Reverse current V_R = 50 V	I_R	-	-	50	nA
Forward voltage I_F = 50 mA	V_F	-	0.95	1.1	V

[1]For calculation of R_{thJA} please refer to Application Note Thermal Resistance

Electrical Characteristics at T_A = 25°C, unless otherwise specified

Parameter	Symbol	Values			Unit
		min.	typ.	max.	
AC Characteristics					
Diode capacitance	C_T				pF
V_R = 1 V, f = 1 MHz		-	0.24	0.5	
V_R = 5 V, f = 1 MHz		-	0.2	0.4	
V_R = 0 V, f = 100 MHz		-	0.2	-	
V_R = 0 V, f = 1...1.8 GHz, BAR50-02L		-	0.1	-	
V_R = 0 V, f = 1...1.8 GHz, all other		-	0.15	-	
Reverse parallel resistance	R_P				kΩ
V_R = 0 V, f = 100 MHz		-	25	-	
V_R = 0 V, f = 1 GHz		-	6	-	
V_R = 0 V, f = 1.8 GHz		-	5	-	
Forward resistance	r_f				Ω
I_F = 0.5 mA, f = 100 MHz		-	25	40	
I_F = 1 mA, f = 100 MHz		-	16.5	25	
I_F = 10 mA, f = 100 MHz		-	3	4.5	
Charge carrier life time	τ_{rr}	-	1100	-	ns
I_F = 10 mA, I_R = 6 mA, measured at I_R = 3 mA, R_L = 100 Ω					
I-region width	W_I	-	56	-	µm
Insertion loss[1)]	I_L				dB
I_F = 3 mA, f = 1.8 GHz		-	0.56	-	
I_F = 5 mA, f = 1.8 GHz		-	0.4	-	
I_F = 10 mA, f = 1.8 GHz		-	0.27	-	
Isolation[1)]	I_{SO}				
V_R = 0 V, f = 0.9 GHz		-	24.5	-	
V_R = 0 V, f = 1.8 GHz		-	20	-	
V_R = 0 V, f = 2.45 GHz		-	18	-	
V_R = 0 V, f = 5.6 GHz		-	12	-	

[1]BAR50-02L in series configuration, Z = 50 Ω

B2: T-Ceram E-20 Dielectric Resonators

Dielectric resonators

Ceramic **dielectric resonators** are an attractive, low cost alternative to metallic resonant cavities where they have the advantage of small size without reduction in performance.

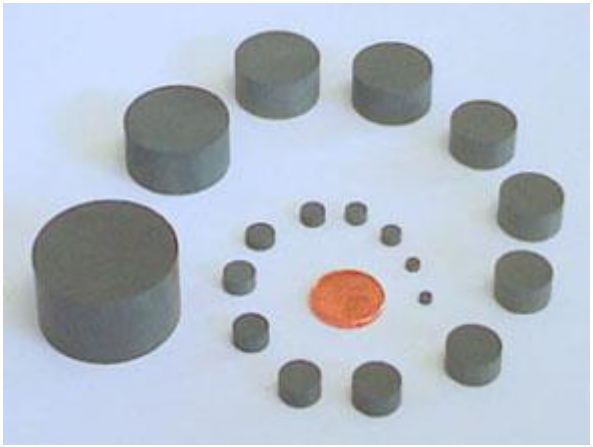

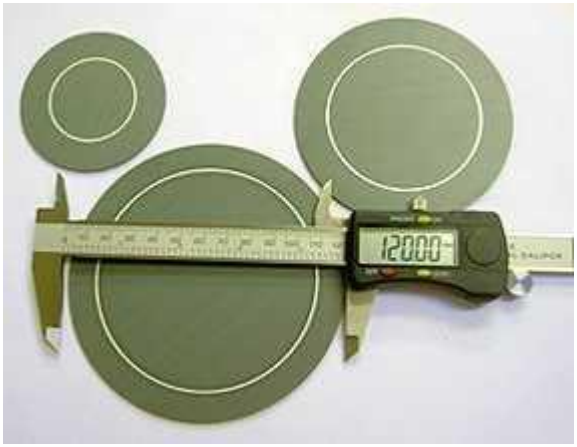

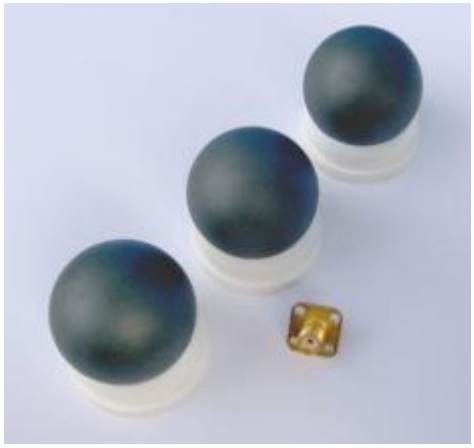

The discontinuity of the permittivity at the resonator surface allows a standing electromagnetic wave to be supported in its interior. High relative permittivity ceramics with high Q and controllable temperature coefficient can be manufactured at low cost and offer new design opportunities for microwave engineers.

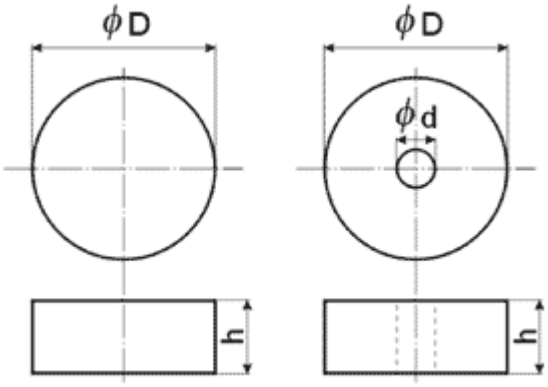

Material		E-37	E-20
Frequency Range	GHz	0.9 ... 18	1.8 ... 24
Frequency tolerances	± %	0.2 ... 1	0.2 ... 1
Unloaded Q-factor at 10 GHz	Q_0	> 4 800	> 5 200
Temperature Coefficient	TC_f (ppm K^{-1})	-6/-3/0/3/6/9 (±2 or 1)	-6/-3/0/3/6/9 (±2 or 1)
Outer diammeter	D (mm)	3 ... 62 (up to 120)	3 ... 62 (up to 120)
Height	h (mm)	1 ... 35	1 ... 35

- **Standard production types are cylinders with rate h/D = 0.4**
- **Resonators of custom diameters, height, temperature coefficient and tolerances can be produced in short terms**
- **Frequency tolerance limits and Q are tested for each resonator**
- **Development kits with exact frequency scale are offered**
- **Free samples can be requested for prototype testing**

B3: Carrier Mobility in Silicon

Doping cm^{-3}	Electron Mobility (cm^2 V-sec)	Hole Mobility (cm^2 V-sec)
10^{14}	1500	450
10^{15}	1500	450
10^{16}	1400	440
10^{17}	1200	410
10^{18}	800	200
10^{19}	200	150
10^{20}	90	50

Actual values will vary.

B4: Electrical properties of Silicon

Breakdown field ≈3·105V/cm

Mobility electrons ≤1400 cm^2 $V^{-1}s^{-1}$

Mobility holes ≤450 cm^2 $V^{-1}s^{-1}$

Diffusion coefficient electrons ≤36 cm^2/s

Diffusion coefficient holes ≤12 cm^2/s

Electron thermal velocity 2.3·105m/s

Hole thermal velocity 1.65·105m/s